Characterisation of the filamentous bacteriophages end-caps

A thesis presented in partial fulfilment of the requirements for the degree of

Doctor of Philosophy

in

Biochemistry

at Massey University, Manawatu,

New Zealand.

Rayén León Quezada

2021

Abstract

Ff (f1, fd, and M13) filamentous phage of *Escherichia coli* have collectively been the workhorse of phage display technology over the past few decades. Their use has expanded in the recent years into nanotechnology, where they serve as filament-like templates (≥ 880 nm x 6 nm) for assembly of nanostructures such as nanowires, nanorings, and more complex assemblies including nano-scale batteries, among others. The filament end-caps are the key to improving phage display applications and design of novel Ff-built nanostructures. Furthermore, proteins pIII and pVI, that form the distal end-cap, are of key importance for understanding the Ff biology. They mediate the Ff assembly-release and entry, two opposing processes that involve, respectively, excision and insertion of the virion out of and into the inner membrane of *E. coli*. The mechanisms of these two processes are a mystery, and the only path towards understanding is to determine the structures of the pIII-pVI complex. While the atomic resolution structure of the Ff filament shaft made of the major coat protein pVIII has been determined, the structure of the phage end-caps remains unresolved, as they constitute only 2% of the virion mass.

To enable the end-cap structural analyses we developed methodology for high-efficiency production and purification of short Ff-derived nanorods, where the end-caps are highly enriched, accounting for up to 38% of the total virion mass. Furthermore, methods for Ff-derived nanorod production have been majorly improved in this thesis by engineering a novel system, resulting in at least 200-fold

increase relative to the systems described previously. The nanorod purification was also improved by including an anion exchange chromatography step.

Highly pure and concentrated 50 nm and 80 nm nanorods were analysed structurally and biochemically to characterise the pIII-pVI complex. Intact nanorods were structurally characterised by cryo-EM single-particle analysis (cryo-EM SPA) that resulted in 2D classes of the filament end-caps. Furthermore, a preliminary 3D model of the pIII-pVI cap was generated at a resolution of 5 Å. Further refinement of the 3D model is under way. Besides the intact particles, analysis was expanded to purified pIII-pVI complex obtained from the DOC-chloroform-disassembled nanorods by size exclusion chromatography. Under native conditions, protein pIII could be detected in a complex larger than 720 kDa, indicating that multiple copies of pVI and pIII form a multimer-dimer that includes a substantial amount of the shaft protein, pVIII.

Applications of nanorods benefit from precise control of the nanorod lengths, which is very difficult to achieve when it comes to non-biological materials. In this thesis, Ff-derived nanorods of novel sizes were designed by eliminating specific DNA regions from the nanorod replication cassettes that controls the length of the nanorod ssDNA backbone. This work showed that the DNA segment between the packaging signal and (-) *ori* is not essential for replication and resulted in production of 40 nm nanorods, shortest ever constructed to date. Two novel lengths, 40 and 70 nm, were added to the of sub-100-nm nanorod collection produced using this system.

Acknowledgements

First and foremost, I would like to thank my primary supervisor, Assoc Prof Jasna Rakonjac, for giving me the opportunity to come to New Zealand to do my PhD in something I have always been passionate about, and for guiding me through all the ups and downs this process has had. Thank you for all the feedback and advice, I have learned so much from you, and I will always be grateful. To my co-supervisor, Assoc Prof Andrew Sutherland-Smith, who has always have been kind and supportive. Your feedback and discussions improved this thesis considerably. I'm very thankful to have had the opportunity to learn from you.

To Dr Vicki Gold and her research team, especially to Rebecca Conners and Mathew McLaren, for their collaboration and contribution to this project, it has led to valuable results.

To my incredible colleagues Catrina Olivera, Cathy Davenport, Vuong Le, and Stephanie Baird who made this intense experience more entertaining. Thank you for all the help, the teaching, the support, and, of course, the laughs. More than colleagues, you became friends that I will never forget. A special thanks to Majela Gonzalez for all your care and support. Thank you for training me and helping me to adapt to this new work environment.

I would also like to thank the team at the MMIC: Matthew Savoian, Niki Minard, and Raoul Solomon, for all your help and training. A special thanks to Trevor Loo for all your assistance, guidance, and patience on protein methods and analysis. To

Yongdong Su, for all your help with the fluorescence reader. And, of course, to Ann Truter for making my life easier, your help was sincerely appreciated.

I would also like to thank Carmine family, anonymous donor for supporting my doctoral scholarship financially.

I am also extremely grateful for the incredible friends or, why not, the family I chose here in New Zealand. Starting something alone in a new country is scary, but you guys always had my back and were always ready to get a coffee or hang out in moments of need. Thank you, Patricia Rubio, Laura Teuma, Angela Bravo, Charline Lormand, Sebastian Rivera, Paul Chambonnière, David Flossdorf, Kate Andrew, Tianyang Wang, Silvia de la Rosa, Mariana Tarallo and Mercedes Rocafort. You made my life happier during this experience.

I'm grateful for my amazing friends in Chile, Brian Rivas, Carla Henriquez, Matias Alegria, Pablo Garcia, Matias Osorio, Macarena Cartes, Fernanda Tapia, Luis Troncoso, Joao Aguilar, Gustavo Sobarzo, among many others. Thank you for all the support through the most challenging times, for lifting me up when I was feeling down, and for always believing in me, even when I did not.

Finally, I would like to thank my family. To my beloved parents, Elena Quezada and José León, and my grandmother, Elena Cárdenas. I could never express enough gratitude for all the things you have done for me. Thank you for making me the person I am today. This is for you.

Table of contents

List of figures

List of tables

List of abbreviations

aa:	Amino acid
Aβ:	β-amyloid
Ala:	Alanine
AD:	Alzheimer's Disease
Amp:	Ampicillin
Amp^R:	Ampicillin resistant
Arg:	Arginine
Å:	Ångström
Asp:	Aspartic Acid
bp:	Base pair
BSFnano:	Biological scalable Ff-derived nanorods
BSA:	Bovine serum albumin
BPB:	Bromophenol blue (3′,3″,5′,5″- tetrabromo-phenol sulfonphthalein)
CsCl:	Caesium chloride
Cm:	Chloramphenicol
cfu:	Colony-forming units
CMC:	Critical Micellar Concentration
Cryo-EM:	Cryo-electron microscopy
Cryo-EM SPA:	Cryo-Electron Microscopy Single Particle Analysis
Cys:	Cysteine
CV:	Column Volumes
DMSO:	Dimethyl sulfoxide
DNA:	Deoxyribonucleic acid
DNase:	Deoxyribonuclease
DOC:	Sodium deoxycholate
dsDNA:	Double stranded DNA
DTT:	Dithiothreitol

EDTA:	Ethylenediaminetetraacetic acid
E. coli:	*Escherichia coli*
EtBr:	Ethidium bromide
fAβ:	β-amyloid fibres
Ff:	F-pilus specific filamentous phage
g:	gram
g:	g-force
GAIM:	General Amyloid Interaction Motif
Glu:	Glutamic Acid
Gly:	Glycine
h:	Hour(s)
HRP:	Horseradish peroxidase
ICS:	Infection-competence segment
IG:	Intergenic sequence/region
IF:	Infective form
IPTG:	Isopropyl β- d-1-thiogalactopyranoside
kb:	Kilobase
kDa:	Kilodalton
Km:	Kanamycin
Km^R:	Kanamycin resistant
L:	Litre
lacUV5:	LacUV5 promoter
LFA:	Lateral Flow Assay
Lys:	Lysine
M:	Molar
MCS:	Multiple cloning site
μm:	Micrometre
μM:	Micromolar
μL:	Microlitre
mAu:	milli Absorption units
mg:	Milligram

min:	Minute(s)
mM:	Millimolar
mL:	Millilitre
mRNA:	Messenger ribonucleic acid
Mw:	Molecular weight
MWCO:	Molecular Weight Cut-Off
ng:	Nanogram
nt:	Nucleotides
OD:	Optical Density
ORF:	Open Reading Frame
ori:	Origin of replication
p_A:	p_A promoter
PAGE:	Polyacrylamide Gel Electrophoresis
PCR:	Polymerase Chain Reaction
PDB:	Protein Data Bank
PEG:	Polyethylene glycol
pfu:	Plaque-forming units
Phe:	Phenylalanine
pp:	Phagemid particle
PS:	Packaging Signal
RF:	Replicative Form
RNase:	Ribonuclease
rpm:	Revolutions per minute
RT	Room Temperature
SDS:	Sodium dodecyl sulphate
Sec:	Seconds
Ser:	Serine
ssDNA:	Single stranded DNA
TAE:	Tris, Acetic acid, EDTA buffer
TBS:	Tris Buffer Saline
TEM:	Transmission Electron Microscopy

Tyr:	Tyrosine
USD:	U.S. Dollar
V:	Volt
V/cm:	Volt/centimetre ratio
vs.:	*Versus*
v/v:	Volume/volume ratio
wt :	Wild-type
w/v:	Weight/volume ratio
ZnS:	Zinc sulfide
º C:	Degree Celsius
2D:	Two Dimensional
3D:	Three Dimensional
(-):	Negative
(+):	Positive

Chapter 1:

Introduction

1.1 Filamentous bacteriophage

Bacteriophage are, as implied by the name (phage, from the Greek phageîn "to eat" bacteria), viruses that infect specific bacterial strains. They are the most abundant group of organisms on the planet, reaching an estimated total number of 10^{32} on Earth. With a high diversity in their morphological forms, genetic content (DNA or RNA), and their specific host, they have been classified into taxonomic categories by the International Committee on Taxonomy of Viruses (ICTV) (Dion *et al*., 2020; Hay & Lithgow, 2019; Wittebole *et al*., 2014).

Filamentous phage belongs to the Inovirus genus within the Inoviridae family. Unlike most phage present in nature, they have a filament-like morphology and are secreted out of the host, which continues the cell cycle at 50% efficiency relative to the uninfected parent. Some filamentous phage replicate as episomes by a rolling circle mechanism, and some integrate into the host chromosome to become prophage (Mai-Prochnow *et al*., 2015; Rakonjac *et al*., 2017). These long, thin, and flexible viruses infect a wide range of Gram-negative bacteria (such as *Escherichia, Pseudomonas, Salmonella, Yersinia*, among others). Only two published reports identified filamentous phage that infect Gram-positive organisms, *Clostridium acetobutylicum* and *Propionibacterium freudenreichii* (Chopin *et al*., 2002; Kim & Blaschek, 1991).

Ff phage are filamentous phage of *Escherichia coli (E. coli)* that use the F-pilus as the primary receptor. They replicate as episomes and do not integrate into the host

chromosome. From their discovery until the present time, Ff phage have been used for a wide range of applications. Biotechnology and biomedical applications include recombinant DNA technology, phage display, *in vivo* protein evolution, and tissue targeting. Due to the ease of genetic manipulation, highly organized structure, self-assembly, resistance to heat, detergents, and a broad pH range, Ff phage applications have also been expanded into nanotechnology (Ngo-Duc *et al*., 2018). As this thesis is focused on bionanotechnological applications of filamentous phage; I will refer only to the Ff phage as they are the only filamentous phage used extensively in bio- and nano-technological applications.

1.2 Ff phage biology

Ff phage (M13, f1, and fd) are the most extensively studied filamentous phage from their discovery in 1960 to date. Most of the understanding of filamentous phage biology, hence, comes from the work on Ff phage. Although the three Ff phage are taxonomically categorised as three species, they are nearly identical, having 98% of DNA sequence identity (Marvin *et al*., 2014; Rakonjac *et al*., 2017; Russel & Model, 1989). Within the studies of their biology and biotechnology applications, they have been used interchangeably, including mixing and matching segments of their genomes.

1.2.1 Ff phage structure

The Ff virions consist of a circular single-stranded DNA (ssDNA) genome in the form of a right-handed helix of variable length, which serves as a filament's backbone. DNA interacts with proteins that form the shaft and caps of the virion (Marzec & Day, 1983; Marzec & Day, 1988). Interestingly, it has been reported that there are no lipids in the virion (Day, 2012). The ssDNA helix ends with two loops, one of which corresponds to a 32-nucleotide Watson-Crick hairpin that serves as a packaging signal at which the virion assembly is initiated (Russel & Model, 1989). The Ff virions' length depends on the size of the encapsidated ssDNA (genome), and for the wild type, it is about 880 nm (Figure 1). The length of engineered Ff variants depends on the size of the recombinant genome, while the virion diameter is ~ 6 nm, with a rise per nucleotide pair, or h, of 0.28 nm (Day, 2012).

The helical capsid surrounding the ssDNA of the wild type Ff phage comprises ~ 2700 copies of a 50 residue α-helical protein, pVIII, which is capped by four minor proteins: pVII and pIX at the proximal end, and pIII and pVI at the distal end (Figure 1B). Based on the symmetry of the virion, Ff phage belongs to the Class I symmetry group, where the pVIII subunits are arranged in a five-start helix with a 2-fold screw axis (C_2S_5); while other phage like Pf1 of *Pseudomonas* and phage Xf of *Xanthomonas* belong to the Class II symmetry group, where the pVIII subunits are arranged as a simple one-start helix ($C_1S_{5.4}$) (Marvin *et al*., 2014; Marzec & Day, 1988). The atomic-resolution information about the structure of the major protein pVIII along the virion filament was acquired as early as three decades ago

(Goldbourt *et al*., 2007; Marvin *et al*., 2006); nevertheless, the structures of the end-caps formed by two pairs of the minor coat proteins pIII-pVI and pVII-pIX remain a mystery. Based on pIII labelling with ZnS quantum dots, it was determined that there are five copies of this minor protein in the virion (Lee *et al*., 2002), and as they have been reported to be present in an equimolar stoichiometry, there have to be five copies of each pVI, pVII and pIX (Grant, Lin, Webster, *et al*., 1981).

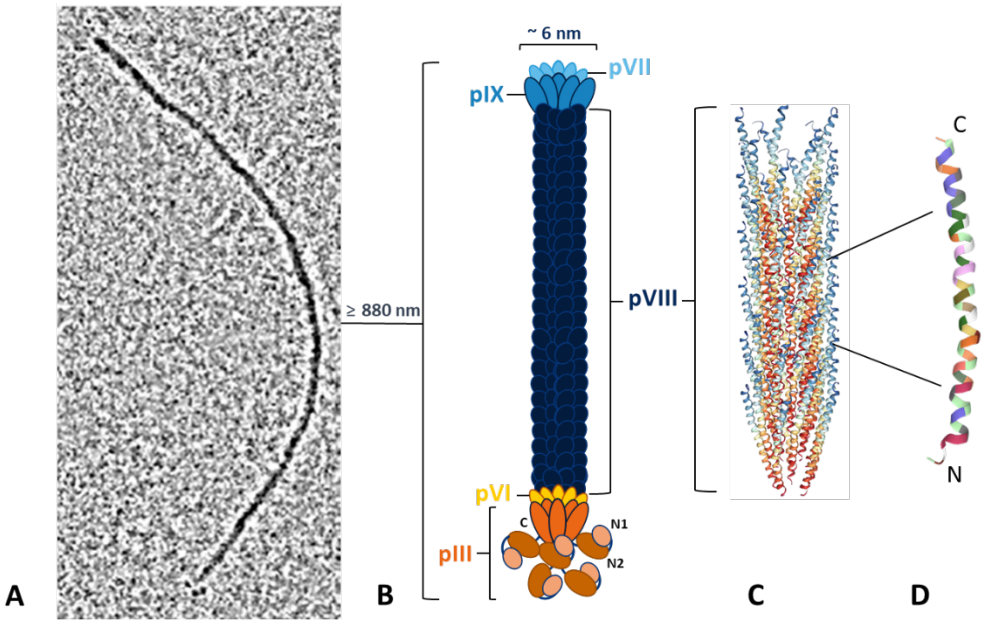

Figure 1.Morphology and structure of the Ff virion.

(A) Electron micrograph of Ff phage. Taken from Gray *et al*. (1981), with permission. (B) Schematic representation of the Ff phage virion. (C) Ribbon representation of the Ff phage capsid. (D) Model of pVIII protein. Adapted from Rakonjac *et al*. (2011), with the authors' permission.

The Ff filament capsid structure, built from thousands of pVIII subunits, has been solved at atomic resolution using X-ray fibre diffraction, NMR, and cryo-EM single-particle analysis (Cryo-EM SPA). It was determined using these analyses that the major coat protein pVIII subunits form an array of α-helices arranged with

the long axes of the helices oriented with an average subunit α-helix tilt angle (θh) of 16-20º to the long axis of the fibre (Figure 1C and D) ((Marvin *et al*., 2014; Overman *et al*., 1996). The major coat protein pVIII is a small protein (5.34 kDa), composed of three different regions (Figure 2): (i) A hydrophilic region at the N-terminus (residues 1 to 20), forms the surface layer of the filament, and is composed of predominantly negatively charged and polar amino acids; (ii) a central region (residues 21 to 39), composed of hydrophobic amino acids which mediate inter-subunit interactions; and (iii) a positively charged region at the C-terminus (residues 40 to 50), corresponding to the inner layer that interacts with ssDNA, composed of basic amino acids including four lysine residues (Figure 2) (Chung *et al*., 2014; Nakashima *et al*., 1975; Zimmermann *et al*., 1986). The segment of pVIII hydrophilic region, from residues 6 to 16, form an amphipathic helix. Here, the helix's hydrophilic face is exposed to the aqueous environment, whereas the hydrophobic face and the adjacent hydrophobic transmembrane helix (residues 24 to 46) interact with the C-terminal regions of other subunits via multiple hydrophobic interactions, holding the capsid together (Chung *et al*., 2014; Marvin *et al*., 2014). Newman *et al*. (1977), calculated the ratio of pVIII subunit per nucleotide as 0.42 ± 0.01.

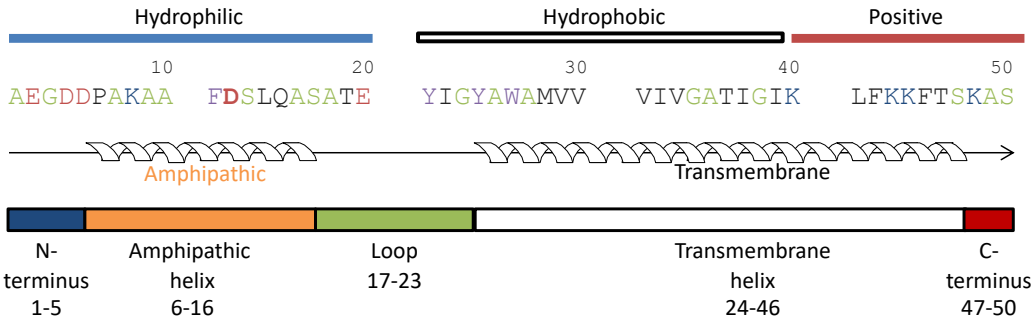

Figure 2. Amino acid sequence of the major coat protein, pVIII including a schematic diagram of the secondary structure.

The primary sequence of pVIII from fd phage. Asp12 (in bold), is Asn12 in phage M13. Colour coding of amino acids in the sequence is as follows: small residues Gly, Ser, and Ala, green; aromatic residues Phe and Tyr, purple; acidic residues Asp and Glu, red; basic residues Lys and Arg, blue. Under the amino acid sequence, a schematic representation of the secondary structure of pVIII, highliting its different structures by coloured boxes; in blue, the N terminus of pVIII; in orange, the amphipatic helix; in green, a loop; in white, the transmembrane helix; in red, the C terminus of pVIII.

Unlike pVIII, there is little information about the structure and organization of the minor virion proteins that form the caps. From immuno-electron microscopy studies, it could be determined that the minor protein pVII (32 residues; 3.6 kDa) is completely hidden inside the virion while pIX (33 residues; 3.7 kDa) is partially exposed on its surface (Endemann & Model, 1995). It has also been predicted that pVII and pIX form hydrophobic α-helices, which are expected to mediate interactions with each other and pVIII in the virion (Marvin, 1998). Protein pIII (424 residues including the signal peptide; 44.6 kDa with the signal peptide and 42.6 kDa for the mature protein) is composed of N1, N2, and C domains (Figure 3). This protein has great importance due to its essential roles in Ff phage infection and assembly. The N1 and N2 domains of pIII are visible in some electron micrographs

as small knob-like structures (Figure 1A) (Gray *et al*., 1981). The N1 and N2 domains of pIII fold independently of the C-terminal domain, to which they are connected by a very long glycine-rich linker (Figure 3A). The recombinant N1 and N2 domains have been expressed and purified on their own, and their structure has been solved at atomic resolution (Figure 3B). These domains consist primarily of β-sheets linked to each other by another glycine-rich linker. The N1 domain is composed of a 5-stranded antiparallel β-sheet, arranged in a barrel-like motif with two β-strands of the N2 domain (β6 and β13), and with an α-helix packed at the N-terminus against the ends of the strands β4 and β5 (Holliger *et al*., 1999; Lubkowski *et al*., 1998). In contrast to the N domains of pIII, there is no structural information about the C domain of pIII. Similarly, there is no information on pVI structure. The C domain of pIII and protein pVI form a tight complex at the cap of the virion; this complex can only be extracted from the virion by a combination of organic solvents and detergents (chloroform, deoxycholate, or Triton X-100) (Gailus & Rasched, 1994). Upon chloroform exposure, Ff virions undergo morphological changes, contracting into two well-defined structures containing the pIII-pVI (distal end-cap) complex: (i) hollow spherical particles, also called spheroids (S-forms; Figure 4A), and (ii) hollow trumpet-like particles with a flared end, called intermediate forms (I-forms; Figure 4B) (Griffith *et al*., 1981; Lopez & Webster, 1982; Manning *et al*., 1981). Protein pVI (112 residues; 12.4 kDa) is mostly hydrophobic, and like other Ff virion proteins, it is an integral membrane protein before assembly into the virion (Endemann & Model, 1995). It is predicted to contain three transmembrane α-helices (with N-terminus in the periplasm and the C-terminus in the cytoplasm) by the TMHMM 2.0 algorithm (Krogh *et al*., 2001).

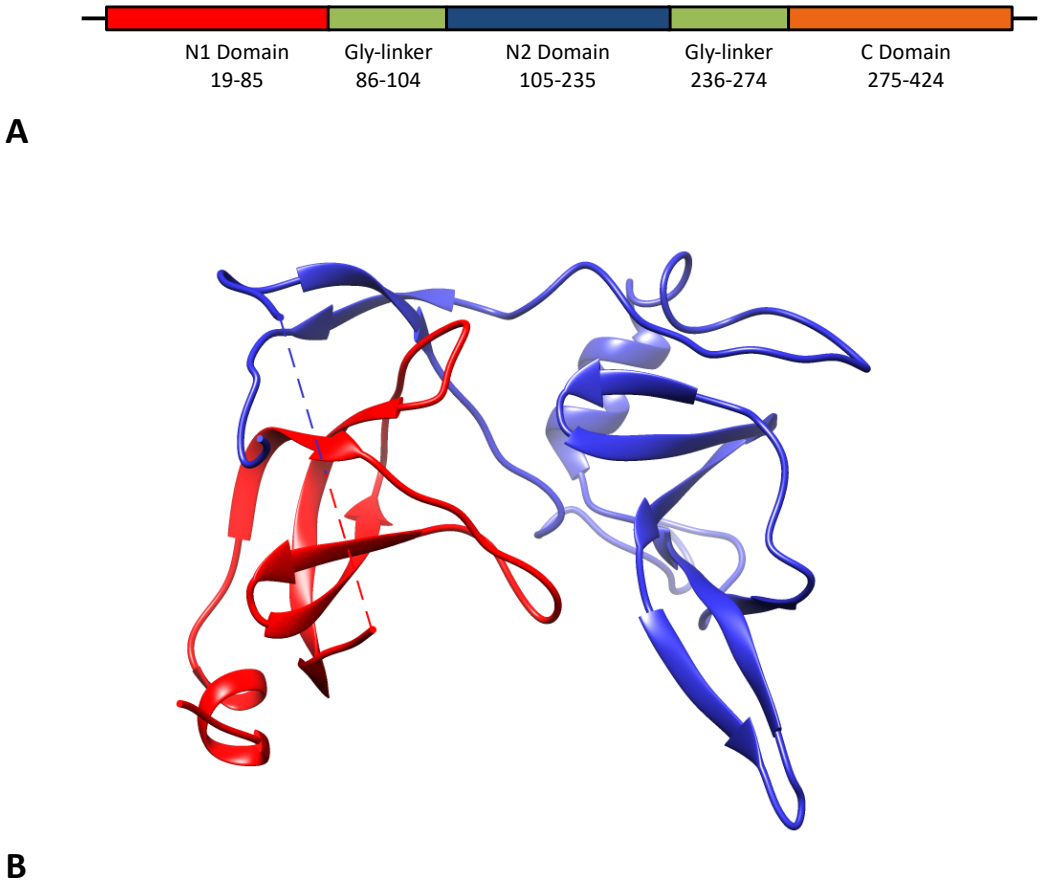

Figure 3. Protein pIII of Ff phage.

(A) Schematic diagram of the secondary structure of protein pIII of Ff phage. Red block represents pIII N1 domain; green blocks represent the glycine-rich linkers between the N domains and between the N2 and the C domain; blue block represents the N2 domain; and orange block represents the C domain. (B) Crystal structure of the N1 and N2 domains of protein pIII. The N1 domain is represented in red, while the N2 domain is represented in blue. The image was obtained from the PDB file (1G3P)(Lubkowski *et al*., 1999).

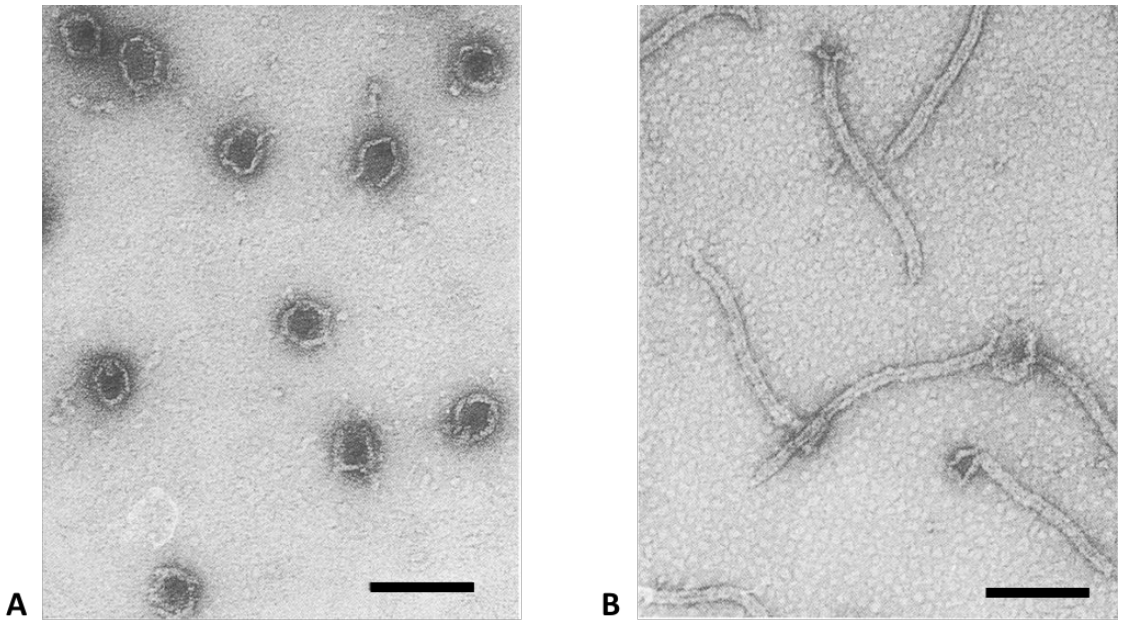

Figure 4. Electron micrographs of f1 phage S-forms and I-forms upon chloroform exposure.

Taken from Lopez & Webster (1982), with the publisher's permission.

1.2.1.1 The roles of pIII C domain in membrane insertion, excision and virion stability

Besides its structural role, the C domain of pIII has another two essential roles involved with transitions of the virion in and out of the host cell. These roles involve the insertion into the membrane during infection and excision from membranes at the assembly termination step.

No structures of C domain homologs have been determined to date; hence reliable modelling is not possible. However, the C domain of pIII has very low homology to another group of proteins capable of assuming soluble and integral membrane

forms, the α-helical pore-forming toxins *(*Bennett *et al., 2011;* Choe *et al., 1992)*. A predominantly α-helical secondary structure was predicted using a 3D modelling program (I-TASSER) and a secondary structure prediction program (Jpred; Figure 5A and B, respectively) (Bennett *et al*., 2011).

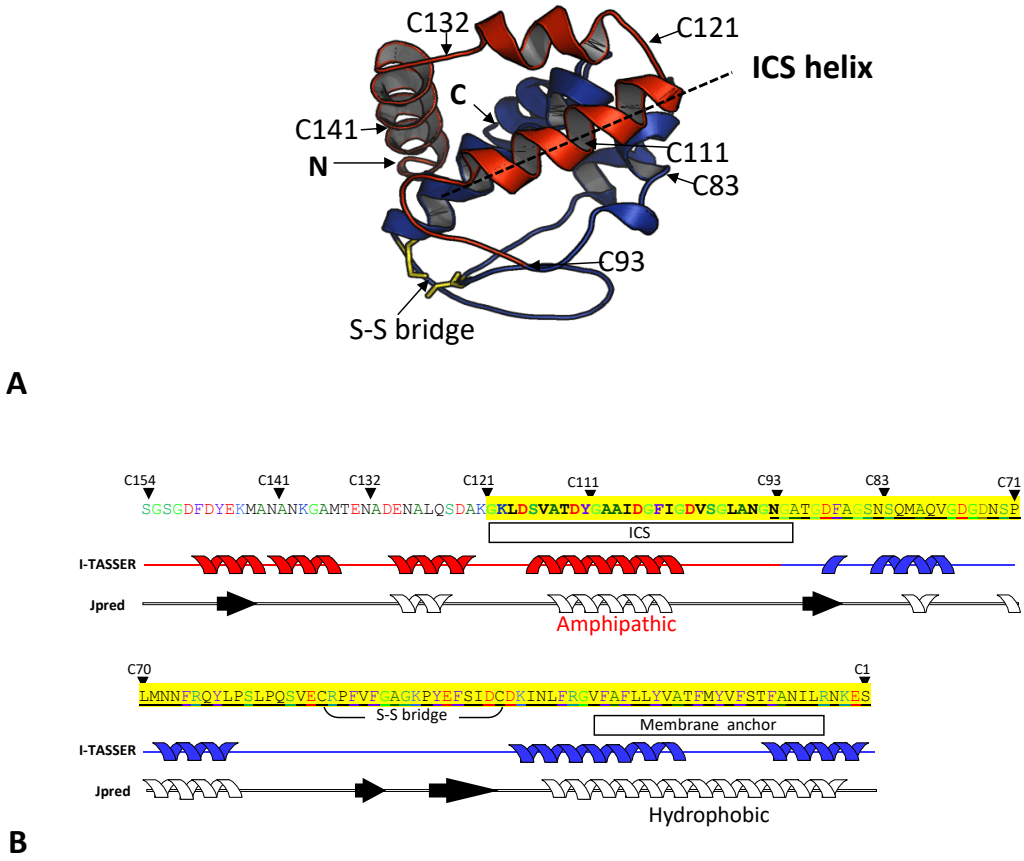

Figure 5. Structural modelling of the pIII C domain.

(A) Ribbon diagram model of the pIII C domain obtained by the I-TASSER protein structural modelling software. The residues defining the C-terminal fragments (C141–C83) in the mutants described by Bennet et al. (2011) are labelled, counting from the C-terminal end. Red, residues 154–94; blue, residues 93–1 (counting from the C-terminus). (B) Primary sequence of the pIII C domain. Colour coding of amino acids in the sequence is as follows: small residues Gly, Ser, and Ala, green; aromatic residues Phe and Tyr, purple; acidic residues Asp and Glu, red; basic residues Lys and Arg, blue. Highlighted in yellow, C-terminal 121 residues required for infection of the host (insertion into host membrane); Bold letters, the infection-competence segment (ICS); Underlined, C-terminal 93 residues

required for termination of assembly (release from the membrane); Box under the sequence, membrane anchor; The disulphide bridge is indicated by a line connecting two Cys residues. Secondary-structure predictions are shown below the sequence. Under the amino acid sequence, a schematic representation of the secondary structure prediction by the I-TASSER and Jpred algorithm. Taken from Bennet *et al*. (2011), with authors' permission.

The C domain contains a hydrophobic membrane anchor (23 residues) at its C-terminus, with only five C-terminal residues located in the cytoplasm. The remaining portion (127 residues N-terminal to membrane anchor) is located in the host cell's periplasm (Davis *et al*., 1985). Bennett and Rakonjac (2006) reported that the C domain of pIII is required for Ff entry. Bennet *et al*. (2011) further demonstrated, from a study of nested internal deletions progressively reducing the portion of C domain deletions, that a C-terminal portion of the C domain of at least 121 residues is required for infection of the host (Figure 5B). Interestingly, this portion of the C domain is also needed for the assembly of a detergent-resistant virion (Rakonjac *et al*., 1999). The C domain of pIII is necessary not only for infection, but also for termination of virion assembly and its release from cell membranes. It contains one disulphide bridge between Cysteines 354-371 (or 43-25 counting from the C-terminus), which is required for assembly (Kremser & Rasched, 1994). Moreover, from assessing assembly termination using a set of nested deletions in this domain, it was possible to determine that a fragment containing C-terminal 83 residues is sufficient for the incorporation of pIII and pVI into the assembling phage particle, however, not for its release. A larger fragment containing only ten more residues (93) can release phages from the cell, and

therefore, these 93 residues at the terminus of the C domain of pIII are essential for the release from the membrane (Rakonjac *et al*., 1999).

Combining the above-described infection and assembly studies, a segment between residues 121 and 93 (counting from the C-terminus) was identified that is required for infection but dispensable for release from the membranes and termination of assembly, and was denoted "infection-competence segment" (ICS) (Bennett *et al*., 2011). Modelling the C domain tertiary structure using I-TASSER and secondary structure using Jpred predicted that the ICS contains an amphipathic α-helix (Figure 5), followed by two amphipathic helices and a hydrophobic α-helix corresponding to the membrane anchor (between the residues 28 and 5, counting from the C-terminus).

1.2.2 Ff phage genome organization and function

The genome of Ff phage contains eleven genes (Table 1) organized in two operons (Figure 6). All Ff genes are clustered in three groups according to their function: (i) replication (*gII*/*gX* and *gV*), (ii) capsid (*gVII, gIX, gVIII, gIII and gVI*), and (iii) assembly and secretion (*gI*/*gXI* and *gIV*).

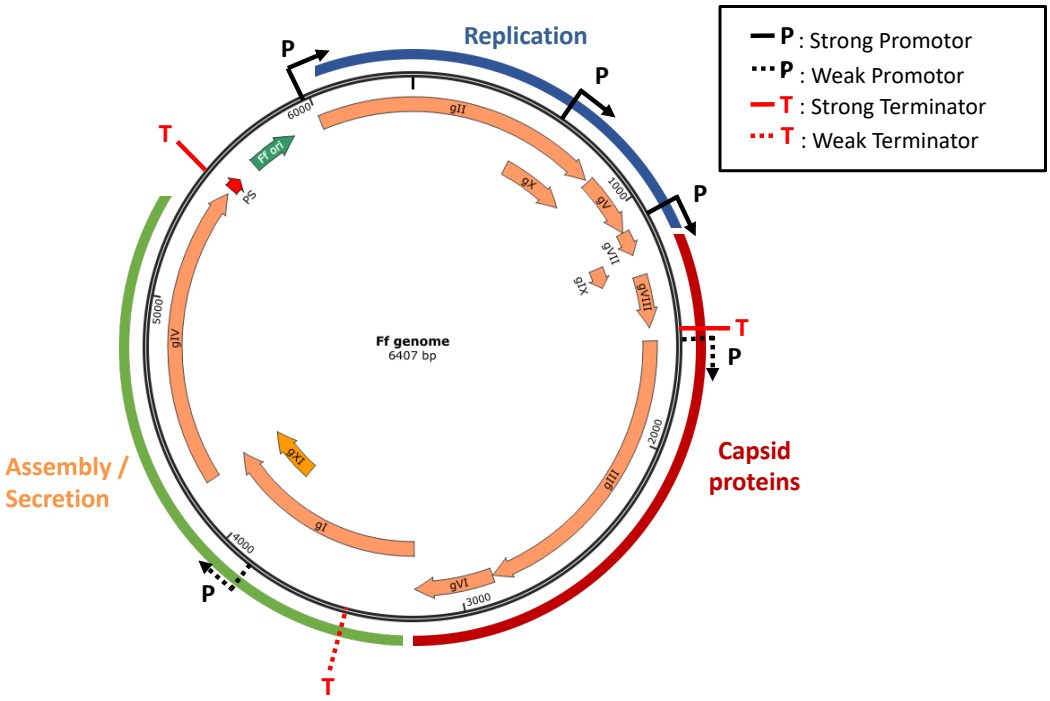

Figure 6. Genes and genome organization of Ff phage.

All the genes, the intergenic region (Ff *ori*) promoters and terminators, are represented on the map. Orange block arrows indicate phage genes; Dark green block arrow indicates the Ff origin of replication; Promoters are represented with black arrows and terminators with red lines, solid lines represent strong promoters or terminators and dashed lines represent the weak ones; Highlighted in blue are the genes encoding for proteins responsible for replication; Highlighted in red are the genes encoding for capsid proteins; Highlighted in light green are the genes encoding for proteins responsible for assembly and secretion. Figure and legend adapted from Smeal *et al*. (2017) with the publisher's permission.

Table 1. Genes and proteins of Ff phage

Gene/ Protein	Function
gI → pI (g1p)	**Morphogenesis (phage assembly-export)** • Inner membrane component of the trans-envelope assembly/secretion system. Interacts with pIV.
gII → pII (g2p)	**Replication** • Replication protein of replication family (rolling circle replication). • Cleaves the (+) strand of the dsDNA replicative form (RF). • Joins the ends of the displaced (+) strand to generate a circular single-stranded DNA.
gIII → pIII (g3p)	**Structural** • Forms the pIII/pVI virion cap. • Interacts with pVI, pVIII, and domain III of TolA protein. • Essential role in all the stages of infection and in termination of Ff assembly, and release of new virions from the host membranes.
gIV → pIV (g4p)	**Morphogenesis (phage assembly-export)** • Forms a gated channel across the host outer membrane through which virions are exported.
gV → pV (g5p)	**Replication** • ssDNA binding protein. • Coats (+) strand ssDNA to form an assembly substrate. • Negatively regulates the translation of *gII* mRNA
gVI → pVI (g6p)	**Structural** • Forms the pIII/pVI virion cap. • Essential role in termination of assembly, and release of new virions from the host membranes.
gVII → pVII (g7p)	**Structural** • Forms the pVII/pIX virion cap

	• Initiates the virion assembly-export process, along with pIX, by interacting with the packaging signal of the viral genome, and pI/pXI complex.
gVIII → pVIII (g8p)	**Structural** • Major coat protein • Assembles to form a helical filament-like capsid, wrapping up the viral genomic DNA.
gIX → pIX (g9p)	**Structural** • Forms the pVII/pIX virion cap • Initiates the virion assembly-export process, along with pVII, by interacting with the packaging signal of the viral genome, and pI/pXI complex.
gX → pX (g10p)	**Replication** • Promotes the RF synthesis and depresses the accumulation of ssDNA. • Inhibits the activity of pII.
gXI → pXI (g11p)	**Morphogenesis (phage assembly-export)** • Part of a trans-membrane complex with pI and pIV to protect pI from cleavage by endogenous proteases.

Transcription of Ff genes is driven by five promoters and terminated by three terminators (Figure 6). The negative strand is the template for all transcripts, resulting in several overlapping RNAs present in specific different amounts (Jacob & Hofschneider, 1969). This differential abundance allows for regulation of protein production (Okamoto *et al*., 1977).

Between genes IV and II, there is a 508-nucleotide intergenic region (IG) that does not code for any proteins (Horiuchi *et al*., 1975; Model *et al*., 1975; Van Den Hondel *et al*., 1976; Vovis *et al*., 1975). This region is highly conserved in Ff phage,

and it contains sequences that are essential for replication and phage assembly (Horiuchi & Zinder, 1976). It is rich in stable loop-hairpin structures and is divided into several independent structural domains containing various regulatory elements for several functions, including a promoter (gene-II promoter) and a terminator (gene-IV terminator). This region contains the f1 origin (*ori*) of replication and a 32-nt packaging signal (PS). The f1 *ori* is composed of positive (+) and negative (-) origins for positive and negative strand replication, respectively (Figure 7) (Suggs & Ray, 1977). The (-) *ori* extends approximately from nucleotide 5609 to 5738 (Gray *et al*., 1978), where two stable hairpins, separated by an unstructured region, are located. These hairpins have a double-stranded character and resemble a typical -35 and -10 promoter (Horiuchi, 1997). The (+) *ori* consists of about 150 nucleotides where the initiation and termination signals are found and can be divided into two domains: A and B. Domain A is 42-nt long and is necessary for replication; it contains three partially overlapping sequences essential for (+) strand replication: (i) the protein II cut-site, (ii) a sequence required for initiation of (+) strand synthesis, and (iii) a sequence required for termination of replication. Domain B, on the other hand, is not absolutely essential. This domain was found to enhance the binding of pII to the (+) *ori* (Horiuchi, 1997). Upon disruption of this sequence, the phage yield lowers 100-fold; hence this domain is also known as the "replication enhancer sequence" (Dotto *et al*., 1984a; Dotto *et al*., 1984b; Dotto & Zinder, 1984; Greenstein & Horiuchi, 1987). Nevertheless, several compensatory mutations have been described in the 5'-untranslated regions of *gII* mRNA that restore phage propagation (Nguyen *et al*., 2014; Zygiel *et al*., 2017).

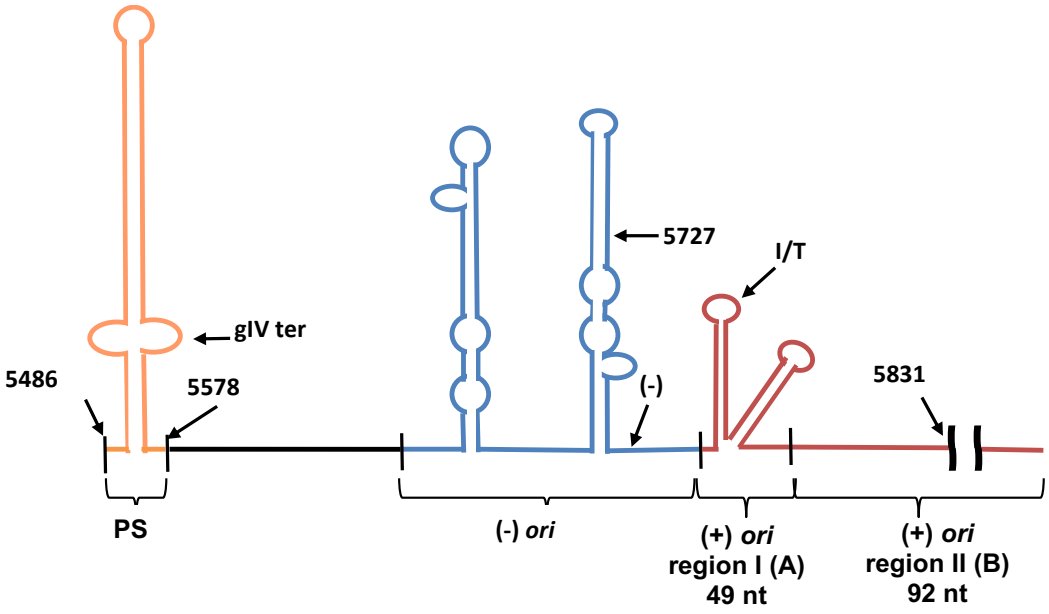

Figure 7. Ff intergenic sequence (IG) containing the origin of replication.

Orange represents the packaging signal (PS); Blue represents (–) *ori*, the negative strand origin of replication; Red represents the (+) *ori*, the positive strand origin of replication containing region I (A) and region II (B). Adapted from Rakonjac *et al*. (2017), with the authors' permission.

1.2.3 Ff phage life cycle

1.2.3.1 Infection

The Ff phage life cycle can be divided into three stages: (i) infection, (ii) replication, and (iii) assembly (Figure 8). The infection starts with the interaction of the virion with the primary and secondary receptor in the host *E. coli*, the conjugative pilus (F), and the TolQRA complex, respectively. The N2 domain of protein pIII binds to the tip of F-pilus on the cell surface. This binding is believed to induce signals

that cause pilus retraction and bring the virion close to the outer membrane and through the periplasmic space (Lubkowski *et al*., 1999; Riechmann & Holliger, 1997). Structural analyses of F-pilus binding by Ff phage has identified specific conformational changes in the pIII N2-domain that "unblock" the secondary-receptor-binding domain N1 (Chatellier *et al*., 1999; Martin & Schmid, 2003a; Martin & Schmid, 2003b). The secondary receptor is domain III of TolA protein, a component of the TolQRA inner membrane complex involved in controlling membrane integrity and cell division (Gerding *et al*., 2007). This complex is highly conserved in Gram-negative bacteria and appears to be a universal secondary receptor for several filamentous phage, including CTXϕ of *Vibrio cholerae* (Heilpern & Waldor, 2000; Holliger & Riechmann, 1997). It is not known how pIII gains access to the periplasm to contact TolA. The F-pilus is not absolutely required for Ff infection; in the presence of Ca^{2+} ions, Ff can infect "female" (F-pilus-negative) *E. coli* at an efficiency of about 0.1% relative to the F-pilus-positive cells (Russel *et al*., 1988). Ca^{2+} ions obviate the charge repulsion that usually exists between the phage and the cell surface, concentrating the phage at the surface; moreover, it also affects the permeability of the host membrane, increasing the accessibility of the TolQRA complex. In contrast to the F-pilus, TolA is absolutely required for Ff infection. It has been suggested that the C-terminus of pIII creates a pore by its insertion in the membrane that could allow the phage DNA access to the host cytoplasm (Glaser-Wuttke *et al*., 1989). This process results in the entry of the ssDNA into the cell, while the capsid proteins and their subunits (pIII, pVI, pVIII, pVII, and pIX) become inserted in the membrane, some of which can be reused for packaging new phage particles (Armstrong *et al*., 1983; Click & Webster, 1998).

1.2.3.2 Replication

Once the ssDNA (+) strand enters into the cytoplasm of the host, the (-) strand is replicated by the host replicative machinery from the (-) strand *ori* (Figure 8). The host RNA polymerase σ^{70} holoenzyme binds and synthetises an RNA primer between nucleotides 5736-5717 in the hairpin structure that mimics a bacterial -35 and -10 promoter sequence (Higashitani *et al*., 1993). Then, the host DNA polymerase III holoenzyme extends the primer to generate the (-) strand. Gyrase introduces negative supercoils to form supercoiled dsDNA called the replicative form (RF) (Geider *et al*., 1982; Hay & Lithgow, 2019; Meyer & Geider, 1979; Smeal *et al*., 2017a). There is evidence that the negative strand can be synthetized using single-stranded circular DNA as a template in the absence of (-) strand *ori*, but with a drastically lowered efficiency (1-5% of that of wild type M13 phage) (Kim *et al*., 1981). The RF serves as a template for transcription of the 11 phage genes and (+) strand replication to synthesize new positive ssDNA (also known as "infective form" or IF). The synthesis of the ssDNA (+) strand is initiated by protein pII, which binds to the (+) *ori* region A in the RF, forming a nick in the (+) strand by a cleavage reaction resembling the action of a strand-transferase at a set site (I or T), and stays covalently linked to the 5'-hydroxyl end of the nicked (+) strand (Horiuchi, 1997). Once the cut is made, the 3'-hydroxyl end serves as a primer for the host DNA polymerase III holoenzyme. The DNA polymerase, together with the *rep* helicase and in the presence of single-stranded binding proteins (SSB), begins synthesis of a new (+) strand while the old one is displaced (Geider *et al*., 1982). Once the circle is completed, pII cleaves the displaced strand at the I/T site and

ligates the two ends of the newly synthesized strand by a strand-transferase reaction displacing pII (Asano *et al*., 1999; Hay & Lithgow, 2019; Russel *et al*., 1988). In the early infection, the RF undergoes multiple rounds of replication increasing the rate of synthesis of IF DNA (positive strand circular ssDNA). As the concentration of phage proteins increases, the rate of RF DNA synthesis starts to decrease (Lerner & Model, 1981). Late in the infection, accumulation of protein pV results in its binding to the IF DNA to prevent its conversion to an RF and instead directs these ssDNA genomes for packaging into progeny phage (Guan *et al*., 1995). It has been described that another way of pV downregulating (+) strand replication is by binding to the untranslated 5' sequence of the mRNA upstream of gene II, blocking ribosome binding and thereby attenuating its translation; furthermore, it appears that pV also attenuates the translation of the other phage proteins, pI, pIII and pX (Michel & Zinder, 1989). pX, a protein translated from an internal start codon within the pII gene and so identical to the C-terminal third of pII, is assumed to have an inhibitory role over pII (Fulford & Model, 1984). For this reason, it has been assigned a regulatory role for RF and IF levels that is not yet well understood (Fulford & Model, 1988; Kokoska & Steege, 1998).

1.2.3.3 Assembly

The ssDNA (+) strand (IF) coated by protein pV, forms an ssDNA-pV complex. This complex (termed "packaging substrate") has an exposed hairpin loop (not covered by pV) that serves as a packaging signal and targets the genome to the membrane-embedded minor proteins pVII and pIX, to commence the virion

assembly by interacting with the inner membrane components of the Ff assembly-secretion complex composed of pI/pXI (Rapoza & Webster, 1993). Protein pI contains an essential ATP-binding Walker motif and, along with the proton motive force across the inner membrane, is likely to provide the energy for the assembly process (Feng *et al*., 1997). It is proposed that the shorter protein pXI, corresponding to the C-terminal portion of pI composed of membrane anchor and periplasmic domain, forms a mixed multimer with pI (Feng *et al*., 1999).

The outer membrane component of the Ff assembly-secretion machinery is pIV, a large homo-multimeric channel that belongs to the secretin family of bacterial channels involved in virulence factor secretion and assembly of type IV pili. The large internal diameter of pIV (8-10 nm) allows passage of Ff through the outer membrane (Opalka *et al*., 2003); however, in the absence of the phage it has a constriction or "gate" across the lumen of the barrel. Based on the solved near-atomic resolution structures of pIV homologues (Korotkov *et al*., 2009; Worrall *et al*., 2016; Yan *et al*., 2017) and genetic evidence, the amino-terminal domains N0 and N1 of pIV reach deep into the periplasm where N0 interacts with the pI/pXI complex (Feng *et al*., 1999), while its carboxy-terminal "secretin homology domain" forms a barrel containing the channel gate and outer membrane anchor (Spagnuolo *et al*., 2010). As ssDNA-pV complex reaches pI/pXI complex at inner membrane level, pV dissociates from DNA and is replaced by the major coat protein pVIII. Once the ssDNA is entirely covered by pVIII, the minor proteins pIII and pVI are added at the end of the virion. These two proteins have two roles: Forming a stable filament end-cap and releasing the filament from bacterial envelope (Rakonjac *et al*., 2011).

As just described, the Ff phage life cycle is not yet fully understood. A complete understanding about their morphogenesis requires as much information as possible about the structure of the phage particle, particularly from their end-caps which and as previously mentioned, remains a mystery.

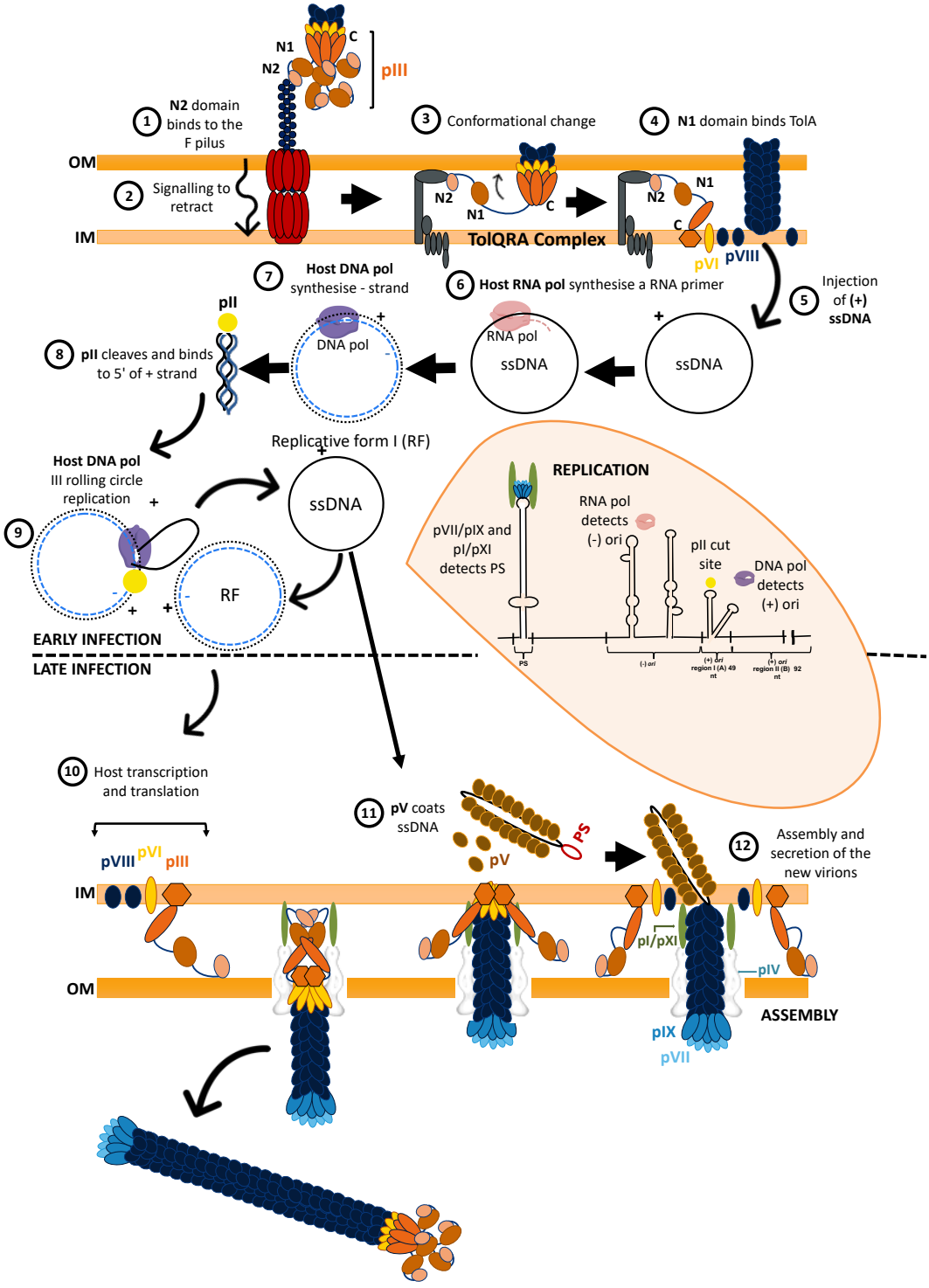

Figure 8. Ff phage life cycle.

Ff phage infection starts with the attachment of the virion to the host cell. The N2 domain of protein pIII binds to the F-pilus (1) which causes its retraction and brings the virion close to the host cell's surface, to the periplasm. Upon pilus binding and retraction, pIII goes through conformational changes,which "unblocks" the pIII N1 domain (3). The N1 domain of pIII binds then to the TolA host protein in the TolQRA complex in the inner membrane

(4). The phage virion disassembles the phage ssDNA allowing it to access the host cytoplasm by an unknown mechanism (5). Once the ssDNA (+) strand (infective form, IF) enters into the cytoplasm, the host RNA polymerase binds to a hairpin at the (-) *ori*, resulting in synthesis of an RNA primer (6). The host DNA polymerase III generates the (-) strand by extending the primer (7), generating the "replicative form" (RF, a double-stranded phage genome). The phage protein pII then binds to the (+) *ori* and nicks the (+) strand (8). The resulting 3'-hydroxyl end is then extended by the host DNA polymerase III, displacing the "old" (+) strand (9). Upon a complete cycle, pII cuts and ligates the newly synthetised (+) strand, resulting in a single-stranded IF and a double-stranded RF. Early in the infection, the RF can undergo multiple rounds of replication and serve as a template for transcription and translation of phage proteins (10). Later in the infection, the accumulation of protein pV results in its binding to the IF DNA (11), directing these ssDNA genomes for packaging and secretion (12). (Inset) Schematic representation of the Ff phage origin of replication, containing the packaging signal (PS), the (-) and (+) *ori*. Adapted from Rakonjac *et al*. (2011) and Hay *et al*. (2019), with permission.

1.2.3.4 Production of Ff like particles

1.2.3.4.1 Phagemid particles

Plasmid-derived replicons, called phagemids, have been used as cloning vectors in molecular biology (Vieira & Messing, 1982) and phage display technology (Barbas, 2001). These replicons are plasmids that contain the complete Ff IG sequence (sometimes referred to as f1 *ori* or M13 *ori* or Ff *ori*). In the presence of a helper phage, phagemids undergo replication from their Ff *ori,* and the resulting circular ssDNA becomes assembled into Ff-like particles. Ff *ori* on the phagemid interferes with helper phage replication, causing a low level of helper phage RF and, in turn, a lower abundance of the proteins required for replication and assembly of both

phagemid and helper phage. The ultimate consequence of the interference is the low titres of both the helper phage and phagemid-containing particles. Interference of phagemid Ff *ori* with helper phage replication was overcome by the construction of helper phage These helpers can contain interference-resistant mutations in *gII* (IR1, helper phage R408) or an additional plasmid *ori* (i.e., M13KO7) which allows the phage to replicate independently of pII, maintaining an adequate copy number for the expression of proteins needed for ssDNA production (Russel *et al*., 1986; Vieira & Messing, 1987). These helpers have allowed an increased yield of phagemid-containing particles in comparison to the wild type Ff phage (Dotto & Horiuchi, 1981; Russel *et al*., 1986).

As the length of filamentous phage is proportional to the length of the circular ssDNA genome, the size of a phagemid vector, therefore, determines the length of the phagemid particles, which can be shorter or longer than the helper phage (Russel *et al*., 1986).

1.2.3.4.2 Small interfering particles

Much shorter particles than wild type Ff can be assembled either spontaneously or can be engineered (La Farina *et al*., 1987; Ravetch *et al*., 1979; Sattar *et al*., 2015; Specthrie *et al*., 1992). Very short virions were first observed in Ff phage mutants that underwent duplication of a virion segment containing Ff *ori* (Figure 9). These mutants arise spontaneously after several passages of f1 phage in the absence of clonal (single plaque) purification. Duplication allows replication between two (+) origins, resulting in two circular ssDNA molecules of different sizes and two types

of particles: (i) circular (+) strand ssDNA that is much shorter than the wild type genome, that is assembled into short virions (Griffith & Kornberg, 1974), and (ii) particles that correspond to the original phage without any duplicated sequence. The short Ff-like particles, also called "defective mini phage" or "defective interfering particles", can outgrow the wild type phage by interfering with the "parent" phage replication, thereby diminishing the production of phage-encoded proteins (Enea *et al*., 1977). Depending on the length of the duplicated region, these short ssDNA replicons (0.2 to 0.5 of the wild type Ff length) may carry one or more of the Ff genes or partial open reading frames flanking the IG sequence, for example, the 3' moiety of *gIV*, or 5' portion of *gII*. These small replicons can only be assembled into Ff-like particles in the presence of their parent phage or externally supplied helper phage (Ravetch *et al*., 1979).

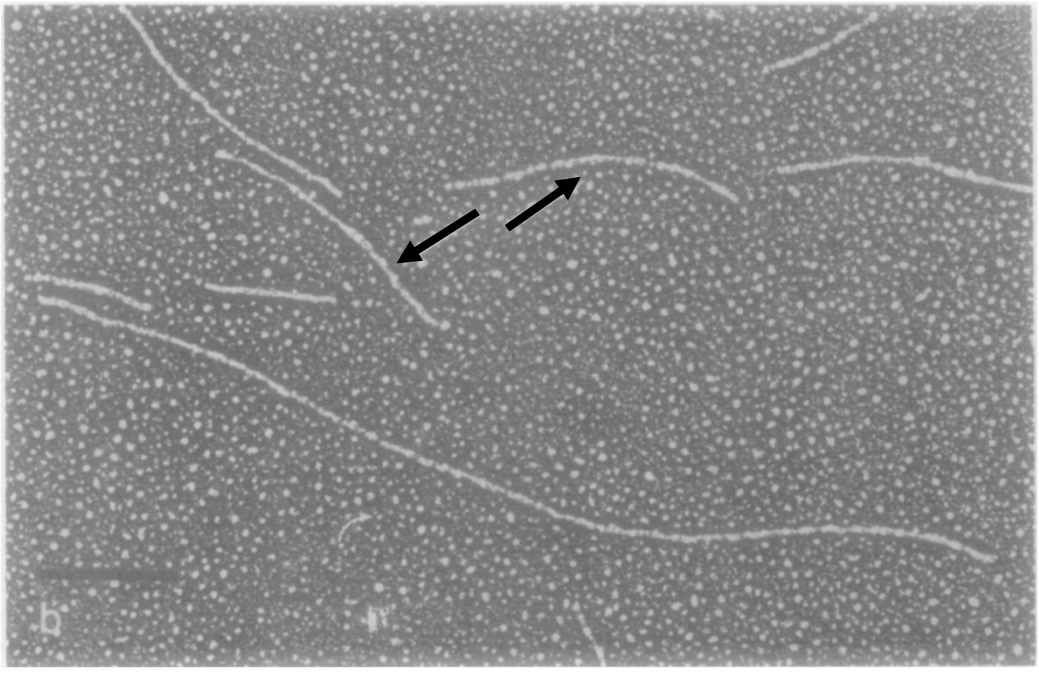

Figure 9. Electron micrograph of Ml3 and mini phage particles.

Normal size (arrows), mini and polyphage particles (3 times unit length) are shown in negative contrast in a preparation obtained by surface spreading and Pt-Pd shadowing. The bar is 0.5 μm. Taken with the publisher's permission from Griffith & Kornberg (1974).

1.2.3.4.3 Engineered short Ff-like particles (microphage, nanophage or nanorods)

Inspired by the observation of small interfering particles, Specthrie *et al*. (1992) engineered a system for the production of very short Ff-derived 50 nm nanorods (5% the length of the wild type Ff; much shorter than defective interfering particles), named microphage or nanophage. This production system is composed of a plasmid containing a replication-assembly cassette designed to give rise to a short (221-nt) (+) strand circular ssDNA in the presence of a helper phage. In contrast to spontaneously formed defective interfering particles described in the section above, which are initially part of the phage genome, the cassette producing

these very short particles was engineered and inserted into a plasmid backbone. Another difference from defective interfering particles (described in the previous section) is that the nanorod replicating cassette has no (-) *ori* and cannot undergo replication of the negative strand. The engineered nanorod replication cassette is composed of two (+) strand replication origins flanking a packaging signal (Figure 10). First (+) *ori* (*ori1*) corresponds to the essential (A) portion of positive origin and is acting as an initiator of the (+) strand synthesis (i.e., it allows binding of pII and initiation of (+) strand replication). The packaging signal follows, and the cassette ends with the second (+) *ori* (*ori2*), a truncated mutant (+) origin, *ori*Δ*29*, where 29 nucleotides were deleted from the 3' end of the essential portion of the (+) *ori*. This deletion removes the pII binding site so (+) *ori*Δ*29* can act only as a terminator of replication, where pII bound to the displaced (+) strand makes a cut and religates the ends to form a (+) strand 221-nt circular ssDNA containing a packaging signal, which is assembled into 50 nm Ff-derived nanorods. The reason for engineering truncated (+) *ori* and omitting (-) strand origin was to minimise the length of ssDNA in order to assemble the shortest possible Ff-derived nanorod. The length of this replication-assembly cassette can be modified by inserting or deleting nucleotides between the (+) origins to manipulate the size of the nanorods. However, the importance of some of the DNA segments in this region, more particularly, the unstructured regions, and how their modification will affect the nanorod production is not yet fully described, and no attempts to design shorter particles have been made to date. Besides the nanorods, in this setup, full-length helper phage are produced (Figure 10B) (Specthrie *et al*., 1992). Like phagemids and small interfering particles, interference-resistant helper phage are required to replicate short ssDNA without interfering with helper phage replication. Helper

phage IR1 mutation was required for the production of the 221-nt ssDNA and the short nanorods (Sattar, 2013; Specthrie *et al.*, 1992), not only to decrease interference but also to increase the pII binding to the (+) *ori1*, which lacks the B region and therefore has low affinity for pII. An M13KO7-derived helper phage, VCSM13, which does not contain the IR1 mutation, did not support the 221-nt ssDNA replication unless pII was overexpressed in the same cell in trans, from an inducible promoter (Sattar, 2013).

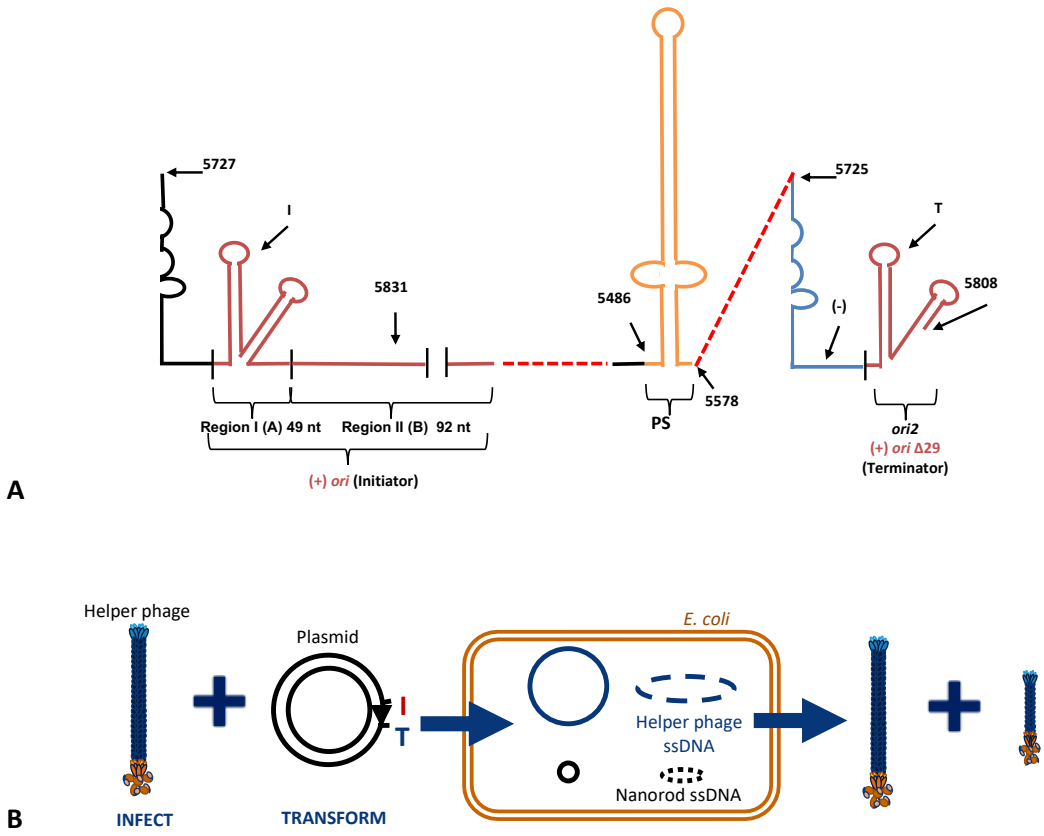

Figure 10. Nanorod production system engineered by Specthrie et al. (1992).

(A) Engineered origin of replication for nanorod production. (+) *ori,* positive origin of replication (red); PS, packaging signal (orange); (-) *ori*, negative origin of replication (blue); *ori2*, truncated (+) *ori Δ29*. (B) Nanorod production system using helper phage. In this production system, the helper phage genome is packed in parallel with the 221-nt ssDNA resulting in the production of helper phage along with nanorods.

Although the IR1 mutation improved production of the 221-nt ssDNA, the use of helper phage results in low efficiency of nanorod production, with nanorods making up only 3% of the total Ff-derived virion population. The nanorod production system has been improved in recent years by engineering a helper phage with lowered production of major coat protein pVIII, thereby favouring shorter over longer virions and increasing the copy number of plasmids carrying the nanorod replication cassette to increase the copy number of 221-nt ssDNA in the cells. Furthermore, a purification protocol improved by adding an electroelution step led to better separation of short nanorods from the long helper phage (Bennett, 2010). Helper phage were also modified to permit the display of proteins fused to the cap protein pIII, enabling the nanorods to be functionalised and used as detector particles in lateral flow assays (Sattar *et al*., 2015). These systems designed and functionalised by Bennet (2010) and Sattar *et al*. (2015), respectively, allowed the production of very short nanorods (~ 50 nm in length) that could be used for several phage-derived applications that benefited from the small particle size. Based on these systems, Nafisi *et al*. (2018) reported the construction of a phagemid to produce scaffolds that have an use in several DNA origami shapes and assembly. However, these production systems turned out to be very laborious and time-consuming as they required transformation and infection steps to produce the nanorods, in addition to requiring several purification steps to separate the longer phage away from the nanorods. These shortcomings made it difficult to upscale the nanorod production to obtain a high yield of nanorods free of contaminating full-length phage.

1.2.4 Ff phage applications

Besides their contribution to the molecular biology field, where Ff phage have been the model used to understand DNA replication and phage display technology, Ff phage has also been used for discovery and development of peptide and antibody libraries for peptide/antibody variants that bind a target of interest (Barbas, 2001; Smith, 1985). Moreover, thanks to their unique structure, ease of production, and manipulation, Ff applications have been expanded to encompass bio- and nanotechnology. Ff phage have been used as building blocks for the construction of novel nanomaterials and as carriers of agents used for diagnostic and therapeutic purposes. Here, I will focus on some of the Ff phage applications that could benefit from the research carried out for this thesis.

1.2.4.1 Phage display

Some three decades ago, Smith (1985) developed a new technology by inserting a foreign DNA fragment into the filamentous phage genome, as a fusion to the gene sequence of the minor virion protein pIII. This insertion resulted in a particle that could display a peptide, a protein, or an antibody fragment on the virion surface. The coding sequence for displayed polypeptide is packaged within the phage particle. Protein and its coding sequence are thereby physically linked . The link between the displayed protein and its coding sequence allows a library of molecules to be screened for those that can bind to immobilised targets in a process called

bio-panning (Ngo-Duc *et al*., 2018). The displayed peptide or antibody variants identified by library screening can then be used for a myriad of applications, including antibody-directed cell-targeting or diagnostics (Ju & Sun, 2017; Pande *et al*., 2010).

Although in past thirty years every capsid protein (pIII, pVI, pVII, pVIII, and pIX) has been engineered to display oligopeptides, the most commonly used are N-terminal fusions to pIII and pVIII (Rakonjac *et al*., 2011; Xu *et al*., 2020). The C-terminal oligopeptide display has been accomplished for both pVIII and pIII (Fuh & Sidhu, 2000; Held & Sidhu, 2004; Urban *et al*., 2017), however this type of fusion is used very rarely. In general, pIII is preferred over pVIII for the display of folded proteins or protein domains, such as the single chain variable fragments (ScFv) of antibodies. In contrast, display on every copy of pVIII is limited to peptides up to ten amino acids unless a mosaic display is used, where wild type and modified pVIII subunits are interspersed (Iannolo *et al*., 1995; Malik *et al*., 1998; Pande *et al*., 2010). Ff phage display still presents some limitations that alter its performance, such as reduction of infectivity and propagation, toxicity of the fusion to the host, or the incompatibility of some peptide sequences with the transport across the membrane that is required for display (Høydahl *et al*., 2016; Krebber *et al*., 1996; Løset *et al*., 2011; Løset & Sandlie, 2012; Peters *et al*., 1994). These limitations decrease the size of the primary phage display library and introduce bias against some variants during library construction, amplification and subsequent screening (panning).

Much of pIII display developments are due to the knowledge of the pIII structure; however, as previously mentioned, the pIII C domain structure is still unknown. Working towards determining/gathering more information about the structure of the pIII C domain and pVI within the virion cap could improve pIII display or nanotechnology applications that rely on an Ff-derived particle as a building block.

1.2.4.2 Ff as delivery carriers and nanomaterials

In the emerging field of nanomedicine, several compounds have been investigated and used for the delivery of therapeutic molecules and drugs for many pathologies, including cancer, vascular diseases, and central nervous system diseases (Bobo *et al*., 2016; Grodzinski *et al*., 2019; Kaushik *et al*., 2018; Li *et al*., 2020).

Ff phage have also been explored in this area, where recombinant and chemical approaches have been combined to allow DNA, peptides, and non-peptide molecules to be delivered to targeted tissues. Furthermore, they present some advantages compared to other biological systems commonly used as gene carriers, such as not having a defined packaging limit compared to eukaryotic viruses (adenoviruses, 8 kb; adeno-associated virus, 4.7 kb; or lentiviruses, 8–10 kb) (Seow & Wood, 2009). In addition, their rod-like structure and high aspect ratio (high length to diameter ratio) increase the number of possible ligand-receptor interactions. Repetitive multicopy display of, for example, targeting peptides along the shaft results in a tendency for filaments to move toward the blood-vessel walls when injected *in vivo*, a property that appears to improve targeted cell penetration

in comparison to that observed using spherically shaped viruses and phage (Bakhshinejad *et al*., 2014; Karimi *et al*., 2016). Due to these properties, the use of Ff phage as carriers have been explored, resulting in the generation of a targeted *in vitro* treatments for prostate cancer (DePorter & McNaughton, 2014; Ghosh *et al*., 2012), delivery of antibiotics (Vaks & Benhar, 2011), and the delivery of therapeutic compounds to cardiac tissue (Zahid *et al*., 2010), and the brain (Ksendzovsky *et al*., 2012; Rakover *et al*., 2010). These studies confirm Ff phage's ability to deliver therapeutic agents and gain access to tissues that are usually unavailable. Nevertheless, despite their success and potential, there are still some limitations due to the possibility of horizontal gene transfer of antibiotic-resistance-encoding genes and their size (≥ 880 nm). For example, they might be too large to penetrate the gut epithelium (Huh *et al*., 2019), where tight junctions in the epithelial cells restrict the flux of foreign molecules, restricting their size as carriers.

Due to the properties mentioned above, Ff phage have also been used as scaffolds to build novel bionanomaterials, among which are nanotubes, films, fibres, and even nanowires, which may find uses in nanoelectronics, sensing, and cancer therapy (Henry *et al*., 2015; Henry & Debarbieux, 2012; Zhou *et al*., 2012). In diagnostics, for example, M13 phage have been successfully used to assemble fluorescent single-walled carbon nanotubes (SWNTs) for targeted fluorescence imaging of tumours (Yi *et al*., 2012). Furthermore, the ability of fluorescently labelled M13 to function as a more sensitive lateral flow assay (LFA) than the commonly used ones (i.e., enzyme-linked immunosorbent assays or colloidal-gold nanoparticle LFAs) to detect viruses has also been demonstrated (Kim *et al*., 2015).

Short phage-derived nanorods (50 nm in length) have also been used as detector particles in LFAs (Sattar *et al*., 2015).

The short length permits the 50 nm nanorods to more easily diffuse along the membranes compared to longer wild type phage, which is an advantage for LFA and other applications. Nevertheless, large-scale applications of these nanorods are not practical because of the lengthy and arduous purification processes.

1.2.4.3 Ff as anti-aggregating agents

A central event in most human neurodegenerative diseases is the association of peptides and proteins into aggregates of various sizes leading to larger structures such as the plaques or fibrils characteristic of Alzheimer's, Parkinson's and other neurodegenerative diseases. Proteins that form aggregates associated with neurodegenerative diseases, such as Alzheimer's disease (AD) and Parkinson's disease, are β-amyloid (Aβ) protein, the micro-tubule-associated protein tau, and pre-synaptic protein α-synuclein (AS) (Cheng *et al*., 2013). It is thought that the aggregates or fibrils made of truncated or misfolded proteins cause the neurodegeneration due to their toxicity. Alzheimer's Disease (AD), for example, is the most common cause form of dementia. It is expected to affect 131 million people worldwide by 2050, with an annual cost above USD 1 billion according to the Alzheimer's Disease International Report (Prince *et al*., 2015), highlighting the urgency of developing therapeutical strategies to reduce AD incidence. Therapeutic approaches for treatment of diseases involving misfolded proteins have focused on

preventing, targeting, and disrupting their aggregates (Cheng *et al*., 2013; Estrada & Soto, 2007; Hung & Fu, 2017). Although different compounds capable of targeting the protein aggregates have been discovered and are currently in clinical trials, to this date, no new drugs have been approved for AD treatment (Huang *et al*., 2020). Identifying new alternatives that can affect multiple targets related to AD might help develop an effective treatment of diseases associated with protein misfolding, particularly AD.

Ff bacteriophages (f1, fd and M13) have been shown to have the ability to prevent aggregation and facilitate dissolving or disaggregating misfolded protein aggregates such as Aβ (Solomon, 2008; Solomon & Goren, 2013), AS (Dimant *et al*., 2009; Dimant & Solomon, 2010), and tau (Krishnan *et al*., 2014). The unique structure of Ff has initially been proposed to be mainly responsible for this ability, particularly that of the minor capsid protein, pIII (Dimant & Solomon, 2010; Solomon & Goren, 2011; Solomon & Goren, 2013). It was subsequently observed that a virion lacking the N1 and N2 domains of the minor protein pIII (removed by treatment with endoproteinase ArgC) can still bind and solubilize AD aggregates, and to a lower extent, Aβ fibres; implying that the C domain of pIII could have a role in disruption of the misfolded protein aggregates (Krishnan *et al*., 2014). Krishnan *et al*. (2014) determined that recombinantly expressed N1N2 domains of pIII are sufficient for the binding and disrupting these aggregates. The authors named protein pIII, more precisely its N1N2 domains, as the General Amyloid Interaction Motif (GAIM). It was, however, unclear whether the pIII C domain that forms the virion cap also contributes to disruption of the β-amyloid aggregates.

Given that Ff phage are harmless to mammalian cells, yet they have potentially valuable therapeutic properties, whole phage or the N1N2 motif GAIM have been proposed as an alternative for treating diseases associated with protein misfolding. The role of the pIII C domain in the Ff interaction with misfolded protein aggregates has not yet been ascertained. If the C domain contributes to the anti-aggregation activity it could facilitate therapeutic applications in combination with the GAIM peptide therapeutical potency.

1.3 Thesis aims

The filament end-caps are the key to understanding the molecular mechanisms of Ff assembly and infection, and for improving the current applications of Ff phage. The major problem in gathering structural information about the filament termini from wild type virions, is the high length-to-width ratio and the virions' inherent flexibility. In contrast, very short Ff-derived nanorods (50 nm in length) have a 20-fold reduced length-to-width ratio, and the end-caps occupy as much as 34% of the nanorod. The short length means more compact particles, reduction in the flexibility of the filament and easier alignment in the cryo-EM single-particle analysis (cryo-EM SPA) to solve their end-cap structures. Any end-cap structural knowledge acquired will, in turn, facilitate the elucidation of membrane transition processes in Ff infection assembly and improving the phage-derived applications such as phage display, and engineering of nanostructures for diagnostics, and the disruption of misfolded proteins associated with disease.

In this thesis, I intend to characterise the structure of the Ff end-caps, construct the shortest possible nanorods, and examine the role of the C domain of the end-cap protein pIII in β-amyloid (Aβ) fibre binding. For this, the specific aims are:

1. Produce and purify suitable Ff derived-nanorods for Cryo-EM SPA with the following objectives:
    i. To design a novel nanorod production system that is more efficient than the pre-existing helper-phage-based system and produce very

short nanorods (50 and 80 nm in length) for structural analysis by Cryo-EM SPA.

ii. To purify the pIII-pVI complex from the resulting new nanorods and examine whether a uniform population of the complex can be obtained.

iii. To manipulate the origin of replication of the nanorod-template plasmids by deleting DNA segments between essential elements required for replication. The outcome of this work is to decrease the nanorod length from ~ 50 nm to ~ 40 nm to maximise the end-caps contribution, as well as precise mapping of some of the Ff replication elements.

2. Explore the reported ability of Ff phage lacking pIII N1 and N2 domains to mediate interaction and disruption of Aβ fibres.

   i. To produce Aβ fibres from β-Amyloid peptide (residues 1-42).

   ii. To produce and purify gene III deletion mutant Ff phage (f1d3) from complementing strains that produce either C domain of pIII or full-length pIII expressed from a plasmid.

   iii. To test the binding of both purified complemented f1d3 phage to Aβ fibres in order to further characterise the roles of the C domain of pIII in these interactions. If positive, the Aβ-binding epitope in pIII C domain will be identified by functional analyses of a series of mutants.

Chapter 2:

Materials and methods

2.1 Bacterial strains, growth conditions and manipulation

The bacterial strains used in this study are listed in Table 2, all of which are *Escherichia coli* strains, derived from the laboratory strain K12.

Table 2. Bacterial strains

Strain[a]	Genotype	Source
K561	*HfrC, S26 RIE, fadL701 phoM510 mcrB rrnB ton A22, gar B10, ompF, relAl, pit 10, spoT1, T2R, lacI^q*	The Rockefeller University (Zinder-Model) collection
K2091	*K561 supD, zed508::Tn10*	(Sattar *et al*., 2015)
K2245	*Δ(araD-araB)567, ΔlacZ4787(::rrnB-3), λ-, ΔrecO737, rph-1, Δ(rhaD-rhaB)568, hsdR514; F'[::Tn10 proAB$^+$ lacI^q Δ(lacZ)M15]*	S. Khanum and J. Rakonjac, (unpublished)
K1976	*TG-1 containing the complementing plasmid pJARA112 which contains wild- type gIII under the control of the filamentous phage-induced psp promoter.*	(Bennett & Rakonjac, 2006)
TG-1	*supE44 Δ(hsdM-mcrB)5 (rk$^-$ mk$^-$ McrB$^-$ thi Δ(lac-proAB) F' [traD36lacI^q Δ(lacZ)M15 proA$^+$B$^+$].*	(Carter *et al*., 1985)

[a]All strains were derived from *Escherichia coli* K12

All strains were propagated in DifcoTM 2xYT (Yeast Extract Tryptone) Medium (Becton, Dickinson and Co. Sparks, USA) at 37 ºC with continuous shaking (200

rpm) or plated on 1% BactoTM Agar (BD) plates and grown at 37 ºC, unless otherwise stated. The media was supplemented with antibiotics sourced from GoldBio where appropriate. Antibiotics were used at the following concentrations: kanamycin (Km) at 50 μg/mL, ampicillin (Amp) at 60 μg/mL, and chloramphenicol (Cm) at 25 μg/mL.

2.2 Plasmids, DNA analysis and manipulation methods

All plasmids and oligonucleotides used in this study are listed in Table 3 and Table 4, respectively.

Table 3. Plasmids

Name	Description	Marker	Source
pRnanoR	pRnano3, *gVIII*$^{-20}$ Y21M, WT *gIII*,	Km^R	This work. The large BamHI/SnaBI fragment from pRnano3 was ligated to the BamHI/SnaBI synthetic fragment containing an *amber* mutation in position -20 relative to the start of mature pVIII and introducing a Y21M mutation into pVIII. This synthetic fragment was

			produced by Genscript and named *gVIII*$^{am\text{-}20}$Y21M.
pSS3	Plasmid containing an MB1 ori, BSFp-nano 221-nt replication cassette (BSFp221) and Amp^R gene	Amp^R	(Sattar, 2013)
pPop-up529Uni	Nanorod-producing plasmid that acts as a self-helper. It expresses all Ff phage proteins; replicates BSFpn-nano 529-nt (BSFpn529) ssDNA; *gII* IR1-B (C143T); *gVIII*$^{-20m}$ pVIII Y21M	Km^R	This work. The large PstI/SwaI fragment from pRnanoR was ligated to the PstI/SwaI BSFpn529 synthetic fragment produced by GenScript.
pPop-up529LacUni	Nanorod-producing plasmid that acts as a self-helper. It expresses all Ff phage proteins and replicates BSFpn-nano 529-nt (BSFpn529) ssDNA. Ff promoter p_A phage promoter is replaced by *placUV5*; *gII* IR1-B(C143T); f1 *gVIII*$^{-20m}$ pVIII Y21M	Km^R	This work. The large SalI/HpaI fragment from pPop-up529Uni was ligated with the SalI/HpaI synthetic fragment produced by Genscript, containing the *lacUV5* promoter and part of *gII*.
pPop-up221Uni	Nanorod-producing plasmid that acts as a self-helper. It expresses all Ff phage proteins and replicates BSFp-nano 221-nt (BSFp221) ssDNA; *gII* IR1-B(C143T); *gVIII*$^{-20m}$ pVIII Y21M	Km^R	This work. The BSFp221 cassette from plasmid pSS3 was amplified using the RL003Fw and RL003Rv primers and cloned into the large PstI/SalI fragment of pPop-up529Uni.

pPop-up221LacUni	Nanorod-producing plasmid that acts as a self-helper. It expresses all Ff phage proteins and replicates BSFp-nano 221-nt (BSFp221) ssDNA; Ff promoter p_A replaced by *placUV5*; *gII* IR1-B(C143T); *gVIII*$^{-20m}$ pVIII Y21M	Km^R	This work. The BSFp221 cassette from plasmid pSS3 was amplified using the RL003Fw and RL003Rv primers and cloned into the large PstI/SalI fragment of pPop-up529LacUni.
pPop-up395LacUni	Nanorod-producing plasmid that acts as a self-helper. It expresses all Ff phage proteins and replicates BSFp-nano 395-nt (BSFp395) ssDNA; Ff promoter p_A replaced by *placUV5*; *gII* IR1-B(C143T); *gVIII*$^{-20m}$ pVIII Y21M		This work. The large PstI/SalI fragment of pPop-up529LacUni was ligated with the PstI/SalI BSFpn395 synthetic fragment produced by GenScript
pPop-up152LacUni	Nanorod-producing plasmid that acts as a self-helper. It expresses all Ff phage proteins; replicates BSFp-nano 152-nt (BSFp152) ssDNA; Ff promoter p_A replaced by *placUV5*; *gII* IR1-B(C143T); *gVIII*$^{-20m}$ pVIII Y21M	Km^R	This work. The large PstI/SalI fragment of pPop-up529LacUni was ligated with the PstI/SalI BSFpn152 synthetic fragment produced by GenScript.
pJARA24	Codes for pIII-154 C-terminal fragment (*tac*-pelB-pIIIC154)	Cm^R	(Rakonjac *et al*., 1999)

Table 4. Primers

Name		Notes
RL1	GCCTTCGTAGTGGCATTACGTATTT	For pVIII Y21M amplification. Contains SnaBI cut site.
RL2	GATATTCACAAACGAATGGATCCTC	For pVIII Y21M amplification. Contains BamHI cut site. For sequencing.
RL3	GAGGGCTGTCTGTGGAATGCTACAG	For pVIII Y21M sequencing.
RL4	CTGTAGCATTCCACAGACAGCCCTC	For pVIII Y21M sequencing.
RL001	GGCCCCGTTAACAGGTTTAAACGAATT CCTTAGACGTT	For microphage origin amplification. Contains HpaI and PmeI cut site.
RL002	CGACTCACTATAGGGGATCCGCGAATTGAATTTAGCGGCCGCGAATTCCCATCGC	For microphage origin amplification. Contains BamHI cut site.
RL003Fw	GGGACTAGTCCTGCAGGTTTAAACGAATTCCTTAGACGTTTTCC	For microphage origin amplification. Contains PstI and PmeI cut-site.
RL003Rv	GGCGAATTGAATTTAGCGGCCGCGTCGACAATTCCCATCGCC	For microphage origin amplification. Contains SalI cut-site.
RL004Fw	ACACAACGTGGCTTTCCCCC	For pPop-upLacUni sequencing.
RL004RV	TGCTGGATCTGGTGCTGTAGC	For pPop-upLacUni sequencing.

2.2.1 Recombinant DNA methods

General molecular biology techniques such as restriction digest of DNA, ligation, preparation of competent cells, transformation, purification of plasmid DNA, DNA sequencing and PCR were carried out as previously described (Sambrock & W. Russel, 2001). Restriction endonucleases were sourced from New England Biolabs Inc. (USA). Oligonucleotides used for cloning, sequencing and PCR reactions (Table 4) were manufactured and purchased by Integrated DNA Technologies Inc. (USA). High-fidelity DNA polymerases PRIMESTAR (Takara, Japan) were used for PCR amplification.

2.2.1.1 Design of the Biological Scalable Functionalisation nanorod (BSF-nano) replication-assembly cassette.

Each cassette is the combination of different DNA units which were amplified from previous plasmids or synthesized by GenScript:

- BSFp: Combination of domain A of the (+) *ori* (initiator), the packaging signal and the (+) *oriΔ29* (terminator). In this work, two different BSFp replication-assembly cassettes were developed, each with different distances between the initiator (*ori1*) and the terminator (*ori2*): i) BSFp221 (303-nt), giving rise to a 221-nt single-stranded circular positive DNA product in the presence of the Ff replication protein pII. The BSFp221

cassette was amplified by PCR using the pSS3 plasmid as template and primers RL003Fw and RL003Rv (Table 4) containing, respectively, PstI and SalI endonuclease restriction cut-sites; ii) BSFp152 (196-nt), giving rise to a 152-nt single-stranded circular positive DNA product in the presence of the Ff replication protein II. The BSFp221 cassette was synthesised by GenScript.

- BSFpn: Combination of the complete (+) *ori* (domains AB; *ori1*), the packaging signal, the (-) *ori* and the (+) *oriΔ29* (terminator; *ori2*). In this work, two different BSFpn replication-assembly cassettes were used or designed containing different numbers of nucleotides between the initiator (*ori1*) and the terminator (*ori2*): BSFpn529 (529-nt, cloned from pNanoZap529 using the restriction sites PstI and SalI) and BSFpn395 (439-nt, custom-synthesized by GenScript).

2.2.1.2 Transformation by electroporation

Electroporation of competent cells was performed as described in Sambrook & Russel (2001) for the purpose of both cloning ligated DNA fragments of recombinant constructs and nanorod production. Briefly, appropriate amounts of plasmid DNA were added to 50-200 μL of electrocompetent cells on ice before transferring to a chilled electroporation cuvette (Bio-Rad). An electrical pulse was applied using the MicroPulser™ electroporator. Transformed cells were then

recovered by the addition of 1 mL of 2xYT medium and incubated at 37 ºC for one hour.

2.2.1.3 Construction of a single-plasmid system for nanorod production

The BSF-nano replication-assembly cassettes (amplified by PCR or custom-synthesized) were cut with PstI and SalI and inserted into the PstI and SalI sites of the helper plasmid, pRnanoR, to obtain pPop-up529Uni and pPop-up221Uni plasmids. The resulting recombinant pPop-upUni plasmids represent a single-plasmid system for the production of BSF nanorods. They each contain a BSF replication-assembly cassette (529 and 221-nt), and the Ff phage genes required for replication from the Ff origin and assembly of the nanorods. The pPop-upUni plasmids also contain a p15A origin of replication and Km^R selection marker for maintenance of the plasmid in *E. coli*.

2.2.1.4 Construction of an inducible single-plasmid for nanorod production

The constitutive Ff promoter (p_A) driving the transcription of *gII-gVIII* operon in the pPop-upUni plasmids, flanked by the SalI and HpaI endonuclease restriction sites, was replaced with a synthetic SalI-HpaI fragment containing the *lacUV5* promoter, to produce the pPop-up529LacUni, pPop-up395LacUni, pPop-up221LacUni and pPop-up152LacUni plasmids.

2.2.2 Agarose gel DNA electrophoresis

All agarose gels (0.6% to 1.2% w/v, depending on the size of the DNA) in this work were prepared in 1X TAE buffer (40 mM Tris base, 20 mM acetic acid, 1 mM EDTA, pH 8.3). Electrophoresis was carried out for 50 min at 70 V/cm, unless otherwise stated, and a 1 Kb Plus ladder (100 ng/lane; NEB or Invitrogen) was used as DNA size marker. DNA was stained using ethidium bromide (EtBr; 10 μg/mL EtBr, 1X TAE, pH 8.3) followed by destaining in water for 10 min. Gels were visualized by using the Molecular Imager® GelDoc™ (Bio-Rad).

2.3 Phage strains and general growth and quantification methods

All phage strains used in this study are listed in Table 5.

Table 5. Phage

Name	Description	Marker	Source
R408	f1ΔPS *gIX*(T30A) g*III*RIB(C143T) gtrxA2		(Russel *et al*., 1986)
R784	VCSM13, *gVIII*9M28L *gIII*::MCS	Kn^R	M. Miro and J. Rakonjac, unpublished
R788	R784, *gVIII*$^{-20}$ Y21M, WT *gIII*	Kn^R	This work. The large BamHI/SnaBI fragment from R784 was ligated with the BamHI/SnaBI synthetic fragment containing an *amber* mutation in position -20 relative to the start of mature pVIII and introducing a Y21M mutation into pVIII. This synthetic fragment was produced by Genscript.
R789	R408, *gVIII*$^{-20}$ Y21M, WT *gIII*	Kn^R	This work. The large BamHI/SnaBI fragment from R408 was ligated with the BamHI/SnaBI *gVIII*$^{-20m}$ pVIII Y21M synthetic fragment.
f1d3	f1, Δ*gIII*		(Rakonjac *et al*., 1997)

2.3.1 Preparation of phage stocks

Phage and phagemids were prepared by infecting an exponential phase culture (OD_{600} ~ 0.2) of an appropriate bacterial strain, at a multiplicity of infection (m.o.i) of 50, for 30 min at 37 ºC without shaking, followed by incubation for 4 h at 37 ºC with continuous shaking to allow culture growth and phage production. The incubated culture was then centrifuged at 6000 *x g* for 15 min to pellet bacterial cells. The supernatant was filtered through a 0.2 μm-pore membrane to remove any residual bacterial cells.

2.3.1.1 Infection and growth of complemented gIII deletion f1 phage and phage-like particles

Strains containing either full-length pIII (K1976) or the pIII-154 C-terminal fragment complementing plasmid (K561//pJARA24) were propagated in 2xYT medium supplemented with ampicillin and chloramphenicol, respectively. For production of virions containing full-length pIII (pIII-WT), exponentially growing cultures (OD_{600} ~ 0.2) were infected with f1d3 phage at an m.o.i of 100 phage per cell, for 15 min. For production of virions containing truncated-pIII, IPTG to a final concentration of 0.04 mM, was added to the culture and incubated at 37 ºC for 15 min. Next, the induced culture was infected with f1d3 phage at an m.o.i of 100 phage per cell, for 15 min. Infected cells were separated from unabsorbed phage by centrifugation at 4500 rpm for 15 min at room temperature, before resuspension in

fresh medium containing their respective antibiotic and, in the case of the truncated-pIII, containing 0.4 mM IPTG. Cultures were then incubated overnight before centrifugation at 4500 rpm for 20 min at 4 ºC to separate the cells from the supernatant containing the phage or phage-like particles.

2.3.2 Phage and phage-like particle concentration and purification

Released phage and long phage-like particles (e.g. phagemid particles derived from pUC118) were concentrated by PEG precipitation (5% w/v PEG 8000 and 0.5 M NaCl) for 1 h at 4 ºC, then centrifuged at 7000 rpm for 45 min at 4 ºC. The pellet containing the virions was resuspended in 1/1000 volumes of TBS buffer (50 mM Tris, 150 mM NaCl, pH 7.6). A second PEG precipitation was carried out in the same manner as described above followed by TBS resuspension. The concentrated virion suspensions were further purified by CsCl density gradient centrifugation. Briefly, the virions were resuspended in CsCl to a final concentration of 0.375 g/mL, followed by ultracentrifugation at 100,000 *x g* for 16 h at 18 ºC. This procedure resulted in a visible density gradient, where the phage and phage-like particles were seen as a grey band. The band was extracted through the use of a 25-gauge syringe needle as described by Sambrock and W. Russel (2001) and dialysed against 3000 volumes of 1X PBS buffer (137 mM NaCl, 2.7 mM KCl, 10 mM Na_2HPO_4, 1.8 mM K_2HPO_4, pH 7.4).

2.3.3 Agarose gel electrophoresis of phage and their quantification

Presence of the phage and phage-particles was detected by native- and disassembled-particle agarose gel electrophoresis. Native particle agarose gel electrophoresis was used to detect intact virions, whereas the disassembled particle electrophoresis was used to detect particle ssDNA released by boiling in an SDS-containing buffer.

The ssDNA of purified phage and phage-like particles was visualized by native virion agarose gel electrophoresis. Briefly, samples were mixed with standard DNA loading buffer (1X TAE, 5% glycerol, and 0.25% BPB), loaded onto agarose gels (0.6 - 0.8%) and then subjected to electrophoresis in TAE running buffer. After electrophoresis, virions were disassembled for detection by soaking the gel in 0.2 M NaOH for 1 h, followed by neutralization in 0.45 M Tris-HCl (pH 7.1) for 45 min. Finally, the exposed ssDNA from the virions was stained by EtBr, destained in water, and visualised with the GelDoc™.

A monophage equivalent is a measure of virion amount and is defined as a particle (or its portion) containing one encapsulated genome. Consequently, a particle containing 10 genomes represents 10 genome equivalents, as do 10 particles containing 1 genome each (Rakonjac & Model, 1998). The number of monophage equivalents was determined by SDS-disassembled agarose gel electrophoresis. Virions were disassembled by incubation in ¼ volume of SDS-containing buffer (1% SDS, 1X TAE, 5% glycerol, 0.25 % BPB) at 99 ºC for 20 min. Once cooled to room temperature, samples were loaded onto an agarose gel and subjected to

electrophoresis in TAE running buffer. After electrophoresis, the ssDNA from the disassembled virions was stained with EtBr, destained in water and visualised with the GelDoc™. Quantification was carried out by densitometry. As the amount of ssDNA in a band is not linearly proportional to the intensity of the fluorescence, every gel contained a set of 2-fold dilutions (typically from 2.5 to 100 ng per lane) of an f1d3 ssDNA standard, which was used for calibration. A third order polynomial function was used to fit a standard curve and conversion of the calculated amount of ssDNA in the samples into the number of phage or phage-like particles was carried out based on the molecular weight of the ssDNA genome of a particular phage strain, in this case f1d3. The molecular weight of ssDNA of f1d3 was calculated based on its base composition and length. From this, it was determined that 1 ng of single-stranded phage DNA equals 3.82 $x10^8$ monophage equivalents for f1d3.

2.3.4 Titration of phage stocks

Phage titres were determined using a plaque assay. Phage R784 was titrated on *E. coli* strain K561, whereas phage R788 and R789 (containing an *amber* mutation in *gVIII*) were titrated on the suppressor strain K2091 and phage f1d3 was titrated on the pIII-complementing strain K1976. Briefly, 10 µL drops of the phage serial dilutions were placed on soft agar containing 0.1 mL of overnight culture of appropriate bacterial strain. Plates were incubated overnight at 37 ºC. Plaques were counted to determine the approximate number of phage nanorods and the titre was expressed as plaque forming units per millilitre (pfu/mL).

2.3.5 Titration of phagemid particles

The titres of phagemid particles carrying an Amp^R marker were determined using a plaque assay on *E. coli* strain K2091. Plates were prepared from 2xYT agar medium. The bottom layer (21 mL) supplemented with 60 μg/mL ampicillin was poured first. After the bottom layer had solidified, it was overlaid by another layer of 2xYT agar without antibiotic (9 mL) and left to solidify. Pre-heated 2xYT medium containing 0.5% agar (2.5 mL per plate) was mixed with indicator bacteria and poured as the top layer. Once the top agar solidified, drops of diluted phagemid samples were placed on its surface to allow in-agar infection before exposure to ampicillin. Plates were incubated overnight at 37ºC. Ampicillin-resistant colonies were counted to determine the approximate number of phagemid particles, and titre was expressed as colony forming units per millilitre (cfu/mL).

2.4 Production of Ff-phage-derived nanorods

2.4.1 Helper-plasmid based nanorod production

Bacterial strain K2091 was used for the production of nanorods. K2091 cells were transformed by electroporation with the helper plasmid, pRnanoR, as described in section 2.2.1.2. Electrocompetent cells carrying the helper plasmid were then prepared and subjected to a second transformation with pSS3. Finally, the transformation mix was added directly to 1 L of 2xYT medium containing kanamycin and ampicillin and incubated overnight at 37 ºC with aeration to produce the nanorods. Nanorods produced from eight experiments were pooled together and subjected to purification. For some experiments, this method was downscaled to 20 mL of original culture.

2.4.2 Nanorod production by a single-plasmid system

K2091 cells were transformed by electroporation, as described in section 2.2.1.2, with one of the pPop-upUni plasmids (pPop-up529Uni or pPop-up221Uni; Table 3). The transformation mix was added directly to 1 L of 2xYT medium containing kanamycin and incubated at 37 ºC with aeration for at least 16 h to produce the nanorods.

2.4.3 Nanorod production by an inducible single-plasmid system

K2091 cells were transformed by electroporation with one of the pPop-upLacUni plasmids (pPop-up529LacUni, pPop-up395LacUni, pPop-up221LacUni or pPop-up152LacUni; Table 3), as described in section 2.2.1.2. The transformation mix was added directly to 1 L of 2xYT medium containing kanamycin and incubated with aeration at 37 ºC, until an OD_{600} of 0.1 was reached. IPTG was then added to a final concentration of 1 mM and incubated with aeration at 37 ºC for at least 16 h to produce the nanorods.

2.4.4 PEG precipitation of the nanorods

The culture containing the nanorods was centrifugated at 8000 *x g* for 30 min at 4 ºC, and the pellet discarded. The supernatant containing the nanorods was filtered using a Nalgene Rapid-Flow™ Top Filter with a PES Membrane (ThermoFisher) before adding PEG to a final concentration of 15% (w/v). Once the PEG was dissolved, NaCl was added to 0.5 M and dissolved. The suspension was incubated on ice for 2 h and then subjected to centrifugation at 8000 *x g* for 45 min to precipitate the nanorods. The "empty" centrifuge bottles were centrifuged again under the same conditions for 10 min to collapse the nanorod pellet to the bottom of the bottle. The pellet was then resuspended in 5 mL of TBS buffer. The suspension was centrifuged at 8000 *x g* at 4 ºC for 30 min to remove insoluble

material and the supernatant was collected. The supernatant was then mixed with 1/9 volume of 10x DNase/RNase buffer containing DNase and RNase (120 μg/mL DNase, RNase 400 μg/mL, 50 mM $MgCl_2$, 100 mM Tris pH 8.0, 40% Glycerol) for 2 h at room temperature. A second PEG precipitation was carried out in the same manner as described above and the pellet containing the nanorods was resuspended in 500 μL TBS buffer and stored at 4ºC.

2.4.5 Nanorod analysis and quantification

Presence of the nanorods was detected by disassembled- and native-particle agarose gel electrophoresis. Gels were made containing 0.8% to 1.2% (w/v) agarose (depending on the size of analysed ssDNA) and run in TAE running buffer. Nanorods were either mixed with SDS-containing buffer or standard DNA loading buffer, respectively, and run and visualised as described in section 2.3.3.

The nanorods do not contain selective markers and cannot replicate, hence were quantified by densitometry of ssDNA from the disassembled-agarose gel (Rakonjac & Model, 1998). Nanorods, along with serial dilutions of a ssDNA standard of known concentrations, were analysed by electrophoresis on 1.2% agarose gel in 1X TAE buffer. All quantification samples were loaded in triplicate. The gel was stained in EtBr, destained and imaged using a GelDoc™. Images were then analysed by the software ImageJ (National Institutes of Health). A second-order polynomial function was used to fit the standard curve generated from the ssDNA standards and used to determine the number of nanorods per mL as previously mentioned in section 2.3.3.

2.5 Purification of Ff-phage-derived nanorods

2.5.1 CsCl density gradient centrifugation

The PEG-precipitated nanorods were purified by CsCl density gradient centrifugation as described in section 2.3.2. When the nanorods were not visible as a grey band, they were collected by puncturing the tube containing the CsCl gradient at the bottom and collecting 100 µL fractions (3-4 drops). Fractions were then analysed by agarose gel electrophoresis of SDS-disassembled and native nanorods to identify the presence of the nanorods in the different fractions. The fractions containing the nanoparticles were combined and dialysed against 3000 volumes of 10 mM Tris (pH 8) using Slide-a-Lyzer® dialysis cassettes (Thermo Fisher Scientific).

2.5.2 Native preparative agarose electrophoresis and electroelution of nanorods

To purify the nanorods of desired size away from longer nanorods produced in the helper plasmid-based production system, they were separated by preparative native-particle agarose gel electrophoresis. The band corresponding to the nanorods of desired size, was cut out of the agarose gel using a sterile blade. The gel slices were

sliced again to a size no longer than 1.5 cm per tube, and transferred to dialysis tubes (Novagen, D-tube dialyzer Maxi, MWCO 12-14 kDa; product number 71510-3) filled with sterile 1X TAE buffer. The tubes were then placed in an electrophoresis chamber also filled with sterile 1X TAE buffer and electrophoresed for 210 min. After this time, the gel slices were taken out of the tube, which was then filled up again with sterile 1X TAE and electrophoresed for 5 min in the opposite direction to detach the nanorods from the membrane of the tubes. The tubes were stored overnight at 4 °C in sterile 1X TAE to allow further detachment of the particles. The next day, the buffer containing nanorods was recovered from each tube and filtered through a 0.22 μm-pore-size filter.

2.5.3 Anion exchange purification of the nanorods

CsCl purified nanorods were subjected to anion exchange chromatography purification. For this purpose, a strong anion Q, -N+(CH3)3 column SepFast™ (BioToolomics) was used. The column was equilibrated with 10 column volumes (CV) of binding buffer (buffer A: 10 mM Tris–HCl pH 8). The sample containing the nanorods was then passed through the column followed by a washing step with buffer A. Subsequently, the bound nanorods were eluted from the column by a gradient of NaCl from 0 to 1.5 M.

2.5.4 Nanorod concentration

Nanorods were concentrated by filtration using centrifugal force (Vivaspin concentrators; GE Healthcare) in the following manner: the samples were loaded onto 100 kDa molecular weight cut-off Vivaspin filtration tubes, which were then placed into collection tubes, and the assembly was subjected to centrifugation at 4500 *x g* for 3 min. Samples were washed by adding new buffer for 4 times followed by a final centrifugation where no buffer was added. The retentate was removed, and concentration of the nanorods was determined by disassembled-particle agarose gel electrophoresis (as described in 2.3.3).

2.6 Methods of protein analysis

2.6.1 Detection of nanorod proteins by SDS-PAGE, Blue Native PAGE (BN-PAGE) electrophoresis and western blotting

2.6.1.1 SDS-PAGE

Proteins from purified nanorods were separated by either 16% SDS-PAGE using a glycine gel system (Laemmli, 1970), in some cases, six-molar urea was used in SDS-PAGE, or by 12.5% SDS-PAGE using a tricine gel system. The protein samples were mixed with 2X SDS loading buffer (4% SDS, 20% glycerol, 0.12 M Tris-HCl, pH 6.8, 0.2% BPB, and 100 mM DTT) and heated at 95 ºC for 5 min. Gels were loaded and run in either 1X Tris-glycine running buffer (25 mM Tris-HCl, pH 8.3, 192 mM glycine, and 0.1% SDS, pH 8.3) or in a 1X Tris-tricine running buffer (100 mM Tris-HCl, 100 mM Tricine, 0.1% SDS, pH 8.3) at 150V and were subsequently stained in Coomassie blue solution (0.5% (w/v) Brilliant Blue R, 40% methanol, 10% glacial acetic acid) for 1 h with gentle shaking. Gels were destained using a destaining solution (40% methanol, 10% glacial acetic acid) and imaged using the GelDoc™.

2.6.1.2 BN-PAGE

The SERVAGel™ Native gels kit (SERVA, 43204.01) was used for blue native gel electrophoresis. Briefly, the sample was mixed with 2X sample buffer for BN (1 M 6-aminocaproic acid, 100 mM Bis-Tris-HCl, pH 7.0, 100 mM NaCl, 20 % glycerol, 0.1 % SERVA Blue G). The anode running buffer was supplied as 10X concentrate buffer, contained 500 mM Bis-Tris-HCl (pH 7.0). The cathode running buffer was supplied as 10X concentrate buffer, contained Tricine, 150 mM Bis-Tris. The cathode buffer was diluted to 1X and 1 % SERVA Blue G solution was added to get a final concentration of 0.002 % (w/v). Wells on the pre-cast gel were rinsed with the 1X cathode buffer and samples were loaded (no heating needed). Electrophoresis was carried out at 50 V for 10 min, followed by 200 V for 120 min After the run, gels were fixed with 20 % (w/v) trichloroacetic acid for 30 min, followed by a wash step in distilled water for 1 min before staining. Staining was performed by incubating the gel in a mixture of Stock solution 1 (0.2 % SERVA Blue R in 90 % (v/v) ethanol) with stock solution 2 (20 % (v/v) acetic acid) for 30 min. The gel was then rinsed in distilled water for 1 min and incubated in destaining solution (20 % (v/v) ethanol, 5 % (v/v) acetic acid, 1 % (w/v) glycerol) for 60 min and imaged using the GelDoc™.

2.6.1.3 Western blotting

For western blotting, unstained SDS-PAGE or Native gels were transferred to a PVDF membrane (Immobilon-P, Millipore) in 1X transfer buffer (25 mM Tris, 192 mM glycine, 20% methanol). The membrane was then blocked with TBST50 (50 mM Tris, pH 8.0, 150 mM NaCl, 0.05% Tween-20) + 5% skim milk overnight. Protein pIII was detected either using monoclonal mouse anti-pIII antibody (1F8;(Tesar *et al*., 1995) which recognises an epitope within the C domain of pIII (residues 292 to 302 of mature pIII), or a rabbit anti-pIII antibody (R164; (Rakonjac & Model, 1998) which is an affinity purified anti-peptide serum obtained by immunization with the peptide that corresponds to the C-terminal 10 amino-acid residues of pIII (residues 396 to 406 of mature pIII). Protein pVI was detected using a rabbit anti-pVI antibody (Endemann & Model, 1995). Membranes were washed three times in TBST50 prior to incubation with secondary antibody. Anti-mouse and anti-rabbit HRP-conjugated IgG were used in dilutions indicated in Table 6 and incubated for 90 min at 37 ºC. The HRP-conjugated antibodies were then detected by the ECL-detection system (SuperSignal™ West Dura Extended Duration Substrate, Thermo Scientific) and were visualised using chemiluminescence with the Azure Biosystems C600 imaging system.

Table 6. Antibodies for western blotting

Name	Dilution used	Source
1F8	1:1000	(Tesar *et al*., 1995)
R164	1:1000	(Rakonjac & Model, 1998)
Anti-pVI	1:1000	(Endemann and Model, 1995)
Anti-mouse HRP	1:10,000	Amersham Biosciences
Anti-rabbit HRP	1:10,000	Merck

2.6.2 Chloroform-DOC dissociation of the pIII-pVI complex of the nanorods

Nanorods were dissociated according to Woolford *et al*. (1977) by adding chloroform (5%, v/v to the final volume) and sodium deoxycholate (DOC) to a final concentration of 60 mM (400 mM stock solution in 10 mM Tris-HCl, pH 8.5), and incubated for 1 h at 37 °C. The suspension was pulsed in a microcentrifuge (~ 10 sec) and the supernatant containing the nanorods was removed by a 25-gauge syringe needle for purification by size exclusion chromatography.

2.6.3 Purification of the chloroform-DOC dissociated pIII-pVI complex

DOC-chloroform dissociated nanorods were subjected to size exclusion chromatography purification either using a Superdex 200 Increase 10/300 GL column (30 cm x 1 cm, pore size 8.6 μm; Merck) or a Zorbax GF-450 column (0.94 cm x 25 cm, pore size 6 μm; Agilent).

2.6.3.1 Superdex 200 Increase 10/300 GL

300 µL of Chloroform-DOC dissociated nanorods were loaded into the Superdex 200 Increase 10/300 GL column (two injections of 150 µL). The buffer was 10 mM Tris-HCl, pH 8, 1 mM EDTA, and 15 mM DOC. The flow rate was set at 0.7 mL/min and 400 µL fractions were collected. The fractions corresponding to the different peaks were pooled together and analysed by SDS-PAGE and western blotting to detect the nanorods proteins. For TEM analysis, the fractions were dialysed against detergent-free buffer and stored at -20 °C.

2.6.3.2 Zorbax GF-450

150 µL of Chloroform-DOC dissociated nanorods were loaded into the Zorbax GF-450 column. The buffer was 10 mM Tris-HCl, pH 8, 1 mM EDTA, and 1 mM DOC. The flow rate was set at 1 mL/min and 200 µL fractions were collected. The fractions corresponding to the different peaks were pooled together and analysed by SDS-PAGE and western blotting to detect the nanorods proteins and visualised by TEM.

2.6.4 Microscopic methods for visualisation and analysis of nanorods and nanorod proteins

2.6.4.1 Negative staining for TEM analysis

Purified intact or chloroform-DOC dissociated nanorods were diluted 10-fold in MilliQ water, followed by adsorption onto carbon coated 400 mesh copper grids (Electron Microscopy Sciences) by placing the grid on top of a 10 µL drop of this dilution for 5 min. The grid was removed from the drop and the excess liquid was removed with filter paper before placing the grid on top of a 10 µL drop of MilliQ water for 30 sec as a washing step. Next, the grid was removed from the drop and the excess liquid was removed with filter paper. Finally, the grid was placed on top of a 10 µL drop of 2% uranyl acetate for 5 min to stain the sample, followed by the removal of the excess liquid. All images were obtained at the Manawatu Microscopy and Imaging Centre (MMIC) using a 100 kVFEI Tecnai G2 Spirit BioTWIN (Czech Republic) TEM.

2.6.4.2 Immunoelectron microscopy staining using gold-conjugated secondary antibodies

Staining using gold-conjugated secondary antibodies was performed according to (Gulati *et al*., 2019). A 10-fold dilution of purified nanorods or the chloroform-DOC dissociated pIII-pVI complex was adsorbed onto carbon grids as described in section 2.6.4.1. The grid was then transferred to a 10 µL drop of blocking buffer (1X PBS buffer, 0.1% Tween 20, and 3% BSA) and incubated for 15 min in a humidified chamber (container with sealable lid containing a water-soaked paper) at room temperature. The grid was then placed on top a 15 µL drop of rabbit anti-pIII (R164) primary antibody (1:1000 dilution in blocking buffer) for 1 h at room temperature. The grid was then washed three times for 3 min each in wash buffer (1X PBS buffer, pH 7.4, 0.1% Tween 20 and 0.3% BSA) and in MilliQ water using the same method. Next, the grid was transferred to a 5 µL colloidal gold–conjugated secondary antibody diluted in blocking buffer (1:10 dilution anti-rabbit IgG gold-conjugated, 5 nm; Sigma) and incubated in the humidified chamber for 1 h. Finally, the grid was washed using the same method previously described and stained as described in section 2.6.4.1.

2.6.4.3 Cryo-EM grid preparation and data collection

All cryo-EM analyses were carried out by Rebecca Conners and Mathew McLaren from Vicki Gold's research group at the Living System Institute, University of

Exeter. Purified nanorods (3 µL of $5x10^{14}$ particles/ml) were applied to glow discharged R1.2/1.3 Cu 300 mesh grids (Quantifoil) and frozen on a Mark IV Vitrobot (Thermo Fisher Scientific, 4°C, 100% relative humidity, wait time 5 sec., drain time 0 sec., blot force 0, blot time 4 sec). Micrographs were collected on a 300 kV Titan Krios microscope (Thermo Fisher Scientific) with a K2 Summit direct electron detector (Gatan) at the Electron Bio-imaging Centre (eBIC) at the Diamond Light Source, UK. Data were collected using EPU software (Thermo Fisher Scientific) with a defocus range from –1.0 to –2.5 μm. The total dose was 40.8 electrons/$Å^2$ at a magnification of 81,000 x, corresponding to a pixel size of 1.8 Å.

2.6.4.4 Cryo-EM image processing

Warp (Tegunov & Cramer, 2019) was used for motion correction, CTF correction and particle picking, with 145,375 particles picked from 4485 micrographs. Both ends ("pointy" and "blunt") of the nanorods were picked together, and these were then imported into Relion (Zivanov *et al*., 2018) and separated after several rounds of 2D classification. *De novo* initial model generation was used to produce an appropriate map as a first reference, followed by iterative 3D classifications and tightly masked refinements to improve the quality. The final gold-standard refined map was generated using 49,460 particles and C5 symmetry.

2.7 Methods of β-amyloid analysis

2.7.1 Assembly of β-amyloid fibres (fAβ)

β-amyloid (1-42) human peptide (Merck; Cat. #A9810) was dissolved in hexafluoroisopropanol (HFIP; Merck; Cat. #105228) to prepare 1 mM peptide stock according to Stine *et al*. (2011). The peptide stock solution was then incubated for 30 min at room temperature. Next, the stock solution was dispensed into 10 μL aliquots (each containing 0.045 mg Aβ42) and HFIP was allowed to evaporate in the hood overnight. Tubes containing the peptide stock solution were then transferred to a SpeedVac and dried down for 1 h without heating to remove any remaining traces of HFIP and moisture, resulting in a clear thin film at the bottom of the tubes which was then stored at -20 °C.

Prior to use, the sample was allowed to equilibrate to room temperature. Fresh dry DMSO (2 μL) was added to the sample and mixed by pipetting thoroughly to prepare 5 mM Aβ-DMSO stock. The Aβ-DMSO stock was then vortexed (~ 10 sec) and pulsed in a microcentrifuge (~ 30 sec) to collect the solution. Next, 10 mM HCl at RT was added, diluting to a final concentration of 100 μM Aβ. The solution was then vortexed (~ 15 sec) and incubated for 24 h at 37 °C. The fibre quality was then monitored by TEM and by performing dye binding studies with Thioflavin T (ThT).

2.7.2 ThT fluorescence

The fAβ-ThT dye binding assay was performed as described by (Bourhim *et al*., 2007). ThT (Merck; Cat. #596200) was dissolved in MilliQ water to prepare a stock solution (1 mg/mL; 3.14 mM) which was aliquoted into 50 µL samples and stored at -20 °C in the dark. To perform the dye binding assay, a 5 µM ThT/Tris solution was prepared by adding 1.6 µL of the ThT stock solution to 1 mL of 50 mM Tris-HCl, pH 7.4. Next, 2.5 µg of fAβ solution was mixed with the 5 µM ThT/Tris solution and the fluorescence intensity was measured by a FluoroMax-4 (Horiba Scientific) spectrofluorometer using an excitation wavelength of 450 nm and an emission wavelength between 470 and 600 nm, and 3 and 6 nm slit widths, respectively. The background signal was subtracted from the signal obtained from the ThT/Tris and fAβ/Tris solution.

2.7.3 fAβ binding assay

Samples of 10 µM of fAβ were incubated with phage (1.3 x 10^{11}/mL) containing full-length pIII (f1d3 pIII-WT) or a pIII-154 C-terminal fragment (f1d3 pIII-Cd) for 3 h at 37 °C. The mixtures were then centrifuged at 7500 *x g* for 10 min and the fractions were separated. The "pellet" was then resuspended in 1X PBS buffer, equal to the original volume. The resuspended "pellet" and the supernatant were then analysed by disassembled-particle agarose gel electrophoresis as described in section 2.3.3.

2.7.4 Statistical analysis

The binding ability between f1d3 phage (either f1d3pIIICd, f1d3 containing only the pIII C domain, or f1d3pIIIWT, wild type f1d3 phage containing full-length pIII) and β-amyloid fibres (fAβ) was determined by pairwise comparison (Student's T-test) of the mean amount of phage or phage-like particles in the presence and absence of fAβ. Nine replicates were used on each binging test. Results are presented as mean ± standard deviation (SD). An independent Student's T-test was performed for each phage (f1d3pIIIWT) or phage-like particle (f1d3pIIICd) assay in the presence or absence of fAβ, and the P value was reported as >0.05 (not significant), <0.05, and <0.001 to denote the significance level of the difference between means.

Tables, plots and statistical analyses were performed using Microsoft Excel and GraphPad Prism™ for Mac OS X, (GraphPad Software, CA, USA).

Chapter 3:

Development of a novel nanorod production system and purification protocol

3.1 Introduction

Ff phage are long thin filaments (880 nm x 6 nm) whose shaft structure has been solved at atomic resolution by X-ray fibre diffraction and nuclear magnetic resonance (NMR) spectroscopy. In contrast to detailed structural information on the filament shaft, the structure of the filament end-caps has not been solved to date, mainly because they represent only 2% of the total virion mass and therefore are not detectable by X-ray fibre diffraction of the whole virion (Marvin *et al*., 2014). Determination of the Ff end-caps' atomic structure will fill the gaps in the knowledge of the mechanism used for DNA entry into the host cell at the start of infection as well as excision from the inner membrane at the termination step of assembly. Knowing the precise structure of pIII in the virion cap, the most commonly used platform in Ff phage display and nanotechnology applications, will improve the assembly of ordered nanostructures involving Ff by permitting spatially defined end-connectors to build predictable 3D structures.

The ultimate purpose of this thesis is to structurally characterise the end-caps of Ff phage. To accomplish this, the contribution of the caps to the virion has to be maximally increased while still retaining the ability to produce a sufficient number of virions for analysis. For this, Ff-phage-derived short nanorods were chosen as a study model, given that the contribution of the caps to the mass of these particles is up to 20-fold higher than in the full-length Ff phage. Short nanorods designed for structural analysis were modified by engineering to contain a point mutation,

Y21M, in the major coat protein pVIII. This mutation has been used in most of the atomic-resolution structural analyses of the Ff filament shaft published to date as it serves to increase the rigidity of the filament, resulting in better-aligned particles which provide better-resolved layer lines for high-resolution structural analysis in comparison with wild type pVIII.

3.2 Results and discussion

3.2.1 Improvements in the two-plasmid nanorod production system

In this thesis, in order to maximise the mass contribution of end-caps it was essential to produce the shortest published nanorods, 50 nm in length (Sattar *et al*., 2015; Specthrie *et al*., 1992). These short nanorods have only been produced to date with the assistance of a helper phage that interferes with production and especially the purification of short nanorods. To overcome this limitation, it was planned to produce 50 nm nanorods in a plasmid system, thereby eliminating the need for a helper phage.

In the Phage Display Laboratory at Massey University, a helper-phage-free system for production of longer (110 nm) nanorods using two plasmids was designed (S. Bisset, J. Zhou, and J. Rakonjac; unpublished). In this system, a helper plasmid

(pRnano3) was used instead of a helper phage. The second "template" plasmid (pBSF-nano736) contained a nanorod replication cassette (BSFpn; Biological Scalable Ff-derived positive and negative) that includes complete (+) and (-) origins of replication and produces 736-nt (110 nm) nanorods. Due to the presence of both positive and negative origins of replication, this system was expected to produce a much higher yield of nanorods in comparison to the 221-nt replication-assembly cassette.

No attempt was, however, made before this thesis work commenced to use this phage-free system for production of shorter (50 nm) nanorods, assuming that the production would be very low due to the truncated pSS3 nanorod replication-assembly cassette. The plasmid used to produce the 50 nm nanorods (Sattar, 2013) harbours a nanorod replication-assembly cassette BSFp221 (biological scalable Ff-derived positive ori 221-nt; for details, see section 2.2.1.1). The BSFp221 cassette contains only the (+) *ori* and then only the A or I portion (core). Given the absence of the (-) *ori* and the B (or II) portion of the (+) *ori*, the BSFp221 nanorod replication-assembly cassette in pSS3 was expected to produce a much lower copy number of the ssDNA in comparison to the plasmid pBSFnano736 (containing the BSFpn736 replication-assembly cassette) that contains not only a complete (+) *ori*, but also the (-) *ori*. In this chapter, we first tested and then improved the phage-free plasmid-based nanorod system for the production of 50 nm in length nanorods for structural analyses. Furthermore, a new single-plasmid inducible production system was designed and used for high-efficiency production of nanorods.

3.2.1.1 Construction of a helper plasmid containing a specific major coat protein mutation required for the Ff high-resolution structural analysis

A new helper plasmid was constructed by introducing Y21M mutation into the major coat protein, pVIII (~ 5.2 kDa). Gene VIII in the helper constructs contained, besides the Y21M mutation, an *amber* codon engineered to replace the Ser codon in the signal sequence (position -20 relative to the start of mature pVIII). The *amber* codon allows a decrease of the overall pVIII amount when nanorods are produced in the Ser suppressor strain (containing a *SupD* mutation) in comparison to the wild type pVIII. This is due to a lower suppressor tRNA incorporation efficiency during translation, in comparison to the translation using the Ser tRNA. This, in turn, lowers the amount of pVIII in *E. coli* and favours the production of short nanorods. Because the suppressor strain incorporates Ser, this mutation is silent when a suppressor host is used. The previously designed helper plasmid, pRnano3, contained an *amber* mutation at position +2 (second codon of the mature pVIII; GAG encoding Glu to TAG). In this case, the suppressor tRNA results in a Glu to Ser replacement, changing the nanorods' pI from 6.8 to 8.3. These nanorods run as smears instead of bands in native agarose gel electrophoresis at pH 8.3 (the pH of the standard TAE electrophoresis buffer). Electrophoresis performed at pH 9 permitted visualisation of the nanorods as bands, presumably due to increase of the negative charge of the nanorods at this pH. Even under this increased pH, these nanorods run as broad rather than sharp bands. Moving the *amber* codon into the signal sequence is expected to shift the pI of pVIII back to 6.8 and thus eliminate smearing in native virion agarose gel electrophoresis.

A fragment containing the engineered mutations (*gVIII*$^{am\text{-}20}$Y21M) was designed, custom-synthetized by GenScript, and cloned first into a phage to confirm that the designed fragment is functional. To construct the *gVIII*$^{am\text{-}20}$Y21M phage, closed circular dsDNA (replicative form; RF) of phage R784 and the *gVIII*$^{am\text{-}20}$Y21M fragment were digested with BamHI and SnaBI restriction endonucleases. The large BamHI-SnaBI fragment of R784 was ligated to the BamHI-SnaBI-digested synthetic fragment to obtain a new recombinant phage named R788 (Figure 11). This new phage was identified by screening the recombinant plaques, taking advantage of the *amber* mutation in R788. Briefly, phage R784 has wild type *gVIII* and therefore forms plaques on non-suppressor strains, whereas phage R788 cannot form plaques in the absence of a suppressor (e.g., *supD*), providing a way to screen for the recombinant clones. To obtain the recombinants, the transformants were initially plated on to a lawn of K2091 (a suppressor D strain, *supD*). The resulting plaques were passaged onto a lawn of the same suppressor strain (K2091) and also of K561 (a non-suppressor strain) to identify the recombinant *amber* mutant phage R788 clones *via* their ability to form plaques on the suppressor strain K2091, but not on the non-suppressor strain K561. Recombinant phage were identified after clonal purification and isolation of RF (circular double-stranded DNA) by sequence analysis of the insert.

The plaques of the R788 phage on the suppressor strain lawn were of similar size as were the plaques of the parent R784, indicating efficient replication and assembly of the recombinant phage. This was further confirmed by titration of the phage stock (1.1×10^{11} pfu/mL).

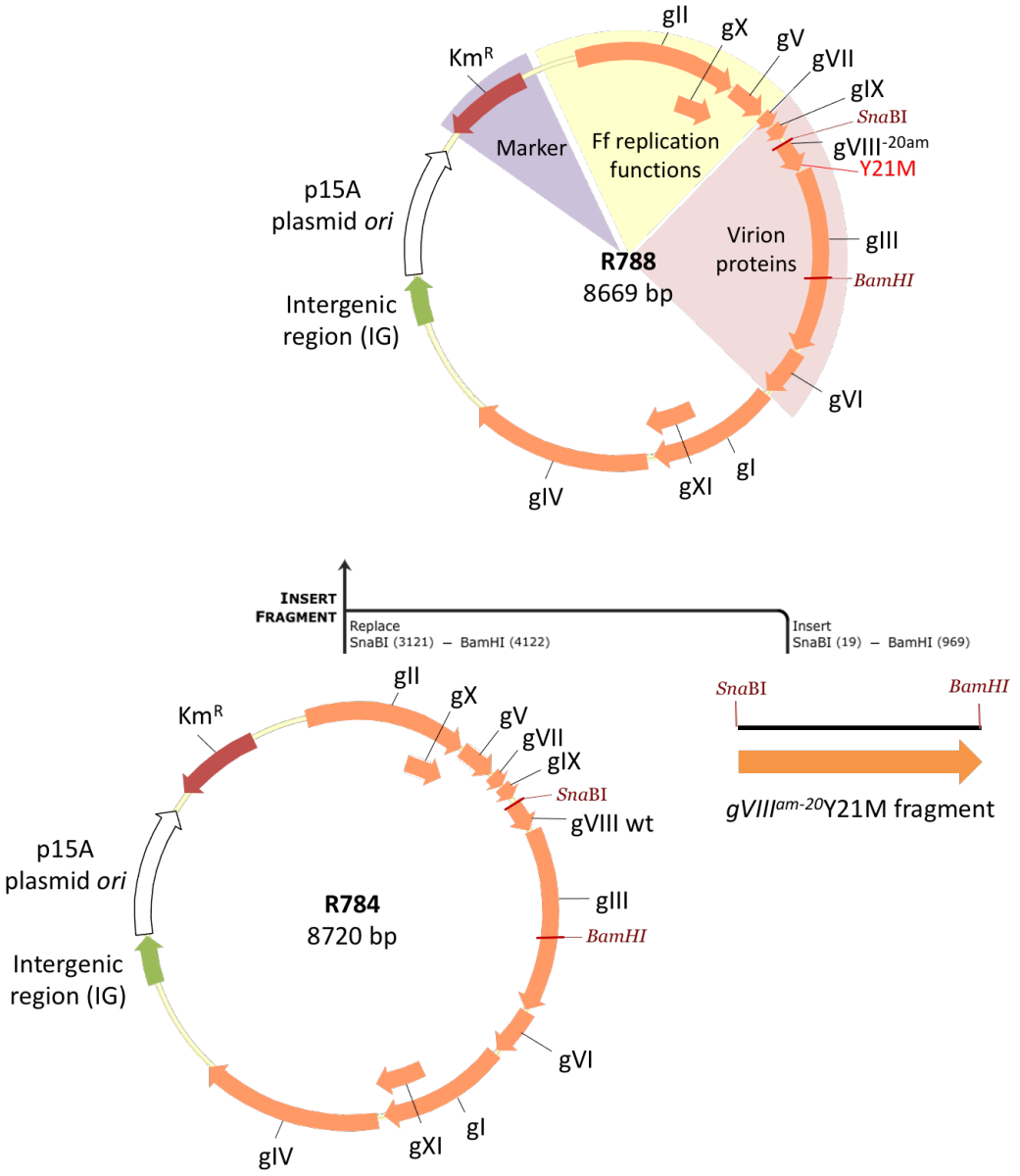

Figure 11. Construction of phage R788.

The synthetic fragment gVIII$^{am\text{-}20}$Y21M, containing part of *gIX*, part of *gIII* and *gVIII* with an *amber* mutation in position -20 and a point mutation Y21M, was cloned into helper phage R784 containing genes *gVI, gI, gXI, gIV, gII, gVII* and part of *gIX*, at BamHI/SnaBI cut-sites. Orange block arrows indicate open reading frames (ORFs) encoding phage proteins; the green block arrow corresponds to the intergenic sequence (IG) containing the origin of replication and packaging signal; the white block arrow corresponds to the p15A plasmid origin of replication; the red block arrow corresponds to the marker, in this case, kanamycin resistance (Km^R).

Now that it had been proven that the *gVIII*$^{am\text{-}20}$Y21M mutations did not interfere with phage production in the suppressor strain, the fragment was cloned into: (i) a helper phage specifically designed for the production of nanorods, and (ii) into a helper plasmid. It was hypothesised that the helper plasmid would allow the production of nanorods in a phage-independent manner. The helper phage R408 contains a mutation in *gII* (IR1B) that allows efficient replication of ssDNA from the BSFp221 nanorod replication-assembly cassette, which only has the A portion of the (+) strand *ori* (Enea & Zinder, 1982; Russel *et al*., 1986). For the construction of the new helper phage, the RF DNA of R408 and the *gVIII*$^{am\text{-}20}$Y21M synthetic fragment were digested with BamHI/SnaBI, and the *gVIII*$^{am\text{-}20}$Y21M fragment was ligated into the large fragment of R408 (Figure 12). Cells were transformed with this plasmid and plated onto a lawn of K2091 to identify recombinant plaques. The individual plaques from the transformation plate were then passaged onto lawns of K2091 and K561 to screen for the *amber* mutant (recombinant) plaques. The recombinants (named R789) were identified as those forming plaques on K2091, but not K561 lawns. To verify that no additional mutations had occurred in the cloning process, the RF DNA of clonally purified R789 candidates was purified, and the recombinants were confirmed by DNA sequencing. Next, phage and phagemid production facilitated by this phage was tested to confirm that this was an efficient helper phage. For this purpose, the phagemid pUC118 was used, and the production of phagemid particles using R789 was compared to production using a "standard" helper phage, R408 and VCSM13 (Table 7). The titres of phagemid particles (pp) obtained using R789 were very similar to the ones of the parent R408 helper phage 3.4 x 10^{10} vs. 3.2 x 10^{10} pp/mL, showing that the mutations in pVIII

did not interfere with phagemid particle production. By extension, it was hypothesised that the pVIII mutations would not interfere with the production of the nanorods in the helper plasmid system.

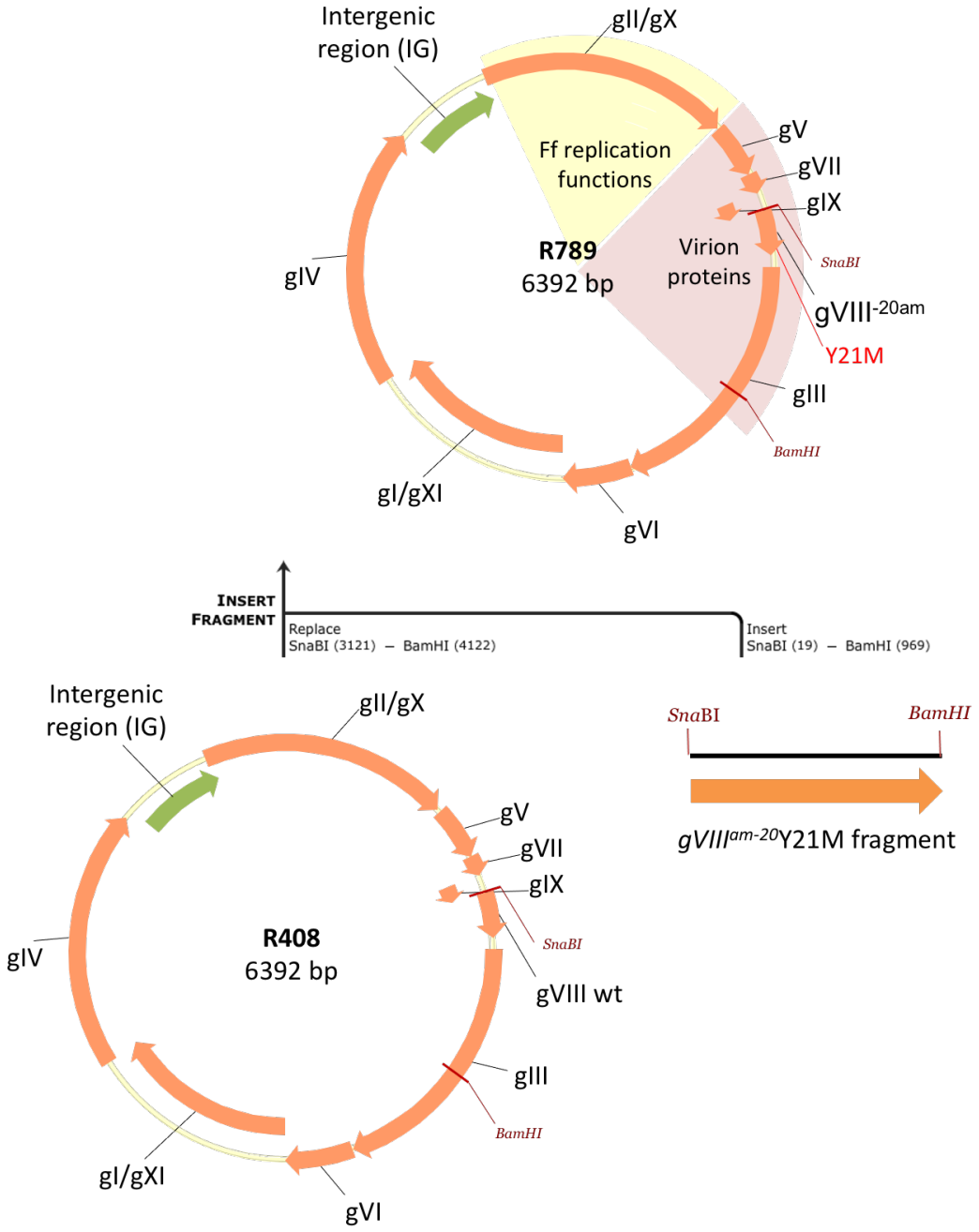

Figure 12. Construction of phage R789.

The synthetic fragment called *gVIII*$^{am\text{-}20}$Y21M, containing part of *gIX*, part of *gIII* and *gVIII* with an *amber* mutation in position -20 and a point mutation Y21M, was cloned into the helper phage R408 containing genes *gVI, gI, gXI, gIV, gII, gVII* and part of *gIX*, at BamHI/SnaBI cut-sites. Orange block arrows indicate open reading frames (ORFs) encoding phage proteins; the green block arrow corresponds to the intergenic sequence (IG) containing the origin of replication and packaging signal.

Table 7. Phage and phagemid titres

Name	Phagemid particle titre (pp/mL)	Phage infective titre (pfu/mL)
R789	$3.4 \pm 0.5 \times 10^{10}$	$3.7 \pm 0.2 \times 10^{9}$
R408	$3.2 \pm 0.4 \times 10^{10}$	$7.6 \pm 0.4 \times 10^{9}$
VCSM	$1.8 \pm 0.2 \times 10^{11}$	$3.3 \pm 0.1 \times 10^{9}$

The use of a helper plasmid instead of a helper phage in nanorod production eliminates the formation of long helper phage along with the nanorods (Figure 13). Helper phage makes up 97% of particles produced in the nanorod production system (Specthrie *et al*., 1992), hence its elimination is expected to greatly facilitate the purification process. The lack of an Ff origin of replication and packaging signal prevents the DNA of the helper plasmid from being replicated in a rolling circle mode and packaged, eliminating the co-production of phage particles. To construct a helper plasmid that assembles nanorods containing a silent *amber* mutation and a missense Y21M mutation in pVIII, the *gVIII*$^{am\text{-}20}$Y21M fragment was cloned into the helper plasmid pRnano3 (Rakonjac J., unpublished). The helper plasmid pRnano3 was digested with BamHI/SnaBI, and the large fragment was ligated into the BamHI/SnaBI digested *gVIII*$^{am\text{-}20}$Y21M fragment and transformed into K2091 electrocompetent cells. The transformants were then selected by their resistance to kanamycin, a marker encoded by the helper plasmid, and the sequence of the insert was confirmed by DNA sequencing. This new helper plasmid was named pRnanoR (Figure 14). Once the pRnanoR helper plasmid was constructed, its function as a helper for phagemid replication was tested. K2091//pRnanoR electrocompetent

cells were transformed with phagemid pUC118, and the pooled transformed cells were incubated overnight. The cells were precipitated by centrifugation, and the supernatant was filtered to remove any remaining bacteria. The phagemid titres in the supernatant reached approximately 10^9 pp/mL, a similar number to that obtained using pRnano3. This finding showed that helper plasmid pRnanoR is capable of supporting the replication and assembly of phagemid particles.

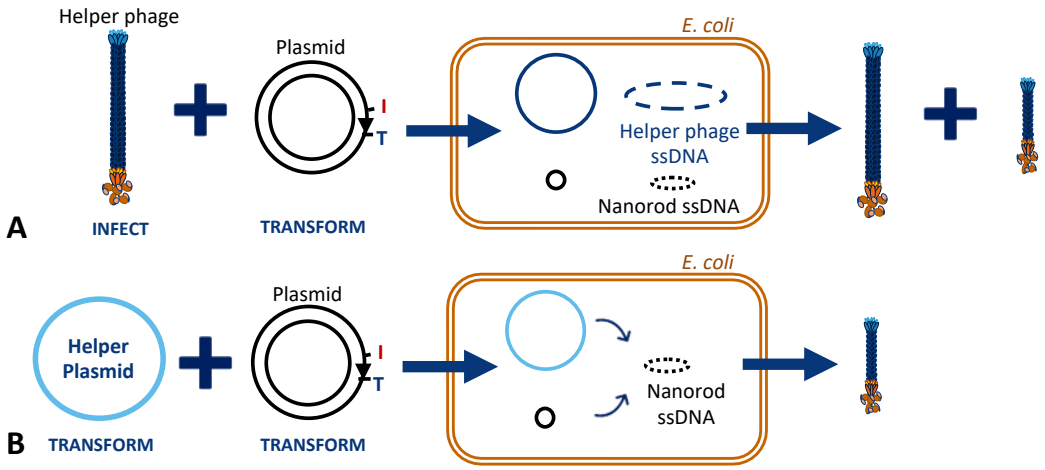

Figure 13. Comparison of the helper phage and helper plasmid nanorod production systems.

(A) Nanorod production using a helper phage. The helper phage genome is packaged at the same time as the short nanorod ssDNA, resulting in the production of the full-length helper phage and nanorod particles. (B) Nanorod production using a helper plasmid. The helper plasmid provides all the proteins normally supplied by the helper phage but is not assembled into phage particles. Only short nanorods are produced in this system.

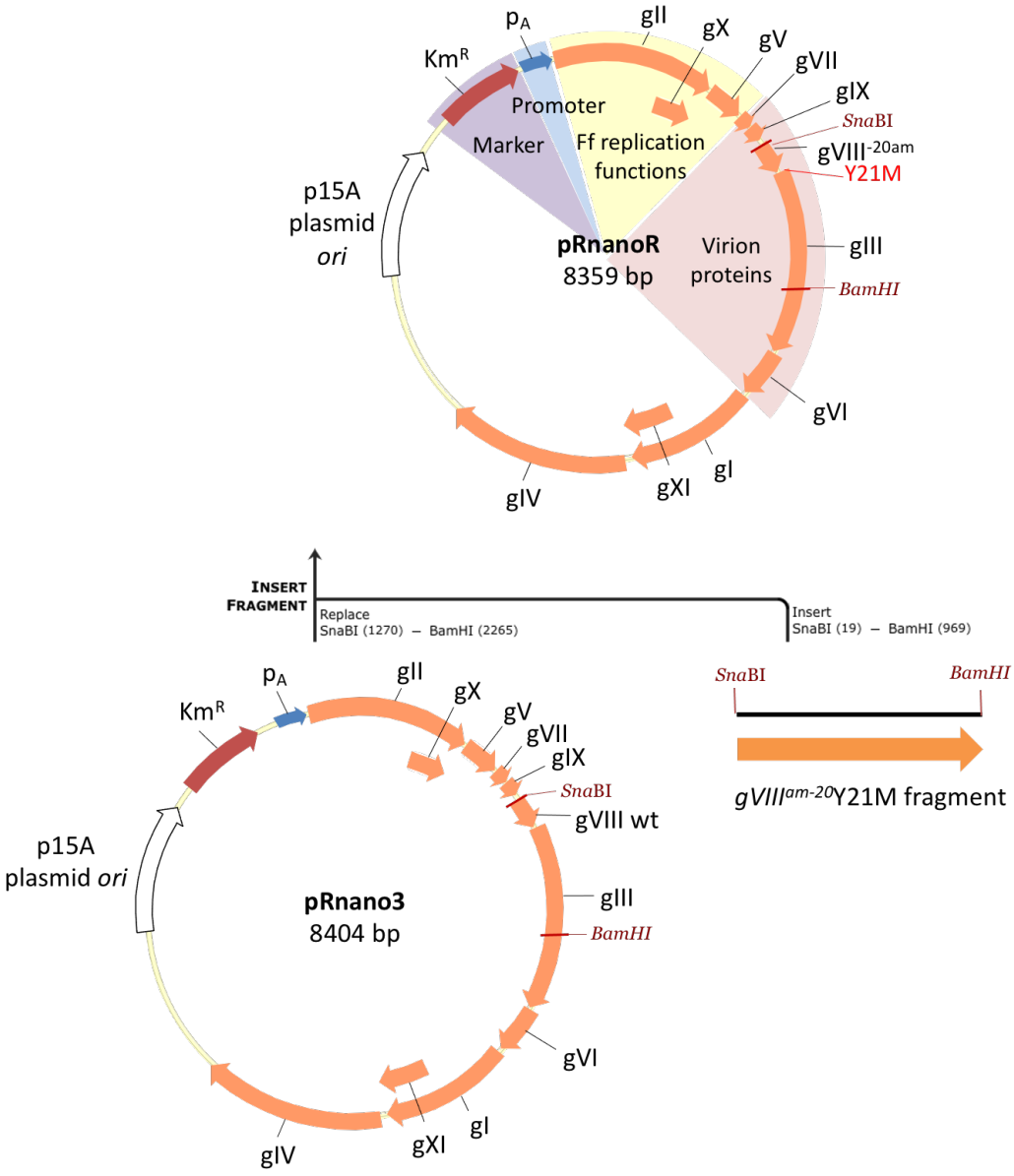

Figure 14. Construction of helper plasmid pRnanoR.

The *gVIII*$^{am\text{-}20}$Y21M fragment from phage R788, containing part of *gIX*, part of *gIII* and *gVIII* with an *amber* mutation in position -20 and a point mutation Y21M, was cloned into helper plasmid pRnano3 containing the genes *gVI, gI, gXI, gIV, gII, gVII* and part of *gIX*, at BamHI/SnaBI cut-sites. Orange block arrows indicate open reading frames (ORFs) encoding phage proteins; white block arrow corresponds to the p15A plasmid origin; the red block arrow corresponds to the marker, in this case, kanamycin resistance (Km^R); the blue block arrow corresponds to the promoter controlling the genes *gII-gV-gVII-gIX-gVIII* operon, in this case, the native Ff promoter p_A.

3.2.1.2 Production and purification of Ff-phage-derived 221-nt nanorods for structural analysis

The phagemid particle titres in the presence of the helper plasmid pRnanoR were equal to those obtained in the presence of pRnano3; however, both titres were lower than those obtained when the helper phage was used. It was therefore a question of how many 221-nt nanorods would be produced in the presence of the pRnanoR helper plasmid. For the production of nanorods, electrocompetent cells of the suppressor strain K2091 were transformed with the helper plasmid pRnanoR (Km^R), followed by a second transformation with the pSS3 plasmid (Amp^R) containing the nanorod-replication-assembly cassette producing a 221-nt circular ssDNA (BSFp221), in order to assemble the 50 nm nanorods. The pooled transformed cells were then incubated overnight in a medium containing kanamycin and ampicillin to produce nanorods (for details, see section 2.4.1). To obtain a sufficient amount of nanorods for structural analysis, 8 L of culture were necessary. The 221-nt nanorods were detected after concentration by two rounds of PEG precipitation that also included a DNAse and RNAse digestion steps to remove cell-derived DNA and RNA from the sample (not shown). These concentrated nanorods were further purified by CsCl density gradient centrifugation. When CsCl-purified nanorods were analysed by SDS-PAGE, protein bands other than the expected virion proteins were identified (Figure 15B; lane labelled “Input”), warranting an additional purification step.

Anion exchange chromatography had been proposed as an efficient method for the purification of phage. This chromatography is based on the electrostatic interactions between the negatively charged groups of the virion and the column's positively charged matrix (Coskun, 2016). In the past decade, at least three different research groups reported phage purification using this technique (Jacinto *et al*., 2018; Monjezi *et al*., 2010; Smrekar *et al*., 2011). Anion exchange chromatography using a SepFast™ Super Q column was undertaken and the fractions containing peaks were analysed by SDS-PAGE to monitor the removal of non-virion proteins (Figure 15). The fractions from which contaminating proteins seen in the input sample (the CsCl-purified nanorods) were removed were identified by SDS-PAGE. Only pVIII (~ 5.2 kDa) and pIII (~ 42.6 kDa; migrating at around 60 kDa in the Laemmli system) should be visible if the contaminating proteins are eliminated. Fractions 4-8 eluted from the anion exchange column, encompassing a major peak eluted at 750 mM NaCl (A), were analysed by SDS-PAGE (Figure 15B), Fraction 8 (Fr 8) appeared to contain the lowest number of contaminant bands. This fraction was analysed by disassembled nanorod agarose gel electrophoresis (Figure 15C) which showed a strong band corresponding to the 221-nt nanorod ssDNA. However, a second band around 2000 bp, representing longer particles, was also visible. This longer ssDNA corresponded to nanorods derived from spontaneous mutants of the pSS3 plasmid, where the second (+) *ori* in the nanorod replication-assembly cassette was deleted (Sattar, 2013). They represent an unwanted population of longer nanorods.

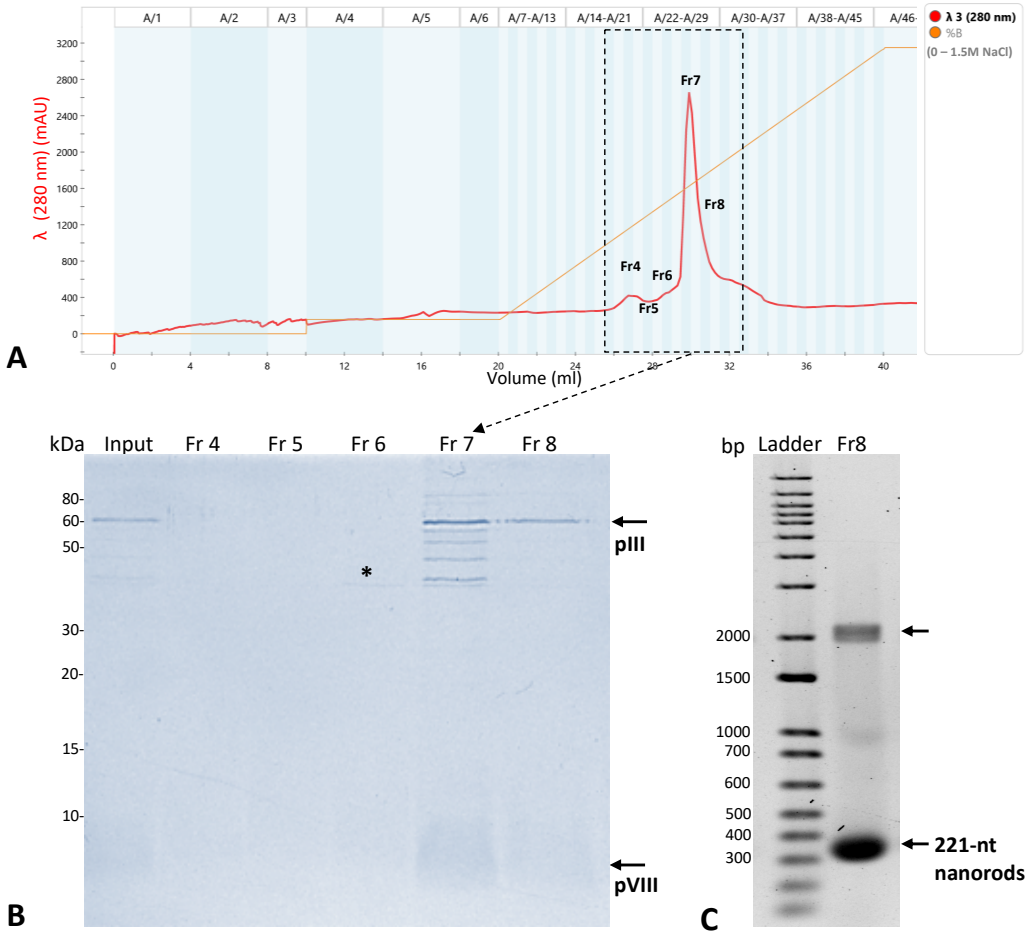

Figure 15. Purification of 221-nt nanorods by anion exchange chromatography.

Nanorod samples produced by the two-plasmid system (pRnanoR-pSS3) that were partially purified by CsCl density gradient centrifugation were subjected to chromatography using a SepFast™ Super Q (Strong anion Q, -N+(CH3)3). (A) Chromatogram. The key parameters are UV absorption (mAu; milli Absorption units) at 280 nm (red line) and %B, corresponding to the salt concentration gradient (gold line, from 0 to 1.5 M of NaCl). (B) 16% Tris-glycine SDS-PAGE of the collected fractions. kDa, sizes of the molecular weight standard bands from Novex Sharp pre-stained marker; Input, sample before chromatography (CsCl purified 221-nt nanorods); Fr4, Fr5, Fr6, Fr7, and Fr8, eluted fractions 4-8 (Fr4:A20-A21, Fr5:A22-A23, Fr6:A24-A25, Fr7:A26-A27-A28, Fr8:A29-A30). Asterisk, one of the major impurities, was removed in Fraction 6. pIII and pVIII are indicated by block arrows. (C) DNA from SDS-disassembled nanorods (Fraction 8 dialysed and concentrated from the anion exchange chromatography) was analysed by agarose (1.2%) gel electrophoresis and visualised by EtBr staining. Lanes: Ladder, 1 Kb plus ladder

(a double-stranded linear DNA standard used as a signpost for migration due to the lack of appropriate circular ssDNA standards; numbers indicate the sizes of the standard bands in base-pairs); Fr 8, the fraction from the anion exchange chromatography (see B) from which contaminating bands were removed (Fraction 8).

To purify 221-nt nanorods away from the longer particles, the sample was subjected to a preparative native-particle agarose gel electrophoresis, then extracted by electroelution. Although this process eliminated the presence of longer particles, it resulted in a considerable loss of the short 221-nt nanorods (Figure 16). The final nanorod concentration was 1.33 x 10^{14} particles/mL and showed a recovery of only 3% relative to the starting material loaded on an agarose gel (Table 8).

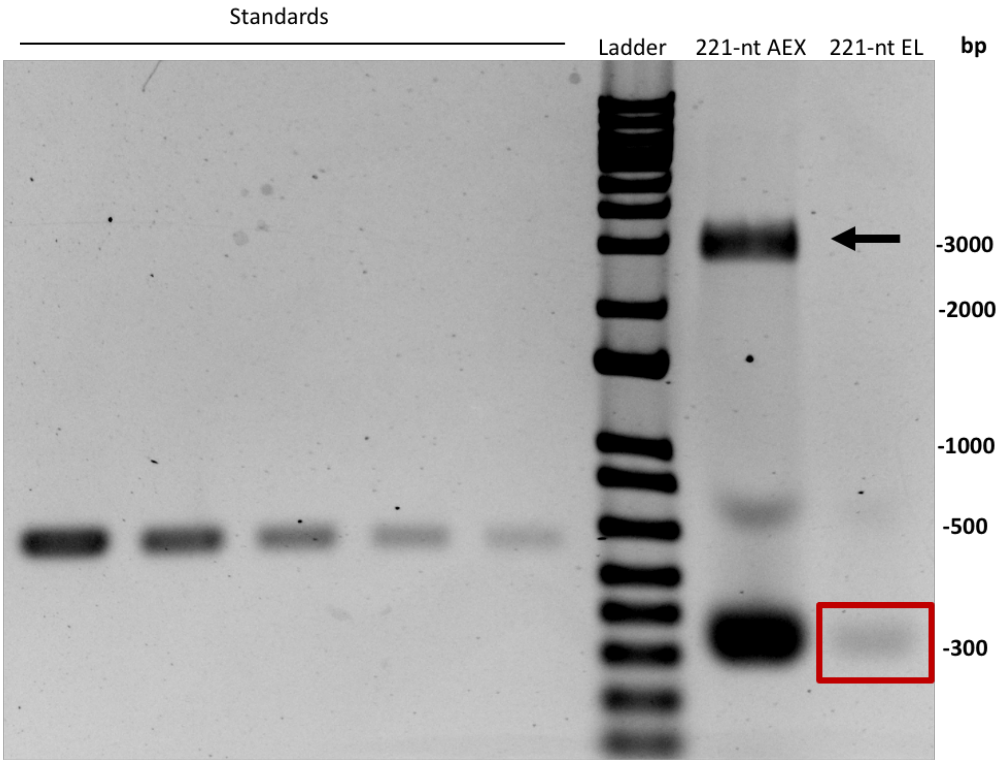

Figure 16. Quantification of electroeluted 221-nt nanorods.

DNA from SDS-disassembled nanorods was analysed by 1.2% agarose gel electrophoresis and visualised by EtBr staining. Lanes: Standards, 100, 50, 10, 5 and 2.5 ng of purified 529-nt ssDNA; Ladder, 1 Kb plus ladder (a double-stranded linear DNA standard used as a signpost for migration due to the lack of appropriate circular ssDNA standards; numbers indicate sizes of the standard bands in base-pairs); 221-nt AEX, 221-nt nanorods before electroelution, from the anion exchange purification (Fraction 8; 7.5 µL out of 300 µL); 221-nt EL, electroeluted 221-nt nanorods after the preparative native virion electrophoresis (7.5 µL out of 150 µL). Arrow points to the unwanted longer nanorod species.

Table 8. Efficiency of 221-nt nanorods purification by electroelution

	Total number	**Percentage of recovery**
221-nt nanorods before electroelution	6.7×10^{14}	(Starting material)
221-nt nanorods after electroelution	2.0×10^{13}	3%

Purified 221-nt nanorods were visualized using transmission electron microscopy (TEM; Figure 17A). The length of 100 nanorods was measured, and the distribution of sizes in the population was conducted using a binning method (Figure 17B). It was expected that some of the nanorods would be longer than 50 nm, as the longer band was not completely eliminated after electroelution (Figure 16). Most of the particles corresponded to a size of approximately 50 nm (80%) and 60 nm (7%), with about 13% being double and triple-length (Figure 17B). Filamentous phage assembly termination is not a 100% efficient event, and about 5% of nanorods were expected to be double-length due to the sequential packaging of two nanorod genomes into a single nanorod (as is the case for the wild type Ff phage). The higher percent of double-length particles observed here could be due to either the small number of analysed particles, biasing the statistics, or the contribution from particles containing a longer genome as detected in Figure 16. In addition, a "blunt" and "pointy" end can be observed in the 221-nt nanorods. No "knobs" or "ball" structures, however, were observed at their "pointy" end previously described by Gray *et al*. (1979), corresponding to the free-moving N1 and N2 domains of pIII.

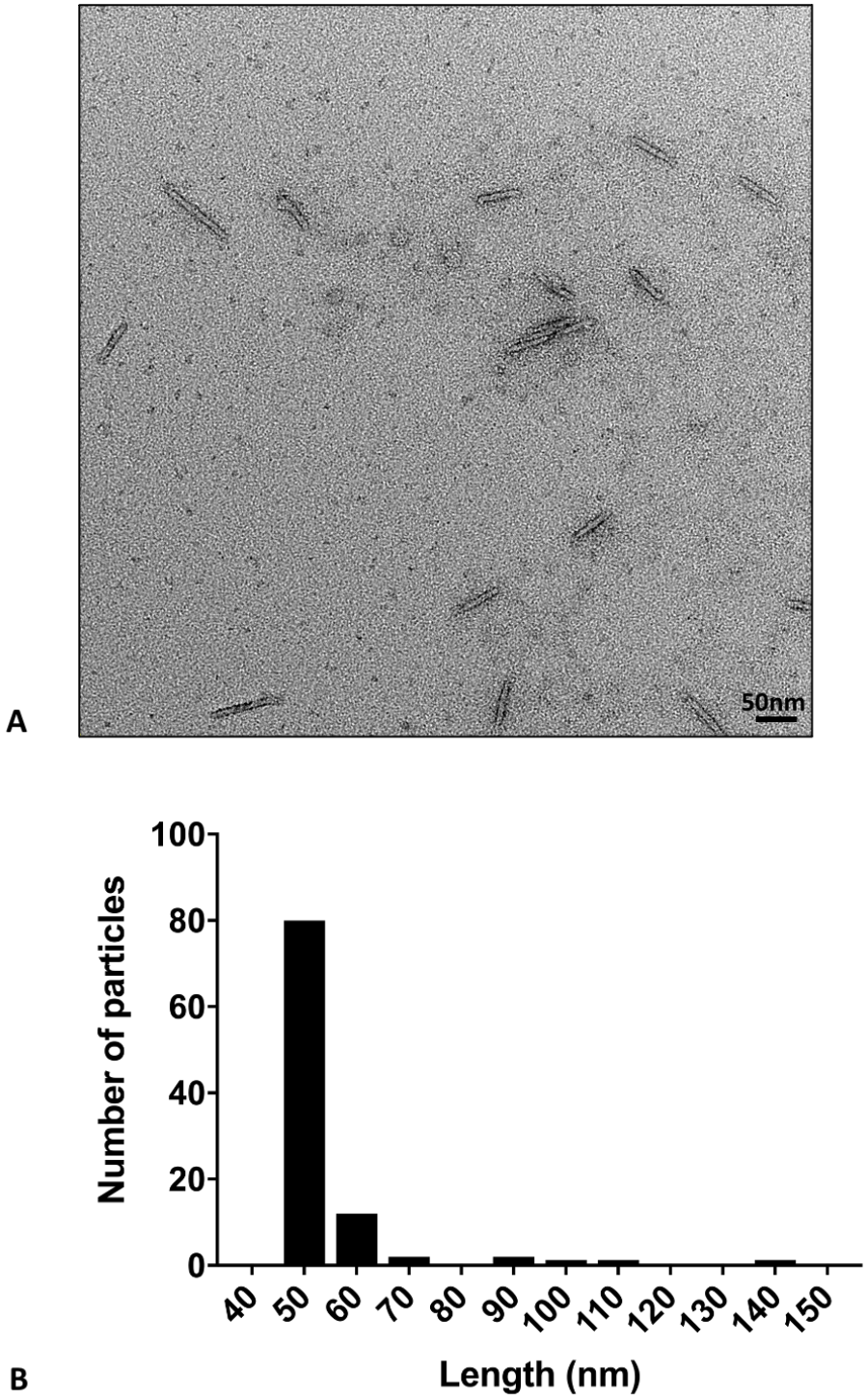

Figure 17. Analysis of 221-nt nanorods.

*(*A) Electron micrographs of negatively stained 221-nt nanorods. (B) Bar graph showing the frequency distribution of the size of the 221-nt nanorods. Size distributions are presented as a bar graph generated by measuring the length of 100 particles using the ImageJ measurement function.

3.2.2 Design and construction of a single-plasmid system for nanorod production

The phage-free system greatly facilitated the production of 221-nt nanorods due to the elimination of differential PEG precipitation that was necessary to remove the long phage at every concentration step when the helper phage were used (Sattar *et al*., 2015).

Having the phage-free system established, the next step was to improve this system in order to further shorten the production protocol and simplify the system. In our two-plasmid system the nanorod production procedure requires two sequential transformations to introduce two plasmids necessary for the nanorod production into the *E. coli* cells. Each plasmid contains complementary sets of elements required for the nanorod production: the helper plasmid carries all genes encoding for the replication, assembly, and virion proteins, whereas the template plasmid contains the BSF replication-assembly cassette that produces the nanorod ssDNA (packaging substrate for nanorod assembly; Figure 18A).

The two-step transformation was required because double-plasmid transformation in one step resulted in too few doubly-transformed cells and consequently a low level of nanorod production that is a result of the high number of generation times required to build up the number of double-transformed cells. The low level of

nanorod production is due to a decrease of ssDNA replication with every generation, caused by interplay between the pII and pX replication proteins (Smeal *et al*., 2017b). Hence, by the time the doubly-transformed cells build up to 10^8 per mL, the number required for significant nanorod yield, the number of ssDNA substrates for packaging per cell is low (S. Bisset and J. Rakonjac, unpublished).

To minimize both labour and production time, a novel single-plasmid system containing all the elements for the production of nanorods was designed and named pPop-upUni (Figure 18B). This system requires only a single transformation, shortening the protocol required for first transformation and preparation of competent cells in the two-plasmid system by three days. The new single-plasmid system was constructed based on the BSFpn replication-assembly cassette (BSFpn529, 529-nt in length; for details, see section 2.2.1.1). This cassette contains both positive and negative origins of replication and is expected to produce a much higher amount of nanorods than the BSFp cassette (lacking the (-) *ori*). When (-) *ori* is missing, the ssDNA that serves as a backbone for the assembly of short nanorods is only replicated from the larger plasmid template, and as a result, the total number of copies per cell is limited. In contrast, when (-) *ori* is present, the negative strand can also be synthetised starting from the short ssDNA as template. Hence, the functionality of the pPop-upUni plasmid, containing the BSFpn cassette, in nanorod production could be easily analysed using volumes of culture below 100 mL.

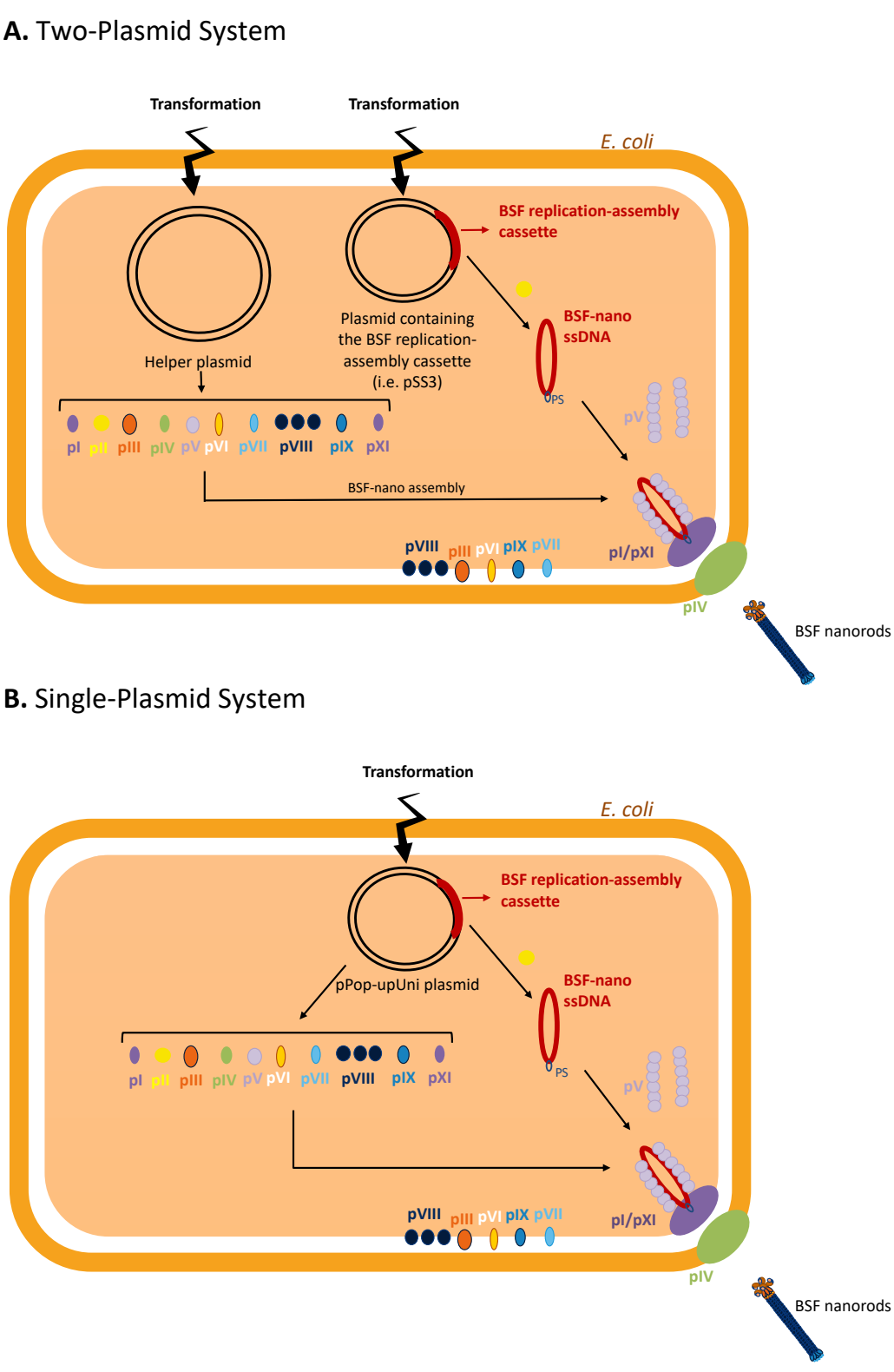

Figure 18. Overview of the production systems.

(A) Two-plasmid production system. Transformation of electrocompetent cells with the helper plasmid is followed by the preparation of electrocompetent cells to be transformed

with the second plasmid containing a BSF-nano replication-assembly cassette. (B) Single-plasmid system. Production of nanorods requires only one transformation step; transforming electrocompetent cells with the single-plasmid containing the BSF replication-assembly cassette and all the genes encoding for proteins required for the replication, assembly and building of the virion (pPop-upUni).

The new single-plasmid system for production of the 529-nt nanorods (named pPop-up529Uni) was constructed by insertion of the synthetic BSFpn fragment, designed to be flanked by PstI and SalI, and included the intrinsic SwaI restriction site within the Ff promoter p_A that controls transcription of the *gII-gV-gVII-gIX-gVIII* operon. This fragment (named BSFpn PstI-SwaI) was digested and ligated into the large fragment of the PstI-SwaI-digested helper plasmid pRnanoR (Figure 19), to produce "Pop-up BSFpn" replication cassette (within new plasmid pPop-up529Uni). Cells transformed with this plasmid produced nanorods so efficiently that were easily detected and purified form small-volume cultures (results not shown), giving motivation to insert the "pPop-up BSFp" cassette in the single-plasmid (plasmid pPop-up221Uni) nanorod production system.

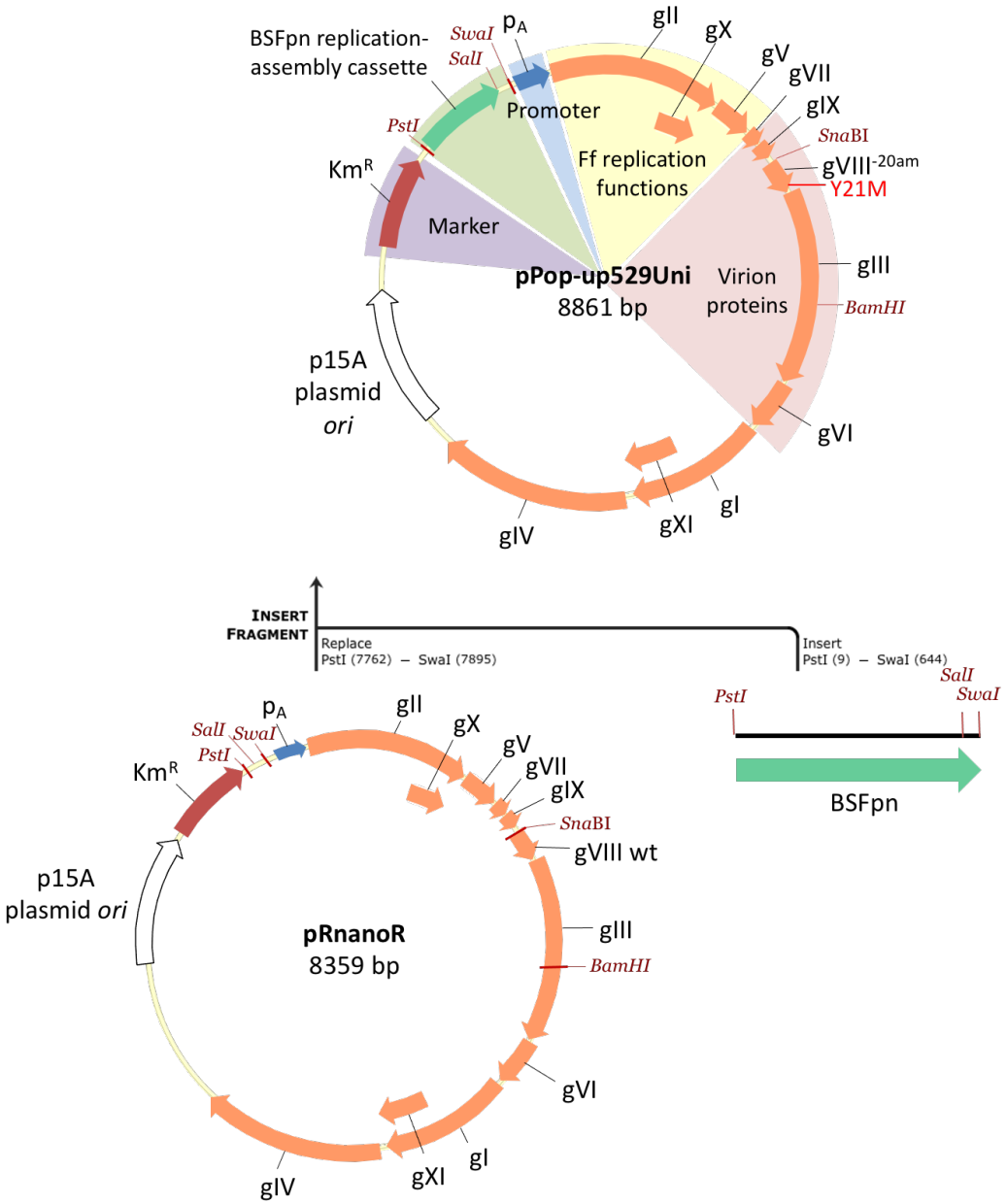

Figure 19. Construction of plasmid pPop-up529Uni.

A synthetic fragment named Pop-up PstI-SwaI, containing the BSFpn replication-assembly cassette (BSFpn529 producing 529-nt circular ssDNA), was cloned into helper plasmid pRnanoR containing all genes encoding for proteins required for replication and assembly of nanorods, at PstI/SwaI cut-sites. Orange block arrows indicate open reading frames (ORFs) encoding phage proteins; the green block arrow corresponds to the BSFpn fragment (BSFpn529); the white block arrow corresponds to the p15A plasmid origin of replication; the red block arrow corresponds to the marker, in this case, kanamycin resistance (Km^R);

the blue block arrow corresponds to the promoter controlling the gene *gII-gV-gVII-gIX-gVIII* operon, in this case, the native Ff promoter p_A.

In order to construct a single-plasmid system for production of 50 nm nanorods (Sattar *et al*., 2015; Specthrie *et al*., 1992), the BSFp221 replication-assembly cassette was amplified by PCR using the pSS3 plasmid as template and primers RL001 and RL002 containing PstI and SalI endonuclease restriction cut sites (for details, see section 2.2.1.1). The PstI-SalI-digested PCR product was ligated into the large fragment of the PstI-SalI-digested plasmid pPop-up529Uni (Figure 20). Recombinants were selected by their resistance to kanamycin and confirmed by DNA sequence analysis. This novel single-plasmid system was named pPop-up221Uni.

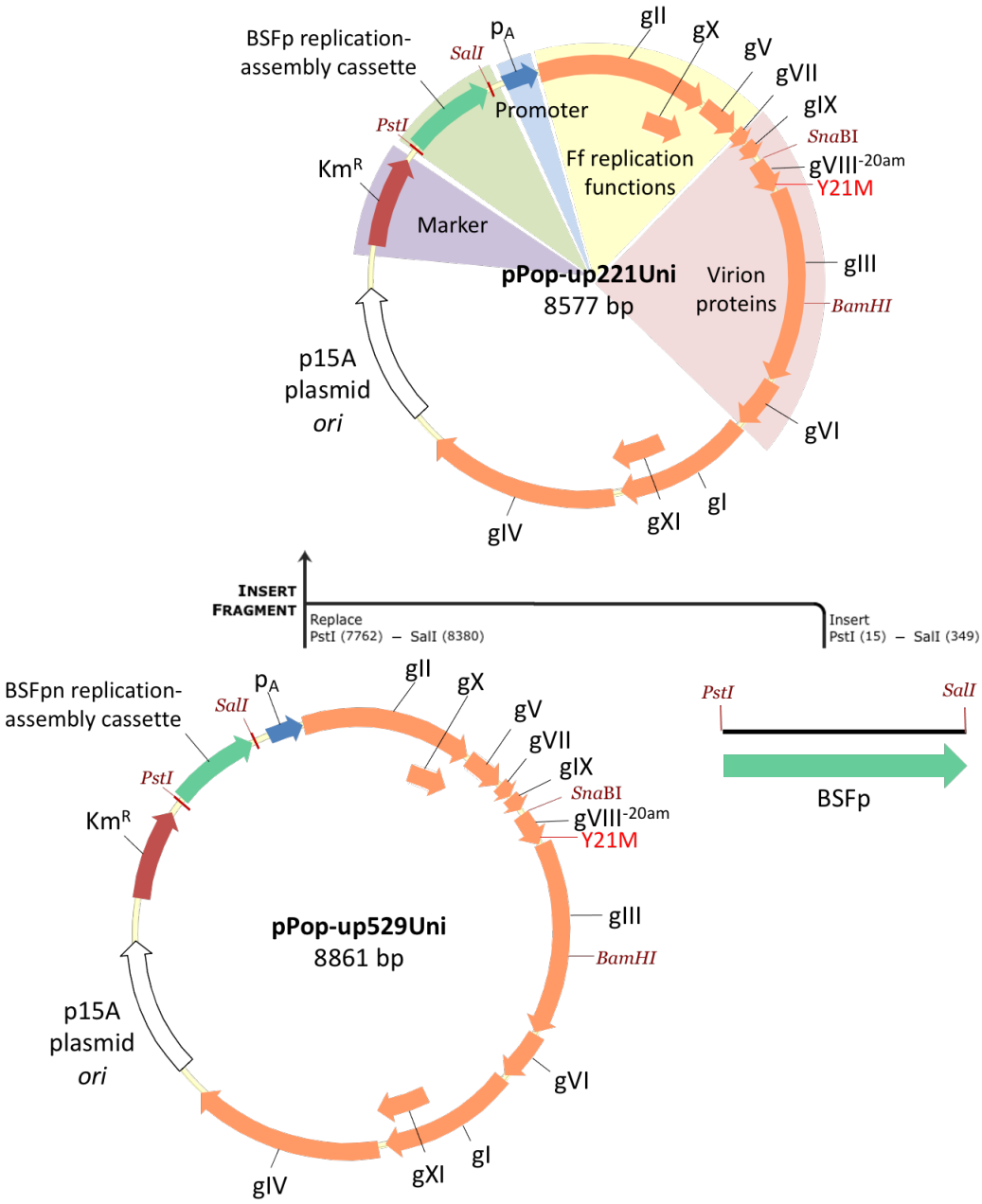

Figure 20. Construction of plasmid pPop-up221Uni.

The PCR-amplified BSFp221 replication-assembly cassette (corresponding to pSS3 producing 221-nt circular ssDNA), was cloned into the pPop-up529Uni plasmid to replace the BSFpn529 cassette. Orange block arrows indicate open reading frames (ORFs) encoding phage proteins; the green block arrow corresponds to the BSFpn or BSFp cassette (BSFpn529 and BSFp221, respectively); the white block arrow corresponds to the p15A plasmid origin of replication; the red block arrow corresponds to the marker, in this case,

kanamycin resistance (Km^R); the blue block arrow corresponds to the promoter controlling the gene *gII-gV-gVII-gIX-gVIII* operon, in this case, the native Ff promoter p_A.

3.2.2.1 Production of 221 and 529-nt nanorods from a single-plasmid production system

K2091 electrocompetent cells were transformed with the pPop-up221Uni or pPop-up529Uni plasmid, and the pool of transformed cells was incubated overnight in a medium containing kanamycin to select for transformants. The production of nanorods in the supernatant of these overnight cultures of transformed cells was assessed to determine the efficiency of the single-plasmid system. Nanorods were concentrated from the culture supernatant by PEG precipitation (for details, see section 2.4.2) and analysed by disassembled- and native-particle agarose gel electrophoresis to compare the amount of nanorods produced by the two plasmids (Figure 21). The amount of nanorods produced by pPop-up529Uni per 1 L of original culture was about 20-fold higher than by pPop-up221Uni (4.9×10^{14} and 2.4×10^{13}; respectively). Thus, the presence of the complete (+) *ori* and the (-) *ori* in the replication-assembly cassette BSFpn increases nanorod production 20-fold compared to the BSFp replication-assembly cassette containing only the A domain of the (+) *ori* and no (-) *ori*, when replication is driven by an IR1B mutant of pII encoded by the pPop-upUni plasmids.

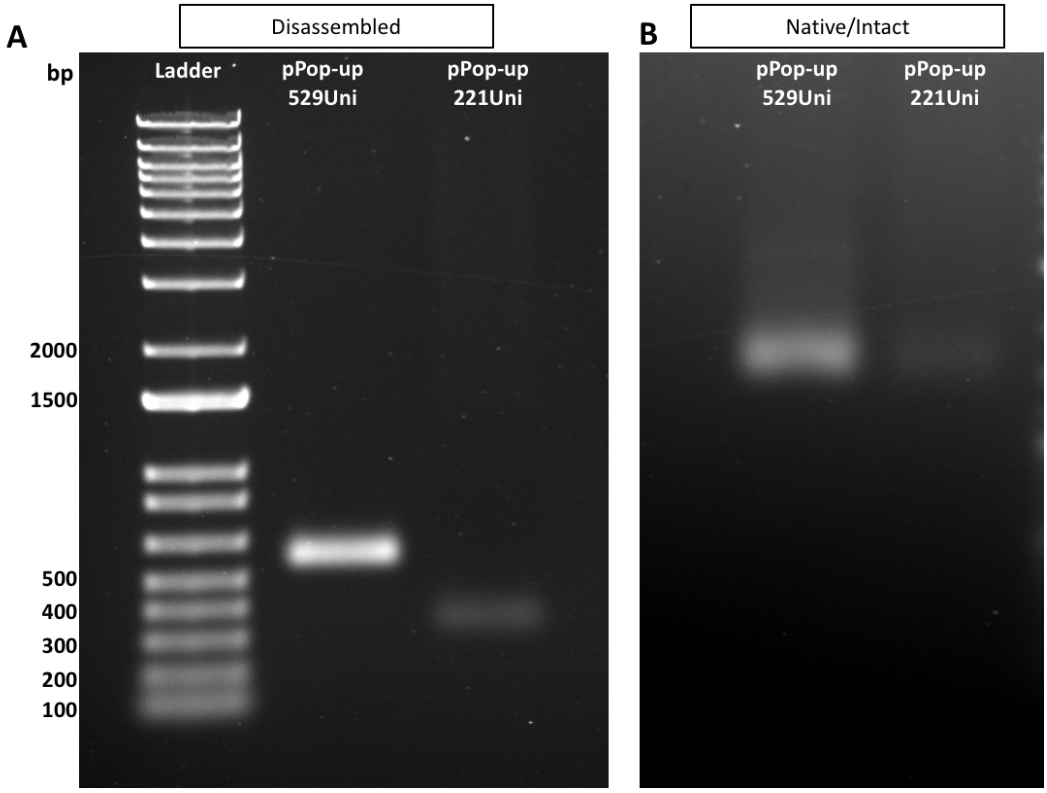

Figure 21. Comparison of the single-plasmid production systems with cassettes containing both positive and negative ori's (pPop-up529Uni) or only A domain of positive ori (pPop-up221Uni).

(A) DNA from SDS-disassembled nanorods was separated by 1.2% agarose gel electrophoresis and visualised by EtBr staining. (B) Native nanorods. Bands corresponding to the native/intact particles were visualized by EtBr staining after soaking the gel in 0.2 M NaOH. Lanes: Ladder, 1 Kb plus ladder (a double-stranded linear DNA standard used as a signpost for migration due to the lack of appropriate circular ssDNA standards; numbers indicate sizes of the standard bands in base-pairs). Pop-up529Uni and Pop-up221Uni denote nanorods derived from the cells transformed with the plasmids pPop-up529Uni and pPop-up221Uni. Nanorods were concentrated 1000-fold by PEG precipitation.

The identity of the 529-nt nanorods was confirmed by TEM (Figure 22A) and from the micrographs obtained, the distribution of sizes in the population was conducted using a binning method (Figure 22B). 78% of the 529-nt nanorods produced by

pPop-up529Uni plasmid were around 80 nm in length, while a 16% were around 90 nm, a 4% around 70 nm, and only a 2% above 100 nm. As explained previously, the number of shorter and longer particles measured could be either due to the small number of analysed particles, deviating the statistics, or that particles sit in random orientations relative to the plane of the grid and could stick together along the length, appearing to be a longer nanorod. Just as for the 221-nt nanorods, a "blunt" and "pointy" end can be observed in the micrographs of 529-nt nanorods. Once again, no "knobs" or "ball" structures corresponding to the free-moving N1 and N2 domains of pIII could be observed at their "pointy" end previously described by Gray *et al*. (1979).

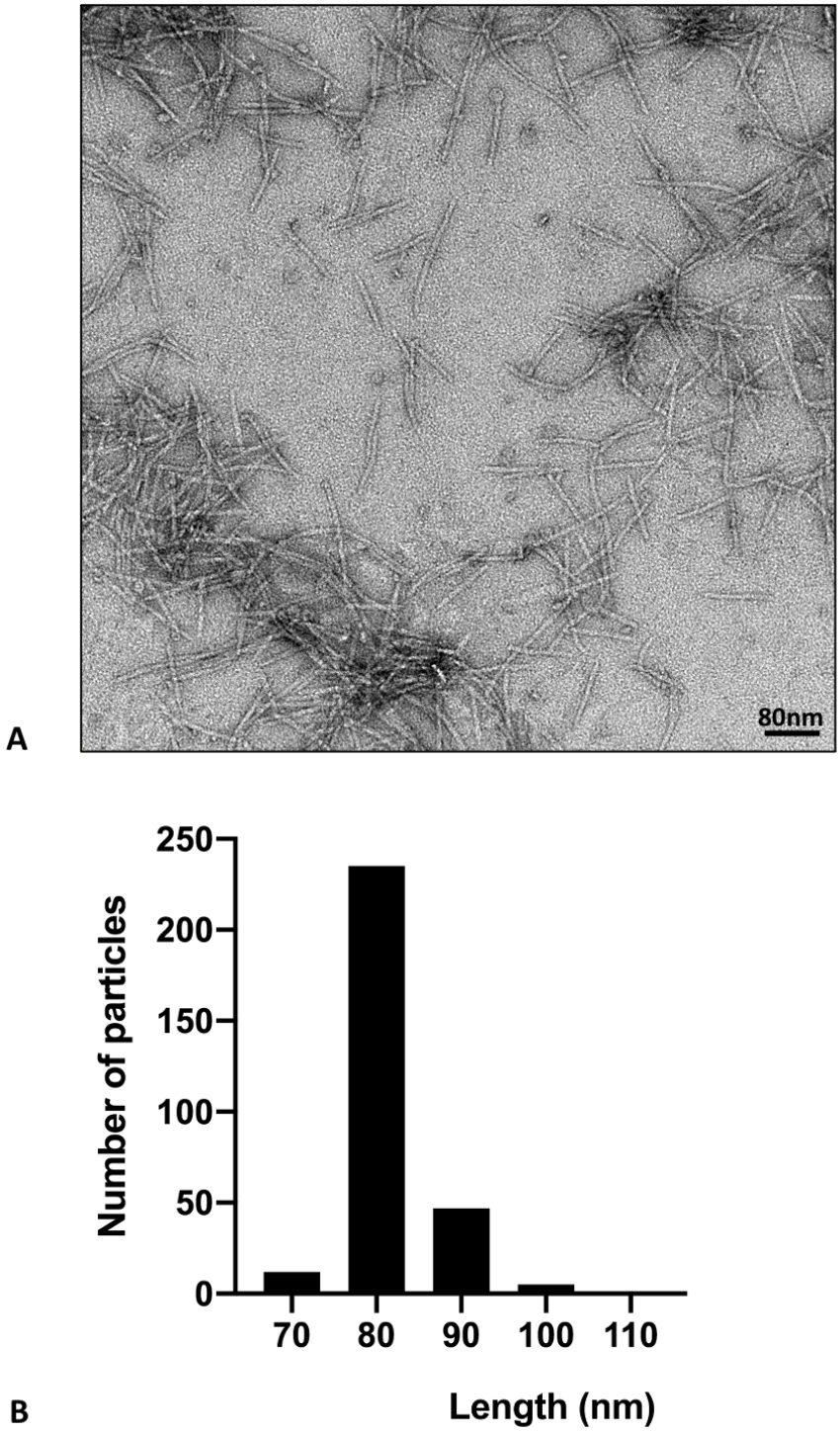

Figure 22. TEM analysis of the 529-nt nanorods.

(A) Electron micrographs of negatively stained 529-nt nanorods. (B) Bar graph showing the frequency distribution of the size of the 529-nt nanorods. Size distributions are presented as bar graph generated by measuring the length of 300 well-separated particles using the ImageJ measurement function.

3.2.3 Increasing the efficiency of the single-plasmid system for nanorod production by introducing inducible replication

Due to the low yield of BSFp221 replication-assembly cassette, only BSFpn529 was used to examine whether the presence of an inducible promoter will result in an overall increase in the total number of produced nanorods. The plasmid was named pPop-up529LacUni. To construct the pPop-up529LacUni plasmid, a fragment containing the *lacUV5* promoter and 5' portion of *gII* flanked by SalI and HpaI restriction sites was designed, custom-synthetized, digested, and then ligated to the large fragment of the SalI-HpaI-cut pPop-up529Uni (Figure 23). Transformants were selected based on their resistance to kanamycin, and correct recombinants were verified as pPop-up529LacUni by DNA sequencing.

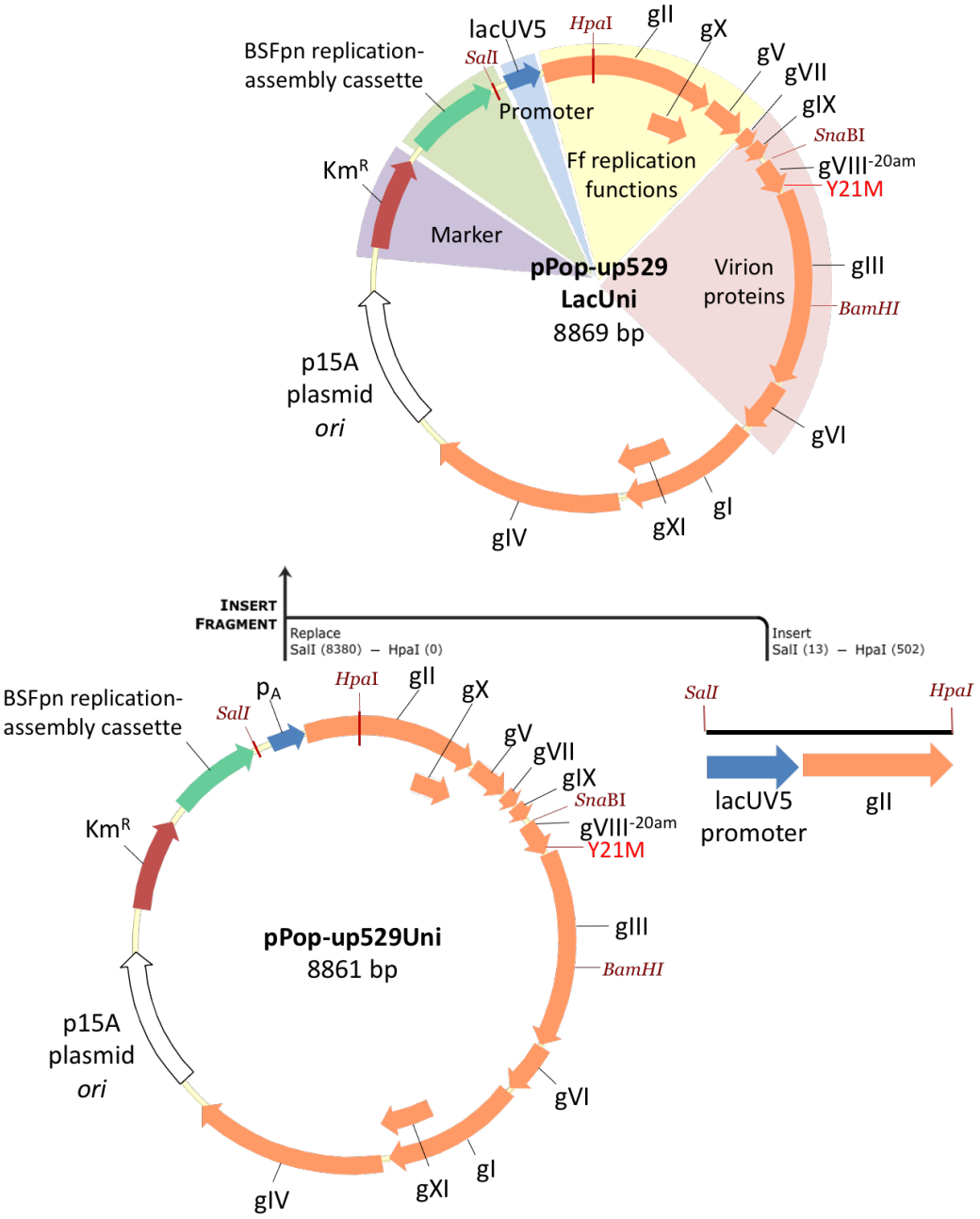

Figure 23. Construction of plasmid pPop-up529LacUni.

A synthetic fragment containing the *lacUV5* promoter and 5' moiety of *gII*, was cloned into the pPop-up529Uni plasmid containing the BSFpn resplication-assembly cassette (BSFpn529 producing 529-nt circular ssDNA) and all genes encoding for proteins required for replication and assembly of nanorods, at SalI/HpaI cut-sites. Orange block arrows indicate open reading frames (ORFs) encoding phage proteins; the green block arrow corresponds to the BSFpn cassette (BSFpn529); the white block arrow corresponds to the

p15A plasmid origin of replication; red block arrow corresponds to the marker, in this case, kanamycin resistance (Km^R); the blue block arrow corresponds to the promoter controlling the genes *gII-gV-gVII-gIX-gVIII* operon, in this case, the *lacUV5* promoter.

3.2.3.1 Production of 529-nt nanorods from an inducible single-plasmid system

K2091 electrocompetent cells were transformed with the pPop-up529LacUni plasmid and incubated in media supplemented with kanamycin until reaching an OD_{600} ~ 0.1. The culture was then split in two, and IPTG was added to one of the two cultures at a final concentration of 1 mM. The induced and uninduced cultures were incubated overnight. As described in section 2.4.4, nanorods were concentrated from the culture supernatants by PEG precipitation. The 529-nt nanorods were then analysed by disassembled- and native-particle agarose gel electrophoresis (Figure 24), where a 10-fold increase in the production was seen in the culture of pPop-up529LacUni in the presence of IPTG in comparison to the nanorods produced using pPop-up529Uni that contained the phage promoter p_A driving the expression of pII (4.8×10^{15} and 4.9×10^{14} nanorods per 1 L of original culture, respectively). Interestingly, 9.7×10^{13} nanorods per 1 L of original culture were produced in the pPop-up529LacUni culture in the absence of IPTG, indicating there was background expression of pII from the *lacUV*5 promoter.

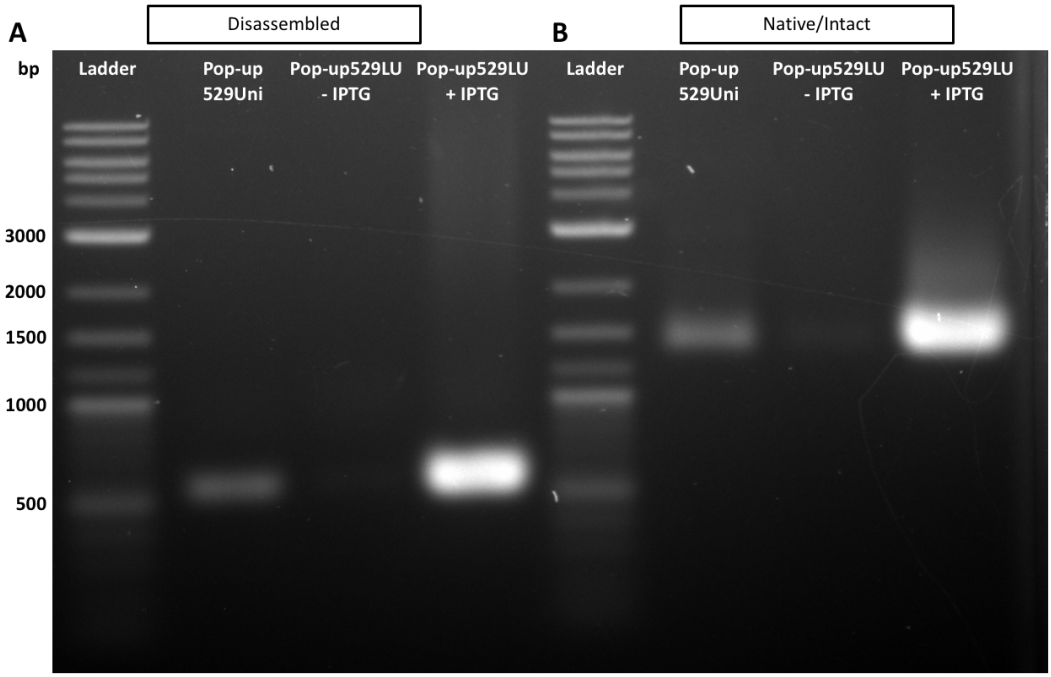

Figure 24. Inducible expression of replication protein pII increases nanorod production.

Agarose gel electrophoresis of SDS-disassembled (A) and native (B) nanorods produced in the single-(pPop-up) plasmid system containing the 529-nt replication-assembly cassette (BSFpn529). Expression of the replication protein pII was driven by the constitutive f1 phage promoter pA (plasmid pPop-up529Uni), or by inducible promoter *lacUV5* (plasmid pPop-up529LacUni). Lanes: Ladder, 1 Kb plus ladder (a double-stranded linear DNA standard used as a signpost for migration due to the lack of appropriate circular ssDNA standards; numbers indicate sizes of the standard bands in base-pairs); Pop-up529Uni, nanorods derived from the plasmid pPop-up529Uni; pPop-up529LU - IPTG, nanorods derived from the plasmid pPop-up529LacUni without IPTG; pPop-up529LU + IPTG, nanorods derived from the plasmid pPop-up529LacUni in the presence of IPTG (1 mM). Nanorods were concentrated 1000-fold by PEG precipitation from the supernatant of a 1 L culture of pooled cells transformed with pPop-up529Uni or pPop-up529LacUni.

All nanorod production systems designed in this chapter and their nanorod production capacities are summarised in Table 9.

Table 9. Nanorods produced by the different systems

Plasmid	Nanorods per 1 L of original culture
pPop-up221Uni	$2.4 \pm 0.2 \times 10^{13}$
pPop-up529Uni	$4.9 \pm 0.3 \times 10^{14}$
pPop-up529LacUni (+) IPTG	$4.8 \pm 0.4 \times 10^{15}$
pPop-up529LacUni (-) IPTG	$9.7 \pm 0.4 \times 10^{13}$

3.2.3.2 Purification of the 529-nt nanorods produced by the inducible single-plasmid system

Since the 529-nt nanorods produced by the inducible single-plasmid system (pPop-up529LacUni plasmid) reached the highest yield of all the nanorods produced in this chapter (Table 9), they were chosen to be structurally characterised. For this, the 529-nt nanorods from 1 L of original culture produced by the pPop-up529LacUni plasmid were purified in the same manner as the 221-nt nanorods in section 3.2.1.2, by CsCl density gradient centrifugation and anion exchange chromatography using a SepFast™ Super Q column (see details of the method in Chapter 2, section 2.5.1 and 2.5.3). Quantities of eluted nanorods (or free proteins) were monitored by the absorbance at 280 nm (Figure 25A) and collected fractions analysed by SDS-PAGE to monitor the removal of the non-virion protein bands (Figure 25B). The chromatogram obtained from this purification has the same pattern as the one for the 221-nt nanorods (Figure 15), showing a major peak collected at 750 mM NaCl containing Fractions 7-8 (Fr7 and Fr8). Figure 25B confirms the presence of pVIII (~ 5.2 kDa) and pIII (~ 42.6 kDa, migrating at

around 60 kDa in the Laemmli system) in Fr7 and Fr8. Almost no presence of other bands containing contaminants were observed in either Fr7 or Fr8. Based on this observation, fractions 7 and 8 were pooled together, as described in Chapter 2 section 2.5.4, and analysed by disassembled nanorod agarose gel electrophoresis (Figure 25C). Detection of only one strong DNA band at the expected position in the gel (529 bp) confirms the presence of the 529-nt nanorods. The purified 529-nt nanorods at an approximate concentration of 2.2 ± 0.2 mg of nanorods/mL were either sent to Vicki Gold's laboratory at the University of Exeter (UK) to be analysed by cryo-EM SPA, or used to attempt the pIII-pVI complex purification.

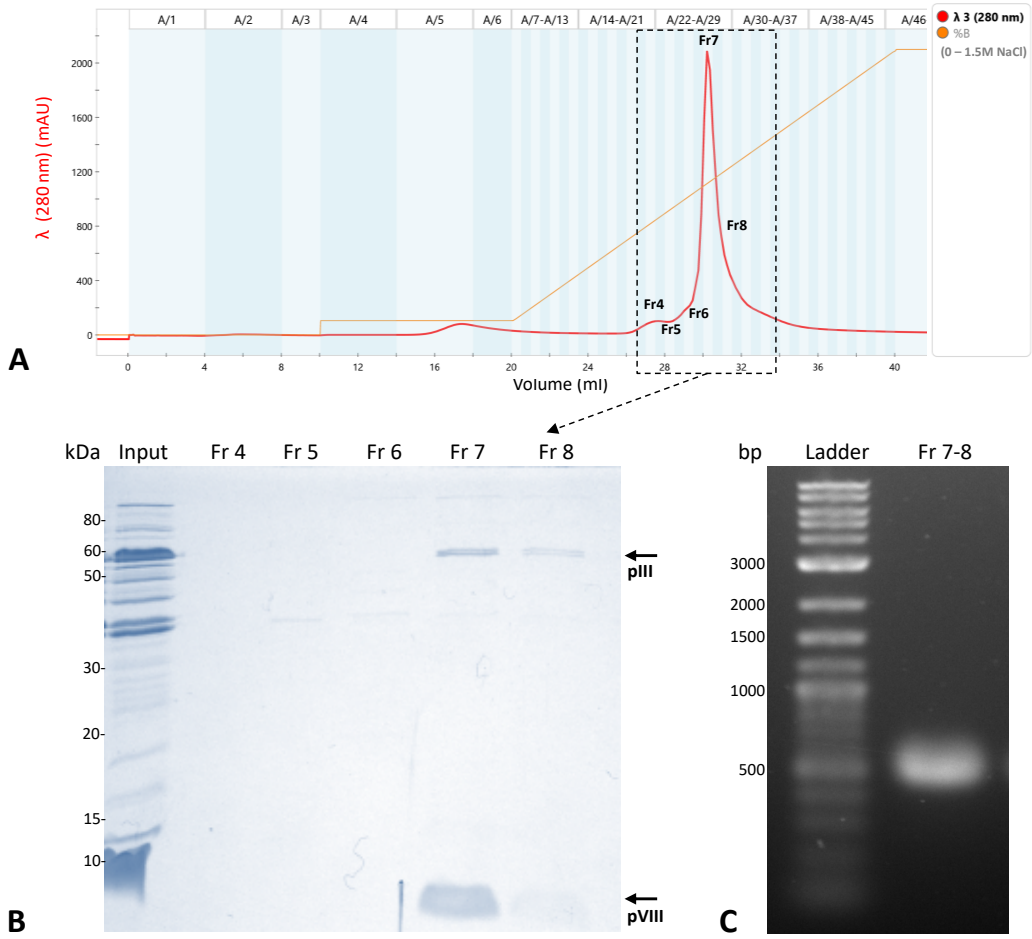

Figure 25. Purification of 529-nt nanorods produced by the inducible single-plasmid (pPop-up529LacUni) by anion exchange chromatography.

Nanorod samples that were partially purified by CsCl density gradient centrifugation were subjected to chromatography using a SepFast™ Super Q (Strong anion Q, -N+(CH3)3). (A) Chromatogram. The key parameters are UV absorption (mAu; milli Absorption units) at 280 nm (red line) and %B, corresponding to the salt concentration gradient (gold line, from 0 to 1.5 M of NaCl). (B) 16% Tris-glycine SDS-PAGE of the collected fractions. kDa, sizes of the molecular weight standard from Novex Sharp pre-stained marker; Input, sample before chromatography (CsCl purified 529-nt nanorods); Fr4, Fr5, Fr6, Fr7, and Fr8, eluted fractions 4-8 (Fr4:A20-A21, Fr5:A22-A23, Fr6:A24-A25, Fr7:A26-A27-A28, Fr8:A29-A30). pIII and pVIII are indicated by block arrows. (C) DNA from SDS-disassembled nanorods (dialysed and concentrated Fraction 7-8 from the anion exchange chromatography) was analysed by agarose (1.2%) gel electrophoresis and visualised by EtBr staining. Lanes: Ladder, 1 Kb plus ladder (a double-stranded liner DNA standard used

as a signpost for migration due to the lack of appropriate circular ssDNA standards; numbers indicate sizes of the standard bands in base-pairs); Fr 7-8, the fractions from the ion exchange chromatography (see B) from which contaminating bands were removed.

3.3 Summary/Conclusions

In this chapter, novel plasmid-based systems for production of Ff phage-derived short nanorods were designed, engineered, and compared to explore strategies to maximise short nanorod production. Furthermore, the purification procedure was optimised by adding an anion exchange chromatography purification step to eliminate *E. coli* proteins that remained in the sample after CsCl density gradient centrifugation. The high purity of the nanorods will facilitate their structural analysis. All the nanorods produced by the systems in this chapter were designed to contain a point mutation in residue 21 of the mature coat protein pVIII (tyrosine to methionine; Y21M), which has been shown in multiple Ff shaft analyses to result in more rigid and better-aligned phage particles which are more suitable for structural studies (Abramov *et al*., 2017; Marvin *et al*., 2006).

We produced 221-nt nanorods (50 nm in length), based on the BSFp nanorod replication-assembly cassette (BSFp221), by a two-plasmid system and a single-plasmid system for structural characterisation by cryo-EM SPA. Their production by both systems, however, resulted in a low yield for structural analysis. On the other hand, the single-plasmid system reduced the production time of these

nanorods by three days. The yield of produced nanorods was increased by 20-fold when using instead the BSFpn nanorod replication-assembly cassette (BSFpn529), but the resulting nanorods were slightly longer nanorods ~ 80 nm in length. Nevertheless, these 529-nt nanorods are still short enough to characterise their end-caps structurally. Unlike the BSFp replication-assembly cassette, the BSFpn replication-assembly cassette contains the negative origin of replication. The presence of the (-) *ori* results in the production of nanorod ssDNA not only by replication of the (+) strand ssDNA from the template plasmid, but also by replication of the (-) strand from the negative origin of the short nanorod ssDNA, or by the (+) strand from the short (529-bp) closed-circular dsDNA. As predicted, the major increase in nanorod production from the BSFpn529 replication-assembly cassette was observed compared to that achieved using the BSFp template (~ 20-fold; Table 9). Moreover, the 529-nt nanorod production was further increased 10-fold by replacing the constitutive Ff promoter present in the single-plasmid system with an inducible promoter, *placUV5*. Therefore, the production of nanorods by the inducible pBSFpn529 resulted in an overall 200-fold increase compared to that produced by pBSFp221 (Table 9).

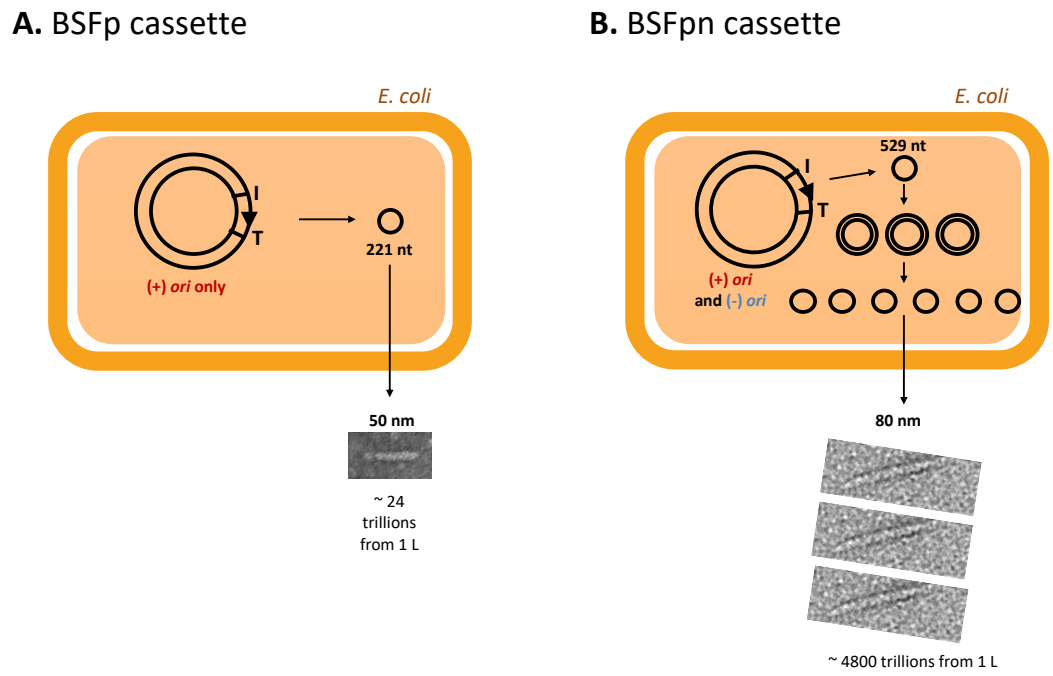

Figure 26. BSF-nano replication and assembly cassettes and their production efficiency.

BSFp (A) and BSFpn (B) replication-assembly cassettes producing 221-nt and 529-nt nanorods of 50 and 80 nm in length, respectively.

In summary, a novel inducible single-plasmid system for efficient production of 529-nt nanorod was reported in this chapter. Furthermore, the current nanorod purification method was majorly improved by adding an anion exchange chromatography step, using a strong anion column (SepFastTM Super Q) that contains large pores, hence, is suitable for separation of large entities like the nanorods. All improvements resulted in the production of highly purified nanorods at over 10^{15} nanorods per 1 L of original culture, which can be used to characterise the Ff end-caps' structures hence-to-forth impossible to analyse within the full-length phage.

Chapter 4:

Structural and biochemical characterisation of the Ff pIII-pVI end-cap in the short Ff phage-derived-nanorods

4.1 Introduction

The pIII-pVI complex located at the distal end of the virion remains one of the Ff phage structure's biggest mysteries. Prior to incorporation into the virion, pIII and pVI form a membrane Triton-X100-dissolvable complex in which pVI is protected from proteolysis by pIII (Rakonjac & Model, 1998). All other virion proteins are also integral membrane proteins. In contrast, upon assembly, all virion proteins form a lipid-less tight complex, with DNA forming the backbone. The pVIII subunits, and presumably the minor proteins including pIII and pVI, form the filament via hydrophobic subunit-subunit interactions and ionic interactions with DNA (via positively charged "tails"). The hydrophobic interaction interfaces with pVIII make separation and structural characterization of the pIII-pVI complex very difficult.

Furthermore, as is the case for integral membrane (or hydrophobic) protein complexes in general, solubilization is expected to present challenges for structural analysis (Carpenter *et al*., 2008; Seddon *et al*., 2004). In particular, it is unclear whether the pIII-pVI complex retains its intrinsic structure and function during solubilization, reconstitution, and crystallization. Proteins pIII and pVI have an essential role in phage display technology and are key to understanding the mechanism of Ff phage infection and assembly. Determining the structure of pIII and pVI in the Ff phage cap would aid in the engineering 3D structures built from Ff phage-derived nanorods. It will also help to understand how these two proteins

mediate unusual membrane transitions in the filamentous phage replication cycle. Consequentially, structural characterisation of this complex is one of the main goals of this thesis, in general, and of this chapter in particular. The key unresolved question that the structural analysis will help answer, is the Ff assembly termination mechanism that must involve major conformational changes in which pIII and pVI and the virion itself, are excised from the membrane as they form the virion cap.

Conversely, at the start of infection, "opening" of the virion cap is required to expose hydrophobic sequences and mediate the integration of virion proteins into the inner membrane (Smilowitz, 1974; Trenkner *et al*., 1967). Gaining insight into the pIII-pVI virion cap structure will help understand and predict conformational transitions whereby the opening of the virion is triggered to allow DNA entry into the host cells. To this end, the current chapter has developed a method for purification of the pIII-pVI complex from the 80 nm Ff-derived nanorods (529-nt) designed and produced in this thesis. The virion was first dissociated by chloroform and the detergent sodium deoxycholate (DOC) to solubilise the pIII-pVI complex. This chapter includes cryo-EM single-particle analysis (cryo-EM SPA) of the nanorods purified in Chapter 3 that resulted in a preliminary 3D model of the pIII-pVI end-cap.

4.2 Results and discussion

4.2.1 Dissociation of the pIII-pVI complex from the 529-nt (80 nm) nanorods

The Ff virions are sensitive to hydrophobic solvents such as chloroform. The intact virions can be destabilised upon exposure to a chloroform-water interface the treatment that transforms long thin filaments (890 nm x 6 nm) into structures in which the filament is unravelled into spheroids (S-form, ~ 25 nm in diameter; Chapter 1, Figure 4A) at 22 °C or an intermediate shortened but broader filament with a flared end (I-form; Chapter 1, Figure 4B) at 4 °C (Griffith *et al*., 1981; Manning *et al*., 1981). These organic-solvent-induced morphological changes possibly mimic the virion *in vivo* conformational rearrangements during adsorption and entry into the host cells, allowing a transition from a highly stable protein filament to a lipid-soluble form capable of integration into the host membrane (Dunker *et al*., 1991; Manning *et al*., 1981). Lopez and Webster (1982) showed that pIII was observed in the I-form at the filament's flared end using ferritin-conjugated pIII-specific antibodies. Given that pIII forms a tight complex with pVI in the virion (Gailus & Rasched, 1994; Grant, Lin, Konigsberg, *et al*., 1981), it is conceivable to assume that pVI is also present in the flared end. Moreover, Manning *et al*. (1981) showed that M13 miniphages (shorter forms; Chapter 1, Figure 9) were able to contract into the I-forms when treated with chloroform at room temperature, concluding that the contraction of Ff phage after chloroform treatment does not

depend on the size of the particle. From this, we hypothesise that conversion of the purified 529-nt nanorods into their I-form by exposure to a chloroform-water interface at 22 °C and 4 °C might allow the observation of the pIII-pVI complex end-cap in electron micrographs.

After chloroform exposure at 22 °C, nanorods and their dissociated forms were visualised by transmission electron microscopy (TEM), and their morphology was compared (Figure 27). S-forms of the purified 529-nt nanorods were observed in the TEM micrographs alongside intact 529-nt nanorods (Figure 27B). These results are consistent with the previous studies by (Griffith *et al*., 1981) and Manning *et al*. (1981), who showed that a large number of full-length phage remaining apparently intact could be observed in addition to spheroids after chloroform exposure. Spheroids had to be further purified away from full-length phage to be separately analysed. Among 50 analysed spheroids derived from the 529-nt nanorods, half (25) were around 30 nm in diameter, while 9, 7, 5, and 4 were around 60, 50, 40, and 20 nm in diameter, respectively (Figure 27D). These results are comparable to those obtained by (Griffith *et al*., 1981), who converted M13 mini-phage (100 - 500 nm) into spheroids, obtaining very few S-forms between 20 and 30 nm in diameter. Interestingly, the 80 nm nanorod spheroids analysed here appear to have somewhat bigger diameter in comparison to the spheroids derived from the larger 100- to 500-nm M13 miniphage. We also attempted to induce the I-forms; however, no apparent flared structures were seen after the chloroform exposure at 22 °C or 4 °C (Figure 27C). Manning *et al*. (1981) observed a 3.5-fold reduction in the length of full-length phage M13 and based on this observation, it is conceivable that the same

reduction occurs in the 529-nt (80 nm) nanorods, shortening them to ~ 23 nm. Such short length of the "stalk" part of the I-form may hinder visualization in the TEM micrographs and this small size could explain why they were not observed here.

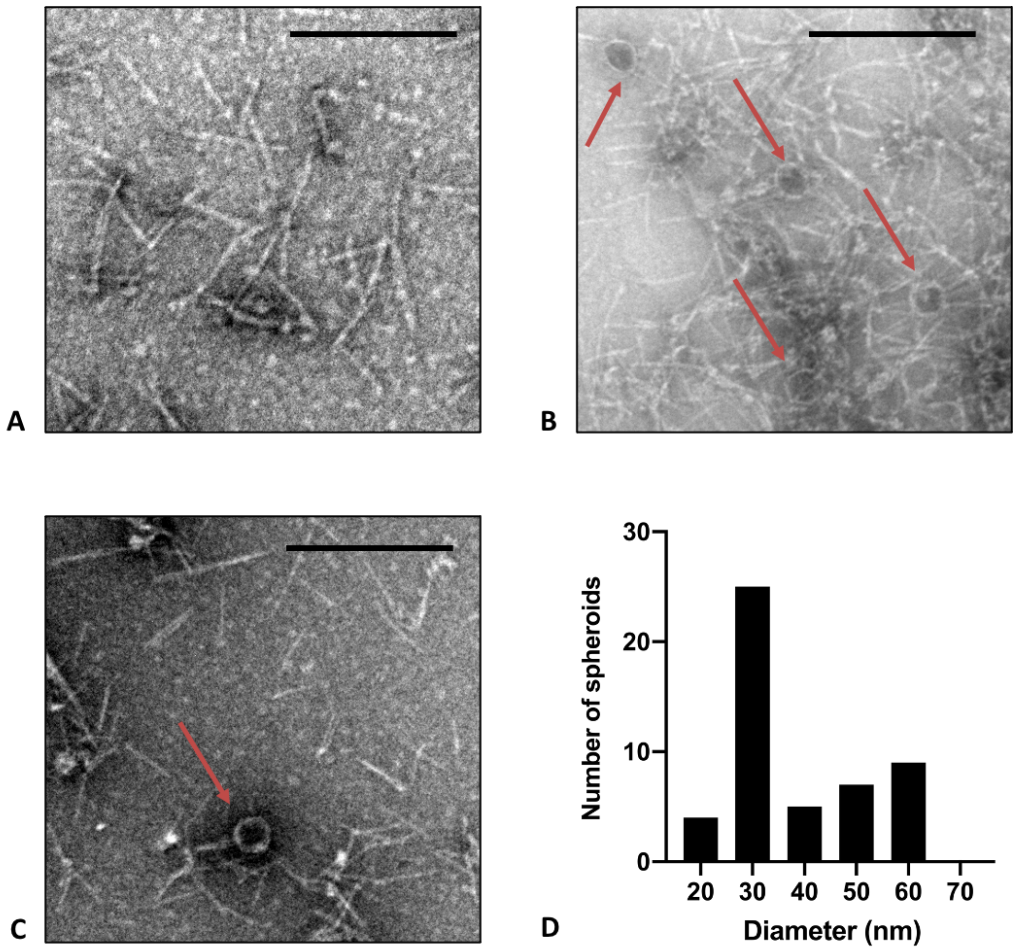

Figure 27. Spheroids derived from the 529-nt nanorods by chloroform treatment.

Negatively-stained electron micrographs of the 529-nt nanorods before (A) and after (B) chloroform treatment. (C) attempting I-form detection after the chloroform exposure at 4 °C. Bar equals 200 nm. (D) Size distribution of spheroids from (B) generated by measuring the diameter of 50 spheroids using the ImageJ measurement function. Red arrows shows the nanorods spheroids.

4.2.2 Purification of the pIII-pVI complex from the 529-nt (80 nm) nanorods

Structural analysis of the Ff virions pIII-pVI end-cap would benefit from the purification of the pIII-pVI complex. Ff virions are resistant to detergents alone, including the polar detergent sodium lauroyl sarcosinate (sarkosyl). As seen in the previous sections, combining hydrophobic solvents such as chloroform with detergents, such as sodium deoxycholate (DOC), destabilises hydrophobic inter-subunit interactions. This results in the conversion of a very stable lipid-devoid virion into combined detergent-protein vesicles (spheroids), from which it is possible to extract solubilised virion proteins, including pIII, pVI, and the major coat protein pVIII. A solvent-detergent combination of chloroform and DOC was therefore used to solubilise virion proteins. It has been shown that under these conditions, the pIII-pVI complex was preserved and could be purified by size exclusion chromatography (Gailus & Rasched, 1994). Based on these findings, the 529-nt nanorods were exposed to the DOC-chloroform combination. The advantage of the nanorods over full-length phage is the enrichment of the end-cap proteins. The ratio of pIII and pVI in the 529-nt nanorods relative to the major coat protein pVIII is very low (pIII:pVI:pVIII=5:5:214), in contrast to the full-length phage where it is 5:5:2683. The background of pVIII subunits is therefore reduced in the 529-nt nanorods 12.5-fold (from 2683 for the full-length phage to 214 for the 529-nt nanorods). To purify the pIII-pVI complex, proteins derived from dissociated nanorods were purified by size exclusion chromatography using a Superdex 200 Increase 10/300 GL column. Proteins in the fractions were monitored by

absorbance at 280 nm (Figure 28A). Four main peaks were observed in the chromatogram. The corresponding fractions were collected (Fractions 1-4; Fr1, Fr2, Fr3, and Fr4) and analysed for the presence of nanorod DNA by SDS-disassembled agarose electrophoresis (Figure 28B) and protein composition by SDS-PAGE combined with either Coomassie blue staining to detect pVIII, or western blotting to visualise pIII and pVI (Figure 28C, D, and E). Tris-tricine is required for observing pVI, as it runs as a smear in the Tris-glycine SDS-PAGE system. Nanorod DNA was observed in the main peak, corresponding to the first fraction (Fr1; Figure 28B). Middle peaks Fr2 and Fr3 contained only pIII and pVI (Figure 28D and E), whereas pVIII was only found in the final eluted fraction (Fr4; Figure 28D). Protein pVI was only observed by western blotting, and was present in protein fractions 2, 3, and 4 in contrast to the results reported by Gailus and Rasched (1994). Similarly, in this study pIII could not be separated from other proteins in the third eluted fraction (Fr3), whereas Gailus and Rasched (1994) reported that pIII was separated from other virion proteins. The ratio of pIII to pVI was not the same in Fr2 and Fr3 (compare Figure 28D and E). Fr2 contained more pIII than Fr3, whereas the amounts were reversed for pVI, with Fr3 containing more pVI than in Fr2. From this, it could be concluded that if these proteins are present as a complex, either the pIII:pVI ratio in the complex is higher in Fr2 than in Fr3, or both fractions contain un-complexed pIII and pVI. Interestingly, Fr2 and Fr3 contained very little (if any) pVIII, whereas Fr4 contained a prominent pVIII band, demonstrating successful removal of pVIII from the main fractions containing pIII and pVI. An intense band migrating around 50 kDa could be observed in fractions 2 and 3, which is not detectable in the input fraction. Several research groups have shared the

Superdex 200 Increase 10/300 GL column to purify a wide variety of samples. It is therefore possible that the band migrating around 50 kDa is due to contaminants retained from a previous unrelated experiment.

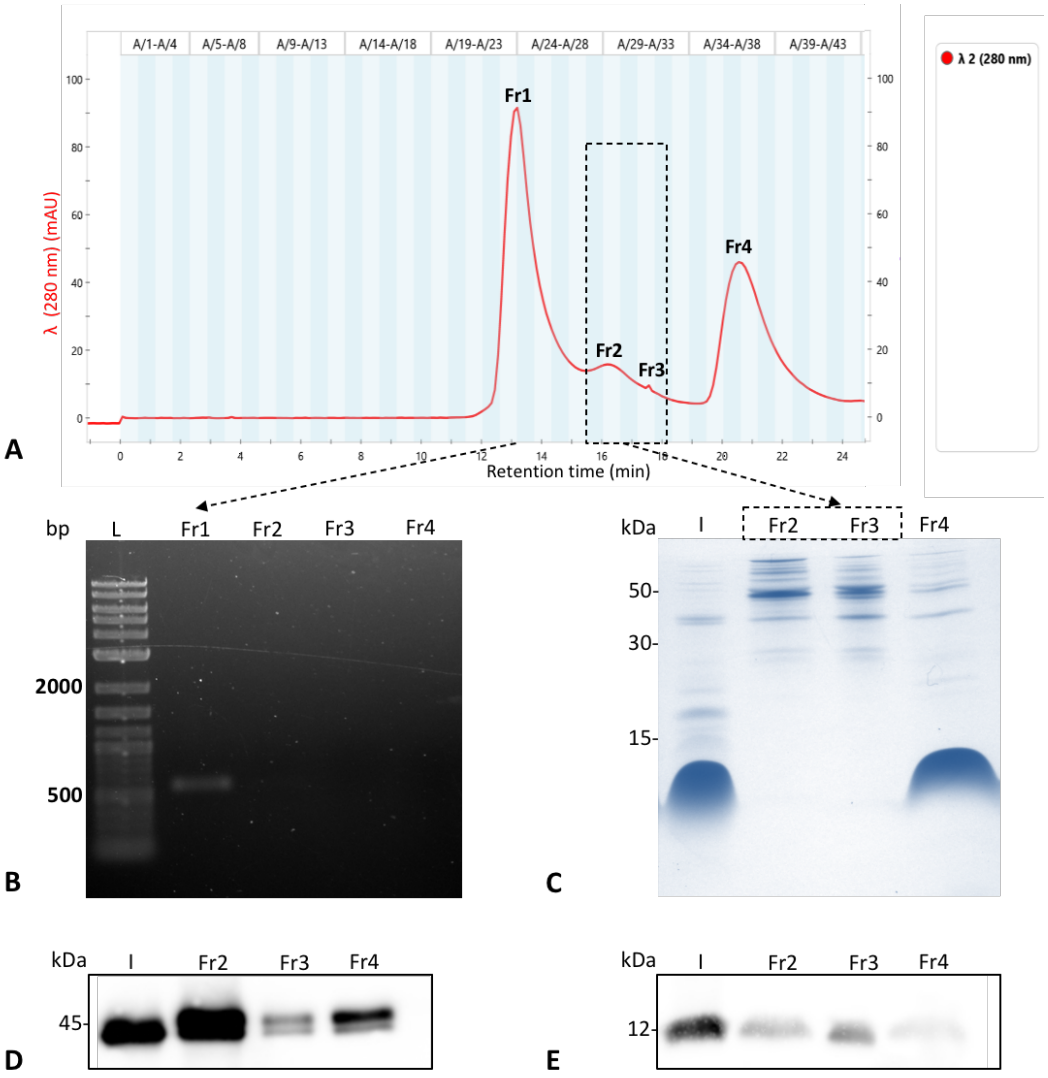

Figure 28. Purification of the pIII-pVI complex from DOC-chloroform treated 529-nt nanorods using an elution buffer containing DOC above the critical micellar concentration (CMC).

(A) Chromatograph of the size exclusion chromatography purification using a Superdex 200 Increase 10/300 GL column. The key parameter is UV absorption (mAu; milli Absorption units) at 280 nm (detecting protein and DNA) vs retention in time. (B) DNA from SDS-denatured fractions was separated by 1.2% agarose gel electrophoresis and

visualised by EtBr staining. Lanes: L, 1 Kb Plus ladder; Fr1, F2, Fr3, and Fr4, eluted fractions 1-4 (Fr1:A23-A25, Fr2:A28-A29, Fr3:A31, Fr4:A34-A38). (C) 16.5% Tris-tricine SDS-PAGE of the collected fractions. Lanes: kDa, sizes of the molecular weight standard bands from Novex Sharp pre-stained marker; I, input sample before SEC (anion exchange purified 529-nt nanorods); Fr1, F2, Fr3, and Fr4, eluted fractions 1-4 (Fr1:A23-A25, Fr2:A28-A29, Fr3:A31, Fr4:A34-A38). (D) and (E), western blot of the 16.5% Tris-tricine SDS-PAGE. pIII (D) and pVI (E) were detected using anti-pIII and anti-pVI antibodies, respectively. Lanes: kDa, sizes of the molecular weight standard bands from Novex Sharp pre-stained marker; I, input sample before SEC (anion exchange purified 529-nt nanorods); Fr1, F2, Fr3, and Fr4, eluted fractions 1-4 (Fr1:A23-A25, Fr2:A28-A29, Fr3:A31, Fr4:A34-A38).

Fraction 2 (Fr2), with a higher volume of the sample, containing both proteins pIII and pVI, was then taken for analysis by TEM in an attempt to visualise a pIII-pVI complex (Figure 29A). However, only micelles were observed, and no protein complexes were visible. These observations can be explained by the use of DOC at 15 mM in the elution buffer, which is much higher than the critical micellar concentration (CMC; 2-6 mM). With that in mind, Fr2 was dialysed against detergent-free buffer (Figure 29B) based on the methods of Gailus and Rasched (1994). This step was followed by ultrafiltration in a 100 kDa cut-off Vivaspin centrifugal device to concentrate the sample before TEM visualization. Some large aggregates and individual small granules or aggregates (indicated by red arrows in Figure 29D) could be seen in the TEM micrographs. The shape and size of these aggregates, 30-50 nm in diameter (from 10 counted dots), were similar to the spheroids observed previously after exposure of the nanorods to chloroform (Figure 27B) but are also comparable to some smaller particles observed in the control

(Figure 29C, the detergent-free elution buffer for dialysis). Therefore, the identity of these aggregates remains unresolved.

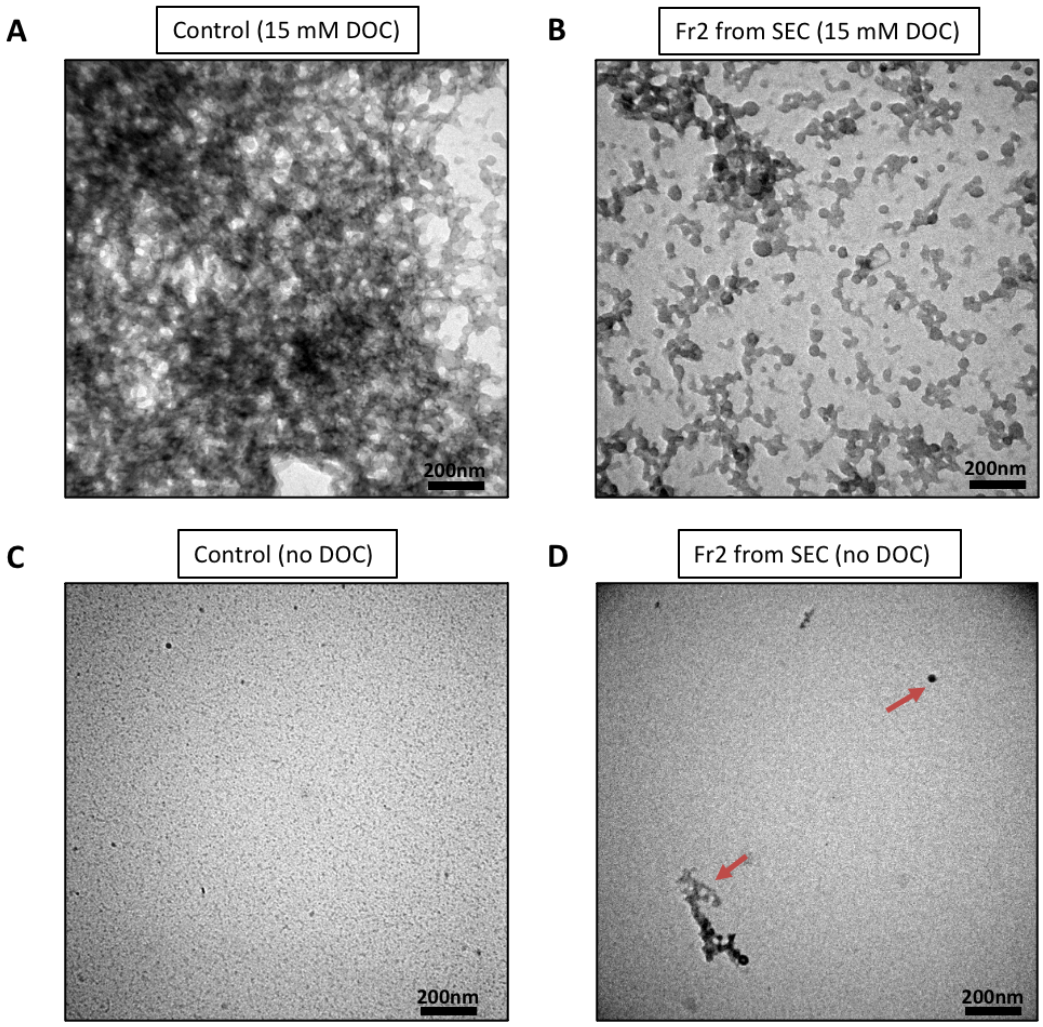

Figure 29. TEM analysis of the fraction containing pIII and pVI from the size-exclusion chromatography (SEC) purification using a Superdex 200 Increase 10/300 GL column.

Negatively-stained micrographs of: (A) the detergent control, the elution buffer (10 mM Tris-HCl, pH 8, 1 mM EDTA, and 15 mM DOC); (B) fraction 2 (Fr2), containing pIII and pVI, from the SEC purification in the elution buffer; (C) Control (no DOC), the detergent-free elution buffer for dialysis; (D) fraction 2 (Fr2), containing pIII and pVI, from SEC purification after dialysis and concentration in a detergent-free buffer. Red arrows show the aggregates possibly corresponfing to the pIII-pVI complex.

To avoid the possible presence of contaminants in the Superdex 200 Increase 10/300 GL column, a newly purchased column identical to the one used by Gailus and Rasched (1994), a Zorbax GF-450, was used. A second pIII-pVI complex extraction was performed as described above, followed by a size exclusion chromatography using the Zorbax GF-450 column. This time, the elution buffer contained deoxycholate at a sub-CMC concentration (1 mM) to avoid issues due to the high concentration of detergent in the eluted protein fractions.

In this experiment, three main peaks were observed in the chromatogram, and their corresponding fractions were collected (Fractions 1-3; Fr1, Fr2, and Fr3) (Figure 30). The protein composition of these fractions was analysed by SDS-PAGE combined with either Coomassie blue staining (to detect pVIII, Figure 30B) or western blotting (to detect pIII and pVI). Protein pIII, migrating at around 60 kDa in the Tris-glycine system, was observed in all the fractions, with Fr2 containing most of it (Figure 30B and D). The Zorbax GF-450 column, in contrast to the Superdex 200 Increase 10/300 GL column, did not separate pIII from pVI. pVI was detected in all eluted fractions with the majority present in Fr2 (Figure 30E), just as for pIII. Protein pVIII was detected only in Fr3 (Figure 30B), and interestingly, it was not completely eluted during this purification. The lower concentration of DOC used in the elution buffer could alter the solubilization of pVIII, which may be retained in the column. To analyse the native state of the proteins in the collected fractions and to determine if they were present as a complex, the different fractions

were analysed using blue-native PAGE (BN-PAGE). This is a native protein PAGE system that allows the resolution of membrane protein complexes in their native state according to their molecular mass, allowing the analysis of the oligomeric states (Kashino, 2003; Schägger *et al*., 1994; Schägger & von Jagow, 1991). The BN-PAGE system was expected to allow the estimation of the molecular mass of the pIII-pVI complex if it was present. The BN-PAGE stained with Coomassie blue did not show the presence of any protein (data not shown), so it had to be analysed by western blotting. Unfortunately, there was not enough sample left to be examined by the use of both anti-pIII and anti-pVI antibodies; therefore, we were able to detect only pIII by the use of an anti-pIII antibody (Figure 30C). A smear containing one or more individual bands migrating above 720 kDa was observed in Fr1 and Fr2. As no western blotting detecting pVI was performed, it cannot be ascertained that this band corresponds to the pIII-pVI complex. The pIII-pVI complex in the virion should be composed of five copies of each of the two proteins. Given that their molecular masses are 42.6 and 12.3 kDa, respectively, the complex molecular mass is expected to be at least ~ 274.5 kDa. The band on the native blue PAGE runs above the 720 kDa; thus, if it does correspond to the complex, which runs as a multimer-dimer (common for complexes that have a large hydrophobic surface exposed at a low detergent concentration (Spagnuolo *et al*., 2010)) or potentially contains a substantial amount of pVIII, which is present in Fr2 and Fr3, as detected by the SDS-PAGE (Figure 30B).

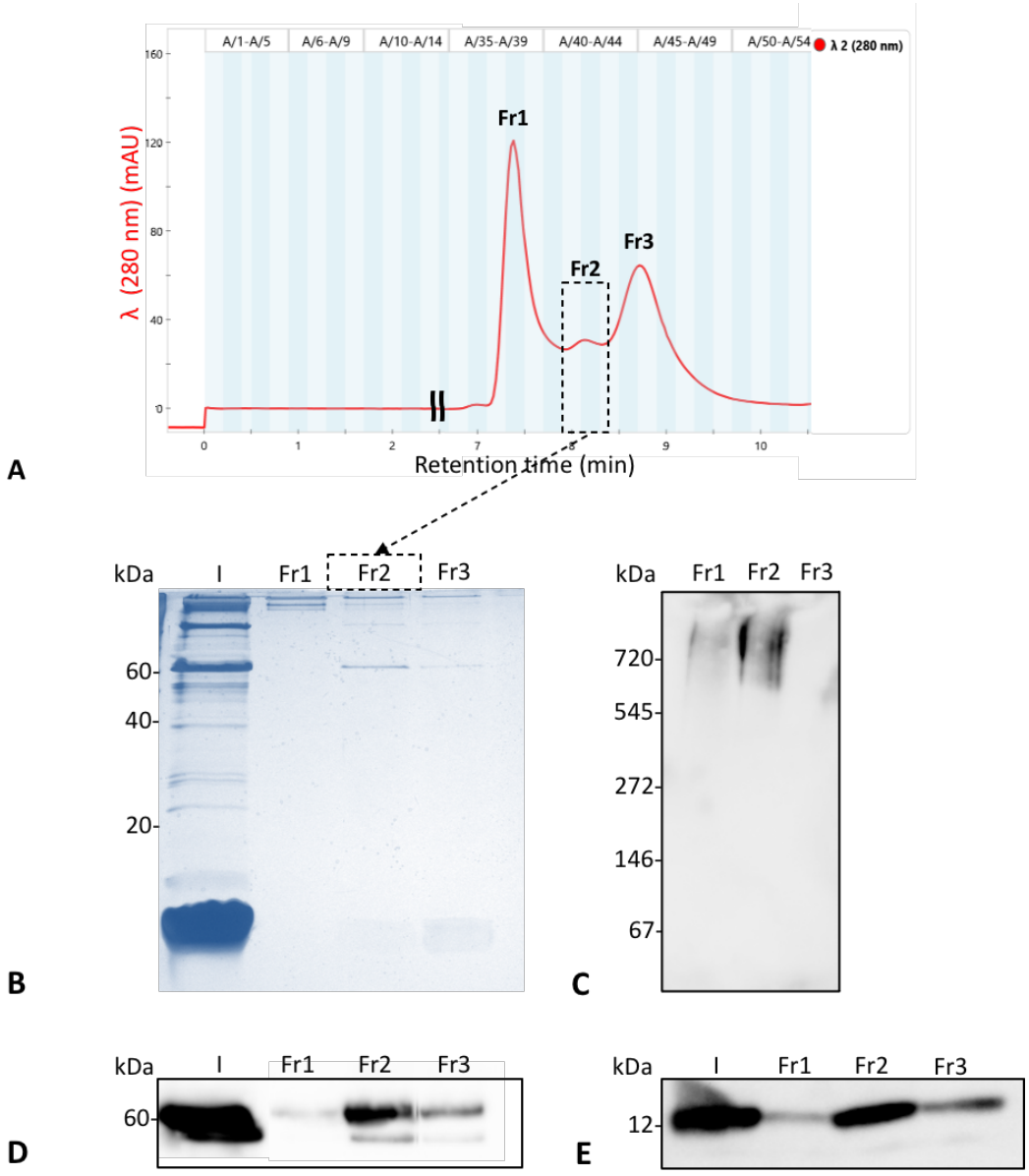

Figure 30. Purification of the pIII-pVI complex from DOC-chloroform treated 529-nt nanorods using an elution buffer below the critical micellar concentration (CMC).

(A) Chromatograph from the size exclusion purification using a Zorbax GF-450 column. The key parameter is UV absorption (mAu; milli Absorption units) at 280 nm (detecting protein and DNA) vs retention in time. (B) Coommassie blue stained SDS-PAGE of the collected fractions. (C) Western blot of pIII after a Blue-Native PAGE to detect the pIII-pVI complex. (D) and (E), western blots of pIII and pVI, respectively, after an SDS-PAGE. Lanes: kDa, sizes of the molecular weight standard bands from Novex Sharp pre-stained marker; I, input sample before SEC (anion exchange purified 529-nt nanorods); Fr1, F2, and Fr3, eluted fractions 1-3 (Fr1:A37-A39, Fr2:A41-A42, Fr3:A44-46).

Fr2 was then analysed by TEM to visualise material within this fraction, in case a protein complex could be visualised (Figure 31). The presence of many aggregates was observed. No apparent symmetrical structures, indicative of a symmetry of the pIII-pVI complex, could be seen. One way to localize individual proteins in protein complexes is to label them with specific markers such as antibodies (Aebi *et al*., 1977; Buhle & Aebi, 1984; Lake & Kahan, 1975; Yanagida & Ahmad-Zadeh, 1970). Moreover, immunoelectron microscopy has been shown to be a powerful technique to identify and visualise viral antigens and their position within a sample (Gulati *et al*., 2019). It was therefore decided to employ "immuno-gold" labelling to identify whether any of the observed aggregates from Figure 31A corresponded to protein pIII. As there was not enough purified sample from Fr2, pVI could not be detected by immunoelectron microscopy. A 10-fold dilution of Fr2 was then incubated with a primary pIII-specific antibody, followed by a gold-conjugated, mouse anti-rabbit secondary antibody and finally, a step of negative staining to be visualised by TEM. Individual TEM micrographs (Figure 31B) are representative of 10 TEMs analysing anti-pIII immuno-gold labelled samples vs. negative controls (from which the anti-pIII primary antibody was omitted). It was observed in a total of 5 immunolabelled micrographs, that 126 gold particles were co-localised with aggregates in comparison with the 61 gold particles co-visualised with smaller aggregates in the 5 negative controls. The epitope of the primary antibody recognises the C-terminal 10 residues of pIII, which in the virion, likely interacts with DNA and is not exposed on the surface of the virion (J. Rakonjac, unpublished

observation). Gold labelling of the aggregates indicates that they contained pIII and that the C-terminus is now exposed to the aqueous phase.

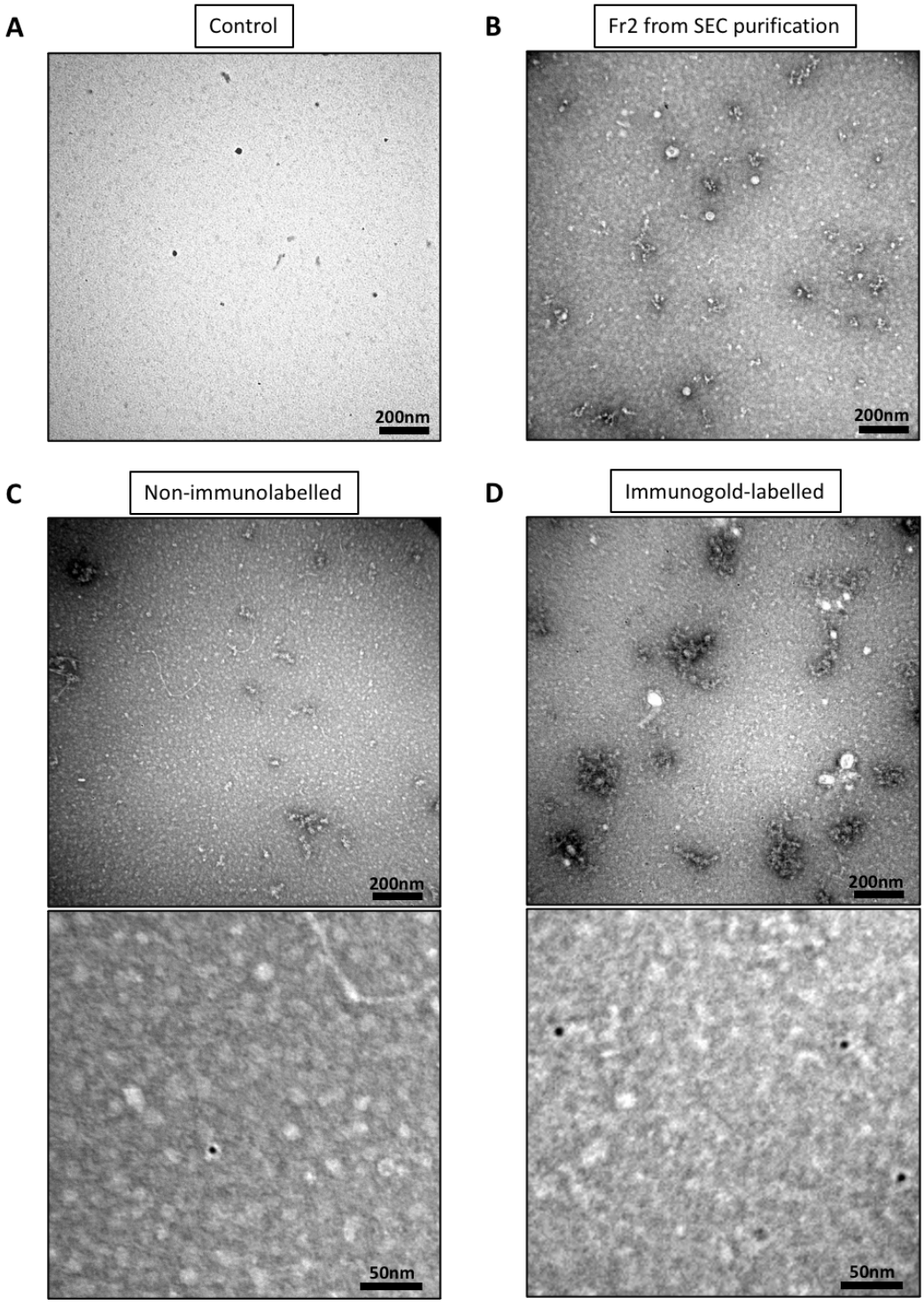

Figure 31. TEM analysis of the fraction containing pIII and pVI from the size-exclusion chromatography (SEC) purification using a Zorbax GF-450 column.

(A) Negatively-stained micrograph of the control, a 10-fold dilution in the elution buffer (10 mM Tris-HCl, pH 8, 1 mM EDTA, and 1 mM DOC), the control. (B) Negatively-stained micrograph of fraction 2 (Fr2) from the SEC purification, containing pIII and pVI.

(C) Representative micrograph from 5 immunoelectron micrographs of non-specifically immunolabelled fraction 2 (Fr2; negative control, no anti-pIII primary antibody). (D) Representative micrograph from 5 immunoelectron micrographs of immunogold-labelled Fr2 using an anti-pIII antibody (R164), targeting the C-terminal pIII decapeptide. Images below (C) and (D) show magnified fields containing putative aggregates labelled with the gold particles. Bar equals 200 or 50 nm, as indicated.

As we could not prove that Fr2 contained proteins pIII and pVI present as a pIII-pVI complex, and given the lack of a population of uniformly-looking aggregates (that could potentially correspond to the pIII-pVI complex) in comparison to other TEMs, for example those of gigantic radially symmetrical secretin channels of similar mass, like pIV (Opalka *et al*., 2003), the aggregates observed in Fr2 are unlikely to be a good enough for structural analyses. It was, therefore, decided not to proceed with further analyses of these samples.

4.2.3 Cryo-EM SPA of the 529-nt (80 nm) nanorods containing the pIII-pVI complex

Given that the purified pIII-pVI "complex" did not convincingly show the presence of a morphologically uniform population under the TEM, these samples were not pursued further for structural analysis. Instead, other strategies were explored to solve the structure of the nanorods pIII-pVI cap.

In the past eight years, cryo-EM has emerged as a powerful technique for determining protein structures reaching resolutions between 2-4 Å (near-atomic resolution), comparable to the structures solved using NMR or X-ray crystallography (Cheng, 2015; Danev *et al*., 2019; Murata & Wolf, 2018). Cryo-EM presents several advantages compared to X-ray crystallography and NMR spectroscopy. It requires a much smaller amount of sample, can be used for whole viruses, large protein complexes, and membrane proteins, and does not require three-dimensional (3D) crystals (Carroni & Saibil, 2016; Nygaard *et al*., 2020; Thonghin *et al*., 2018). Based on these characteristics, it was chosen to solve the structure of the Ff phage end-caps by using the nanorods designed, produced, and purified in Chapter 3.

The 529-nt (80 nm) nanorods produced by the inducible single-plasmid system (pPop-up529LacUni plasmid) were chosen for analysis by cryo-EM SPA as they were produced at titres ~ 200-fold higher than the 221-nt (50 nm) nanorods. Purified 529-nt nanorods were sent to Dr Vicki Gold's laboratory at the University of Exeter (UK) at an approximate concentration of 2.2 ± 0.2 mg of particles/mL to be analysed by cryo-EM SPA. In their cryo-EM micrographs (Figure 32A), the presence of the 529-nt nanorod filament with two very distinctive ends was observed: one "blunt" and one "pointy". These results are consistent with the findings of Gray *et al*. (1979), except that the "knob" or "ball on a string" structures were not observed. This is not surprising as these knobs are not detectable in the majority of Ff TEM micrographs. Based on the cryo-EM micrographs, Dr Vicki

Gold's research team generated preliminary 2D classes of the filament, "blunt-end", and "pointy-end" of the 529-nt nanorods (Figure 32B).

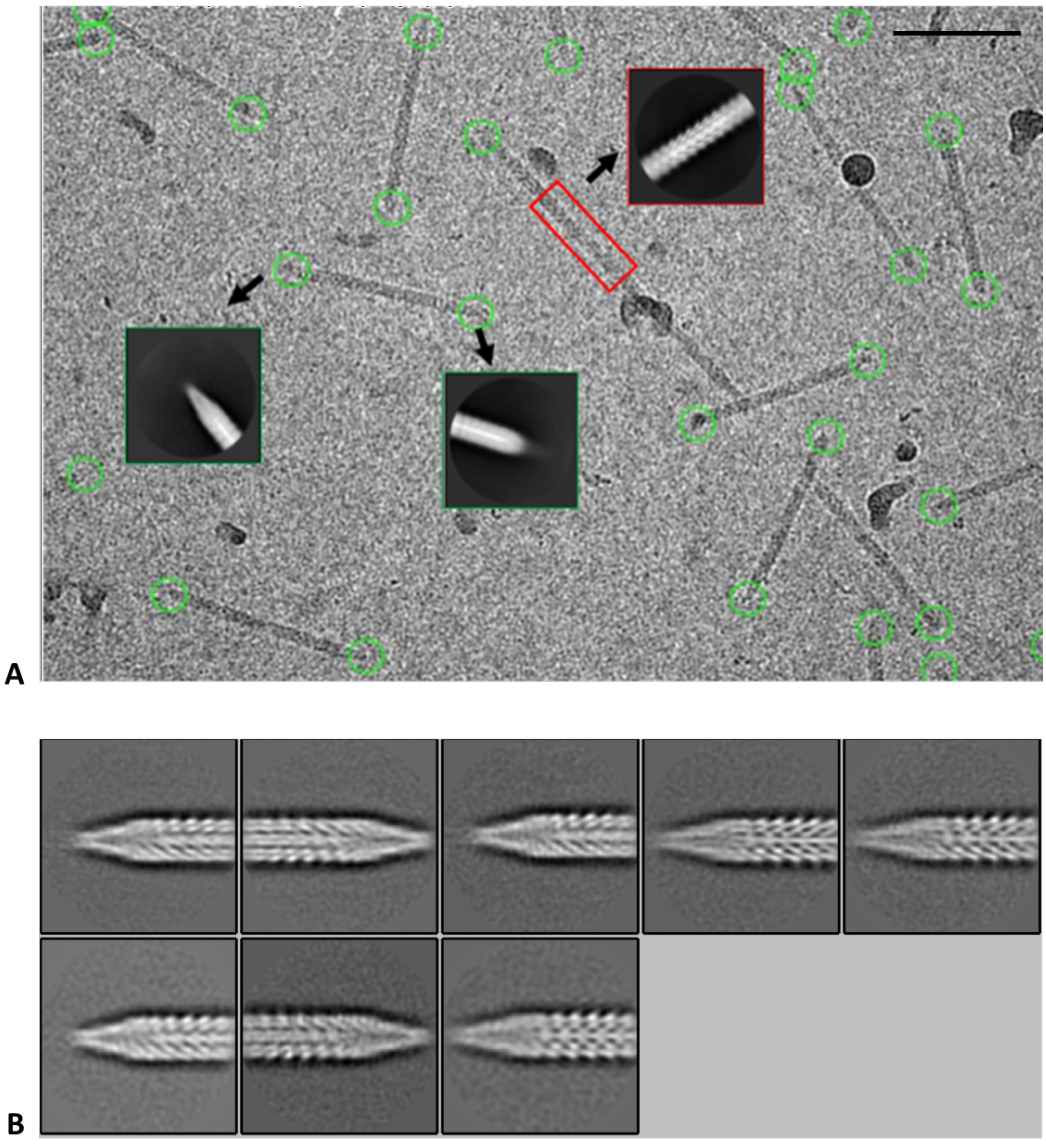

Figure 32. Cryo-EM data of 529-nt nanorods.

(A) Cryo-EM micrograph of the 529-nt (80 nm) nanorods. Green circles indicate the ends of the filament and the arrows point at the 2D classes generated for each part of the nanorod: the core of the filament, "blunt-end", and "pointy-end". (B) 2D classes of the "pointy-end" of the 529-nt nanorod filament containing proteins pIII and pVI. Bar equals 50 nm.

Based on the 2D classes of the pIII-pVI end-cap of the 529-nt nanorods, a preliminary 3D model was built at 5 Å resolution by Vicki Gold, Rebecca Conners, and Mathew McLaren (Figure 33). Further data collection and processing is required to confirm whether this model is correct as no densities for the amino acid side chains were observed. Furthermore, it remains to be determined whether the 5-fold symmetry imposed on the pIII-pVI cap is consistent with the known shaft symmetry (Marvin *et al*., 2014), is correct. The pVIII shaft structure has been solved by X-ray fibre diffraction, indicating that it is largely α-helical with an average pVIII subunit α-helix tilt angle (θh) of 16-20º with respect to the virion axis (Marvin *et al*., 2006). The same pattern can be observed in the preliminary model where densities along the filament at the level of the DNA were observed with a tilt relative to the virion axis similar to that expected for pVIII and appeared to be interacting with the nanorod DNA (Figure 33; red and black arrows). From this, the position where the pVIII shaft transitions into the pIII-pVI end-cap can be roughly estimated within 5-10 nm (Figure 33A and B; black vertical dashed lines). Until the model is confirmed, individual proteins detected, and the main peptide chains traced, details of this cap structure cannot be determined.

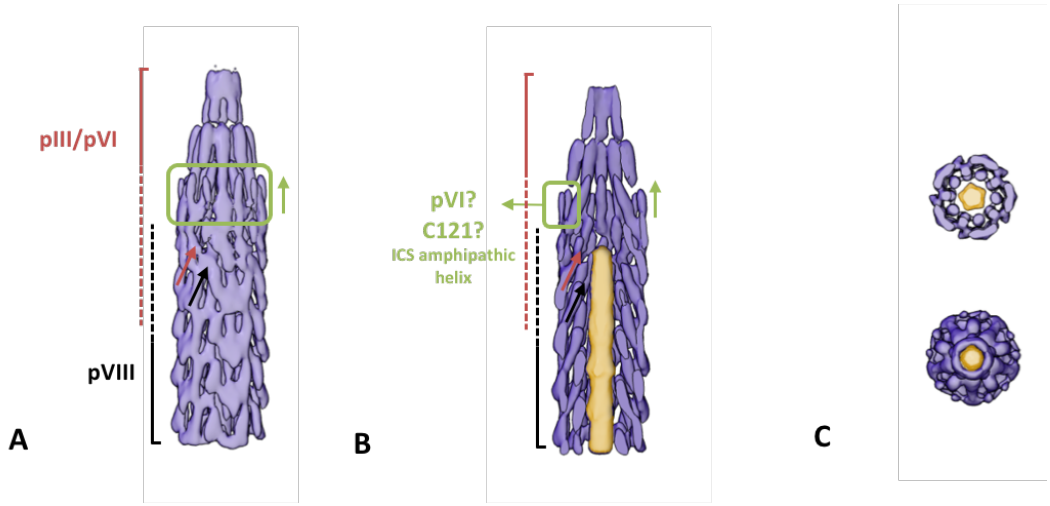

Figure 33. Preliminary 3D model of the pIII-pVI end-cap of 529-nt nanorods determined by single-particle reconstruction cryo-EM.

Side view (A), cross-section (B), and top view (C) of the density map obtained by the cryo-EM SPA. Red bracket, position of the pIII-pVI end cap; in black, the position of the shaft of the filament containing the pVIII subunits (Dashed lines indicate the putative region of the transition from the pVIII shaft to the pIII-pVI end-cap); in green, parallel densities observed in the model which could correspond to the C-terminus of pVI or the amphipathic ICS helix of the pIII C domain (Bennett *et al*., 2011).

The N1 and N2 domains of pIII, which are sometimes observed as small knob-like structures connected to the virion by a "string" (Gray *et al*., 1981), possibly corresponding to the pIII N2-C domain flexible glycine-rich linkers, were not visible in the cryo-EM micrographs. The dimensions and globular character of the N1N2 domain are unlikely to be seen in the model; because the individual N1N2 domains are each attached to the virion by a flexible linker enabling them to move around so they are not detectable in the average density derived from many individual nanorods. Notwithstanding these limitations, it is certain that the structures observed towards the end of DNA at the tip of this model correspond to

the C domain of pIII and the protein pVI. It is in this area where some elongated densities are parallel to the virion axis (Figure 33A and B, green squares and arrows).

Despite the uncertainty of the 3D cap model accuracy, it is tempting to speculate on the possible arrangement of pVI and pIII in the nanorod cap. Protein pVI is highly hydrophobic, and the TMHMM server (Krogh *et al*., 2001) predicts that in the cell, prior to assembly into the virion, pVI is an integral membrane protein composed of three 23-residue hydrophobic transmembrane helices separated by two 14-residue hydrophilic "loops" (Figure 34). The hydrophilic N-terminus is predicted to be located in the periplasm, whereas the first loop and the C-terminal hydrophilic tail are predicted to face the cytoplasm. On insertion into the virion, it is expected, based on its hydrophobicity, that pVI is largely buried inside the virion. Its C-terminus has, however, been used as a point of protein fusion in phage display (Jespers *et al*., 1995); hence, there is a possibility the pVI C-terminus in the virion is exposed to the environment. The densities parallel to the virion axis at the border between the conical tip structure and the main barrel of the virion (Figure 33) could correspond to the C-terminal end of pVI.

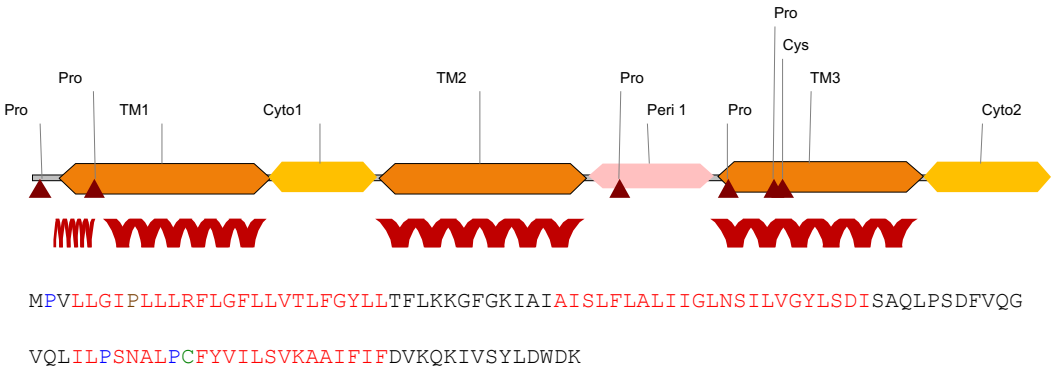

Figure 34. Annotated pVI scheme predicted by the TMHMM Server.

Transmembrane regions (TM) are cloured orange, hydrophilic loops facing the cytoplasm (Cyto) are coloured yellow, while the hydrophilic loop facing the periplasm (Peri), is coloured pink. The hydrophobic transmembrane helices coloured red above the primary amino acid sequence. The presence of proline and cysteine amino acids in the sequence is indicated by burgondy triangles.

Another more likely alternative is that these densities (Figure 33) could represent the amphipathic α-helix corresponding to the infection-competence segment (ICS; Figure 5, Chapter 1) of the pIII C domain. The ICS segment is absolutely required for phage entry but is dispensable for release of the virions from the membrane at the end of assembly (Bennett *et al*., 2011). Moreover, the ICS is also responsible for the detergent resistance of the Ff particle (Rakonjac *et al*., 1999), and is therefore more likely to be exposed on the surface of the virion end-cap than the short pVI C-terminal "loop". There is no structure of a pIII C domain homologue in the PDB database; hence both, secondary and tertiary structures were predicted using the Jpred and I-TASSER algorithms, respectively (Bennett *et al*., 2011). The I-TASSER algorithm does not require coordinates of close homologues for modelling (Zhang, 2008). Given that ten years have passed since the pIII C-domain model was

published, I-TASSER was used again to model the pIII C domain 3D structure, bearing in mind the new high-resolution structures of proteins that have been determined in the interim that may have resulted in an updated model. Interestingly, a similar model structures were obtained presently (I-TASSER 2021 model, Figure 35B). Both predictions showed a similar secondary-structures for the ICS and the membrane anchor helices, and, as in 2011, with a low C-score (-3.87; Figure 35B). The Cys residues in the I-TASSER2021 model did not seem close enough to form the S-S bridge observed in the I-TASSER2011 model of Bennett *et al*. (2011). This S-S bridge has been shown to be essential for the assembly of phage particles (Kremser & Rasched, 1994), reducing even more confidence in the newly predicted model. Alternatively, inter-subunit S-S bridges could be formed between the Cys residues in the pIII C domain. Nevertheless, most of the proteins with a similar structure to this model were membrane proteins (including the multidrug exporter AcrB, a component of the inner membrane complex of the AcrAB-TolC drug efflux system in *E coli*), so maybe this model could make biological sense.

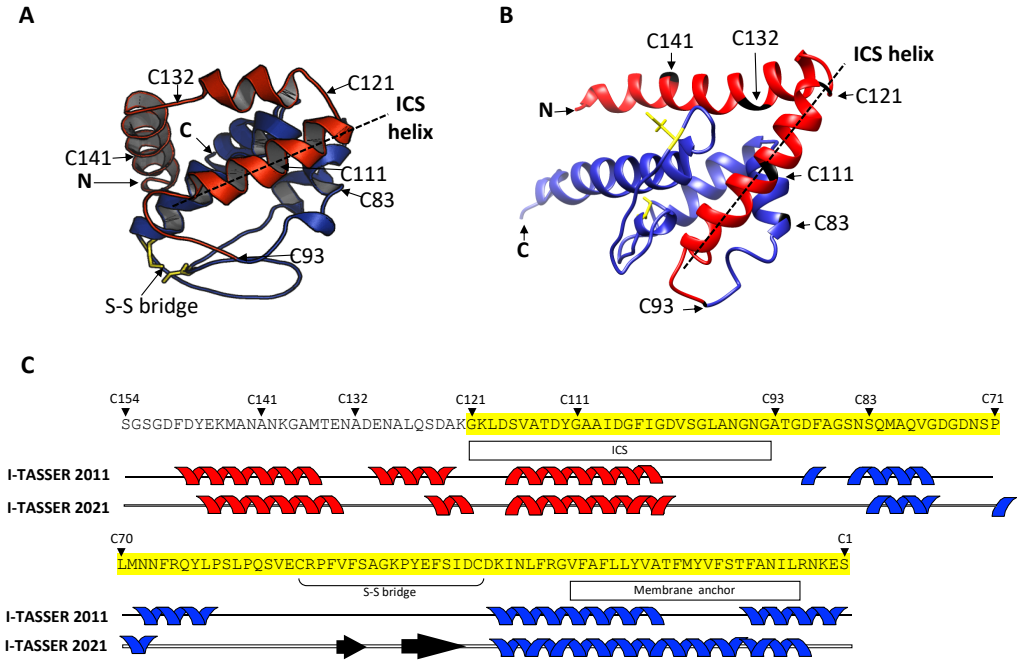

Figure 35. Tertiary and secondary structure predictions of pIII C domain by the I-TASSER algorithm.

A and B, Ribbon diagrammes of the I-TASSER pIII C domain models from Bennett *et al*. (2011) and the present work, respectively. ICS helix is indicated by a dashed line along the axis. Cys residues are indicated in yellow. (C) Comparison of the secondary-structure predictions from I-TASSER by Bennet *et al*. (2011) (I-TASSER 2011) and this thesis (I-TASSER 2021). Boxes under the sequence, ICS and membrane anchor. The S-S bridge is indicated by a line connecting two Cys residues. Secondary-structure predictions are shown below the sequence. Residues limiting the C-terminal points of nested deletion analysed in previous publications (C141, C132, C121, C111, C93 and C83) are labelled, counting from the C-terminal end. In the models (A and B) and linear predictions (C), segments that are not required for assembly are labelled red (residues C154–C94); whereas segmentsrequired for assembly are coloured blue (residues C93–C1), counting from the C terminus.

4.3 Summary/Conclusions

The main goal of this chapter was to structurally characterise the end-caps of Ff phage. Given that the "pointy-end", composed of proteins pIII (406 residues) and pVI (112 residues) holds the key to understanding the mechanism of membrane transitions during infection and termination, most effort was focused on this end-cap. The nanorod's "blunt-end" is composed of the very short hydrophobic proteins pVII and pIX (33 and 32 residues, respectively). It is, therefore, easy to imagine that these two proteins form a simple "plug" at the "blunt-end" of the phage, with the positively charged C-termini facing DNA and the negatively charged N-termini facing the solvent.

Two approaches were undertaken to characterise the pIII-pVI end-cap of 529-nt: (i) extraction from the virion, purification, and analysis of the isolated complex; (ii) characterisation within the intact nanorods.

(i) The pIII-pVI complex was dissociated from the nanorod and separated away from the nanorod DNA and the major coat protein pVIII by size exclusion chromatography (Figure 30). Analysis by transmission electron microscopy, however, did not result in complexes of uniform appearance (Figure 31). This finding agrees with the pIII-pVI complex running as a smear above the 720 KDa standard band in the Blue-Native PAGE. This observation decreased confidence

that the complex could be crystallised and analysed by X-ray crystallography. Even so, an interesting observation from this experiment, was that the C-terminus of pIII, which is not accessible to the antibody against the C-terminal decapeptide in the intact virion (J. Rakonjac, unpublished), appears to become exposed in the purified complex. Our finding that the separation of the complex from DNA is accompanied by the exposure of the C-terminus to the solvent confirms the common, but never tested assumption, that the pIII C-terminus is buried inside the virion, and due to its positive charge, mediates interactions with DNA.

(ii) The second approach was the structural analysis of the virion cap in the intact 529-nt nanorods by cryo-EM SPA. From the processing and reconstruction carried out by Dr Vicky Gold and her research group (University of Exeter, UK), a preliminary 3D model of the "pointy" end of the 529-nt nanorods containing the pIII-pVI complex was generated at a resolution of 5 Å (Figure 33). This is a preliminary model that is currently being refined. This model nevertheless gives some tantalising clues of the organisation of the pIII-pVI end-cap, like the transition between pVIII-built nanorod shaft to the pIII-pVI cap, and the possible position of some key pIII C domain structural elements, based on the published structure-function analyses. The near-atomic resolution structure of the end-cap that will clarify the structural details of the pIII-pVI end-cap is pending.

Chapter 5:

Tuning the nanorod length to achieve the shortest ever Ff phage-derived nanorods

5.1 Introduction

In Chapter 3, nanorods of 50 and 80 nm in length were produced based on the BSFp and BSFpn replication-assembly cassettes, respectively. The design of these cassettes was based on the knowledge of the function and structure of the different regions of the Ff origin of replication. This information comes from various studies made mainly in the '70s and '80s (Beck *et al*., 1978; Dotto *et al*., 1981; Dotto *et al*., 1984a; Gray *et al*., 1978; Horiuchi, 1997), where the different regions of the Ff origin of replication (such as the (-) and (+) *ori,* and the packaging signal) and their roles in replication were identified. Despite all this information, there are still regions in the Ff origin of replication and, therefore, in the BSFp cassette (Specthrie *et al*., 1992) that have not been further dissected due to a limited number of deletion constructs that could be made prior to the invention of PCR or the chemical synthesis of long DNA fragments.

This chapter has set out to engineer minimal BSFpn (section 5.2.1) and BSFp (section 5.2.3) nanorod replication-assembly cassettes by designing specific synthetic DNA fragments from which sequences predicted not to be essential for replication and assembly were trimmed to determine whether they were necessary for replication. The requirement for these sequences for replication was determined by quantifying the production of nanorods from these cassettes. TEM analysis of the nanorods produced using the trimmed cassette BSFp showed that the shortest nanorods were 40 nm in length, and were the shortest nanorods produced to date.

Minimising the length of the nanorods could be translated into new applications that would benefit from the shorter lengths, such as lateral-flow diagnostic devices, developing novel ssDNA standards or nanotechnology applications including the formation of designer nanostructures.

5.2 Results and discussion

5.2.1 Design of a novel BSFpn cassette for production of 395-nt (70 nm) nanorods

The BSFpn529 replication-assembly cassette is the shortest replication unit containing the positive and negative origins of replication that has been designed, to date, and is capable of efficiently producing the 80 nm nanorods at a concentration of ~ 5 x 10^{15} nanorods per L of culture (Table 9, Chapter 3). This cassette contains, besides the known elements of f1 (Ff) replication and assembly, packaging signal, (+) and (-) *ori*, which all form well-defined secondary structures (Horiuchi, 1997; Russel *et al*., 1988), a truncated *Δ29* (+) *ori* acting as a terminator.

The sequence of the BSFpn529 cassette (Figure 36A), described previously in Chapter 3, contains the complete (+) *ori* (141-nt), followed by a DNA segment of

114-nt derived from the pUC118 multiple cloning site, then continued with the Ff intergenic sequence fragment composed of the packaging signal (PS), complete (-) *ori* and finally a truncated (+) *ori* [(+) *ori Δ29*] that acts as the terminator of ssDNA replication. The intergenic sequence in the BSFpn cassette (and wild type Ff) contains a segment of 36-nt in between the PS and the (-) *ori* that is not assigned a secondary structure (Horiuchi, 1997). However, it is not known whether this sequence is required for replication and assembly of nanorods in the BSFpn529 cassette. Given that the size of a cassette (distance between the two pII cut sites, in the initiator and terminator) defines the size of the nanorod to be produced, shortening the BSF replication cassette should result in production of shorter nanorods. This hypothesis was tested by construction of a new shortened BSFpn and BSFp cassettes and analyses of the amounts and length of the nanorods produced from this shortened replication cassettes.

.

The shortened BSFpn cassette was designed by trimming the segment between the (+) *ori* [(+) *ori1,* initiator] and PS, derived from pUC118 vector, from 114 to 23-nt and the removal of the complete 36-nt segment between the PS and (-) *ori* (present in the wild type Ff IG region; Figure 36B). The designed DNA segment started from nucleotide 5764 (the f1 genome coordinates) and contained the complete (+) *ori* [(+) *ori1*], a 23-nt DNA segment, the PS followed immediately by the complete (-) *ori* (due to a 36-nt deletion), and finally, the terminator corresponding to the truncated (+) *ori* Δ29 [(+) *ori2*]. The synthetic segment was 439-nt in length and, if functional, in the presence of pII it was expected to produce a ssDNA "genome" 395-nt in length. The cassette was therefore named BSFpn395.

This novel cassette is expected to give rise to ~ 67 nm nanorods based on calculations assuming: (i) 2.3 bases per coat protein (Day *et al*., 1979; Specthrie *et al*., 1992), (ii) 395-nt ssDNA genome, (iii) particle length increase of 3.3 Å per coat protein (Caspar & Makowski, 1981), (iv) minor proteins arranged with same mass per unit length as the major coat proteins (1795 Da/Å), (v) five copies of each minor protein (pIII, pVI, pVII, and pIX); making a total of 311000 Da. Based on this, the major coat proteins plus the ssDNA in the nanorod contribute to a total length of ~ 567 Å or ~ 56.7 nm [395 bases divided by 2.3 (bases/protein) multiplied by 3.3 (Å/protein)]. The minor proteins add a length of ~ 173 Å or ~ 17.3 nm (311000 Da divided by 1795 Da/Å) (Specthrie *et al*., 1992).

A. BSFpn529 cassette

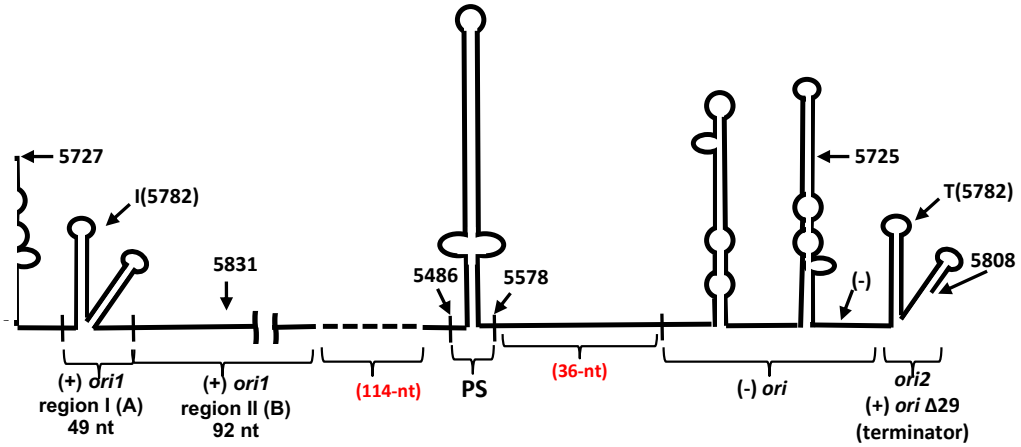

B. BSFpn395 cassette

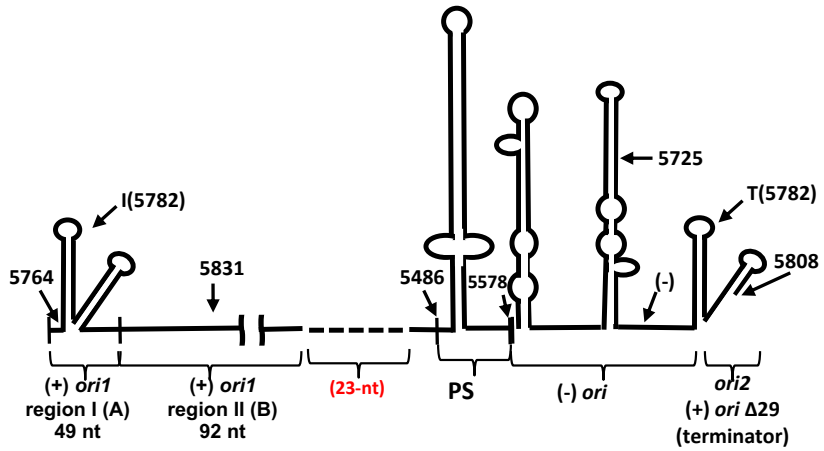

Figure 36. Engineered BSFpn replication-assembly cassettes for nanorod production.

The BSFpn cassettes include (+) *ori1* (complete positive origin of replication) *(-) ori*, packaging signal (PS), and (+) *ori2 (Δ29)*. Coordinates correspond to the wild-type f1 sequence. I and T are the nucleotides where the (+) strand replication is initiated and replicated, respectively. Coordinates correspond to the f1 genome sequence. (A) BSFpn529 cassette (610-nt), nanorod replication-assembly cassette producing circular ssDNA of 529 nt that assembles into 80 nm nanorods. (B) BSFpn395 cassette (439-nt), nanorod replication-assembly cassette producing 395-nt circular ssDNA that assembles, theoretically, into ~ 67 nm nanorods.

The production of 529-nt nanorods using the single-plasmid system under the inducible promoter *lacUV5* controlling the expression of the replication proteins (pPop-up529LacUni) had already been shown to be more efficient than other nanorod-producing systems (i.e., the two-plasmid system and the one-plasmid system with constitutive expression of replication proteins) by at least 10-fold (Table 9, Chapter 3). Therefore, this inducible single-plasmid system was chosen as the production system for the new BSFpn cassette. The BSFpn395 cassette, flanked by PstI and SalI recognition sites, was inserted into the pPop-up529LacUni plasmid in place of the BSFpn529 cassette, using PstI and SalI restriction enzymes. The recombinants were selected by their resistance to kanamycin and confirmed by DNA sequence analysis. The resulting plasmid was then called pPop-up395LacUni (Figure 37).

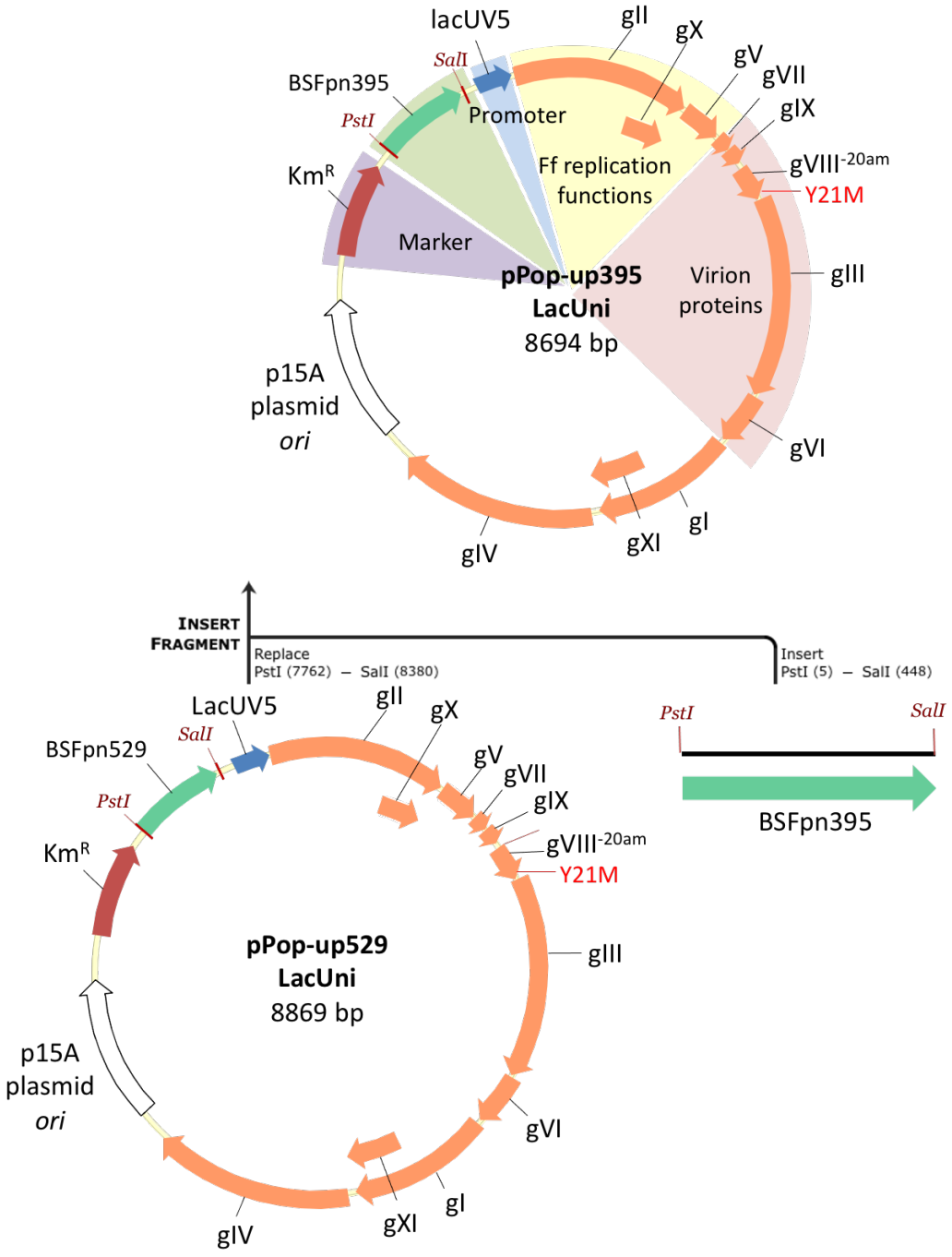

Figure 37. Construction of plasmid pPop-up395LacUni for production of 395-nt nanorods.

A synthetic fragment named BSFpn395, containing the BSFpn395 nanorod replication-assembly cassette (producing 395-nt circular ssDNA), was cut with PstI and SalI and cloned into the pPop-up529LacUni plasmid cut with PstI and SalI. The backbone plasmid contains all genes encoding for proteins required for replication and assembly of short

nanorods. Orange block arrows indicate open reading frames (ORFs) encoding phage proteins; the green block arrow corresponds to the BSFpn cassette (BSFpn529 or BSFpn395); the white block arrow corresponds to the p15A plasmid origin of replication; the red block arrow corresponds to the marker, in this case, kanamycin resistance (Km^R); the blue block arrow corresponds to the promoter controlling the *gII-gV-gVII-gIX-gVIII* operon, in this case, the *lacUV5* promoter.

5.2.2 Production of 395-nt (70 nm) nanorods from the BSFpn395 replication-assembly cassette in an inducible single-plasmid production system

For 395-nt nanorod production, K2092 electrocompetent cells were transformed with the pPop-up395LacUni plasmid and incubated overnight after induction with 1 mM IPTG. Nanorods were then concentrated from the culture supernatant by PEG precipitation, as described in section 2.4.4. The 395-nt nanorods were then analysed by disassembled- and native-particle agarose gel electrophoresis and compared with the 529-nt nanorods produced in the same system (Figure 38), which showed that the BSFpn395 cassette was able to produce nanorods. Interestingly, when the nanorods of different sizes were analysed under native conditions, they migrated similarly to the 529-nt nanorods. The migration in the native gel depends on the particle's size and charge, and as the size only changed by 134-nt and 56 copies of pVIII, the migration of these two groups of nanorods was very similar. The amount of 395-nt nanorods produced was compared with that of the 529-nt nanorods to check the new cassette's efficiency of replication and assembly. The number of

395-nt nanorods was 1.7 x 10^{15} per L of culture, about 2.6-fold lower than the number of 529 nanorods (4.8 x 10^{15} per L of culture; Table 10). It can be concluded from this result that trimming the DNA region between the packaging signal and the (-) *ori* as in BSFpn395 did not majorly decrease the capability of the replication-assembly cassette to produce shorter nanorods. Trimming of the pUC118 sequence between the (+) *ori* and PS was not expected to influence the nanorod replication and assembly, and this has been confirmed. Shortening the BSFpn cassette by removing two DNA segments decreased the nanorod yield by approximately 2.6-fold.

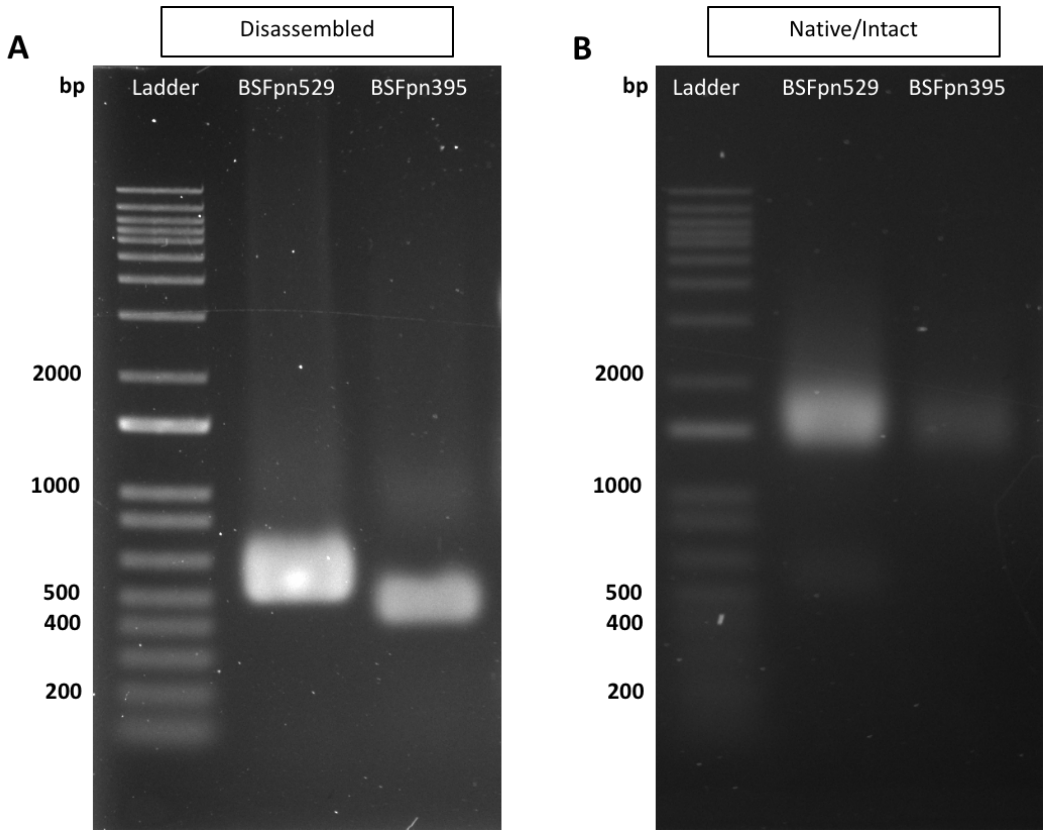

Figure 38. Comparison of the nanorods produced in the single-plasmid production system containing BSFpn529 and BSFpn395 cassettes (pPop-up529LacUni and pPop-up395LacUni).

(A) DNA from SDS-disassembled nanorods was separated by 1.2% agarose gel electrophoresis and visualised by EtBr staining. (B) Native nanorods. Bands corresponding to the native/intact particles were visualised after soaking the gel in 0.2 M NaOH. Lanes: Ladder, 1 Kb Plus ladder (a double-stranded linear DNA standard used as a signpost for migration due to the lack of appropriate circular ssDNA standards; numbers indicate sizes of the standard bands in base-pairs); BSFpn529, particles produced by the pPop-up529LacUni plasmid; BSFpn395, particles produced by the pPop-up395LacUni plasmid. Particles were produced in 1 L of 2xYT medium.

These represent the shortest Ff phage-derived nanorods that can be produced at the order of 10^{15} particles per L of culture. Removal of the 36-nt segment between the PS and the (-) *ori* did not majorly interfere with the nanorod replication or assembly, proving that this segment is not absolutely required for replication and assembly of nanorods.

Table 10. Nanorods produced by the different BSFpn cassettes

Plasmid	Nanorods per 1 L of original culture
pPop-up529LacUni (+) IPTG	$4.8 \pm 0.4 \times 10^{15}$
pPop-up395LacUni (+) IPTG	$1.7 \pm 0.4 \times 10^{15}$

5.2.3 Design of a new BSFp replication-assembly cassette for production of 152-nt (40 nm) nanorods

To study the role of the unstructured DNA segments in the replication-assembly cassette BSFp, containing only the positive f1 *ori*, deletions of sequences between the annotated segments of the 221-nt cassette: *(+) ori1* (A portion; initiator), PS, and *(+) oriΔ29* [(+) *ori2*, the terminator] were made. The BSFp221 cassette is the smallest f1 replication and assembly cassette that had ever been designed (Sattar *et al*., 2015; Specthrie *et al*., 1992) prior to this work. A trade-off for producing the very short (50 nm) nanorods by the BSFp221 cassette was the lower efficiency of production in comparison to the BSFpn cassette (BSFpn529, Table 9), due to the

lack of the (-) *ori* (Table 9, Chapter 3). Testing whether removing DNA segments from this cassette would still support the replication and production of nanorods and how it will affect the production efficiency was undertaken to examine whether these regions are required for replication and if they could be further manipulated to obtain even smaller nanorods.

To test this, the BSFp221 cassette was first cloned into the pPop-up529LacUni plasmid. The pPop-upLacUni backbone demonstrated the highest production of nanorods when carrying the BSFpn529 cassette (Table 9, Chapter 3). The BSFp221 replication-assembly cassette was amplified by PCR, which introduced PstI and SalI sites required for cloning into the pPop-up529LacUni plasmid. The amplification template was plasmid pSS3 (Sattar *et al.,* 2015). The PstI-SalI-digested PCR product was ligated to the large fragment of the PstI-SalI-digested pPop-up529LacUni plasmid, replacing the BSFpn529 cassette (Figure 39). The recombinants were selected by their resistance to kanamycin and confirmed by DNA sequence analysis. The resulting plasmid was then named pPop-up221LacUni.

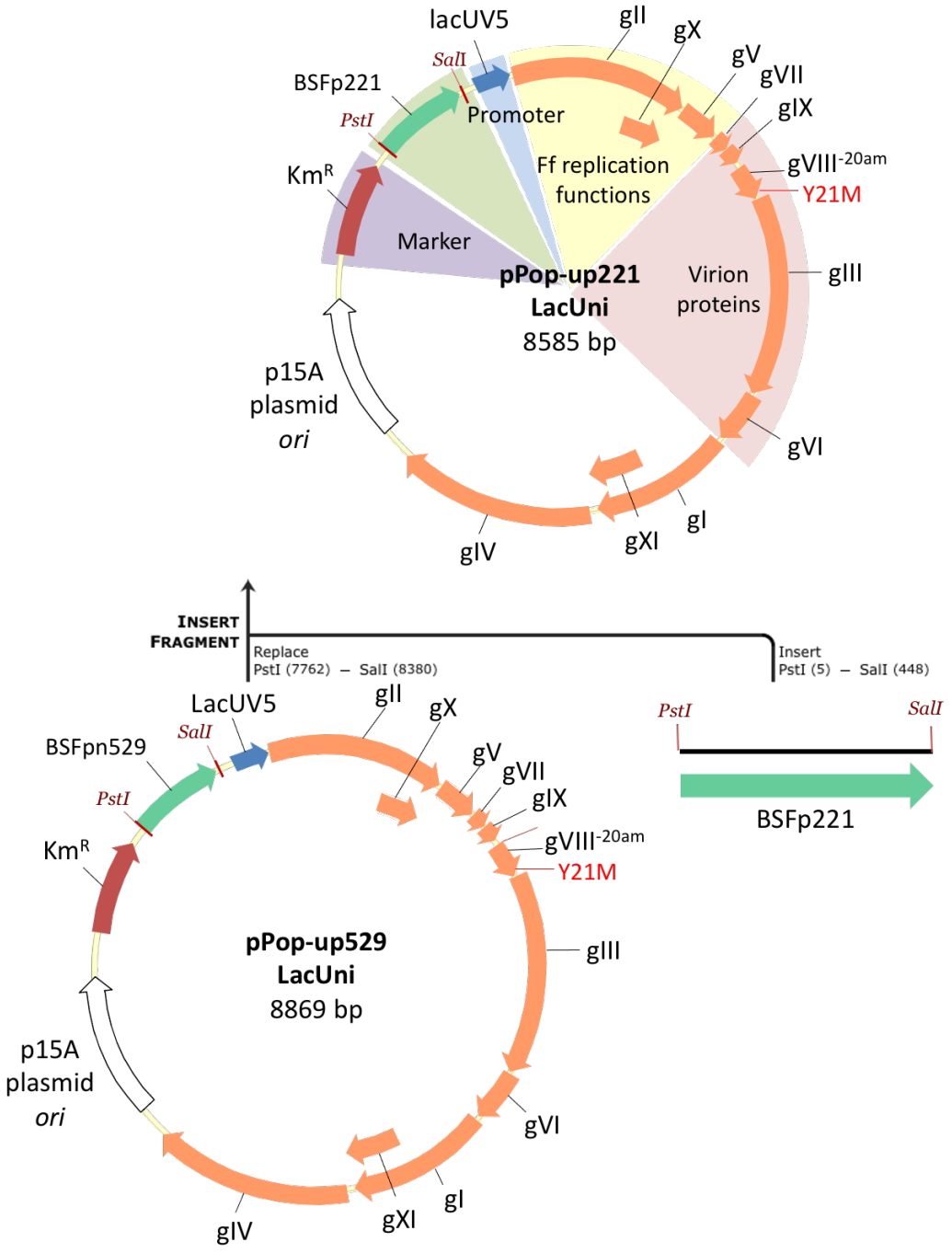

Figure 39. Construction of plasmid pPop-up221LacUni for production of 221-nt nanorods.

The PCR-amplified BSFp221 replication-assembly cassette (corresponding to pSS3 producing 221-nt circular ssDNA) was cloned into the pPop-up529LacUni plasmid, containing all genes encoding proteins required for replication and assembly of short nanorods, between PstI and SalI sites. Orange block arrows indicate open reading frames

(ORFs) encoding phage proteins; the green block arrow corresponds to the BSFpn or BSFp cassette (BSFpn529 or BSFp221, respectively); the white block arrow corresponds to the p15A plasmid origin of replication; the red block arrow corresponds to the marker, in this case, kanamycin resistance (Km^R); the blue block arrow corresponds to the promoter controlling the genes *gII-gV-gVII-gIX-gVIII* operon, in this case, the *lacUV5* promoter.

The BSFp221 cassette contains the A or I portion of the (+) *ori* [(+) *ori1*], starting from nucleotide 5727 of the f1 sequence, followed by an unstructured DNA segment of 16-nt, the PS, another DNA segment of 55-nt, and finally, a truncated (+) *ori Δ29* [(+) *ori2*] that serves as a terminator of the (+) strand replication (Figure 40A). For the new shorter BSFp cassette, the DNA regions between the PS and the second (+) *oriΔ29* (the terminator) were shortened and removed. A DNA fragment of 196-nt was designed starting from nucleotide 5764 of the f1 origin of replication, followed by the complete (+) *ori*, the PS, an unstructured DNA segment of only 6-nt, and finally, the (+) *oriΔ29* (Figure 40B). The initiator and terminator in this synthetic fragment are 152-nt apart, hence, it was named BSFp152 replication-assembly cassette. The sequence between the pII cut site in the initiator and terminator was predicted to be able to be replicated by pII, to give a single-stranded circular DNA of 152-nt that, theoretically, will be packaged into nanorods of approximately 39 nm in length. The length was predicted based on calculations assuming: (i) 2.3 bases per coat protein (Day *et al*., 1979; Specthrie *et al*., 1992), (ii) 152-nt ssDNA genome, (iii) particle length increase of 3.3 Å per coat protein (Caspar & Makowski, 1981), (iv) minor proteins arranged with same mass per unit length as the major coat proteins (1795 Da/Å), (v) five copies of each minor protein (pIII, pVI, pVII, and pIX); making a total of 311000 Da. Based on this, the major

coat proteins plus the ssDNA in the nanorod contribute to a total length of ~ 218 Å or ~ 22 nm [152 bases divided by 2.3 (bases/protein) multiplied by 3.3 (Å/protein)]. The minor proteins add a length of ~ 173 Å or ~ 17.3 nm (311000 Da divided by 1795 Da/Å) (Specthrie *et al*., 1992).

A. BSFp221 cassette

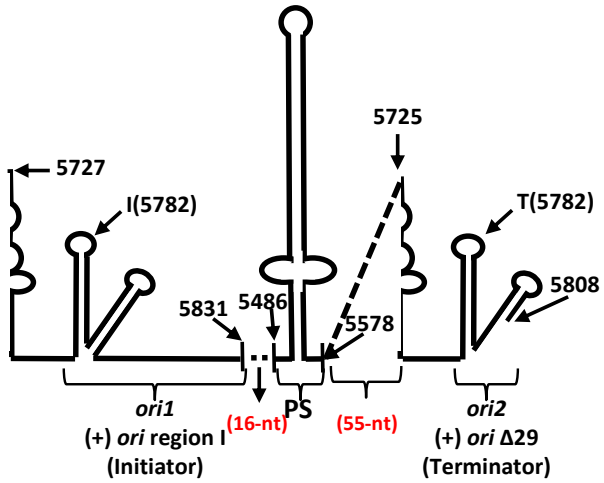

B. BSFp152 cassette

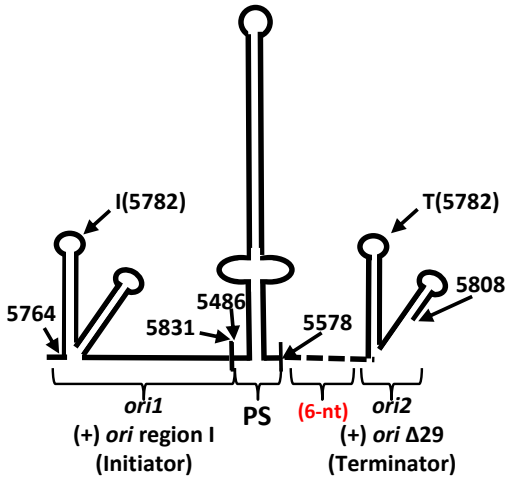

Figure 40. Engineered BSFp replication-assembly cassettes for nanorod production.

The BSFp cassettes include a packaging signal between two (+) origins of replication, an initiator (+) *ori* essential region (A or I, (+) *ori1*), and a truncated one (+) *oriΔ29* [(+) *ori2*]. (A) BSFp221 cassette (303 bp), nanorod replication by pII between initiator (I) and terminator (T) results in 221nt single-stranded circular DNA that is packaged into 50 nm nanorods. (B) BSFp152 cassette (196 bp), nanorod replication by pII between initiator (I) and terminator (T) results in 152-nt single-stranded circular DNA that is packaged into, theoretically, ~ 39 nm nanorods.

The synthetic BSFp152 cassette, flanked by PstI and SalI recognition sites, was inserted into the pPop-up529LacUni plasmid using PstI and SalI restriction enzymes in place of the BSFpn529 cassette (Figure 41). This new plasmid was named pPop-up152LacUni. The recombinants were selected by their resistance to kanamycin and their identity was confirmed by DNA sequence analysis.

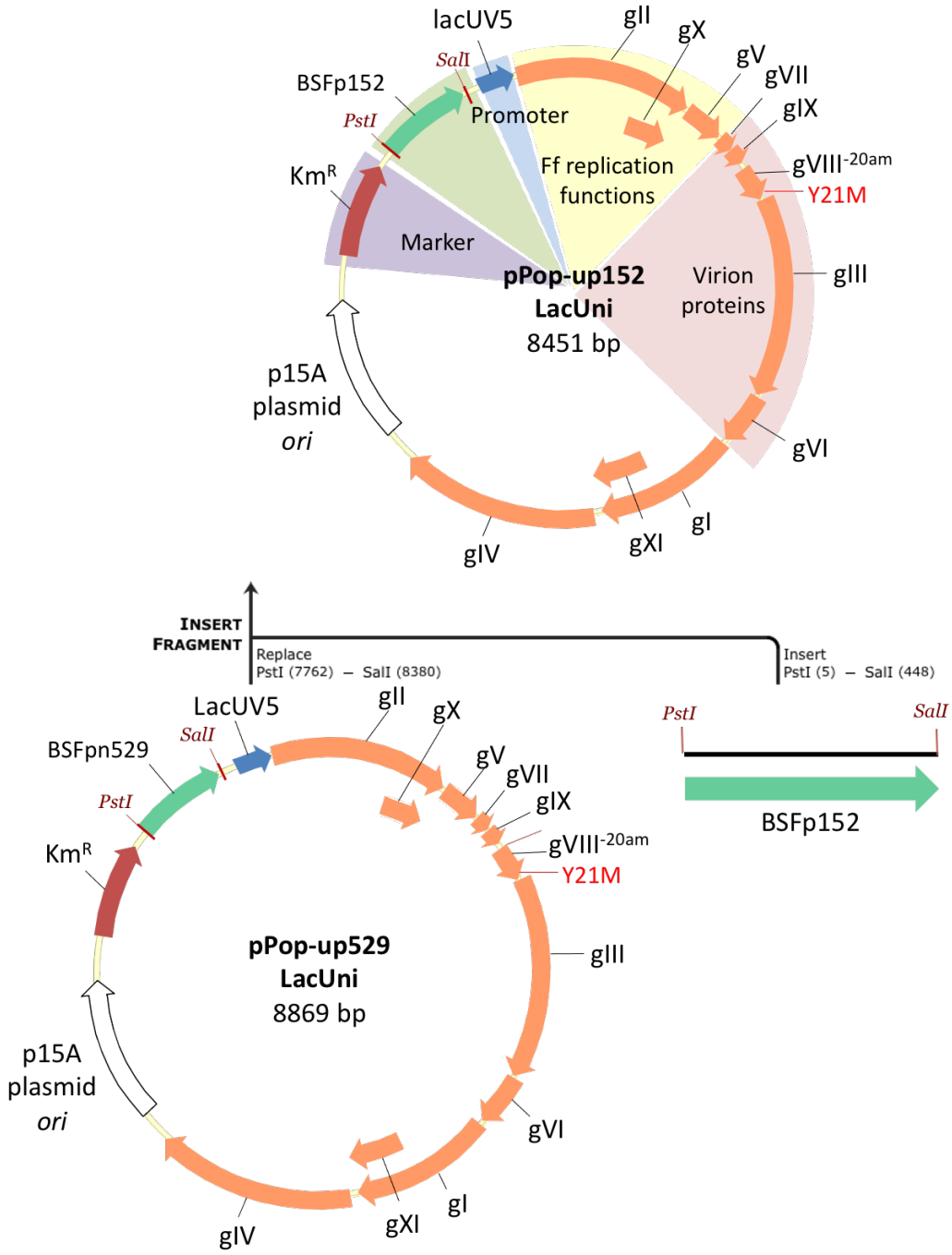

Figure 41. Construction of plasmid pPop-up152LacUni for production of 152-nt nanorods.

A synthetic fragment called BSFp152, containing the BSFp152 nanorod replication-assembly cassette (producing 152-nt circular ssDNA), was cloned into the pPop-up529LacUni plasmid, containing all genes encoding for proteins required for replication and assembly of short nanorods, at PstI/SalI cut-sites. Orange block arrows indicate open

reading frames (ORFs) encoding phage proteins; the green block arrow corresponds to the BSFpn or BSFp cassette (BSFpn529 or BSFp152, respectively); the white block arrow corresponds to the p15A plasmid origin of replication; the red block arrow corresponds to the marker, in this case, kanamycin (Km^R); the blue block arrow corresponds to the promoter controlling the genes *gII-gV-gVII-gIX-gVIII* operon, in this case, the *lacUV5* promoter.

5.2.4 Production of 221 and 152-nt nanorods by an inducible single-plasmid production system

Two batches of K2091 electrocompetent *E. coli* cells were transformed with the pPop-up221LacUni or pPop-up152LacUni plasmids to produce 221 or 152-nt nanorods, respectively. The transformed cultures were induced with 1 mM IPTG at OD_{600} ~ 0.2, then incubated overnight. Next, nanorods were concentrated from the culture supernatants by PEG precipitation, as described in section 2.4.4. Finally, the 221 and 152-nt nanorods were analysed and compared by disassembled- and native-particle agarose gel electrophoresis (Figure 42). Both systems were able to produce nanorods at concentrations of 1.9 x 10^{14} and 1.8 x 10^{14} particles per 1 L of original culture, respectively (Table 11). DNA carried inside of the nanorods was analysed by disassembled-particle agarose gel electrophoresis. Fast-migrating bands corresponding to 221 and 152-nt ssDNA were detected, however, the presence of an intense band of high-molecular weight DNA migrating at the level between the 4000 and 5000 bp standards was observed. This slow-migrating band was very strong in the purified 221-nt nanorods sample and very weak in the 152-nt nanorods sample, and corresponded to longer particles produced by a population of pPop-

upLacUni plasmid mutants where the terminator was mutated or rearranged in the sequence, as was observed for the pSS3 template plasmid (Sattar, 2013). In contrast to the positive-origin-only BSFp cassettes, no longer particles were detected when the BSFpn cassettes, containing both (+) and (-) *ori*, were used for nanorod production (Figure 38).

There is very little difference in migration of native 221 and 152-nt nanorods in agarose gel electrophoresis (Figure 42B), possibly due to the minor difference in their total size. The SDS-disassembled nanorods in the PEG-precipitated samples contained an extra band running between 850 and 1000 bp bands of the ladder. This was not a DNA band, but rather a non-nucleotide species that bind SDS, also stained by EtBr. This band does not show in the native electrophoresis and was not visible when ssDNA was extracted from nanorods and purified using a nucleic-acid-binding silica-based column (R. Leon and J. Rakonjac, unpublished observation).

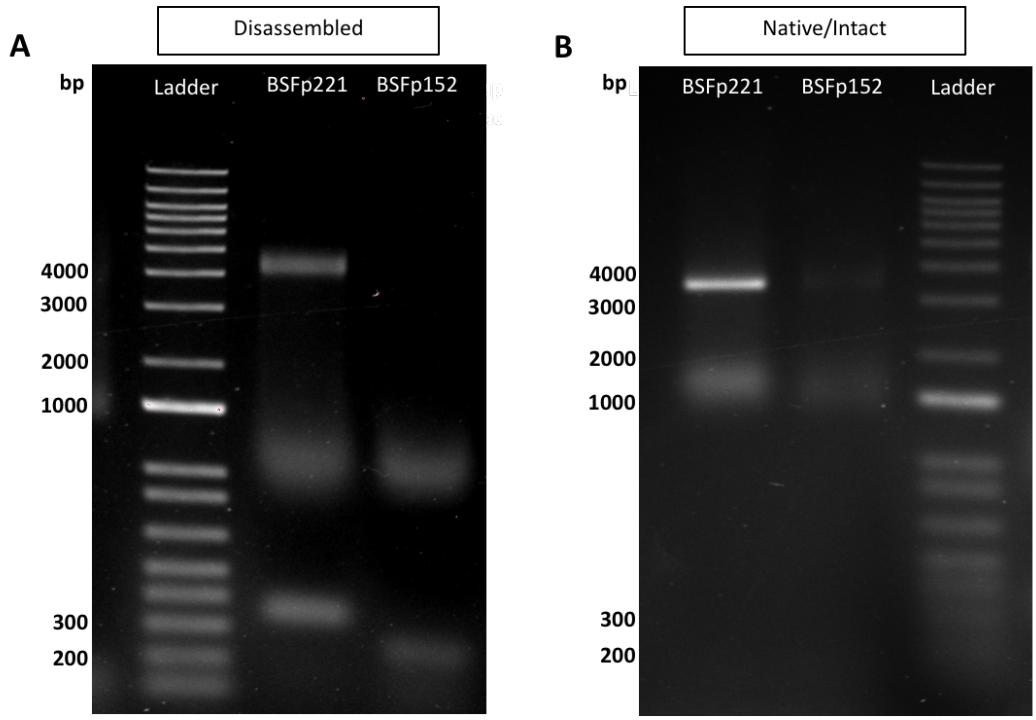

Figure 42. Comparison of the single-plasmid production system containing 221-nt and 152-nt BSFp cassettes, from pPop-up221LacUni and pPop-up152LacUni plasmids.

(A) DNA from SDS-disassembled nanorods was separated by 1.2% agarose gel electrophoresis and visualised by EtBr staining. (B) Native nanorods. Bands corresponding to the native/intact particles were visualized after soaking the gel in 0.2 M NaOH. Lanes: Ladder, 1 Kb Plus ladder (a double-stranded linear DNA standard used as a signpost for migration due to the lack of appropriate circular ssDNA standards; numbers indicate sizes of the standard bands in base-pairs); BSFp221, BSFp221 particles produced by the pPop-up221LacUni plasmid; BSFp152, BSFp152 particles produced by the pPop-up152LacUni plasmid. Particles were produced in 1 L of 2xYT medium and concentrated by two rounds of PEG precipitation to 1 mL.

These represent the shortest Ff phage-derived nanorods that can be produced in the order of 10^{14} particles per L of culture. Removal of the 36-nt segment between the PS and the (-) *ori* did not majorly interfere with the nanorod replication or assembly,

proving that this segment is not absolutely required for replication and assembly of nanorods.

Table 11. Nanorods produced by the different BSFp cassettes

Plasmid	**Nanorods per 1 L of original culture**
pPop-up221LacUni (+) IPTG	$1.9 \pm 0.1 \times 10^{14}$
pPop-up152LacUni (+) IPTG	$1.8 \pm 0.1 \times 10^{14}$

As seen in the comparison of pPop-up221Uni with pPop-up529Uni (Table 9, Chapter 3), the yield of nanorods from the BSFp cassettes, which do not have (-) *ori* and therefore cannot undergo negative-strand replication using the ssDNA as a template, was around 10-fold lower than those from the BSFpn cassettes. Given that pVIII production is toxic to *E. coli*, the selective pressure of excess pVIII in the cells containing BSFp cassettes is likely why those cells containing mutants or recombinants of the pPop-up221LacUni plasmid producing longer particles gain a selective advantage in the culture.

5.3 TEM analysis of the nanorods produced by the BSFpn395 and the BSFp152 replication-assembly cassettes

The PEG precipitated nanorods produced by the BSFpn395 and BSFp152 replication-assembly cassettes were visualised by TEM (Figure 43A and Figure 44A). The length of 100 nanorods produced by the BSFpn395 cassette was measured, and the distribution of sizes in the population was carried out using a binning method (Figure 43B), that showed most of the particles were approximately 70 nm (70%) in length or >100 nm (21%). In comparison, only 7% and 2% of the particles were around 80 and 90 nm, respectively. The majority of the nanorods were therefore approximately 70 nm in length, in accordance with their calculated size. Therefore, the engineered BSFpn395 replication-assembly cassette is capable of producing circular ssDNA of 395-nt that assembles into 70 nm nanorods. On the other hand, only 76 well-separated 152-nt nanorods produced by the BSFp152 cassette could be counted and measured from their electron micrographs (Figure 44A). The distribution of sizes in the population conducted using a binning method (Figure 44B), showed that most of the particles (79%) were approximately 40 nm in length (close to their calculated size), while 12% and 8% had sizes of approximately 80 and >100 nm, respectively.

Like the other nanorods made from the BSFpn and BSFp cassettes, these nanorods showed asymmetric particle termini (one "pointed" and one "blunt"), just as reported for the Ff phage; however, once again, no "knob" or "ball on the string" attached to the "pointy-end" that are sometimes observed in the TEM micrographs of Ff phage (Gray *et al*., 1978) were observed here. The presence of longer particles in the TEM micrographs produced by both systems is similar to what is seen for full-length Ff phage. The observed longer nanorods are made up of either more than one particle interacting side-by-side, or are longer than unit-length nanorods by a factor of two or more and contain two or more sequentially packed genomes in one particle (Rakonjac & Model, 1998; Sattar *et al*., 2015). Some minor differences in the nanorod lengths (+/- 10 nm) were also reported to be observed when short Ff phage-derived nanorods are analysed (Sattar *et al*., 2015; Specthrie *et al*., 1992). These differences could be due to pIII N1N2 domain being either associated or dissociate from the body of the nanorod.

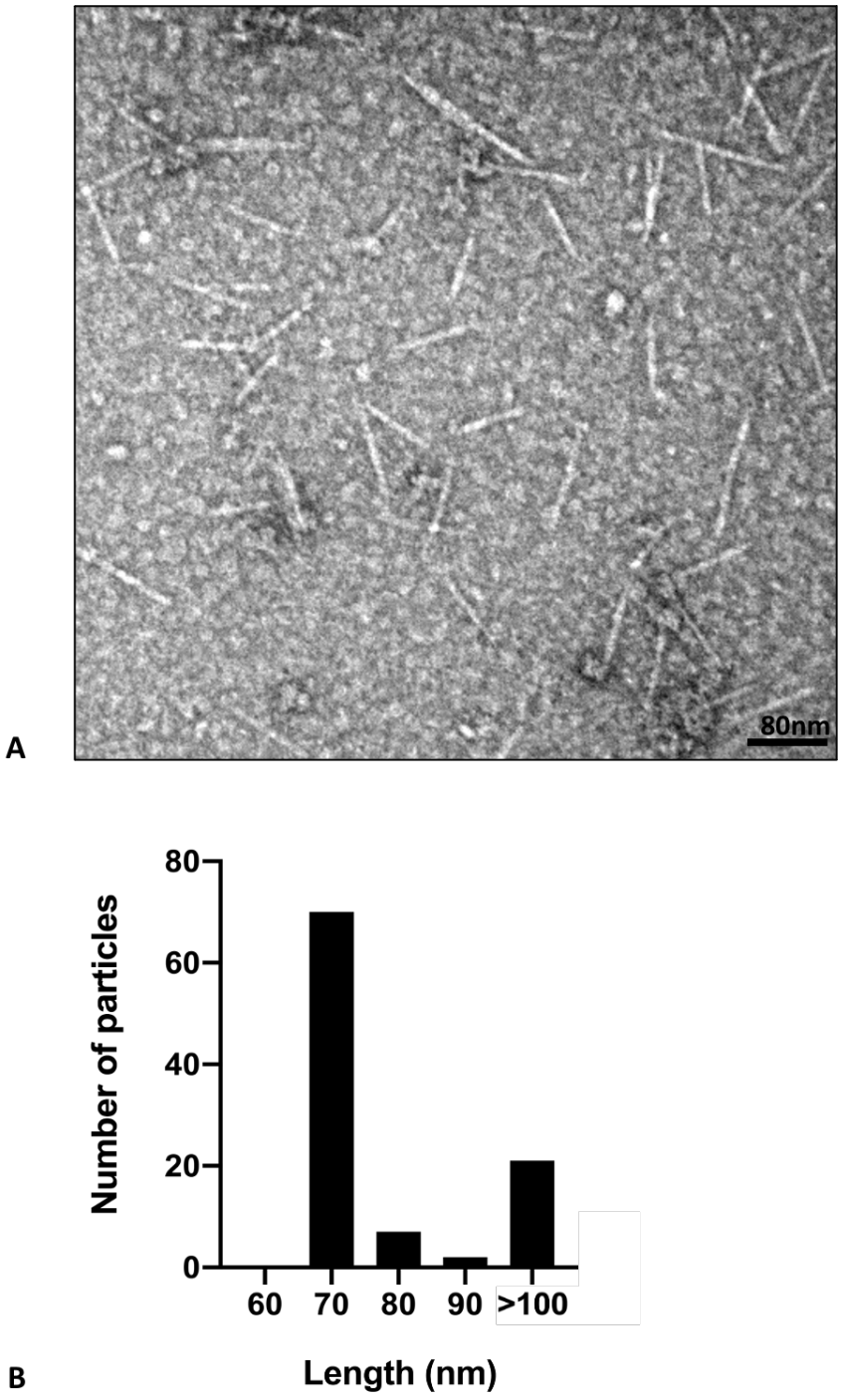

Figure 43. Analysis of the 395-nt nanorods produced by the BSFpn395 replication-assembly cassette.

(A) Electron micrograph of negatively stained 395-nt nanorods. (B) Bar graph showing the frequency distribution of the size of the 395-nt nanorods (bin width of 10 nm). Size distributions are presented as a bar graph generated by measuring the length of 100 particles using the ImageJ measurement function.

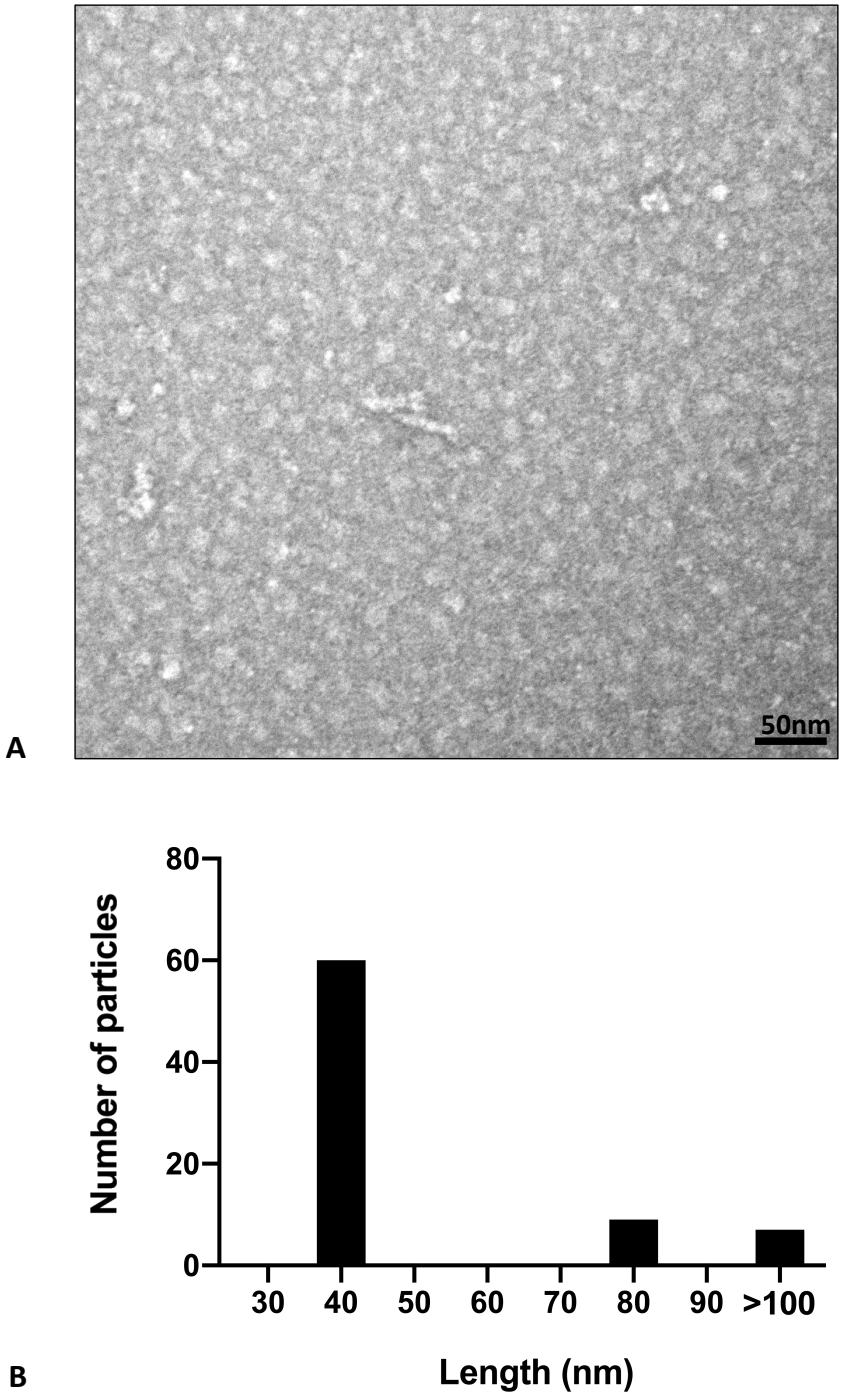

Figure 44. Analysis of the 152-nt nanorods produced by the BSFp152 replication-assembly cassette.

(A) Electron micrograph of negatively stained 152-nt nanorods. (B) Bar graph showing the frequency distribution of the size of the 152-nt nanorods. Size distributions are presented as a bar graph (bin width of 10) generated by measuring the length of 76 particles using the ImageJ measurement function.

5.4 Summary/Conclusions

In this chapter, the shortest BSFpn and BSFp nanorod replication-assembly cassettes, to date, comprising only 395 and 152-nt, were constructed and shown to be able to assemble nanorods of 70 and 40 nm in length, respectively, albeit with somewhat lower efficiency than the existing 529 and 221-nt cassettes. Their production proves the feasibility of minimising the BSFpn and BSFp cassettes sizes by removing the DNA segments between the packaging signal and the origins of Ff replication which, according to this work, are not essential for replication. Moreover, the work done in this study proves that the sizes of these cassettes can be tuned by manipulating the length of these DNA segments to produce nanorods of various sizes.

The technology reported in this chapter can be used to produce biological scalable nanorods. These nanorods could be used for applications that require short particles, such as delivering therapeutical compounds to tissues that restrict the carrier size (i.e., gut epithelium, Huh *et al*. (2019)), diagnostic methods that rely on lateral flow diffusion and require smaller particles to easily diffuse through membranes (Sattar *et al*., 2015), the assembly of nanorod-based nanostructures, and for the production of ssDNA standards.

Chapter 6:

Exploring the interaction of the pIII C domain with β-amyloid fibres

6.1 Introduction

Ff phage have been used for a wide range of applications, from nano-scale batteries to cancer therapies. In the past decade, the use of the Ff phage as disaggregating agents towards misfolded proteins such as β-amyloid (Aβ) oligomers and fibres (fAβ) has been explored as a potential treatment for Alzheimer's disease (Messing, 2016).

The ability to bind and disaggregate misfolded proteins has been attributed to the pIII protein on the Ff virion's surface, which appears to represent a unique type of amyloid target motif, the so-called "general amyloid interaction motif (GAIM)" (Asp *et al*., 2019; Krishnan, 2014; Krishnan *et al*., 2014). This motif has shown to bind to various misfolded proteins associated with Alzheimer's disease, such as fAβ, the micro-tubule-associated protein tau, and the pre-synaptic protein α-synuclein (AS) (Dimant & Solomon, 2010; Krishnan, 2014). The roles of the pIII N1N2 domains in this binding and disaggregation are well characterised (Krishnan *et al*., 2014). In contrast, little is known about the role of the pIII C domain. It was reported that the enzymatic removal of the pIII N1N2 domains from M13 phage decreases by an estimated two-thirds but, does not eliminate the phage-fAβ interaction (Krishnan, 2014; Krishnan *et al*., 2014). Based on this observation, the authors suggested a role of the C domain of pIII in the phage-Aβ interaction. To follow this up, we aimed to map the Aβ-binding motif in the C domain of pIII and determine whether the phage itself contributes to the interaction.

Given that enzymatic cleavage of N1N2 and subsequent separation of the cleaved domains from the phage may not have been complete in the published work, we aimed to confirm the Aβ-binding activity in the complete absence of N1N2 domains before undertaking mapping of the Aβ-binding motif in the C domain and the capsid of the filamentous phage. The reported interaction between the C domain of pIII to fAβ could have been due to contamination of the sample with N1N2 domains and/or the presence of undigested phage in the reaction. To eliminate a possibility of N1N2 contamination, we produced a recombinant phage containing only the C domain of pIII, with no N1N2 domains present at any stage during its production and purification, and tested binding of these virions to Aβ. Confirming the role of the C domain of pIII in binding the β-Amyloid fibre and mapping a motif that mediates it would aid in the ongoing research of the possible use of Ff phage in treatment of Alzheimer's disease.

This chapter will explore the binding ability of the C domain of pIII with fAβ by performing a binding assay between fAβ and a mutant f1 phage containing only the C domain of pIII.

6.2 Results and discussion

6.2.1 Production and purification of f1 phage particles recombinantly devoid of pIII N1 and N2 domains

Krishnan *et al*. (2014) showed that specific ArgC endoproteinase-mediated removal of the N1 and N2 domains of pIII diminished the ability of the resulting Ff phage to bind to fAβ. However, it was not clear if the fAβ binding was completely abolished as no statistical analysis was performed that showed this difference was significant. Briefly, Krishnan *et al*. (2014) mixed ArgC (1 mg/mL), which specifically hydrolyses the amide bonds at the carboxylic side of the residue arginine in a polypeptide, with fluorescently labelled M13 phage (1 x 10^{14} phage/mL) and incubated this protease reaction mix at 37 °C for two days. To measure binding of ArgC-treated M13 to fAβ, authors added the latter to the mix which was then incubated at 37 °C for two or three hours, followed by centrifugation to separate the aggregates of interacting M13 and fAβ from the soluble components (Figure 45A). The fAβ-bound phage in the pellet was then analysed by fluorescence measurements. However, it was not resolved in Krishnan *et al*. (2014) whether the fluorescence in the pellet was due to the binding mediated by the pIII C domain at the virion end-cap, the shaft of the phage filament, and/or pIII N domains (GAIM) that remained in the aggregate due to incomplete enzymatic reaction or incomplete removal of digested N1N2 domains from the aggregates.

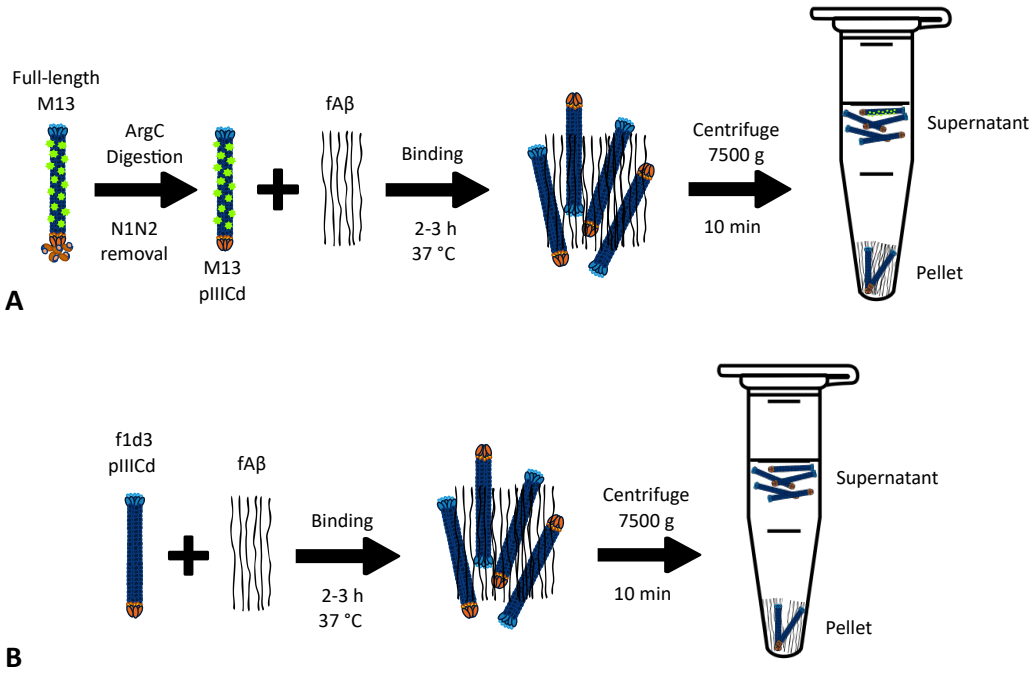

Figure 45. Binding assay.

(A) Method developed by Krishnan *et al*. (2014) to determine the binding ability of the pIII C domain to fAβ. Briefly, pIII N1N2 domains were removed from fluorescent labelled (Alexa488-M13) wild type M13 phage by enzymatic treatment with the endoproteinase ArgC. Next, Alexa488-ArgCM13 phage were incubated with fAβ and centrifuged at 7500 *x g* to pellet the fAβ-bound phage and separate it from the unbound phage. fAβ-bound phage was determined by measuring the fluorescence of the pellet. (B) A modified method developed in this thesis, to determine the binding ability of the pIII C domain to fAβ. Briefly, pIII C-terminal domain only f1d3 phage (f1d3pIIICd) were produced and purify, followed by their incubation with fAβ and centrifugation (7500 *x g*) to pellet the fAβ-bound f1d3pIIICd. fAβ-bound f1d3pIIICd was quantified by measuring the phage DNA concentration in the pellet.

To produce N1N2-less phage and exclude the possibility of intrinsic contamination from the enzymatic removal, phage that are assembled in the absence of N1N2 pIII domains were produced. These phage (f1d3pIIICd) were obtained by

complementing an f1 deletion mutant lacking the entire *gIII* coding sequence (f1d3) with the complete C domain of pIII (C-terminal 154 residues) expressed from a complementing plasmid, pJARA24 (Rakonjac *et al*., 1999; Rakonjac & Model, 1998). The complete C domain of pIII suffices to terminate the assembly and form a stable virion. As a N1N2-positive control (f1d3pIIIWT), the same phage (f1d3) was complemented with a full-length pIII expressed from plasmid pJARA112 (Figure 46)(Rakonjac *et al*., 1997). The two phage were produced, concentrated by PEG precipitation, purified by CsCl gradient centrifugation, and used in an Aβ co-sedimentation binding assay (as described in section 2.3.1.1, 2.3.2, and 2.7.3). Using this procedure, $4.9 \pm 0.1 \times 10^{12}$ and $9.7 \pm 4 \times 10^{12}$, respectively, of f1d3pIIICd and f1d3pIIIWT purified phage particles, respectively, were obtained from 1 L of the original culture. As the phage containing the pIII C-terminal domain only (pIIICd) are not infectious due to the lack of the receptor-binding N1 and N2 domains, the concentration of the pIII-truncated particles was calculated from the amount of the ssDNA in the virions by densitometric analysis of EtBr-stained bands after agarose gel electrophoresis of SDS-disassembled virions (Figure 47).

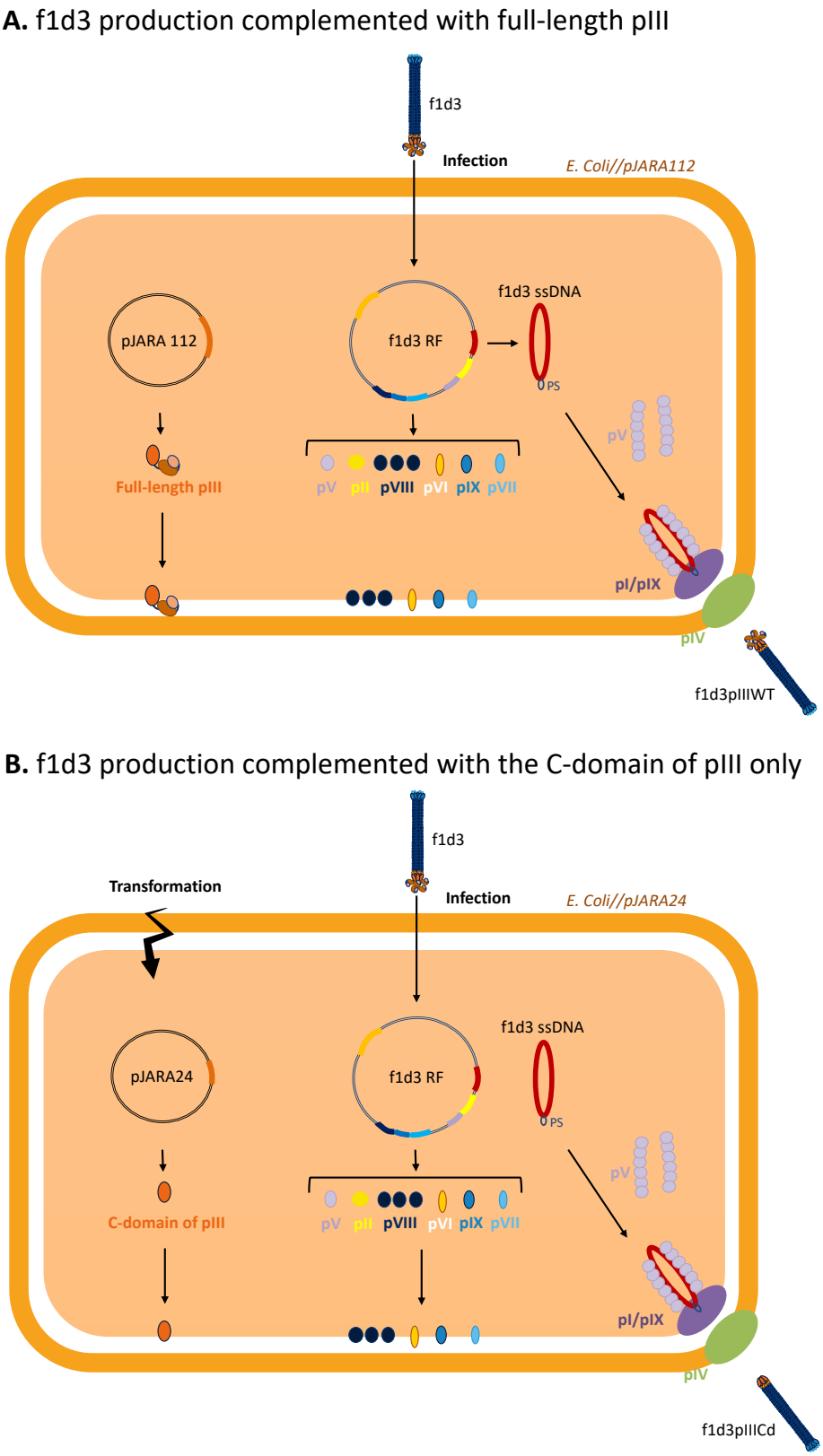

Figure 46. Scheme of f1d3 production.

Production of f1d3 containing either full-length pIII (A) or its C domain only (B).

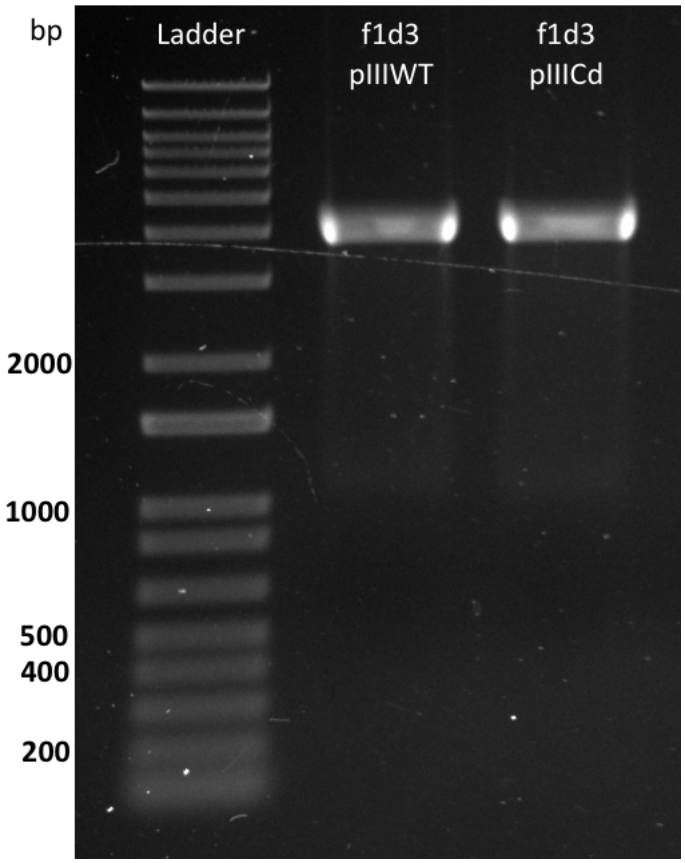

Figure 47. Purified f1d3 phage that contained full-length pIII or pIII C domain.

Lanes: Ladder, 1 Kb Plus (a double-stranded linear DNA standard used as a signpost for migration due to the lack of appropriate circular ssDNA standards; numbers indicate sizes of the standard bands in base-pairs); f1d3pIIIWT, phage with a complete deletion of *gIII* produced in a complementing strain containing the full-length *gIII* from a plasmid; f1d3pIIICd, phage with a complete deletion of *gIII* complemented with a fragment containing the C domain of pIII from a strain containing a plasmid with the nested deletion in *gIII*.

6.2.2 Production of β-amyloid fibres (fAβ)

β-amyloid fibres (fAβ) were produced from the β-amyloid (1-42) human peptide as described by Stine *et al*. (2011) (see section 2.7.1 for details) and were analysed by TEM and Thioflavin T (ThT) fluorescence (Figure 48). The TEM micrographs confirmed the presence of fibres along with some oligomeric structures after a 24-hour incubation. ThT is a fluorescent dye commonly used to monitor *in vitro* Aβ fibre formation, and gives a signal at approximately 482 nm when excited at 450 nm upon fibril binding (Biancalana & Koide, 2010; Naiki *et al*., 1989; Xue *et al*., 2017). Figure 48B shows that the fluorescence intensity increased at least 5-fold compared to the background signal after the 24-hour incubation, confirming the fibril formation.

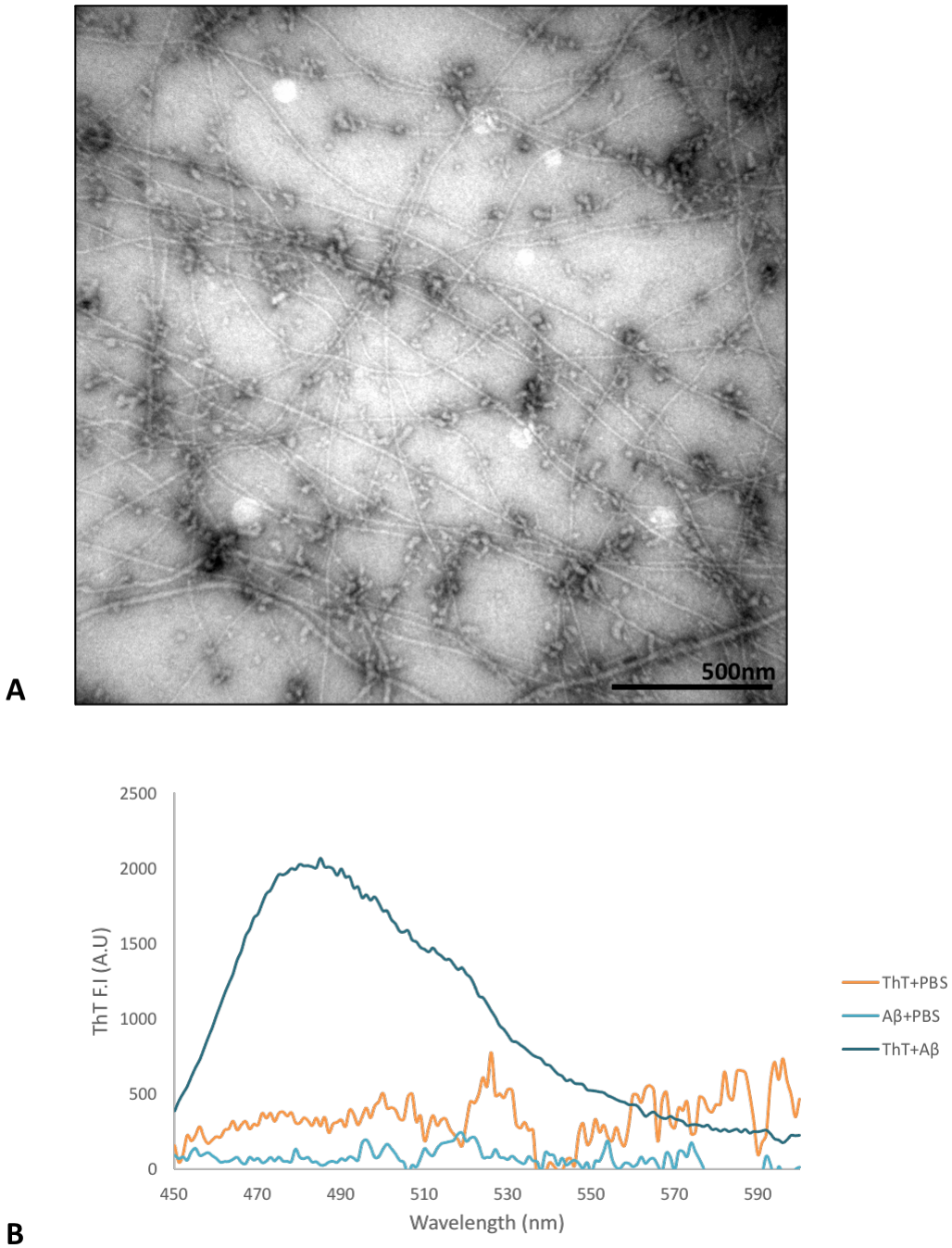

Figure 48. Aβ(1-42) fibril formation.

(A) Representative images of fAβ (1-42) fibrils. (B) ThT fluorescence (λex 450 nm, λem 450-600 nm) upon the interaction of 100 μM fAβ and 5 μM ThT.

6.2.3 Co-sedimentation binding assay between phage containing either full length pIII or truncated-pIII with fAβ

Krishnan *et al*. (2014), described a binding assay to characterise the interactions between Ff phage M13 (98% identical to f1) and β-amyloid fibres (fAβ) by exploiting the differential sedimentation properties of the f1 phage and the fAβ (Figure 45A). Ff phage does not sediment at low centrifugal forces (7500 *x g*), remaining in the supernatant unless they interact with fAβ (Krishnan *et al*., 2014; Mok & Howlett, 2006). In this study, a modified assay was used to examine the ability of f1d3pIIICd and f1d3pIIIWT (positive control), to bind to fAβ (Figure 45B). Briefly, after the fAβ fibrils have been formed, either f1d3pIIIWT or f1d3pIIICd was incubated in the presence or absence of them for 3 hrs at 37 °C. This mixture was centrifuged at a low centrifugal force to separate the supernatant (free phage) from the "pellet" (fAβ-bound phage). The "pellet" was resuspended in PBS buffer, whereas the supernatant was directly analysed by agarose gel electrophoresis to monitor the amount of phage in these two samples (Figure 49). Phage ssDNA was released by boiling of the samples in SDS, followed by agarose gel electrophoresis and visualisation by staining with EtBr.

When using fAβ on its own as a negative control, no band was visualised either in the pellet or supernatant due to the lack of the phage in these samples. When f1d3pIIIWT were analysed without fAβ in the reaction, a strong band was visualised in the supernatant while a faint band is also observed in the "pellet". To minimise the influence of human error, these treatments were repeated three times

over a period of three weeks, and the influence of time was estimated from a randomised block design. On the other hand, when the fAβ was added to the reaction, the band's intensity from the "pellet" increased, representing the binding between the phage with the fAβ. Quantification was made by densitometric analysis of the EtBr-stained band, confirming that the phage amount in the "pellet" increases at least 7.1-fold (Figure 49B) when fAβ is added (from $2.3 \pm 1.5 \times 10^{12}$ to $1.7 \pm 1.3 \times 10^{13}$; $p<0.0001$), confirming the ability of the f1d3pIIIWT to bind to fAβ in agreement with what Krishnan *et al*. (2014) stated. When f1d3pIIICd are analysed, similar results as for wild type phage were observed in the control (phage without the presence of fAβ) where most of the phage particles were present in the supernatant (Figure 49A); however, after adding the fAβ to the reaction, no evident increase in the band intensity was observed. To confirm this, the band intensity of the "pellet" was quantified before and after adding fAβ to the reaction. It was observed that the amount of phage-like particles in the "pellet" remains practically the same (Figure 49B) in the presence or absence of fAβ ($3.6\pm1.8\times10^{12}$ and $2.5\pm1.4\times10^{12}$, respectively; $p>0.05$), ruling out binding of the pIII C domain to fAβ.

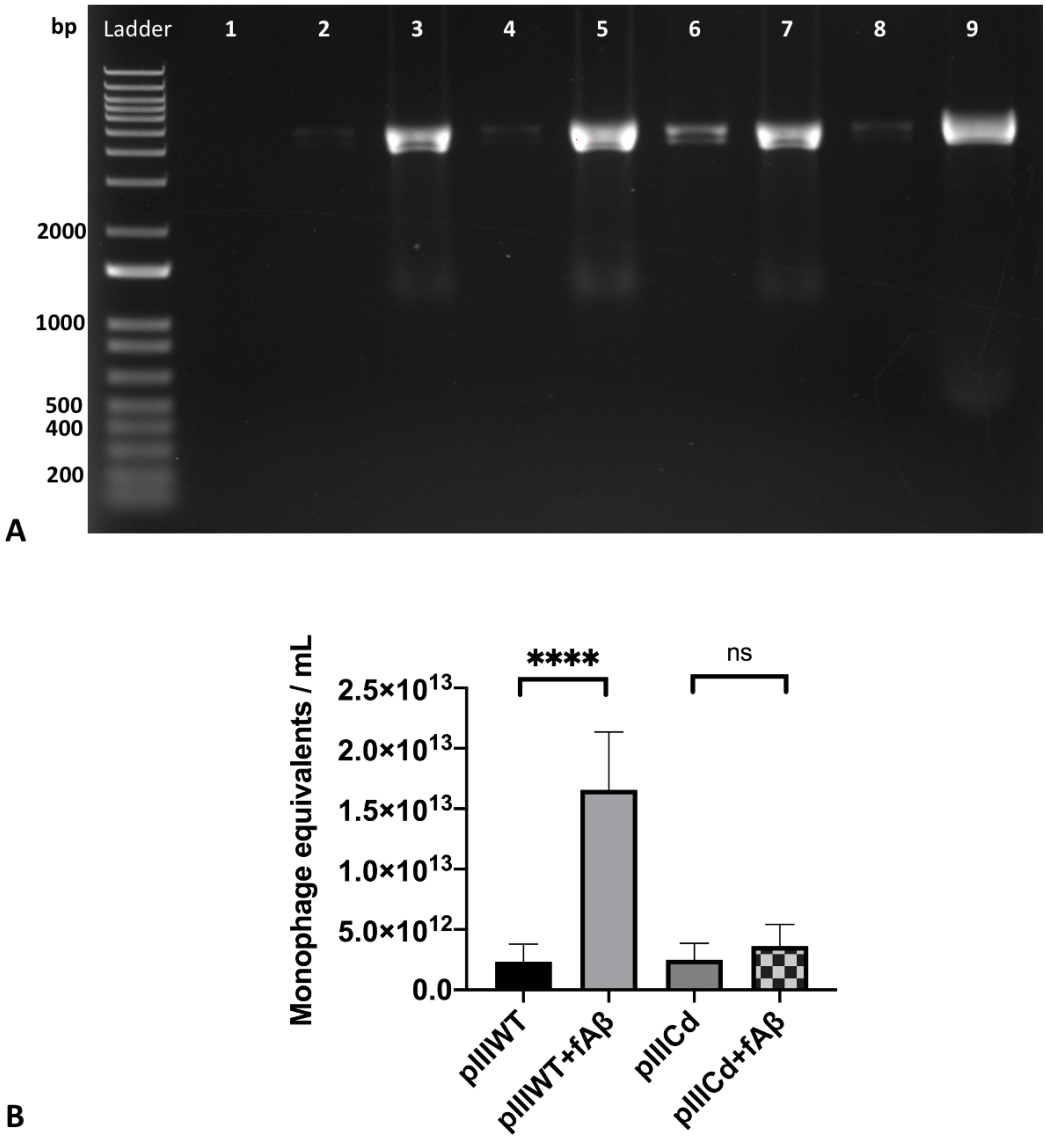

Figure 49. Interaction between f1d3 phage complemented with either full-length pIII or only its C domain and β-amyloid fibres (fAβ).

(A) DNA from SDS-disassembled virions of the different fractions from the sedimentation by centrifugation was separated by agarose gel electrophoresis and visualised by EtBr staining. Lanes:1, pellet, fAβ – only sample; 2-5, samples containing phage only: 2, pellet, f1d3pIIIWT; 3, supernatant f1d3pIIIWT; 4, pellet, f1d3pIIICd; 5, supernatant f1d3pIIICd; 6-9, samples containing a mixture of phage and: 6, pellet, f1d3pIIIWT + fAβ; 7, supernatant f1d3pIIIWT + fAβ; 8, pellet, f1d3pIIICd + fAβ; 9, supernatant, f1d3pIIICd + fAβ. The reactions contained, where applicable, phage at 1.3 x 10^{12} particles/mL, and/or fAβ at 100 μM. fAβ-bound phage were quantified by densitometry, and a Student t-test was used to

compare the amounts of phage in samples (B). Error bars indicate the standard deviation (SD) of nine replicates. Symbols: **** $p<0.001$ and ns $p>0.05$.

It has also been suggested that the shape of Ff phage could be mainly responsible for its amyloid fibre binding and disaggregation. The long and thin structure of the phage (890 nm x 6 nm) was argued to contribute to these processes by the way it binds along the fAβ fibrils. It is possible the high α-helical content of the filament shaft (pVIII) could potentially interfere with the β-sheet structure of the fAβ fibrils (Solomon & Goren, 2011). Other viruses with a similar shape and structure, such as the tobacco mosaic virus (TMV), have also been reported to promote disaggregation of the fAβ (Solomon & Goren, 2011). However, the results presented in this study showed that f1d3 filaments lacking the N1N2 domains of pIII did not bind to the fAβ fibres, in contrast to the results obtained by (Krishnan *et al*., 2014; Levenson *et al*., 2016); Figure 49). Furthermore, Krishnan *et al*. (2014) showed that a recombinant soluble g3p fragment (G3P), containing the N1N2 domains and a glycine-rich linker between them, was capable of binding to fAβ but had a reduced potency for binding and disaggregation in comparison to wild type phage. Taken these results together, the theoretical ability of the C domain of pIII to bind to fAβ implied by Krishnan *et al*. (2014), is more likely to be due to the partial digestion of the N1N2 domains of pIII, rather than to the C domain of pIII itself or the shaft (main body) of the virion.

6.3 Summary/Conclusions

In this chapter, we investigated the assumption that the pIII C domain or the shaft (body) of the filamentous virion has a role in the reported binding of Ff phage to β-amyloid fibres (fAβ). This knowledge will be of interest when using Ff phage, pIII or pIII-derived molecules as a disaggregating agent for the treatment of diseases such as AD, where the fAβ are considered to be a pathogenesis factor.

Our results show that the N1N2 domains of pIII are solely responsible for the interaction between Ff phage and the β-amyloid fibres, as described by Krishnan *et al*. (2014). In contrast to this published work, this thesis shows that the C domain of pIII and the body of the Ff filament have no role in this interaction. Given that the pIII C domain has no role in binding β-amyloid fibres, a prerequisite for breaking the fibres, the dissection of the putative C domain activity was void.

In conclusion, this work has shown that, in contrast to prior reports using enzymatic removal of N1N2 domains from the phage, our genetic approach of constructing N1N2-domain-free virions has determined that the C domain of pIII has no role in breaking up the β-amyloid fibres, and therefore it should not be considered as a β-amyloid disaggregating agent when studying potential AD therapeutical candidates.

Chapter 7:

General discussion, conclusions, and future directions

7.1 Introduction

With the increasing popularity of Ff phage for bio- and nanotechnological applications (Cao *et al*., 2019; Hemminga *et al*., 2010; Paczesny & Bielec, 2020; Yang *et al*., 2013), more detailed knowledge of their structure is vital when it comes to improving or developing new applications based on these viruses. To date, the structure of the Ff phage end-caps remains a mystery, as they represent only 2% of the wild type Ff phage virion mass and, therefore, have been invisible for the crystallographic methods commonly used to solve protein structures (Marvin *et al*., 2014). Without an understanding of the end-cap structures, it is not surprising that the Ff life cycle (the infection and assembly processes more precisely), is not yet either fully understood. A precise understanding of structures and interactions between proteins forming the pIII-pVI end-cap is crucial for understanding these processes. Proteins pIII and pVI mediate the insertion of the virion proteins into the host membrane during both entry into and excision from the host membrane upon the termination of assembly, and release of the virion from the host envelope. In this study, the development of a system for the production of extremely short Ff phage-derived nanorods has enabled structural analysis of the "pointy-end" of the Ff filament containing the pIII-pVI complex. This structural analysis will aid understanding of how filamentous phage are released from cells and enter into a new host, while also facilitating the improvement/development of the applications where these proteins have a determining role, e.g., phage display technology and bio- and nanotechnology.

While Chapters 3 and 4 focused on producing suitable Ff phage-derived-nanorods and structurally characterising their end-caps proteins, chapters 5 and 6 focused on exploring and expanding the bases for applications of Ff phage-derived nanorods and Ff phage therapies. Based on these themes, the general discussion of this thesis will be separated into two sections.

7.1.1 Short Ff phage-derived nanorods as a model to decipher the pIII-pVI end-cap structure of Ff phage

In this study, we described a novel system for the production of Ff phage-derived nanorods, 50 and 80 nm in length, where the end-caps' mass contribution accounted for 34% and 21% of the total mass of the virion, respectively. In contrast, the wild-type Ff phage end-caps correspond to only 2% of the mass (Marvin *et al*., 2014).

Improvements made to the nanorod production system and purification protocols developed in this study enabled structural analyses of the end-caps by cryo-EM and single particle analysis. Nanorods were produced by two different systems: i) a two-plasmid production system for the production of 221-nt nanorods by the cells containing a helper plasmid (pRnanoR) combined with a nanorod "template" plasmid containing a nanorod replication-assembly cassette; ii) a single-plasmid system (pPop-up) nanorod production system. In this system, a single plasmid provides all open reading frames for the viral proteins as well as the replication-assembly cassettes required for production of nanorods containing ssDNA of 221-

nt or 529-nt; iii) a single-plasmid variant with inducible-replication. The inducible single-plasmid system majorly improved the yields over those using the constitutive-replication system developed in previous versions of the system that were both unpublished and published (phage-based systems) (Bennett, 2010; Sattar *et al*., 2015). Inducible pII expression was the main improvement in the nanorod production, as it overcomes the bottleneck of transformation, which, even at its maximal efficiency, still results in a relatively small number of transformed cells. Delay of pII expression limited nanorod replication, allowing induction of replication once the number of pPop-up-transformed cells reached about 10^8 per mL, which is optimal growth phase for the production of Ff phage-derived particles. Overall, the inducible single-plasmid system, developed in this thesis, is a faster, high-yield, and easy-to-upscale method for nanorod production that is an improvement on the helper phage system developed previously in the literature (Bennett, 2010; Nafisi *et al*., 2018; Sattar *et al*., 2015), and to the two-plasmid system developed previously in the Massey University Phage Display Laboratory (unpublished). These advantages make the inducible single-plasmid system more suitable for upscaling that is often required for practical applications.

Improvements were also made to the nanorod purification. Density gradient ultracentrifugation using CsCl has been widely employed to concentrate and purify viruses and bacteriophages (Fouladvand *et al*., 2020). However, when purifying the nanorods produced as a result of plasmid electroporation, a somewhat higher burden of bacterial proteins was observed than in Ff extracted from the infected cells. This is probably due to the massive cell death of untransformed *E. coli*, which represents the majority in the cell population after transformation. Contamination

with host proteins makes the processing of EM images more complex, due to the increased level of background (Carroni & Saibil, 2016). To increase the purity of the nanorods for SPA cryo-EM analysis, another step was added to the purification protocol, anion exchange chromatography. A SepFast™ Super Q column which had been successfully used to purify the Ff phage M13 (Ling *et al*., 2004; Monjezi *et al*., 2010) was used. This purification method has also been used to purify several other bacteriophages (Jacinto *et al*., 2018; Kramberger *et al*., 2010; Monjezi *et al*., 2010). When used, it increased the purity of the 221 and 529-nt nanorods after the CsCl density gradient purification (Chapter 3, Figure 15 and Figure 25).

Structural characterisation of the pIII-pVI end-caps in the nanorods by cryo-EM or crystallographic methods is challenging as these proteins are overshadowed by the high concentration of pVIII in the virions. To overcome this issue, we dissociated the purified 529-nt nanorods using a combination of chloroform and DOC. Ff phage are well known for their sophisticated use of the physicochemical properties of the host membrane during infection and assembly processes (Stopar *et al*., 2003). Despite their popularity, the molecular details on the changes from protein-protein interactions to protein-lipid interactions during infection (and the reverse during assembly) these viruses undergo, however, are still not fully understood. Although the major coat protein pVIII is solubilised in the host membranes during the infection process *in vivo*, it is resistant *in vitro* to the addition of phospholipids and even ionic detergent sarkosyl to a phage solution (Stopar *et al*., 2003). Similarly, this protein is insensitive to a broad range of pH and salt concentrations (Ikehara *et al*., 1975; Jończyk *et al*., 2011; Marvin *et al*., 1994). Nevertheless, Ff phage are

sensitive to organic solvents. For example, upon chloroform exposure, especially in the presence of detergent sodium deoxycholate (DOC), morphological changes have been reported that could possibly mimic the virion *in vivo* conformational rearrangements that occur during infection, where the filament "opens" at the pIII-pVI end, resulting in the integration of the virion proteins into the host inner membrane (Dunker *et al*., 1991; Manning *et al*., 1981). When combined, chloroform and DOC treatment of the nanorods separated the pIII-pVI complex from the ssDNA and pVIII, as shown using size-exclusion chromatography (SEC). These findings are in agreement with those reported for the full-length Ff (Gailus & Rasched, 1994). Both, the agarose and SDS-PAGE analyses confirmed that the ssDNA had been separated from pIII and pVIII (Figure 30). When the fractions enriched for pVI and pIII were analysed by PAGE under the native conditions (blue native), the complex migrated above the 720 kDa standard, which was much greater than what had been observed by Gailus and Rasched (1994), of only 330 kDa. The reason for a difference in the apparent molecular mass of the pIII-pVI complex obtained in this study is not clear, but could be attributed to somewhat different condition used to dissociate the nanorods in the different experiments (different DOC concentrations; 15 mM vs 1 mM), and to over 10-fold lower pIII-pVI to pVIII ratio in the nanorods vs. wild type phage. Sattar *et al*. (2015), showed that phage-derived-nanorods are more resistant to heat/SDS, requiring heating to 100 °C instead of 70 °C to disassemble the virion. By extension, the 529-nt nanorods could be possibly more resistant to the DOC-chloroform dissociation method used here in comparison to the full-length Ff. Other possibilities are that the complex isolated from the nanorods could contain more pVIII than the equivalent complex extracted from the wild type Ff, or that, once dissociated from the virion, pVIII forms a

multimer-dimer to minimise the exposed hydrophobic surfaces. Multimer dimers have been observed for the large outer membrane channel, pIV, that mediates secretion-assembly of Ff (Opalka *et al*., 2003). From this, further work is needed to optimize nanorod dissociation conditions prior to the purification. Interestingly, some particles were visualised by TEM after purification (Chapter 4; Figure 31). However, our data must be interpreted with caution as it is not certain whether the particles observed in the TEM micrographs represent the pIII-pVI complex as it is structured in the nanorod, or random aggregates of phage proteins (pIII, pVI, and pVIII). Due to time limitation, we did not further pursue optimisation of the complex dissociation, purification, and structural characterisation. Nevertheless, the dissociation and purification conditions established in this study will serve as a starting point to continue optimizing the pIII-pVI complex purification process and subsequent structural analysis. There are some parameters, such as the choice and concentration of detergent used, that could be altered to improve purification (Seddon *et al*., 2004).

Nanorods produced and purified at Massey University were analysed by the research group of Dr Vicki Gold at the University of Exeter, to determine the structure of the pIII-pVI end-cap. They were able to determine 2D classes of the 529-nt nanorods ("blunt" end, filament shaft, and "pointy" end; Chapter 4, Figure 32). From these classes, they were able to reconstruct a 3D preliminary model of the "pointy-end" of the nanorod virion containing the pIII-pVI complex at 5 Å resolution by cryo-EM SPA (Chapter 4, Figure 33) by imposing a five-fold symmetry. Despite the promising results, giving unprecedented details of the pIII-pVI end-cap electron densities, the main polypeptide chains of the proteins have

not yet been traced. SPA is still in progress, and it is expected that a higher resolution model will result soon. Previous studies reported a low-resolution model (8 Å; 2HI5) for the phage fd major coat protein by helical real-space reconstruction (IHRSR) cryo-EM (Wang *et al*., 2006). This model was further refined by Straus *et al*. (2008), yielding a model close to the X-ray/NMR model 2C0X (Marvin *et al*., 2006). Despite having some intrinsic flaws, this cryo-EM model showed that this technique was able to give useful structural information and presents several advantages compared to crystallographic approaches that require crystals in order to solve structures (Marvin *et al*., 2014). The cryo-EM model shown here already has a higher resolution than the models reported in the literature for the well-studied major coat protein and represents a promising model for determining the structure of the end-cap proteins of Ff phage.

Besides the end-caps, 2D classes for the major coat protein were also determined in this analysis. This information could be used in the future as a building block to obtain another 3D model with an atomic or near-atomic resolution for the shaft of Ff phage based on our nanorods. In the model obtained here, pVIII subunits can be clearly distinguished from the pIII-pVI cap structure. The end of the DNA backbone is clearly visible, and the protein densities around the end of DNA and above clearly differ from the pVIII densities along the shaft (Chapter 4, Figure 33). They form the "pointy-end" of the nanorod and correspond to pVI and pIII. An interesting feature observed in this model is the presence of densities in parallel with the virion axis at the junction between the filament shaft and the cone of the end-cap, and exposed to the solvent. These densities could be speculated to either represent the C-terminus of protein pVI, that is thought to be exposed on the surface of the virion

(Jespers *et al*., 1995), or one of the polar faces of the amphipathic helices predicted for the C-domain of pIII. The density is unlikely to be derived from pVI, given that this is a mostly hydrophobic protein, with no predicted amphipathic structures large enough to face the aqueous environment. In contrast, the model of the pIII C domain has several predicted hydrophilic and amphipathic helices. One of these has been mapped as being required for phage entry and is suggested to be most likely responsible for the opening of the virion to be inserted in the membrane of the targeted cells during phage infection (Bennett *et al*., 2011). This helix was named "the infection-competence sequence" (ICS) by Bennett *et al*. (2011). The same helix is required to preserve the resistance to detergents of the Ff virion (Rakonjac *et al*., 1999). A shorter pIII C domain fragment lacking the ICS renders the phage sensitive to the ionic detergent sarkosyl, to which the phage containing the ICS are resistant.

Solving the Ff phage pIII-pVI end-cap structure at near-atomic resolution is expected to give a deeper understanding of the life cycle of these viruses. More particularly, to the infection and assembly mechanisms. A deep understanding of the structure of the proteins and their membrane biogenesis is essential for designing nanostructures assembled from the Ff-derived nanorods. The interactions that bind building blocks together during self-assembly need to be understood to enable more precise engineering (Zhang, 2003) and to expand the potential of phage display technology, ensuring efficient and successful protein insertion into the membrane to be utilized for display (Loh *et al*., 2019).

7.1.2 Expanding the potential applications and understanding of the Ff phage-derived nanorods and Ff phage

One of the fields where Ff phage have been widely studied is nanomedicine. Some of their limitations, however, are the possibility of horizontal transfer of antibiotic-resistance-encoding genes and their relatively large size. These features have already been taken into account by Sattar *et al*. (2015) by producing 50 nm in length Ff phage-derived nanorods (Ff-nano). Ff-nano are protein-DNA complexes that cannot replicate independently and contain no coding sequences in contrast to standard Ff-derived vectors that replicate in *E. coli* and contain antibiotic-resistance genes. Besides improving the system for production of short Ff phage-derived-nanorods, as mentioned in the section above, in this thesis strides were made towards expanding their applications by tuning the BSF replication-assembly cassette to produce nanorods of even smaller dimensions. The design of this cassette is informed by several studies that determined the role of the different segments in the Ff origin of replication (Beck *et al*., 1978; Dotto *et al*., 1981; Dotto *et al*., 1984a; Gray *et al*., 1978; Horiuchi, 1997), The importance of some of the DNA segments in this region, however, has not been characterised to date. The results of this study indicate that the DNA segment between the packaging signal and the negative origin of replication, does not have an essential role in replication. Its removal allowed the generation of the shortest phage-derived particles ever produced (40 nm) and decreased the size of the nanorods produced by the BSFpn cassette from 80 to 70 nm.

Being able to tune the nanorod length could aid in many of the size-dependent applications of the Ff phage-derived nanorods. Their nanometre size offers some advantages over longer particles for drug delivery. For example, Desai *et al*. (1996), described a size-dependent exclusion phenomenon in gastrointestinal mucosal tissue particle uptake, which should be taken into account when designing nanoparticle-based oral drug delivery systems (Desai *et al*., 1996). In another study, it was shown that smaller particles are expected to penetrate deep into tissues through fine capillaries and are generally taken up more efficiently by the cells (Panyam & Labhasetwar, 2003). The short nanorods are also expected to diffuse more rapidly in lateral flow diagnostic assays (Barabé *et al*., 2020; Sattar *et al*., 2015). Moreover, ssDNA extracted from the sub-nanometre-scale nanorods has facilitated generation of new scaffolds to expand the space of possible DNA origami designs by drastically reducing the phage DNA that interferes with formation of ssDNA elements (Nafisi *et al*., 2018) to construct new nanoscale structures. Oppositely, increasing the nanorod size could lead to phage being able to settle on the surface of cells, leading to improved transduction efficiency of hybrid-phage delivery carriers (Yata *et al*., 2014). From this, tunning the particle sizes while minimising the phage-derived sequence content is a promising approach to improve the role of phage-derived nanorods based on their desired applications, either to direct different nanomaterials into different cellular pathways (Scheinberg *et al*., 2010), maximize affinity of ligands, construct novel nanostructures, or to develop ssDNA markers that are currently not available in the market.

Several reports published during the course of this study have described a constitutive two-plasmid system for nanorod production. Interestingly, two of those state that the truncated (+) *ori* Δ29 is poor terminator, and that it can initiate replication (Cha *et al*., 2021; Nafisi *et al*., 2018), producing as much as 50% of ssDNA products initiating at (+) *ori2* Δ29. In our experience, however, long ssDNA's that terminate beyond the (+) *ori2* Δ29 are not produced in the template plasmids or pPop-up plasmids containing BSFpn cassette, where the negative *ori* is included. In the BSFp cassette (221 and 152-nt), longer ssDNA is only detected after serial passage of the transformed cells (section 5.2.4, Figure 42). Moreover, Sattar (2013) reported that the rare particles (typically present at a frequency of 10^{-6}) that carry Amp^R gene encoded by the template plasmid, contained a single (+) *ori* that was generated by deletion of the terminator (+) *ori* Δ29. In our system we use *gVIII amber* mutant not only to decrease the amount of pVIII and hence stimulate production of short nanorods, but also to avoid pVIII toxicity during construction and purification of the helper and Pop-up plasmids, and during production of short nanorods. Excess pVIII is known to be toxic to *E. coli*, hence those cells that produce short nanorods and use up less than 10% of produced pVIII. It is expected that full-blown pVIII expression would impose selection for long templates produced in the single-*ori* recombinants. From observations in this study, it could be concluded that the longer DNA reported by Praetorius *et al*. (2017), Nafisi *et al*. (2018), Shepherd *et al*. (2019) and Cha *et al*. (2021), is likely due to the combination selective pressure for those templates that use up most of the produced pVIII in the cells, and recombination that eliminates the (+) *ori Δ29*. It is of note that the template described by Cha *et al*. (2021) does not have a (-) *ori* and hence is an equivalent to BSFp, which in our hands results in ~ 10-fold lower nanorod

production in comparison to the BSFpn templates, and ~50-fold lower than inducible-replication BSFpn-cassette systems. For example, recombination is observable after several passages in our BSFp single-plasmid system (pPop-up221; Figure 42), but not in the BSFpn pPop-up529 system (Figure 38). Nafisi *et al*. (2018) showed that deletions of sequences within (+) *ori1* and (+) *ori2* Δ29 majorly decreased the longer ssDNA products. This suggested that including these deletions could stabilise our single-plasmid BSFp system (pPop-up221, pPop-upLac221 and pPop-upLac152).

Ff phage have been pursued over the past 20 years as therapeutical agents themselves. It was shown that they could disaggregate misfolded proteins, which are thought to be one of the causes of neurological diseases, such as Alzheimer's and Parkinson's diseases, making the Ff phage a promising therapeutic candidate (Sohrab *et al*., 2014; Solomon, 2008). Based on their potential, gathering more information on the role of their different proteins and protein domains involved in this disaggregating action would aid in their ongoing research. The whole Ff phage or the pIII N1N2 domains shown to have the ability to bind and dissociate β-amyloid plaques Solomon and Goren (2011), while the Ff phage with enzymatically removed pIII N1N2 domains were shown to bind and disaggregate β-amyloid fibres, albeit at a diminished level (Krishnan, 2014; Krishnan *et al*., 2014). Work in this thesis, using Ff phage mutant particles lacking N1N2 domain, showed that, in the absence of these domains, Ff lost the ability to bind β-amyloid fibres. This experiment, therefore, showed that only the N1N2 domains of pIII are responsible for binding β-amyloid fibres, and by extension, their disaggregation. From this, any

therapeutic candidates derived from the Ff phage should focus only on the N1 and N2 domains of pIII.

7.2 Conclusions

Despite their extensive use, there are many unresolved questions about Ff phage. This study set out to further characterize Ff phage biology and structure, and broaden the scope of possible Ff phage-derived applications. The achievements of this study are:

i. The development of a novel system for the rapid and efficient production of Ff phage-derived nanorods that could be used in many applications requiring short (<100 nm) monodisperse nanorods. Combining all the elements required for nanorod production onto one plasmid with the expression of the gene encoding for the replication protein pII controlled by an inducible promoter (*LacUV5*) achieved both, a reduction in the production time and an enhancement in the amount of Ff phage-derived-nanorods produced by 200-fold.

ii. The development of an improved system for production of short nanorods allowed reconstruction of a 3D molecular model of the Ff phage pIII-pVI end-cap at nearly 5 Å resolution. To date, there are no models of the Ff end structure; hence, this model is a first glimpse of the pIII-pVI end-cap structure. Once refined to near-atomic resolution, this model will help elucidate the termination of assembly and release of the Ff phage from *E. coli* membranes and the mechanism of entry into the host cell. This will

finally allow a complete understanding of the Ff phage life cycle and, in turn, will help to improve the Ff phage-derived applications that may involve designing of, e.g., 3D nanostructures built from the Ff-derived nanorods.

iii. Finding that the DNA segments between various functional elements in the Ff origin of replication are not required for replication and can therefore be removed to further shorten the replication-assembly cassettes. This knowledge allowed the production of the shortest ever Ff-derived nanorods, 40 nm in length.

iv. Refuted the assumption that the pIII C domain and the body of the Ff filament have a role in Ff-β-amyloid fibre-binding and, by derivation, disaggregation of the amyloid plaque.

7.3 Future directions

The nanorods produced in this study are the only approach to date that has provided a pathway for solving the structure of the filament end-caps of Ff phage. The methodology used also represents a powerful alternative to full-length phages or long phagemid particles for almost every Ff phage-derived application. This is because they are safer than wild type phage due to the lack of antibiotic resistance genes, and because of the ability to precisely tune their length. The inducible production system achieves a high production level of nearly 5 x 10^{15} nanorods per L, thereby helping to keep the production costs low, an essential characteristic for the construction of nanomaterials. Besides their anisotropic shape and monodispersity as a result of their high-fidelity biological reproduction, Ff phage-derived nanorods also have shown to exhibit liquid-crystalline properties, which allows the formation of ordered structures (Yang *et al*., 2013), giving rise to their use as a model system in soft matter physics (Dogic, 2016). The tuneable length and physical properties described for the nanorods produced in this thesis is an attractive feature for application in soft matter physics. For example, these nanorods could be used in the study on how rotational dynamics of rods in the isotropic phase scales with their length (Dogic, 2016; Maguire *et al*., 1980), the effect of the nanorod length in phase transitions (i.e., isotropic-nematic) (Dogic, 2016; Dogic & Fraden, 2001), and in studies of colloidal membranes, to investigate the effect of different nanorod lengths on the stability of colloidal clusters (Dogic, 2016; Sharma *et al*., 2014). In the future, crystallization of the nanorods described in this thesis may be used as models in soft matter physics and for X-ray crystallographic studies.

Obtaining an atomic-resolution model of the structure of the Ff phage end-caps by X-ray crystallography is planned and will aid understanding the entry and termination of infection. It will also provide knowledge about the unique processes and interactions by which supramolecular architectures are assembled. While this study allowed the determination of a preliminary cryo-EM 3D model for the structure of the pIII-pVI end-cap of the Ff phage virion, deducing a model at near-atomic resolution is in progress at University of Exeter.

To confirm and aid in location of pIII domains within the 3D model of the pIII-pVI end-cap, it is planned to generate site-specific tags at key residues of pIII that will be detectable by TEM of avidin-gold-labelled nanorods and cryo-EM, to help in assigning specific structures to the sequences despite the relatively low resolution. Introducing site-specific labels (e.g., avidin-binding peptide) in pIII would allow labelling the position of its different domains in the virion cap that could be detectable by cryo-EM.

It was not possible to distinguish the N1 and N2 domains of pIII, in the end-cap model. The atomic-resolution structure of the N1N2 domain has been solved, demonstrating that these two sub-domains fold into a globular domain tethered to the pIII C domain and the rest of the virion via glycine-rich linker (Eckert & Schmid, 2007; Lubkowski *et al*., 1998). N1 and N2 likely correspond to the "knots" or "balls (Gray *et al*., 1981) tethered to the C domain and the rest of the virion via a long glycine-rich linker. The removal of these domains by digesting the virion with subtilisin or by assembling nanorods from plasmids encoding only the pIII C

domain followed by Cryo-EM SPA analysis will help determine whether N1N2 domains are present in the current model of the end-caps and allow the identification of the pIII C domain and pVI in it. Finally, analyses of nanorods containing nested deletions in the pIII C domain will allow structure-function assignments of pIII C domain in the end-cap to aid structural analyses.

References

Abramov, G., Shaharabani, R., Morag, O., Avinery, R., Haimovich, A., Oz, I., . . . Goldbourt, A. (2017). Structural Effects of Single Mutations in a Filamentous Viral Capsid Across Multiple Length Scales. *Biomacromolecules, 18*(8), 2258-2266. doi:10.1021/acs.biomac.7b00125

Aebi, U., ten Heggeler, B., Onorato, L., Kistler, J., & Showe, M. K. (1977). New method for localizing proteins in periodic structures: Fab fragment labeling combined with image processing of electron micrographs. *Proceedings of the National Academy of Sciences of the United States of America, 74*(12), 5514-5518. doi:10.1073/pnas.74.12.5514

Armstrong, J., Hewitt, J. A., & Perham, R. N. (1983). Chemical modification of the coat protein in bacteriophage fd and orientation of the virion during assembly and disassembly. *The EMBO journal, 2*(10), 1641-1646.

Asano, S., Higashitani, A., & Horiuchi, K. (1999). Filamentous phage replication initiator protein gpII forms a covalent complex with the 5' end of the nick it introduced. *Nucleic Acids Research, 27*(8), 1882-1889.

Asp, E., Proschitsky, M., Lulu, M., Rockwell-Postel, C., Tsubery, H., & Krishnan, R. (2019). Stability and Inter-domain Interactions Modulate Amyloid Binding Activity of a General Amyloid Interaction Motif. *Journal of Molecular Biology, 431*(10), 1920-1939. doi:10.1016/j.jmb.2019.03.022

Bakhshinejad, B., Karimi, M., & Sadeghizadeh, M. (2014). Bacteriophages and medical oncology: targeted gene therapy of cancer. *Medical Oncology (Northwood, London, England), 31*(8), 110. doi:10.1007/s12032-014-0110-9

Barabé, B., Abakumov, S., Gunes, D. Z., & Lettinga, M. P. (2020). Sedimentation of large particles in a suspension of colloidal rods. *Physics of Fluids, 32*(5), 053105. doi:10.1063/5.0006076

Barbas, C. F., Burton, D. R., Scott, J. K. & Silverman, G. J. (2001). Phage Display: A Laboratory Manual. . *The Quarterly Review of Biology, 76*(4), 487-488. doi:10.1086/420571

Beck, E., Sommer, R., Auerswald, E. A., Kurz, C., Zink, B., Osterburg, G., . . . Takanami, M. (1978). Nucleotide sequence of bacteriophage fd DNA. *Nucleic Acids Research, 5*(12), 4495-4503. doi:10.1093/nar/5.12.4495

Bennett, N. J. (2010). *Unlocking the M13 (f1 and fd) virion : investigation into the role of the pIII C-domain of F specific filamentous bacteriophage in infection : a thesis presented in partial fulfilment of the requirements for the degree of Doctor of Philosophy in Biochemistry at Massey University, Palmerston North, New Zealand*. (Doctor of Philosophy (Ph.D.) Doctoral), Massey University. Retrieved from http://hdl.handle.net/10179/1221

Bennett, N. J., Gagic, D., Sutherland-Smith, A. J., & Rakonjac, J. (2011). Characterization of a Dual-Function Domain That Mediates Membrane Insertion and Excision of Ff Filamentous Bacteriophage. *Journal of Molecular Biology, 411*(5), 972-985. doi:10.1016/j.jmb.2011.07.002

Bennett, N. J., & Rakonjac, J. (2006). Unlocking of the filamentous bacteriophage virion during infection is mediated by the C domain of pIII. *Journal of Molecular Biology, 356*(2), 266-273. doi:10.1016/j.jmb.2005.11.069

Biancalana, M., & Koide, S. (2010). Molecular mechanism of Thioflavin-T binding to amyloid fibrils. *Biochimica et Biophysica Acta (BBA) 1804*(7), 1405-1412. doi:10.1016/j.bbapap.2010.04.001

Bobo, D., Robinson, K. J., Islam, J., Thurecht, K. J., & Corrie, S. R. (2016). Nanoparticle-Based Medicines: A Review of FDA-Approved Materials and Clinical Trials to Date. *Pharmaceutical Research, 33*(10), 2373-2387. doi:10.1007/s11095-016-1958-5

Bourhim, M., Kruzel, M., Srikrishnan, T., & Nicotera, T. (2007). Linear quantitation of Aβ aggregation using Thioflavin T: Reduction in fibril formation by colostrinin. *Journal of Neuroscience Methods, 160*(2), 264-268. doi:10.1016/j.jneumeth.2006.09.013

Buhle, E. L., & Aebi, U. (1984). Specific labeling of protein domains with antibody fragments. *Journal of Ultrastructure Research, 89*(2), 165-178. doi:10.1016/S0022-5320(84)80012-X

Cao, B., Li, Y., Yang, T., Bao, Q., Yang, M., & Mao, C. (2019). Bacteriophage-based biomaterials for tissue regeneration. *Advanced Drug Delivery Reviews, 145*, 73-95. doi:10.1016/j.addr.2018.11.004

Carpenter, E. P., Beis, K., Cameron, A. D., & Iwata, S. (2008). Overcoming the challenges of membrane protein crystallography. *Current Opinion in Structural Biology, 18*(5), 581-586. doi:10.1016/j.sbi.2008.07.001

Carroni, M., & Saibil, H. R. (2016). Cryo electron microscopy to determine the structure of macromolecular complexes. *Methods (San Diego, Calif.), 95*, 78-85. doi:10.1016/j.ymeth.2015.11.023

Carter, P., Bedouelle, H., & Winter, G. (1985). Improved oligonucleotide site-directed mutagenesis using M13 vectors. *Nucleic Acids Research, 13*(12), 4431-4443. doi:10.1093/nar/13.12.4431

Caspar, D. L. D., & Makowski, L. (1981). The symmetries of filamentous phage particles. *Journal of Molecular Biology, 145*(3), 611-617. doi:10.1016/0022-2836(81)90549-0

Cha, T.-G., Tsedev, U., Ransil, A., Embree, A., Gordon, D. B., Belcher, A. M., & Voigt, C. A. (2021). Genetic Control of Aerogel and Nanofoam Properties, Applied to Ni–MnOx Cathode Design. *Advanced Functional Materials, 31*(35), 2010867. doi:10.1002/adfm.202010867

Chatellier, J., Hartley, O., Griffiths, A. D., Fersht, A. R., Winter, G., & Riechmann, L. (1999). Interdomain interactions within the gene 3 protein of filamentous phage. *FEBS Letters, 463*(3), 371-374. doi:10.1016/S0014-5793(99)01658-0

Cheng, B., Gong, H., Xiao, H., Petersen, R. B., Zheng, L., & Huang, K. (2013). Inhibiting toxic aggregation of amyloidogenic proteins: A therapeutic strategy for protein misfolding diseases. *Biochimica et Biophysica Acta (BBA) - General Subjects, 1830*(10), 4860-4871. doi:10.1016/j.bbagen.2013.06.029

Cheng, Y. (2015). Single-Particle Cryo-EM at Crystallographic Resolution. *Cell, 161*(3), 450-457. doi:10.1016/j.cell.2015.03.049

Choe, S., Bennett, M. J., Fujii, G., Curmi, P. M., Kantardjieff, K. A., Collier, R. J., & Eisenberg, D. (1992). The crystal structure of diphtheria toxin. *Nature, 357*(6375), 216-222. doi:10.1038/357216a0

Chopin, M. C., Rouault, A., Ehrlich, S. D., & Gautier, M. (2002). Filamentous phage active on the gram-positive bacterium *Propionibacterium freudenreichii*. *Journal of Bacteriology, 184*(7), 2030-2033.

Chung, W.-J., Lee, D.-Y., & Yoo, S. Y. (2014). Chemical modulation of M13 bacteriophage and its functional opportunities for nanomedicine. *International Journal of Nanomedicine, 9*, 5825-5836. doi:10.2147/IJN.S73883

Click, E. M., & Webster, R. E. (1998). The TolQRA Proteins Are Required for Membrane Insertion of the Major Capsid Protein of the Filamentous Phage f1 during Infection. *Journal of Bacteriology, 180*(7), 1723-1728.

Coskun, O. (2016). Separation techniques: Chromatography. *Northern clinics of Istanbul, 3*(2), 156-160. doi:10.14744/nci.2016.32757

Danev, R., Yanagisawa, H., & Kikkawa, M. (2019). Cryo-Electron Microscopy Methodology: Current Aspects and Future Directions. *Trends in Biochemical Sciences, 44*(10), 837-848. doi:10.1016/j.tibs.2019.04.008

Davis, N. G., Boeke, J. D., & Model, P. (1985). Fine structure of a membrane anchor domain. *Journal of Molecular Biology, 181*(1), 111-121. doi:10.1016/0022-2836(85)90329-8

Day, L. A. (2012). Family - Inoviridae. In A. M. Q. King, M. J. Adams, E. B. Carstens, & E. J. Lefkowitz (Eds.), *Virus Taxonomy* (pp. 375-383). San Diego: Elsevier.

Day, L. A., Wiseman, R. L., & Marzec, C. J. (1979). Structure models for DNA in filamentous viruses with phosphates near the center. *Nucleic Acids Research, 7*(6), 1393-1403. doi:10.1093/nar/7.6.1393

DePorter, S. M., & McNaughton, B. R. (2014). Engineered M13 Bacteriophage Nanocarriers for Intracellular Delivery of Exogenous Proteins to Human Prostate Cancer Cells. *Bioconjugate Chemistry, 25*(9), 1620-1625. doi:10.1021/bc500339k

Desai, M. P., Labhasetwar, V., Amidon, G. L., & Levy, R. J. (1996). Gastrointestinal uptake of biodegradable microparticles: effect of particle size. *Pharmaceutical Research, 13*(12), 1838-1845. doi:10.1023/a:1016085108889

Dimant, H., Sharon, N., & Solomon, B. (2009). Modulation effect of filamentous phage on alpha-synuclein aggregation. *Biochemical and Biophysical Research Communications, 383*(4), 491-496. doi:10.1016/j.bbrc.2009.04.048

Dimant, H., & Solomon, B. (2010). Filamentous phages reduce alpha-synuclein oligomerization in the membrane fraction of SH-SY5Y cells. *Neuro-degenerative Diseases, 7*(1-3), 203-205. doi:10.1159/000295664

Dion, M. B., Oechslin, F., & Moineau, S. (2020). Phage diversity, genomics and phylogeny. *Nature Reviews Microbiology, 18*(3), 125-138. doi:10.1038/s41579-019-0311-5

Dogic, Z. (2016). Filamentous Phages As a Model System in Soft Matter Physics. *Frontiers in Microbiology, 7*(1013). doi:10.3389/fmicb.2016.01013

Dogic, Z., & Fraden, S. (2001). Development of model colloidal liquid crystals and the kinetics of the isotropic–smectic transition. *Philosophical Transactions*

of the Royal Society of London. Series A: Mathematical, Physical and Engineering Sciences, 359(1782), 997-1015. doi:10.1098/rsta.2000.0814

Dotto, G. P., Enea, V., & Zinderi, N. D. (1981). Functional analysis of bacteriophage f1 intergenic region. *Virology, 114*(2), 463-473. doi:10.1016/0042-6822(81)90226-9

Dotto, G. P., & Horiuchi, K. (1981). Replication of a plasmid containing two origins of bacteriophage f1. *Journal of Molecular Biology, 153*(1), 169-176. doi:10.1016/0022-2836(81)90532-5

Dotto, G. P., Horiuchi, K., & Zinder, N. D. (1984a). The functional origin of bacteriophage f1 DNA replication. Its signals and domains. *Journal of Molecular Biology, 172*(4), 507-521. doi:10.1016/s0022-2836(84)80020-0

Dotto, G. P., Horiuchi, K., & Zinder, N. D. (1984b). The origin of DNA replication of bacteriophage f1 and its interaction with the phage gene II protein. *Advances in experimental medicine and biology, 179*, 185-191.

Dotto, G. P., & Zinder, N. D. (1984). Reduction of the minimal sequence for initiation of DNA synthesis by qualitative or quantitative changes of an initiator protein. *Nature, 311*(5983), 279-280. doi:10.1038/311279a0

Dunker, A. K., Ensign, L. D., Arnold, G. E., & Roberts, L. M. (1991). A model for fd phage penetration and assembly. *FEBS Letters, 292*(1), 271-274. doi:10.1016/0014-5793(91)80882-4

Eckert, B., & Schmid, F. X. (2007). A conformational unfolding reaction activates phage fd for the infection of Escherichia coli. *Journal of Molecular Biology, 373*(2), 452-461. doi:10.1016/j.jmb.2007.07.060

Endemann, H., & Model, P. (1995). Lcoation of Filamentous Phage Minor Coat Proteins in Phage and in Infected Cells. *Journal of Molecular Biology, 250*(4), 496-506. doi:10.1006/jmbi.1995.0393

Enea, V., Horiuchi, K., Turgeon, B. G., & Zinder, N. D. (1977). Physical map of defective interfering particles of bacteriophage f1. *Journal of Molecular Biology, 111*(4), 395-414. doi:10.1016/S0022-2836(77)80061-2

Enea, V., & Zinder, N. D. (1982). Interference resistant mutants of phage f1. *Virology, 122*(1), 222-226. doi:10.1016/0042-6822(82)90395-6

Estrada, L. D., & Soto, C. (2007). Disrupting beta-amyloid aggregation for Alzheimer disease treatment. *Current topics in medicinal chemistry, 7*(1), 115-126.

Feng, J. N., Model, P., & Russel, M. (1999). A trans-envelope protein complex needed for filamentous phage assembly and export. *Molecular Microbiology, 34*(4), 745-755. doi:10.1046/j.1365-2958.1999.01636.x

Feng, J. N., Russel, M., & Model, P. (1997). A permeabilized cell system that assembles filamentous bacteriophage. *Proceedings of the National Academy of Sciences of the United States of America, 94*(8), 4068-4073. doi:10.1073/pnas.94.8.4068

Fouladvand, F., Bemani, P., Mohammadi, M., Amini, R., & Azizi Jalilian, F. (2020). A Review of the Methods for Concentrating M13 Phage. *Journal of Applied Biotechnology Reports, 7*(1), 7-15. doi:10.30491/jabr.2020.105916

Fuh, G., & Sidhu, S. S. (2000). Efficient phage display of polypeptides fused to the carboxy-terminus of the M13 gene-3 minor coat protein. *FEBS Letters, 480*(2), 231-234. doi:10.1016/S0014-5793(00)01946-3

Fulford, W., & Model, P. (1984). Gene X of bacteriophage f1 is required for phage DNA synthesis: Mutagenesis of in-frame overlapping genes. *Journal of Molecular Biology, 178*(2), 137-153. doi:10.1016/0022-2836(84)90136-0

Fulford, W., & Model, P. (1988). Regulation of bacteriophage f1 DNA replication: I. New functions for genes II and X. *Journal of Molecular Biology, 203*(1), 49-62. doi:10.1016/0022-2836(88)90090-3

Gailus, V., & Rasched, I. (1994). The adsorption protein of bacteriophage fd and its neighbour minor coat protein build a structural entity. *European Journal of Biochemistry, 222*(3), 927-931.

Geider, K., Bäumel, I., & Meyer, T. F. (1982). Intermediate stages in enzymatic replication of bacteriophage fd duplex DNA. *Journal of Biological Chemistry, 257*(11), 6488-6493.

Gerding, M. A., Ogata, Y., Pecora, N. D., Niki, H., & de Boer, P. A. J. (2007). The trans-envelope Tol-Pal complex is part of the cell division machinery and required for proper outer-membrane invagination during cell constriction in *E. coli*. *Molecular Microbiology, 63*(4), 1008-1025. doi:10.1111/j.1365-2958.2006.05571.x

Ghosh, D., Kohli, A. G., Moser, F., Endy, D., & Belcher, A. M. (2012). Refactored M13 bacteriophage as a platform for tumor cell imaging and drug delivery. *ACS Synthetic Biology, 1*(12), 576-582. doi:10.1021/sb300052u

Glaser-Wuttke, G., Keppner, J., & Rasched, I. (1989). Pore-forming properties of the adsorption protein of filamentous phage fd. *Biochimica et Biophysica Acta (BBA) - Biomembranes, 985*(3), 239-247. doi:10.1016/0005-2736(89)90408-2

Goldbourt, A., Gross, B. J., Day, L. A., & McDermott, A. E. (2007). Filamentous phage studied by magic-angle spinning NMR: resonance assignment and secondary structure of the coat protein in Pf1. *Journal of the American Chemical Society, 129*(8), 2338-2344. doi:10.1021/ja066928u

Grant, R. A., Lin, T. C., Konigsberg, W., & Webster, R. E. (1981). Structure of the filamentous bacteriophage fl. Location of the A, C, and D minor coat proteins. *Journal of Biological Chemistry, 256*(1), 539-546.

Grant, R. A., Lin, T. C., Webster, R. E., & Konigsberg, W. (1981). Structure of filamentous bacteriophage: isolation, characterization, and localization of the minor coat proteins and orientation of the DNA. *Progress in Clinical and Biological Research, 64*, 413-428.

Gray, C., Brown, R., & Marvin, D. (1979). *Direct visualization of adsorption protein of fd phage*. Paper presented at the Journal Of Supramolecular Structure.

Gray, C. P., Sommer, R., Polke, C., Beck, E., & Schaller, H. (1978). Structure of the orgin of DNA replication of bacteriophage fd. *Proceedings of the National Academy of Sciences of the United States of America, 75*(1), 50-53. doi:10.1073/pnas.75.1.50

Gray, C. W., Brown, R. S., & Marvin, D. A. (1981). Adsorption complex of filamentous fd virus. *Journal of Molecular Biology, 146*(4), 621-627. doi:10.1016/0022-2836(81)90050-4

Greenstein, D., & Horiuchi, K. (1987). Interaction between the replication origin and the initiator protein of the filamentous phage f1. Binding occurs in two steps. *Journal of Molecular Biology, 197*(2), 157-174. doi:10.1016/0022-2836(87)90115-x

Griffith, J., & Kornberg, A. (1974). Mini M13 bacteriophage: Circular fragments of M13 DNA are replicated and packaged during normal infections. *Virology, 59*(1), 139-152. doi:10.1016/0042-6822(74)90211-6

Griffith, J., Manning, M., & Dunn, K. (1981). Filamentous bacteriophage contract into hollow spherical particles upon exposure to a chloroform-water interface. *Cell, 23*(3), 747-753. doi:10.1016/0092-8674(81)90438-4

Grodzinski, P., Kircher, M., Goldberg, M., & Gabizon, A. (2019). Integrating Nanotechnology into Cancer Care. *ACS Nano, 13*(7), 7370-7376. doi:10.1021/acsnano.9b04266

Guan, Y., Zhang, H., & Wang, A. H. (1995). Electrostatic potential distribution of the gene V protein from Ff phage facilitates cooperative DNA binding: a model of the GVP-ssDNA complex. *Protein science : a publication of the Protein Society, 4*(2), 187-197. doi:10.1002/pro.5560040206

Gulati, N. M., Torian, U., Gallagher, J. R., & Harris, A. K. (2019). Immunoelectron Microscopy of Viral Antigens. *Current Protocols in Microbiology, 53*(1), e86. doi:10.1002/cpmc.86

Hay, I. D., & Lithgow, T. (2019). Filamentous phages: masters of a microbial sharing economy. *EMBO Reports, 20*(6). doi:10.15252/embr.201847427

Heilpern, A. J., & Waldor, M. K. (2000). CTXphi infection of Vibrio cholerae requires the tolQRA gene products. *Journal of Bacteriology, 182*(6), 1739-1747. doi:10.1128/jb.182.6.1739-1747.2000

Held, H. A., & Sidhu, S. S. (2004). Comprehensive Mutational Analysis of the M13 Major Coat Protein: Improved Scaffolds for C-terminal Phage Display. *Journal of Molecular Biology, 340*(3), 587-597. doi:10.1016/j.jmb.2004.04.060

Hemminga, M. A., Vos, W. L., Nazarov, P. V., Koehorst, R. B. M., Wolfs, C. J. A. M., Spruijt, R. B., & Stopar, D. (2010). Viruses: incredible nanomachines. New advances with filamentous phages. *European Biophysics Journal, 39*(4), 541-550. doi:10.1007/s00249-009-0523-0

Henry, K. A., Arbabi-Ghahroudi, M., & Scott, J. K. (2015). Beyond phage display: non-traditional applications of the filamentous bacteriophage as a vaccine carrier, therapeutic biologic, and bioconjugation scaffold. *Frontiers in Microbiology, 6*(755). doi:10.3389/fmicb.2015.00755

Henry, M., & Debarbieux, L. (2012). Tools from viruses: bacteriophage successes and beyond. *Virology, 434*(2), 151-161. doi:10.1016/j.virol.2012.09.017

Higashitani, N., Higashitani, A., & Horiuchi, K. (1993). Nucleotide sequence of the primer RNA for DNA replication of filamentous bacteriophages. *Journal of Virology, 67*(4), 2175-2181.

Holliger, P., & Riechmann, L. (1997). A conserved infection pathway for filamentous bacteriophages is suggested by the structure of the membrane penetration domain of the minor coat protein g3p from phage fd. *Structure, 5*(2), 265-275. doi:10.1016/s0969-2126(97)00184-6

Holliger, P., Riechmann, L., & Williams, R. L. (1999). Crystal structure of the two N-terminal domains of g3p from filamentous phage fd at 1.9 A: evidence for conformational lability. *Journal of Molecular Biology, 288*(4), 649-657. doi:10.1006/jmbi.1999.2720

Horiuchi, K. (1997). Initiation mechanisms in replication of filamentous phage DNA. *Genes Cells, 2*(7), 425-432.

Horiuchi, K., Vovis, G. F., Enea, V., & Zinder, N. D. (1975). Cleavage map of bacteriophage f1: Location of the *Escherichia coli* B-specific modification sites. *Journal of Molecular Biology, 95*(2), 147-165. doi:10.1016/0022-2836(75)90388-5

Horiuchi, K., & Zinder, N. D. (1976). Origin and Direction of Synthesis of Bacteriophage f1 DNA. *Proceedings of the National Academy of Sciences of the United States of America, 73*(7), 2341-2345.

Høydahl, L. S., Nilssen, N. R., Gunnarsen, K. S., Pré, M. F. d., Iversen, R., Roos, N., . . . Løset, G. Å. (2016). Multivalent pIX phage display selects for distinct and improved antibody properties. *Scientific Reports, 6*(1), 39066. doi:10.1038/srep39066

Huang, L.-K., Chao, S.-P., & Hu, C.-J. (2020). Clinical trials of new drugs for Alzheimer disease. *Journal of Biomedical Science, 27*(1), 18-18. doi:10.1186/s12929-019-0609-7

Huh, H., Wong, S., St Jean, J., & Slavcev, R. (2019). Bacteriophage interactions with mammalian tissue: Therapeutic applications. *Advanced Drug Delivery Reviews, 145*, 4-17. doi:10.1016/j.addr.2019.01.003

Hung, S.-Y., & Fu, W.-M. (2017). Drug candidates in clinical trials for Alzheimer's disease. *Journal of Biomedical Science, 24*(1), 47-47. doi:10.1186/s12929-017-0355-7

Iannolo, G., Minenkova, O., Petruzzelli, R., & Cesareni, G. (1995). Modifying Filamentous Phage Capsid: Limits in the Size of the Major Capsid Protein. *Journal of Molecular Biology, 248*(4), 835-844. doi:10.1006/jmbi.1995.0264

Ikehara, K., Utiyama, H., & Kurata, M. (1975). Studies on the structure of filamentous bacteriophage fd: II. All-or-none disassembly in guanidine-HCl and sodium dodecyl sulfate. *Virology, 66*(1), 306-315. doi:10.1016/0042-6822(75)90200-7

Jacinto, M. J., Patinha, D. J. S., Marrucho, I. M., Gonçalves, J., Willson, R. C., Azevedo, A. M., & Aires-Barros, M. R. (2018). M13 bacteriophage purification using poly(ionic liquids) as alternative separation matrices. *Journal of Chromatography A, 1532*, 246-250. doi:10.1016/j.chroma.2017.12.005

Jacob, E., & Hofschneider, P. H. (1969). Replication of the single-stranded DNA bacteriophage M13: Messenger RNA synthesis directed by M13 replicative form DNA. *Journal of Molecular Biology, 46*(2), 359-363. doi:10.1016/0022-2836(69)90429-X

Jespers, L. S., Messens, J. H., Keyser, A. D., Eeckhout, D., Brande, I. V. D., Gansemans, Y. G., . . . Stanssens, P. E. (1995). Surface Expression and Ligand-Based Selection of cDNAs Fused to Filamentous Phage Gene VI. *Bio/Technology, 13*(4), 378-382. doi:10.1038/nbt0495-378

Jończyk, E., Kłak, M., Międzybrodzki, R., & Górski, A. (2011). The influence of external factors on bacteriophages--review. *Folia microbiologica, 56*(3), 191-200. doi:10.1007/s12223-011-0039-8

Ju, Z., & Sun, W. (2017). Drug delivery vectors based on filamentous bacteriophages and phage-mimetic nanoparticles. *Drug Delivery, 24*(1), 1898-1908. doi:10.1080/10717544.2017.1410259

Karimi, M., Mirshekari, H., Moosavi Basri, S. M., Bahrami, S., Moghoofei, M., & Hamblin, M. R. (2016). Bacteriophages and phage-inspired nanocarriers for

targeted delivery of therapeutic cargos. *Advanced Drug Delivery Reviews, 106*(Pt A), 45-62. doi:10.1016/j.addr.2016.03.003

Kashino, Y. (2003). Separation methods in the analysis of protein membrane complexes. *Journal of Chromatography B, 797*(1), 191-216. doi:10.1016/S1570-0232(03)00428-8

Kaushik, A., Jayant, R. D., Bhardwaj, V., & Nair, M. (2018). Personalized nanomedicine for CNS diseases. *Drug Discovery Today, 23*(5), 1007-1015. doi:10.1016/j.drudis.2017.11.010

Kim, A. Y., & Blaschek, H. P. (1991). Isolation and characterization of a filamentous viruslike particle from *Clostridium acetobutylicum* NCIB 6444. *Journal of Bacteriology, 173*(2), 530-535. doi:10.1128/jb.173.2.530-535.1991

Kim, J., Adhikari, M., Dhamane, S., Hagström, A. E. V., Kourentzi, K., Strych, U., . . . Conrad, J. C. (2015). Detection of Viruses By Counting Single Fluorescent Genetically Biotinylated Reporter Immunophage Using a Lateral Flow Assay. *ACS Applied Materials & Interfaces, 7*(4), 2891-2898. doi:10.1021/am5082556

Kim, M. H., Hines, J. C., & Ray, D. S. (1981). Viable deletions of the M13 complementary strand origin. *Proceedings of the National Academy of Sciences of the United States of America, 78*(11), 6784-6788. doi:10.1073/pnas.78.11.6784

Kokoska, R. J., & Steege, D. A. (1998). Appropriate expression of filamentous phage f1 DNA replication genes II and X requires RNase E-dependent processing and separate mRNAs. *Journal of Bacteriology, 180*(12), 3245-3249.

Korotkov, K. V., Pardon, E., Steyaert, J., & Hol, W. G. J. (2009). Crystal structure of the N-terminal domain of the secretin GspD from ETEC determined with the assistance of a nanobody. *Structure (London, England : 1993), 17*(2), 255-265. doi:10.1016/j.str.2008.11.011

Kramberger, P., Honour, R. C., Herman, R. E., Smrekar, F., & Peterka, M. (2010). Purification of the *Staphylococcus aureus* bacteriophages VDX-10 on methacrylate monoliths. *Journal of Virological Methods, 166*(1-2), 60-64. doi:10.1016/j.jviromet.2010.02.020

Krebber, A., Burmester, J., & Plückthun, A. (1996). Inclusion of an upstream transcriptional terminator in phage display vectors abolishes background expression of toxic fusions with coat protein g3p. *Gene, 178*(1), 71-74. doi:10.1016/0378-1119(96)00337-X

Kremser, A., & Rasched, I. (1994). The adsorption protein of filamentous phage fd: assignment of its disulfide bridges and identification of the domain incorporated in the coat. *Biochemistry, 33*(46), 13954-13958. doi:10.1021/bi00250a051

Krishnan, R. (2014).*Use of P3 bacteriophage fusion proteins as amyloid binding agents*. U.S. PCT/US2013/062862.

Krishnan, R., Tsubery, H., Proschitsky, M. Y., Asp, E., Lulu, M., Gilead, S., . . . Fisher, R. A. (2014). A Bacteriophage Capsid Protein Provides a General Amyloid Interaction Motif (GAIM) That Binds and Remodels Misfolded Protein Assemblies. *Journal of Molecular Biology, 426*(13), 2500-2519. doi:10.1016/j.jmb.2014.04.015

Krogh, A., Larsson, B., von Heijne, G., & Sonnhammer, E. L. (2001). Predicting transmembrane protein topology with a hidden Markov model: application to complete genomes. *Journal of Molecular Biology, 305*(3), 567-580. doi:10.1006/jmbi.2000.4315

Ksendzovsky, A., Walbridge, S., Saunders, R. C., Asthagiri, A. R., Heiss, J. D., & Lonser, R. R. (2012). Convection-enhanced delivery of M13 bacteriophage to the brain. *Journal of Neurosurgery, 117*(2), 197-203. doi:10.3171/2012.4.Jns111528

La Farina, M., Izzo, V., Duro, G., Barbieri, R., Costa, M. A., & Mutolo, V. (1987). Intragenomic recombination between homologous regions of genes II and IV promotes formation of bacteriophage f1 miniphages. *Nucleic Acids Research, 15*(17), 7190-7190. doi:10.1093/nar/15.17.7190

Laemmli, U. K. (1970). Cleavage of structural proteins during the assembly of the head of bacteriophage T4. *Nature, 227*(5259), 680-685.

Lake, J. A., & Kahan, L. (1975). Ribosomal proteins S5, S11, S13 and S19 localized by electron microscopy of antibody-labeled subunits. *Journal of Molecular Biology, 99*(4), 631-644. doi:10.1016/s0022-2836(75)80177-x

Lee, S. W., Mao, C., Flynn, C. E., & Belcher, A. M. (2002). Ordering of quantum dots using genetically engineered viruses. *Science, 296*(5569), 892-895. doi:10.1126/science.1068054

Lerner, T. J., & Model, P. (1981). The "steady state" of coliphage f1: DNA synthesis late in infection. *Virology, 115*(2), 282-294. doi:10.1016/0042-6822(81)90111-2

Levenson, J. M., Schroeter, S., Carroll, J. C., Cullen, V., Asp, E., Proschitsky, M., . . . Gannon, K. S. (2016). NPT088 reduces both amyloid-β and tau pathologies in transgenic mice. *Alzheimer's & dementia (New York, N. Y.), 2*(3), 141-155. doi:10.1016/j.trci.2016.06.004

Li, Y.-J., Wu, J.-Y., Wang, J.-M., & Xiang, D.-X. (2020). Emerging nanomedicine-based strategies for preventing metastasis of pancreatic cancer. *Journal of Controlled Release, 320*, 105-111. doi:10.1016/j.jconrel.2020.01.041

Ling, T. C., Loong, C. K., Tan, W. S., Tey, B. T., Abdullah, W. M., & Ariff, A. (2004). Purification of filamentous bacteriophage M13 by expanded bed anion exchange chromatography. *Journal of Microbiology (Seoul, Korea), 42*(3), 228-232.

Loh, B., Kuhn, A., & Leptihn, S. (2019). The fascinating biology behind phage display: filamentous phage assembly. *Molecular Microbiology, 111*(5), 1132-1138. doi:10.1111/mmi.14187

Lopez, J., & Webster, R. E. (1982). Minor coat protein composition and location of the A protein in bacteriophage f1 spheroids and I-forms. *Journal of Virology, 42*(3), 1099-1107.

Løset, G. Å., Roos, N., Bogen, B., & Sandlie, I. (2011). Expanding the Versatility of Phage Display II: Improved Affinity Selection of Folded Domains on Protein VII and IX of the Filamentous Phage. *PLOS ONE, 6*(2), e17433. doi:10.1371/journal.pone.0017433

Løset, G. Å., & Sandlie, I. (2012). Next generation phage display by use of pVII and pIX as display scaffolds. *Methods, 58*(1), 40-46. doi:10.1016/j.ymeth.2012.07.005

Lubkowski, J., Hennecke, F., Pluckthun, A., & Wlodawer, A. (1998). The structural basis of phage display elucidated by the crystal structure of the N-terminal domains of g3p. *Nature Structural Biology, 5*(2), 140-147.

Lubkowski, J., Hennecke, F., Plückthun, A., & Wlodawer, A. (1999). Filamentous phage infection: crystal structure of g3p in complex with its coreceptor, the C-terminal domain of TolA. *Structure, 7*(6), 711-722. doi:10.1016/S0969-2126(99)80092-6

Maguire, J. F., McTague, J. P., & Rondelez, F. (1980). Rotational Diffusion of Sterically Interacting Rodlike Macromolecules. *Physical Review Letters, 45*(23), 1891-1894. doi:10.1103/PhysRevLett.45.1891

Mai-Prochnow, A., Hui, J. G., Kjelleberg, S., Rakonjac, J., McDougald, D., & Rice, S. A. (2015). 'Big things in small packages: the genetics of filamentous phage and effects on fitness of their host'. *FEMS Microbiology Reviews, 39*(4), 465-487. doi:10.1093/femsre/fuu007

Malik, P., Terry, T. D., Bellintani, F., & Perham, R. N. (1998). Factors limiting display of foreign peptides on the major coat protein of filamentous bacteriophage capsids and a potential role for leader peptidase. *FEBS Letters, 436*(2), 263-266. doi:10.1016/S0014-5793(98)01140-5

Manning, M., Chrysogelos, S., & Griffith, J. (1981). Mechanism of coliphage M13 contraction: intermediate structures trapped at low temperatures. *Journal of Virology, 40*(3), 912-919.

Martin, A., & Schmid, F. X. (2003a). The folding mechanism of a two-domain protein: folding kinetics and domain docking of the gene-3 protein of phage fd. *Journal of Molecular Biology, 329*(3), 599-610. doi:10.1016/s0022-2836(03)00433-9

Martin, A., & Schmid, F. X. (2003b). A Proline Switch Controls Folding and Domain Interactions in the Gene-3-protein of the Filamentous Phage fd. *Journal of Molecular Biology, 331*(5), 1131-1140. doi:10.1016/S0022-2836(03)00864-7

Marvin, D. A. (1998). Filamentous phage structure, infection and assembly. *Current Opinion in Structural Biology, 8*(2), 150-158. doi:10.1016/S0959-440X(98)80032-8

Marvin, D. A., Hale, R. D., Nave, C., & Citterich, M. H. (1994). Molecular models and structural comparisons of native and mutant class I filamentous bacteriophages: Ff (fd, f1, M13), If1 and IKe. *Journal of Molecular Biology, 235*(1), 260-286. doi:10.1016/S0022-2836(05)80032-4

Marvin, D. A., Symmons, M. F., & Straus, S. K. (2014). Structure and assembly of filamentous bacteriophages. *Progress in Biophysics and Molecular Biology, 114*(2), 80-122. doi:10.1016/j.pbiomolbio.2014.02.003

Marvin, D. A., Welsh, L. C., Symmons, M. F., Scott, W. R., & Straus, S. K. (2006). Molecular structure of fd (f1, M13) filamentous bacteriophage refined with respect to X-ray fibre diffraction and solid-state NMR data supports specific models of phage assembly at the bacterial membrane. *Journal of Molecular Biology, 355*(2), 294-309. doi:10.1016/j.jmb.2005.10.048

Marzec, C. J., & Day, L. A. (1983). DNA and protein lattice-lattice interactions in the filamentous bacteriophages. *Biophysical Journal, 42*(2), 171-180. doi:10.1016/S0006-3495(83)84383-5

Marzec, C. J., & Day, L. A. (1988). A theory of the symmetries of filamentous bacteriophages. *Biophysical Journal, 53*(3), 425-440. doi:10.1016/S0006-3495(88)83119-9

Messing, J. (2016). Phage M13 for the treatment of Alzheimer and Parkinson disease. *Gene, 583*(2), 85-89. doi:10.1016/j.gene.2016.02.005

Meyer, T. F., & Geider, K. (1979). Bacteriophage fd gene II-protein. II. Specific cleavage and relaxation of supercoiled RF from filamentous phages. *Journal of Biological Chemistry, 254*(24), 12642-12646. doi:10.1016/S0021-9258(19)86362-7

Michel, B., & Zinder, N. D. (1989). Translational repression in bacteriophage f1: characterization of the gene V protein target on the gene II mRNA. *Proceedings of the National Academy of Sciences of the United States of America, 86*(11), 4002-4006. doi:10.1073/pnas.86.11.4002

Model, P., Horiuchi, K., McGill, C., & Zinder, N. D. (1975). Template activity of f1 RFI cleaved with endonucleases R·Hind, R·EcoP1 or R·EcoB. *Nature, 253*(5487), 132-134. doi:10.1038/253132a0

Mok, Y. F., & Howlett, G. J. (2006). Sedimentation Velocity Analysis of Amyloid Oligomers and Fibrils. In *Methods in Enzymology* (Vol. 413, pp. 199-217): Academic Press.

Monjezi, R., Tey, B. T., Sieo, C. C., & Tan, W. S. (2010). Purification of bacteriophage M13 by anion exchange chromatography. *Journal of Chromatography B, 878*(21), 1855-1859. doi:10.1016/j.jchromb.2010.05.028

Murata, K., & Wolf, M. (2018). Cryo-electron microscopy for structural analysis of dynamic biological macromolecules. *Biochimica et Biophysica Acta (BBA) - General Subjects, 1862*(2), 324-334. doi:10.1016/j.bbagen.2017.07.020

Nafisi, P. M., Aksel, T., & Douglas, S. M. (2018). Construction of a novel phagemid to produce custom DNA origami scaffolds. *Synthetic Biology, 3*(1). doi:10.1093/synbio/ysy015

Naiki, H., Higuchi, K., Hosokawa, M., & Takeda, T. (1989). Fluorometric determination of amyloid fibrils in vitro using the fluorescent dye, thioflavin T1. *Analytical Biochemistry, 177*(2), 244-249. doi:10.1016/0003-2697(89)90046-8

Nakashima, Y., Wiseman, R. L., Konigsberg, W., & Marvin, D. A. (1975). Primary structure and sidechain interactions of PFL filamentous bacterial virus coat protein. *Nature, 253*(5486), 68-71. doi:10.1038/253068a0

Newman, J., Swinney, H. L., & Day, L. A. (1977). Hydrodynamic properties and structure of fd virus. *Journal of Molecular Biology, 116*(3), 593-603. doi:10.1016/0022-2836(77)90086-9

Ngo-Duc, T.-T., Plank, J. M., Chen, G., Harrison, R. E. S., Morikis, D., Liu, H., & Haberer, E. D. (2018). M13 bacteriophage spheroids as scaffolds for directed synthesis of spiky gold nanostructures. *Nanoscale, 10*(27), 13055-13063. doi:10.1039/C8NR03229G

Nguyen, K. T., Adamkiewicz, M. A., Hebert, L. E., Zygiel, E. M., Boyle, H. R., Martone, C. M., . . . Hall, M. F. (2014). Identification and characterization of mutant clones with enhanced propagation rates from phage-displayed peptide libraries. *Analytical Biochemistry, 462*, 35-43. doi:10.1016/j.ab.2014.06.007

Nygaard, R., Kim, J., & Mancia, F. (2020). Cryo-electron microscopy analysis of small membrane proteins. *Current Opinion in Structural Biology, 64*, 26-33. doi:10.1016/j.sbi.2020.05.009

Okamoto, T., Sugimoto, K., Sugisaki, H., & Takanami, M. (1977). DNA regions essential for the function of a bacteriophage fd promoter. *Nucleic Acids Research, 4*(7), 2213-2222.

Opalka, N., Beckmann, R., Boisset, N., Simon, M. N., Russel, M., & Darst, S. A. (2003). Structure of the Filamentous Phage pIV Multimer by Cryo-electron Microscopy. *Journal of Molecular Biology, 325*(3), 461-470. doi:10.1016/S0022-2836(02)01246-9

Overman, S. A., Tsuboi, M., & Thomas, G. J., Jr. (1996). Subunit orientation in the filamentous virus Ff(fd, f1, M13). *Journal of Molecular Biology, 259*(3), 331-336. doi:10.1006/jmbi.1996.0323

Paczesny, J., & Bielec, K. (2020). Application of Bacteriophages in Nanotechnology. *Nanomaterials (Basel), 10*(10). doi:10.3390/nano10101944

Pande, J., Szewczyk, M. M., & Grover, A. K. (2010). Phage display: Concept, innovations, applications and future. *Biotechnology Advances, 28*(6), 849-858. doi:10.1016/j.biotechadv.2010.07.004

Panyam, J., & Labhasetwar, V. (2003). Biodegradable nanoparticles for drug and gene delivery to cells and tissue. *Advanced Drug Delivery Reviews, 55*(3), 329-347. doi:10.1016/S0169-409X(02)00228-4

Peters, E. A., Schatz, P. J., Johnson, S. S., & Dower, W. J. (1994). Membrane insertion defects caused by positive charges in the early mature region of protein pIII of filamentous phage fd can be corrected by prlA suppressors. *Journal of Bacteriology, 176*(14), 4296-4305. doi:10.1128/jb.176.14.4296-4305.1994

Praetorius, F., Kick, B., Behler, K. L., Honemann, M. N., Weuster-Botz, D., & Dietz, H. (2017). Biotechnological mass production of DNA origami. *Nature, 552*(7683), 84-87. doi:10.1038/nature24650

Prince, M., Wimo, A., Guerchet, M., Ali, G.-C., Wu, Y.-T., & Prina, M. (2015). *World Alzheimer Report 2015. The Global Impact of Dementia. An Analysis of Prevalence, Incidence, Cost and Trends*.

Rakonjac, J., Bennett, N. J., Spagnuolo, J., Gagic, D., & Russel, M. (2011). Filamentous bacteriophage: biology, phage display and nanotechnology applications. *Current Issues in Molecular Biology, 13*(2), 51-76.

Rakonjac, J., Feng, J., & Model, P. (1999). Filamentous phage are released from the bacterial membrane by a two-step mechanism involving a short C-terminal fragment of pIII. *Journal of Molecular Biology, 289*(5), 1253-1265. doi:10.1006/jmbi.1999.2851

Rakonjac, J., Jovanovic, G., & Model, P. (1997). Filamentous phage infection-mediated gene expression: construction and propagation of the gIII deletion mutant helper phage R408d3. *Gene, 198*(1), 99-103. doi:10.1016/S0378-1119(97)00298-9

Rakonjac, J., & Model, P. (1998). Roles of pIII in filamentous phage assembly. *Journal of Molecular Biology, 282*(1), 25-41. doi:10.1006/jmbi.1998.2006

Rakonjac, J., Russel, M., Khanum, S., Brooke, S. J., & Rajic, M. (2017). Filamentous Phage: Structure and Biology. *Advances in experimental medicine and biology, 1053*, 1-20. doi:10.1007/978-3-319-72077-7_1

Rakover, I. S., Zabavnik, N., Kopel, R., Paz-Rozner, M., & Solomon, B. (2010). Antigen-specific therapy of EAE via intranasal delivery of filamentous phage displaying a myelin immunodominant epitope. *Journal of Neuroimmunology, 225*(1), 68-76. doi:10.1016/j.jneuroim.2010.04.014

Rapoza, M. P., & Webster, R. E. (1993). The filamentous bacteriophage assembly proteins require the bacterial SecA protein for correct localization to the membrane. *Journal of Bacteriology, 175*(6), 1856-1859. doi:10.1128/jb.175.6.1856-1859.1993

Ravetch, J. V., Horiuchi, K., & Zinder, N. D. (1979). DNA sequence analysis of the defective interfering particles of bacteriophage f1. *Journal of Molecular Biology, 128*(3), 305-318. doi:10.1016/0022-2836(79)90090-1

Riechmann, L., & Holliger, P. (1997). The C-terminal domain of TolA is the coreceptor for filamentous phage infection of *E. coli*. *Cell, 90*(2), 351-360. doi:10.1016/s0092-8674(00)80342-6

Russel, M., Kidd, S., & Kelley, M. R. (1986). An improved filamentous helper phage for generating single-stranded plasmid DNA. *Gene, 45*(3), 333-338. doi:10.1016/0378-1119(86)90032-6

Russel, M., & Model, P. (1989). Genetic analysis of the filamentous bacteriophage packaging signal and of the proteins that interact with it. *Journal of Virology, 63*(8), 3284-3295.

Russel, M., Whirlow, H., Sun, T. P., & Webster, R. E. (1988). Low-frequency infection of F- bacteria by transducing particles of filamentous bacteriophages. *Journal of Bacteriology, 170*(11), 5312-5316. doi:10.1128/jb.170.11.5312-5316.1988

Sambrock, J., & W. Russel, D. (2001). *Molecular Cloning: A Laboratory Manual* (Third ed.). Cold Spring Harbor, N.Y.: Cold Spring Harbor Laboratory Press.

Sattar, S. (2013). *Filamentous phage-derived nano-rods for applications in diagnostics and vaccines : a thesis presented in partial fulfillment of the requirements for the degree of Doctor of Philosophy in Biochemistry at Massey University, Palmerston North, New Zealand*. (Doctor of Philosophy (Ph.D.) Doctoral), Massey University. Retrieved from http://hdl.handle.net/10179/5539

Sattar, S., Bennett, N. J., Wen, W. X., Guthrie, J. M., Blackwell, L. F., Conway, J. F., & Rakonjac, J. (2015b). Ff-nano, short functionalized nanorods derived from Ff (f1, fd, or M13) filamentous bacteriophage. *Frontiers in Microbiology, 6*(316). doi:10.3389/fmicb.2015.00316

Schägger, H., Cramer, W. A., & von Jagow, G. (1994). Analysis of molecular masses and oligomeric states of protein complexes by blue native electrophoresis and isolation of membrane protein complexes by two-dimensional native electrophoresis. *Analytical Biochemistry, 217*(2), 220-230. doi:10.1006/abio.1994.1112

Schägger, H., & von Jagow, G. (1991). Blue native electrophoresis for isolation of membrane protein complexes in enzymatically active form. *Analytical Biochemistry, 199*(2), 223-231. doi:10.1016/0003-2697(91)90094-A

Scheinberg, D. A., Villa, C. H., Escorcia, F. E., & McDevitt, M. R. (2010). Conscripts of the infinite armada: systemic cancer therapy using nanomaterials. *Nature Reviews Clinical Oncology, 7*(5), 266-276. doi:10.1038/nrclinonc.2010.38

Seddon, A. M., Curnow, P., & Booth, P. J. (2004). Membrane proteins, lipids and detergents: not just a soap opera. *Biochim Biophys Acta, 1666*(1-2), 105-117. doi:10.1016/j.bbamem.2004.04.011

Seow, Y., & Wood, M. J. (2009). Biological Gene Delivery Vehicles: Beyond Viral Vectors. *Molecular Therapy, 17*(5), 767-777. doi:10.1038/mt.2009.41

Sharma, P., Ward, A., Gibaud, T., Hagan, M. F., & Dogic, Z. (2014). Hierarchical organization of chiral rafts in colloidal membranes. *Nature, 513*, 77. doi:10.1038/nature13694

Shepherd, T. R., Du, R. R., Huang, H., Wamhoff, E.-C., & Bathe, M. (2019). Bioproduction of pure, kilobase-scale single-stranded DNA. *Scientific Reports, 9*(1), 6121. doi:10.1038/s41598-019-42665-1

Smeal, S. W., Schmitt, M. A., Pereira, R. R., Prasad, A., & Fisk, J. D. (2017a). Simulation of the M13 life cycle I: Assembly of a genetically-structured deterministic chemical kinetic simulation. *Virology, 500*, 259-274. doi:10.1016/j.virol.2016.08.017

Smeal, S. W., Schmitt, M. A., Pereira, R. R., Prasad, A., & Fisk, J. D. (2017b). Simulation of the M13 life cycle II: Investigation of the control mechanisms of M13 infection and establishment of the carrier state. *Virology, 500*, 275-284. doi:10.1016/j.virol.2016.08.015

Smilowitz, H. (1974). Bacteriophage f1 infection: fate of the parental major coat protein. *Journal of Virology, 13*(1), 94-99. doi:10.1128/JVI.13.1.94-99.1974

Smith, G. P. (1985). Filamentous fusion phage: novel expression vectors that display cloned antigens on the virion surface. *Science, 228*(4705), 1315-1317. doi:10.1126/science.4001944

Smrekar, F., Ciringer, M., Strancar, A., & Podgornik, A. (2011). Characterisation of methacrylate monoliths for bacteriophage purification. *Journal of Chromatography A, 1218*(17), 2438-2444. doi:10.1016/j.chroma.2010.12.083

Sohrab, S. S., Karim, S., Kamal, M. A., Abuzenadah, A. M., Chaudhary, A. G., Al-Qahtani, M. H., & Mirza, Z. (2014). Bacteriophage--a common divergent therapeutic approach for Alzheimer's disease and type II diabetes mellitus. *CNS & Neurological Disorders Drug Targets, 13*(3), 491-500. doi:10.2174/18715273113126660158.

Solomon, B. (2008). Filamentous Bacteriophage as a Novel Therapeutic Tool for Alzheimer's Disease Treatment. *Journal of Alzheimer's disease, 15*, 193-198. doi:10.3233/jad-2008-15205

Solomon, B., & Goren, O. (2011).Method For Treating Inflammation Associated With Amyloid Deposits And Brain Inflammation Involving Activated Microglia. US. US 81529406 A. https://lens.org/116-093-898-724-568

Solomon, B., & Goren, O. (2013).Method And Filamentous Phage For Treating Inflammation Associated With Amyloid Deposits And Brain Inflammation Involving Activated Microglia. US. US 8361458 B2. https://lens.org/135-485-677-555-934

Spagnuolo, J., Opalka, N., Wen, W. X., Gagic, D., Chabaud, E., Bellini, P., . . . Rakonjac, J. (2010). Identification of the gate regions in the primary structure of the secretin pIV. *Molecular Microbiology, 76*(1), 133-150. doi:10.1111/j.1365-2958.2010.07085.x

Specthrie, L., Bullitt, E., Horiuchi, K., Model, P., Russel, M., & Makowski, L. (1992). Construction of a microphage variant of filamentous bacteriophage. *Journal of Molecular Biology, 228*(3), 720-724. doi:10.1016/0022-2836(92)90858-H

Stine, W. B., Jungbauer, L., Yu, C., & LaDu, M. J. (2011). Preparing synthetic Aβ in different aggregation states. *Methods in Molecular Biology, 670*, 13-32. doi:10.1007/978-1-60761-744-0_2

Stopar, D., Spruijt, R. B., Wolfs, C. J. A. M., & Hemminga, M. A. (2003). Protein–lipid interactions of bacteriophage M13 major coat protein. *Biochimica et Biophysica Acta (BBA) - Biomembranes, 1611*(1), 5-15. doi:10.1016/S0005-2736(03)00047-6

Straus, S. K., Scott, W. R., Symmons, M. F., & Marvin, D. A. (2008). On the structures of filamentous bacteriophage Ff (fd, f1, M13). *European Biophysics Journal : EBJ, 37*(4), 521-527. doi:10.1007/s00249-007-0222-7

Suggs, S. V., & Ray, D. S. (1977). Replication of bacteriophage M13: XI. Localization of the origin for M13 single-strand synthesis. *Journal of Molecular Biology, 110*(1), 147-163. doi:10.1016/S0022-2836(77)80103-4

Tegunov, D., & Cramer, P. (2019). Real-time cryo-electron microscopy data preprocessing with Warp. *Nature Methods, 16*(11), 1146-1152. doi:10.1038/s41592-019-0580-y

Tesar, M., Beckmann, C., Röttgen, P., Haase, B., Faude, U., & Timmis, K. N. (1995). Monoclonal antibody against pIII of filamentous phage: an immunological tool to study pIII fusion protein expression in phage display systems. *Immunotechnology, 1*(1), 53-64. doi:10.1016/1380-2933(95)00005-4

Thonghin, N., Kargas, V., Clews, J., & Ford, R. C. (2018). Cryo-electron microscopy of membrane proteins. *Methods, 147*, 176-186. doi:10.1016/j.ymeth.2018.04.018

Trenkner, E., Bonhoeffer, F., & Gierer, A. (1967). The fate of the protein component of bacteriophage fd during infection. *Biochemical and Biophysical Research Communications, 28*(6), 932-939. doi:10.1016/0006-291X(67)90069-1

Urban, J. H., Moosmeier, M. A., Aumüller, T., Thein, M., Bosma, T., Rink, R., . . . Prassler, J. (2017). Phage display and selection of lanthipeptides on the carboxy-terminus of the gene-3 minor coat protein. *Nature Communications, 8*(1), 1500-1500. doi:10.1038/s41467-017-01413-7

Vaks, L., & Benhar, I. (2011). In vivo characteristics of targeted drug-carrying filamentous bacteriophage nanomedicines. *J Nanobiotechnology, 9*, 58. doi:10.1186/1477-3155-9-58

Van Den Hondel, C. A., Pennings, L., & Schoenmakers, J. G. (1976). Restriction-enzyme-cleavage maps of bacteriophage M13. Existence of an intergenic region on the M13 genome. *European Journal of Biochemistry, 68*(1), 55-70. doi:10.1111/j.1432-1033.1976.tb10764.x

Vieira, J., & Messing, J. (1982). The pUC plasmids, an M13mp7-derived system for insertion mutagenesis and sequencing with synthetic universal primers. *Gene, 19*(3), 259-268. doi:10.1016/0378-1119(82)90015-4

Vieira, J., & Messing, J. (1987). [1] Production of single-stranded plasmid DNA. In *Methods in Enzymology* (Vol. 153, pp. 3-11): Academic Press.

Vovis, G. F., Horiuchi, K., & Zinder, N. D. (1975). Endonuclease R-EcoRII restriction of bacteriophage f1 DNA in vitro: ordering of genes V and VII, location of an RNA promotor for gene VIII. *Journal of Virology, 16*(3), 674-684. doi:10.1128/JVI.16.3.674-684.1975

Wang, Y. A., Yu, X., Overman, S., Tsuboi, M., Thomas, G. J., & Egelman, E. H. (2006). The Structure of a Filamentous Bacteriophage. *Journal of Molecular Biology, 361*(2), 209-215. doi:10.1016/j.jmb.2006.06.027

Wittebole, X., De Roock, S., & Opal, S. M. (2014). A historical overview of bacteriophage therapy as an alternative to antibiotics for the treatment of bacterial pathogens. *Virulence, 5*(1), 226-235. doi:10.4161/viru.25991

Woolford, J. L., Steinman, H. M., & Webster, R. E. (1977). Adsorption protein of bacteriophage fl: solubilization in deoxycholate and localization in the fl virion. *Biochemistry, 16*(12), 2694-2700. doi:10.1021/bi00631a017

Worrall, L. J., Hong, C., Vuckovic, M., Deng, W., Bergeron, J. R. C., Majewski, D. D., . . . Strynadka, N. C. J. (2016). Near-atomic-resolution cryo-EM analysis of the *Salmonella* T3S injectisome basal body. *Nature, 540*(7634), 597-601. doi:10.1038/nature20576

Xu, H., Cao, B., Li, Y., & Mao, C. (2020). Phage nanofibers in nanomedicine: Biopanning for early diagnosis, targeted therapy, and proteomics analysis. *Wiley Interdiscip Rev Nanomed Nanobiotechnol, 12*(4), e1623. doi:10.1002/wnan.1623

Xue, C., Lin, T. Y., Chang, D., & Guo, Z. (2017). Thioflavin T as an amyloid dye: fibril quantification, optimal concentration and effect on aggregation. *Royal Society open science, 4*(1), 160696-160696. doi:10.1098/rsos.160696

Yan, Z., Yin, M., Xu, D., Zhu, Y., & Li, X. (2017). Structural insights into the secretin translocation channel in the type II secretion system. *Nature Structural & Molecular Biology, 24*(2), 177-183. doi:10.1038/nsmb.3350

Yanagida, M., & Ahmad-Zadeh, C. (1970). Determination of gene product positions in bacteriophage T4 by specific antibody association. *Journal of Molecular Biology, 51*(2), 411-421. doi:10.1016/0022-2836(70)90151-8

Yang, S. H., Chung, W.-J., McFarland, S., & Lee, S.-W. (2013). Assembly of Bacteriophage into Functional Materials. *The Chemical Record, 13*(1), 43-59. doi:10.1002/tcr.201200012

Yata, T., Lee, K.-Y., Dharakul, T., Songsivilai, S., Bismarck, A., Mintz, P. J., & Hajitou, A. (2014). Hybrid Nanomaterial Complexes for Advanced Phage-guided Gene Delivery. *Molecular Therapy - Nucleic Acids, 3*, e185. doi:10.1038/mtna.2014.37

Yi, H., Ghosh, D., Ham, M.-H., Qi, J., Barone, P. W., Strano, M. S., & Belcher, A. M. (2012). M13 Phage-Functionalized Single-Walled Carbon Nanotubes As Nanoprobes for Second Near-Infrared Window Fluorescence Imaging of Targeted Tumors. *Nano Letters, 12*(3), 1176-1183. doi:10.1021/nl2031663

Zahid, M., Phillips, B. E., Albers, S. M., Giannoukakis, N., Watkins, S. C., & Robbins, P. D. (2010). Identification of a Cardiac Specific Protein Transduction Domain by In Vivo Biopanning Using a M13 Phage Peptide Display Library in Mice. *PLOS ONE, 5*(8), e12252. doi:10.1371/journal.pone.0012252

Zhang, S. (2003). Fabrication of novel biomaterials through molecular self-assembly. *Nature Biotechnology, 21*(10), 1171-1178. doi:10.1038/nbt874

Zhang, Y. (2008). I-TASSER server for protein 3D structure prediction. *BMC Bioinformatics, 9*, 40. doi:10.1186/1471-2105-9-40

Zhou, J. C., Soto, C. M., Chen, M.-S., Bruckman, M. A., Moore, M. H., Barry, E., . . . Confer, T. S. (2012). Biotemplating rod-like viruses for the synthesis of copper nanorods and nanowires. *Journal of Nanobiotechnology, 10*(1), 18. doi:10.1186/1477-3155-10-18

Zimmermann, K., Hagedorn, H., Heuck, C. C., Hinrichsen, M., & Ludwig, H. (1986). The ionic properties of the filamentous bacteriophages Pf1 and fd. *Journal of Biological Chemistry, 261*(4), 1653-1655.

Zivanov, J., Nakane, T., Forsberg, B. O., Kimanius, D., Hagen, W. J., Lindahl, E., & Scheres, S. H. (2018). New tools for automated high-resolution cryo-EM structure determination in RELION-3. *Elife, 7*. doi:10.7554/eLife.42166

Zygiel, E. M., Noren, K. A., Adamkiewicz, M. A., Aprile, R. J., Bowditch, H. K., Carroll, C. L., . . . Hall, M. F. (2017). Various mutations compensate for a deleterious lacZα insert in the replication enhancer of M13 bacteriophage. *PLOS ONE, 12*(4), e0176421. doi:10.1371/journal.pone.0176421